UNIVERSITÀ DEGLI STUDI DI TRIESTE

XXVII CICLO DEL DOTTORATO DI RICERCA IN

SCIENZE E TECNOLOGIE CHIMICHE E FARMACEUTICHE

THEORETICAL STUDY OF MOLECULAR PHOTOIONIZATION: DIFFRACTION AND CORRELATION EFFECTS

Settore scientifico disciplinare: CHIM/02

DOTTORANDA:

AURORA PONZI

COORDINATORE:

PROF. MAURO STENER

SUPERVISORE DI TESI:

PROF. PIERO DECLEVA

ANNO ACCADEMICO 2013/2014

To thee, old Cause!
(Walt Whitman, Leaves of Grass)

Riassunto

Questa tesi raccoglie i risultati dell'attività di ricerca del mio dottorato che ha riguardato lo studio di molecole sottoposte a fotoionizzazione e il calcolo delle grandezze dinamiche coinvolte in questo tipo di processo. Una prima linea di ricerca ha seguito la descrizione degli effetti di interferenza e diffrazione nei profili di fotoionizzazione ad alte energie, attraverso un approccio basato sul metodo *Density Functional Theory* (DFT) accoppiato all'uso di una base di B-spline. Le oscillazioni derivanti da questi effetti di interferenza e diffrazione rappresentano un fenomeno universale, presente in tutte le molecole poliatomiche in esame, dalle biatomiche a quelle più complesse non simmetriche, dalla shell di core a quella di valenza più esterna. Nella regione di core abbiamo analizzato le oscillazioni presenti nel rapporto di intensità C2,3/C1,4 nello spettro di fotoelettone C 1s del 2-butino. Nella regione di valenza più interna abbiamo invece preso in esame gli spettri di fotoionizzazione di semplici molecole poliatomiche (propano, butano, isobutano e cis/trans-2-butene) e i risultati ottenuti sono stati confrontati con quelli sperimentali raccolti presso il sincrotrone Soleil di Parigi. Abbiamo poi analizzato l'effetto dovuto all'emissione coerente da centri equivalenti e quello dovuto alla diffrazione da atomi vicini non equivalenti negli spettri di core e di valenza. Nell'ambito di questa analisi, abbiamo preso in esame acetileni mono e disostituti con fluoro e iodio, comparando i risultati con quelli ottenuti nel caso del più semplice sistema acetilenico. Ci siamo inoltre occupati dello studio di effetti di intereferenza nella ionizzazione di valenza esterna di semplici idrocarburi e, nella stessa regione, abbiamo analizzato come la struttura geometrica di composti permetilati, in particolare la distanza metallo-anello, influenzi i loro profili di fotoionizzazione. Infine, nella regione di valenza interna, sono stati considerati i profili di ionizzazione per il caso di $Ar@C_{60}$. I risultati sono stati messi a confronto con quelli ottenuti da uno studio precedente sulla molecola di C_{60}.

Una seconda linea di ricerca ha invece seguito la descrizione delle osservabili di fotoionizzaione considerando il contributo della correlazione elettronica. Questo può essere fatto attraverso l'implementazione di un formalismo *close-coupling* dove la funzione del continuo finale è espressa secondo un'espansione analoga a quella *Configuration Interaction* (CI) per gli stati legati. Il primo livello dell'implementazione *ab initio* è stato quello di descrivere accuratamente solo la correlazione negli stati legati. A questo scopo, sono stati utilizzati gli orbitali di Dyson. L'uso di questi orbitali è stato applicato alla descrizione delle osservabili di fotoionizzazione nel caso della molecola biatomica CS. Nello spettro di questa molecola è infatti presente un satellite ben risolto dovuto a effetti di correlazione elettronica che non possono essere descritti a livello DFT.

Abstract

The thesis is focused on the study of the dynamics of photoemission processes for atoms and molecules. A first line of research has followed the description of diffraction and interference effects in the photoionization profiles at high energy for several systems, through an approach based on the DFT method combined with the use of a B-spline basis. These diffraction and interference effects appear in the spectra as a result of wave propagation. The resulting oscillations represent a general phenomenon, present in polyatomic targets, from diatomics to complex non-symmetrical molecules, and from the deep core to the outer-valence shell. Firstly, in the core region, we analysed the oscillations in the intensity ratio C2,3/C1,4 in the carbon 1s photoelectron spectrum for 2-butyne. Then in the inner-valence shell region, the interference effects in the photoionization spectra of simple polyatomic molecules (propane, butane, isobutane and cis/trans-2-butene) were studied and the results have been compared with experimental data collected at the SOLEIL Synchrotron in Paris.

Furthermore, we have analysed the effect due to coherent emission from equivalent centers and diffraction from neighbouring non-equivalent atoms in core and valence photoelectron spectra. For this, we investigated mono and disubstituted fluoro- and iodo-acetylenes and compared them to the simple acetylene system. We also focused on interference effects in the outer-valence ionization cross sections of simple hydrocarbons and, in the same shell, we also studied the influence of geometrical structures on photoionization profiles of permethylated compounds. Finally, in the inner-valence shell region, we considered the photoionization profiles for the case of $Ar@C_{60}$. The results were compared with a previous study on the C_{60} molecule.

A second line of research has followed the correlated description of photoionization observables. We developed a new method based on an *ab initio* close-coupling formalism. The use of the Dyson orbitals allowed to study the photoemission observables of highly correlated systems. As a first application of this method, we performed highly correlated calculations on the primary ionic states and the prominent satellite present in the outer-valence photoelectron spectrum of CS. Dyson orbitals are coupled to accurate one-particle continuum orbitals to provide a correlated description of energy-dependent cross sections, asymmetry parameters, branching ratios and Molecular Frame Photoelectron Angular Distributions (MFPADs).

Contents

Chapter 1

Introduction

1.1 Photoionization and historical background

One of the most common processes that may occur when incident light interacts with matter is *photoionization*. This is specifically defined as a physical process of interaction between electromagnetic radiation and atoms or molecules which causes the ejection of one or more electrons. Photoionization, in general, comes from excitation of valence electrons to the *continuum*, but it is also possible that the photon energy is high enough to ionize inner-shell electrons.

The technique called *Photoelectron spectroscopy* (PES) utilizes photoionization and through the analysis of the spectra corresponding to the emitted electrons (*photoelectrons*), one can obtain rich and detailed information on the processes involved and the examined targets [1, 2]. PE spectroscopy is distinguished from conventional forms of spectroscopy because it uses electrons instead of photons as its primary source of information. This technique measures the kinetic energies of ejected electrons rather than the absorbance or transmittance of photons [3].

The application of PE spectroscopy to molecules in gas phase has contributed significantly to our understanding of chemical bonding in molecules of different sizes, as well the understanding of electronic configuration and mechanisms of chemical reactions. This technique, from a theoretical perspective, has justified the use of the molecular orbitals in the discussion of chemical processes and has rendered these orbitals, for a long time considered as abstract entities, accessible to experimental studies [4]. The result of a PE experiment is a PE spectrum and molecular orbitals provide a simple basis for its interpretation. The analysis of

a spectrum consists of assigning each spectral band to an electronic state of the molecular ion and identifying the orbitals from which electrons are ejected. As a consequence, a PE spectrum represents a unique signature of a molecule and PE spectroscopy is a powerful method for chemical analysis. In particular, since the positions of lines in a PE spectrum correspond to energy differences between the levels of a neutral and ionic species, this technique also permits one to derive spectroscopic information on molecular ions. This is typically very difficult to study at high resolution because of their high reactivity.

Furthermore, employing PE spectroscopy allows one to obtain the direct measures of the ionization potentials. These potentials can be related to other properties such as electron affinities and dissociation energies. In the beginning of the development of this spectroscopic technique, the studies focused on simple systems, such as rare-gas atoms or small closed-shell molecules and strong transitions (photolectron main lines) in a very limited energy range. Whereas, today a wide variety of systems, including open-shell molecules, ions and clusters are object of study. In addition, not only main lines, but also satellite transitions, multiple-electron ejections and ionization of excited states can be observed and described in detail [5].

Thus far we have illustrated the reasons that make PE spectroscopy a fundamental technique in chemistry and physical chemistry. In the present work we study, from a theoretical perspective, the photoionization process applied to samples in gas phase and the specific effects connected to that. Indeed it is worth highlighting the importance of theoretical studies related to this technique and the symbiosis constituted from the complementary nature of PE spectroscopic measurements and quantum chemical predictions [6, 7]. The theory permits us to understand and predict the results of experimental investigations and, at the same time, electron spectra constitute ideal test cases for different theoretical methods.

Historically, theoretical studies for the interpretation of spectra from atoms and molecules went hand in hand with experimental developments. The basic interpretation of the various phenomena by means of one-electron concepts evolved mainly during the 1960s and early 1970s until to inclusion of many-electron contributions. This is due to the ability of the experimental techniques to consider the many-electron features in the spectra and also to the development of computational schemes for many-electron wave functions. In general, developments in the theory permitted one to obtain a plethora of information that can be derived by analysing different aspects of a PE spectrum. PE spectroscopy is based

on the photoelectric effect. This effect, discovered by Heinrich Hertz in 1887 [8], concerned the interaction between a solid and light, and refers to the emission of charged particles by the surface of the solid when it absorbs electromagnetic radiation. This is the first observation of the ionization of matter and represents the precursor of the photoelectric effect in the gas targets.

Hertz's discovery caught the attention of many scientists. From the experimental point of view, several investigations were carried out by Wilhelm Hallwachs [9], Julius Elster, Hans Geitel [10] and Philipp Lenard [11]. The latter concluded, in 1900, that the charged particles emitted were the same as those found in cathode rays.

It was necessary to wait until 1905 to have a theoretical interpretation of the photoelectric effect. During his *Annus Mirabilis*, Albert Einstein published the formulation of this effect in terms of photons [12]. He explained the ejection of electrons from the surface of a metal, in response to incident light, on the basis of Max Planck's hypothesis [13], according to which light behaves like small particles (light quanta or, indeed, photons). Einstein's interpretation of the photoelectric process is a statement of conservation of energy: the photon is absorbed if its energy exceeds the binding energy of an electron in the bound state of the target and any energy in excess of the ionization energy appears as the kinetic energy of the ejected electron.

The ionization process, starting from the discovery and interpretation of the photoelectric effect, has continued to be the object of many experimental and theoretical studies. It permits one, indeed, to obtain important and detailed informations about the chemical and physical properties of matter.

An extremely important contribution to the experimental developments in high-precision spectroscopic techniques, based on the photoelectric effect, came from the physicist Karl Siegbahn (Nobel prize 1924). He developed an apparatus to accurately measure the X-ray wavelengths produced by atoms of different elements. This experimental technique represented, therefore, a powerful tool to identify elements and to provide detailed information about their physical environment.

The modern PES was chiefly developed during the 1950s and 1960s when the physicist Kai Siegbahn (Nobel prize 1981) and coworkers built an instrument to study high energy photoelectrons expelled by X-radiation at very high resolution [14]. Until then, experimental difficulties related to high resolution electron detection hindered the physical and chemical applications of electron spectroscopy.

In the Siegbahn's laboratory, the electron spectroscopy was originally used to measure the electron binding energies in atomic and solid state physics and, in the subsequent years, this spectroscopy began to have important applications in chemistry. The research developed by Siegbahn resulted in the birth, in 1965, of *Electron Spectroscopy for Chemical Analysis* (ESCA) [15, 16]. This spectroscopy permits one to analyse solids, liquids and gaseous species as well. During the same period, David Turner at Imperial College developed the *Ultraviolet photoelectron spectroscopy* (UPS) on molecular species using helium lamps. In 1962 he published his first paper on the determination of ionization potentials by photoelectron energy measurement [17].

It is clear from the historical development of PES that the most common types of radiation used were vacuum UV radiation and X-rays [14–16, 18–20]. The first one permits us to examine valence levels with high resolution ($\sim$0.01 eV), whereas the latter allows the ejection of electrons from both valence and core orbitals, but with a low resolution ($\sim$0.5 eV). Historically, most spectroscopic studies examined the valence-shell excitation regions. For a considerable time, the difficulty in investigating the inner-shell region was due to the lack of appropriate light sources, characterized by low intensity and poor coherence. Furthermore, since traditional sources furnish high intensities but only at certain characteristic energies, they cannot be used to probe the photon energy dependence of PE spectra. Development of *Synchrotron radiation* (SR) has filled the gap between the low energy (VUV) and high-energy (X-ray) sources and has permitted one to extend the knowledge of the electronic structure of atoms and molecules.

The observation of synchrotron radiation for the first time dates back to 1947, in the General Electric Research Laboratory in Schenectady, New York, and it was used to study collisions between high energy particles [21]. The physicists who conducted the experiment observed a brilliant beam of light emanating from the machine. It was a result of the electrons moving with speeds close to the speed of light in the accelerator track. This process has been exploited in many experiments over the years after 1947, but all of them employed machines that had been originally directed to study high-energy particle physics. One of the most significant steps forward to use synchrotron radiation to study light-matter interaction took place at the end of the 1970s, when a plan was approved to build the world's first dedicated synchrotron light source producing X-rays at Daresbury in the UK. It started to carry out experiments in 1981. Today there are more than 50 synchrotron light sources all over the world dedicated to generating synchrotron light

and supporting a huge range of applications, from condensed matter physics to structural biology, engineering, environmental science and medicine. The new generation of synchrotron radiation sources (such as ELETTRA in Italy and SOLEIL in France) include ondulators that force the electrons (or positrons) to go through sinusoidal or spiral trajectories. Monochromators and reflection mirrors are set up in the beam line according to the purpose and characteristics of the radiation to be used in an experiment. Synchrotron radiation, together with these additional devices, constitutes a powerful research tool to investigate outer and inner-shell excitations and ionization processes in the molecules.

Historical remarks

- 1887, Heinrich Hertz: photoelectric effect. "On an effect of UV light upon the electrical discharge" [8].
- 1895, W. K. Röntgen: discovery of X-rays.
- 1897, J. J. Thomson: cathode ray tube experiments for measuring e/m of electrons (a primitive electron spectrometer).
- 1905, A. Einstein equation for the photoelectric effect. "Heuristic viewpoint on the production and conversion of light" [12].
- 1907: P. D. Innes "On the velocity of the cathode particles emitted by various metals under the influence of Röntgen rays" [22].
- 1914, Robinson and Rawlinson: photoemission from X-ray irradiated Au.
- 1925, H. Robinson "An accurate knowledge of the energies associated with the different electronic orbits within the atoms is essential to the further development of the theory of atomic structure" [23].
- 1950, R. G. Steinhardt Jr. "An X-ray photoelectron spectrometer for chemical analysis" (Leihigh University, Ph.D. thesis), "X-Ray Photoelectron Spectrometer for Chemical Analysis" [24].
- 1954, Kai Siegbahn: high resolution photoelectron spectrometer.

Thus far we have illustrated the process for which absorption of radiation

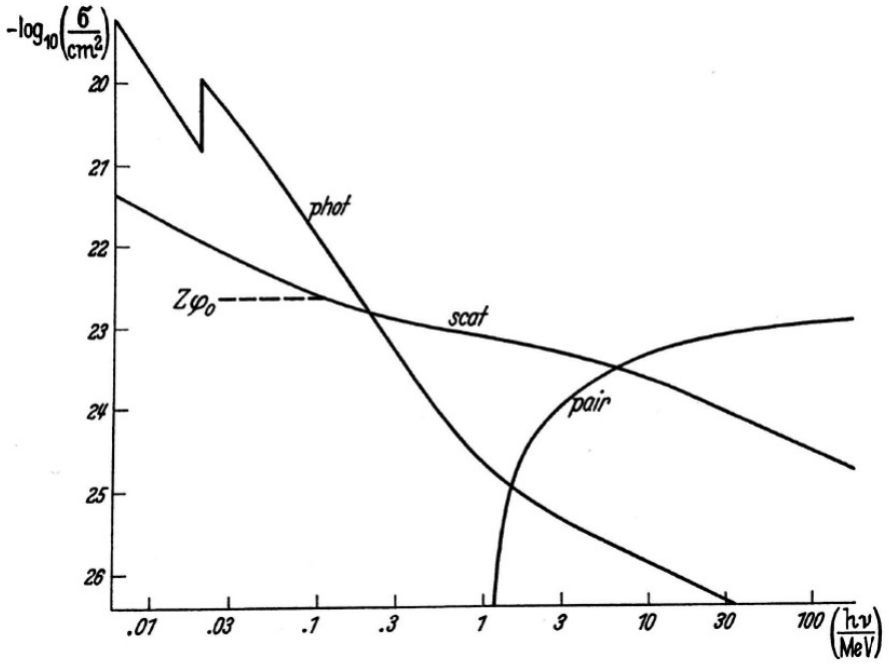

FIGURE 1.1: The cross sections σ for various processes undergone by a photon of energy $h\nu$ in passing through molybdenum (Z = 42), plotted on a log-log scale. The curves labelled "phot", "scat" and "pair" are for photoelectric absorption, photon scattering and pair creation, respectively. The dotted line labelled $Z\varphi_0$ is the Thomson cross-section from Z free electrons.

by an atom in a bound state causes the ejection of one of its electrons into a continuum state, and how this process has been exploited, in the course of time, in the development of PE spectroscopy. However, there are other effects which also contribute to the attenuation of X-rays while passing through matter. One of these is the scattering of a photon by an electron, called Compton scattering, in which the photons change energy as well as the direction in contrast with the case of elastic scattering. It is interesting to consider the existence of different processes and at which energy they become dominant with respect to each other by observing the cross-section profile for the case of molybdenum in Fig. 1.1 [25]. By considering the different cross-section profiles plotted on a logarithmic scale we can observe that, at low energies, the atomic photoelectric effect predominates, while at intermediate energies this effect is much less important than Compton scattering. The effect of the relative motion of the electrons with respect to the incident photon beam can be noted, instead, at extremely relativistic energies. In this energy range, the photon attenuation by pair creation competes with the photoelectric effect and scattering. This two-particles process is a specific effect of the Dirac theory and consists of the creation of the electron-positron pair.

Although, on the one hand, the photoelectric effect provides indisputable evidence for a corpuscolar theory of light, the existence of diffraction and interference phenomena demonstrate that light also exhibits a wave behaviour.

The dual aspect of electromagnetic radiation had animated the debate within the scientific community, starting from the contrast between the positions of Isaac Newton, in favour of a particle-like behaviour, and that of Christian Huygens, supporter of the wave-like interpretation. The experiment carried out by Young in 1801, known as the Young's double-slit experiment [26], proved the wave character of light. He observed that the light, passing through two slits placed in a panel, formed an interference pattern on a screen behind the panel. The contradictory behaviours of the light were explained by its duality nature, which constitutes the heart of Quantum Mechanics. An analogous situation is revealed in interference and diffraction effects observed in photoionization. These processes are related to the fact that, at high photon energy, the wavelength of the ejected electron is comparable to or smaller than the size of the molecule, and, consequently, ejected electrons are subjected to the same phenomena of normal waves. Wave-particle duality is in fact a basic property of all quantum objects and the double-slit experiment has been, in the course of scientific development, the precursor of similar experiments performed on small molecules as well as on heavy species such as fullerenes. H. Cohen and U. Fano were the first, in 1966, to theorize the possibility of realizing the double-slit experiment in the photoionization of homonuclear, diatomic molecules [27]. Their research was directed towards the interpretation of the oscillatory behaviour of the photoabsorption spectra of N_2 and O_2 molecules. In this case, indeed, the electrons are emitted by two equivalent atomic centers, constituting, therefore, a molecular equivalent of the Young's double-slit experiment. The absorption of a single photon by the homonuclear molecule generates two coherent electron waves which give rise to interference oscillations. They proposed a wavefunction to describe coherent emission from both atomic sites and to predict oscillating partial cross-sections of photoelectron emission. J. L. Dehmer and D. Dill, in 1975, published a paper on the study of the partial photoionization cross sections of N_2 [28]. The weak modulation in these profiles was interpreted as a diffraction pattern. Their study, however, established the effect for the photoionization of core electrons in N_2 (K shell), rather than of valence electrons, as Cohen and Fano had reported. S. E. Canton et al. [29], after the investigation on valence photoionization for N_2 and H_2, obtained evidence that valence photoionization could produce interference behaviour. They also observed the presence of

Cohen-Fano oscillations also in heteronuclear diatomic molecules such as carbon monoxide (CO). In these molecules, the inner-most electrons are almost completely localized at either of the two atoms, so that Cohen-Fano oscillations cannot occur. However, if the delocalization of the valence orbitals of CO is sufficiently large to cover both atoms in the molecule, then the emission of electrons could become coherent. These findings reveal that delocalized orbitals can represent a source of two-centre interference, analogous to a Young's double-slit experiment in which the two slits have different widths.

In recent years the interference studies have been focused on larger systems, such as C_{60} [30–42]. Fullerenes may be regarded as three-dimensional molecular double-slits, exhibiting photoemission behaviour similar to that of one-dimensional diatomic molecules. The new measurements of the partial cross section data over a large energy range, related to the development of synchrotron radiation sources, permitted one to analyse the observed oscillations in terms of the structural information of fullerene. The interference and diffraction patterns constitute, finally, a great potential for future applications and an interesting subject of research with many unexpected results still to be revealed.

1.2 Fundamentals

1.2.1 Experimental setup

The fundamental experiment in PE spectroscopy consists in exposing the target to an incident radiation with an sharply defined energy $h\nu$ and then observing the resultant emission of photoelectrons. From each emitted photoelectron, one can evaluate ionization energy, intensity as a function of photon energy and angular distribution. These properties permit one to have an insight about the electronic structure of the target molecules.

The basic structure of a photoelectron spectrometer is constituted by: a source of electromagnetic radiation, a sample chamber, an energy analyser, an electron detector and, finally, a recorder [43]. The sources of radiation used in a photoelectron experiment, as already mentioned, are: VUV, X-rays and synchrotron radiation (SR). The VUV source is usually the He(I) resonance line [18] at 21.2 eV or the He(II) line [44] at 40.8 eV. They are generated by the discharge through helium gas. For the case of X-rays, indeed, the two most commonly used

sources are Mg Kα radiation and Al Kα radiation generated in an X-ray anode with energies of, respectively, 1253.6 eV and 1486.6 eV. The third source of radiation, finally, is the SR source which is the most useful continuum source for PE spectroscopy. In a synchrotron light source the electrons are forced, by means of magnetic fields, to move over approximately circular orbits, with speed near to the speed of the light. The centripetal force, acting on the relativistic electrons, renders them sources of electromagnetic radiation, which is conveyed in suitable ramifications on the outside of the ring (called *beamlines*). The result is light with very peculiar characteristics that make it different from the conventional sources of radiation and, consequently, a unique tool for PES experiments [45–47]. The radiation emerging from storage ring has an intensity that can be of the order of a billion times greater respect to that from a conventional X-ray source and, furthermore, is characterized by intense spectral brightness. The divergence of the beam is very low, that is, the beam is highly collimated and SR is pulsed with pulses typically 10 to 100 picoseconds in length separated by 10 to 100 nanoseconds. SR is almost 100% polarized in the plane of the ring and extends from infrared light to hard X-rays. This means that its spectrum is a smooth continuum. The SR is also unique for its tunability that enables the user to select a wavelength appropriate for the experiment.

The most important component in a PE spectrometer is the energy analyzer, which receives the electrons emitted when photoionization occurs in the sample. The analyser separates the photoelectrons with respect to their kinetic energy and, finally, counts them furnishing an intensity distribution which represents the PE spectrum. The aim of the electron analyser is to provide high resolution and high sensitivity. The most common type of this instrument used in PES is the deflection analyzer: it uses electric or magnetic fields to make electrons of different energies follow different paths, in order to separate them.

After passing through the energy analyser, the photoelectrons reach the detector. The type especially used to detect the electron flux is called the electron multiplier. This operates on the basis of a cascade effect wherein secondary electrons are produced by the primary ejected electrons which strike the walls of the multiplier. At the end of this process, a current pulse, which can be detected and recorded, is produced. On the one hand, a spectrometer in which electrons of only one energy a time are able to reach the detector produces *differential spectra*. On the other hand, spectrometers in which all electrons of more than a certain energy can reach the detector simultaneously produce *integral spectra*.

The performance of an instrument can be evaluated by considering the accuracy with which it can measure the energies and relative intensities of the photoelectrons. Accurate energy measurements depend both on the resolution of the spectrometer and on the proper calibration of the instrumental energy scale.

1.2.2 Photoelectron spectra and IP

The result of a photoelectron experiment, as already specified, is a spectrum, that is a record of the number of ejected electrons detected at each energy. In a PE spectrum, the information about the energy distribution of the emitted electrons can be extracted from three principal sources: line energies, line intensities and line shapes (in particular the widths). When the electrons are ejected from different energy levels of a molecule, the molecular ions in different electronic states are produced. The ionization energies, which are measured, are the energy differences between the ground state of the molecule and the electronic states of the molecular ion. The PE spectrum contains, indeed, many vibrational lines for each type of electron ionized. The collection of lines that corresponds to ionization from a molecular orbital constitutes a band. The energies associated to these bands correspond to the energies of the ion states formed with respect to the ground state of the system considered. The analysis of a PE spectrum consists, in part, in assigning each spectral band to an electronic state of the molecular ion and identifying the orbital from which the electron is ejected. The simplest way to individuate the number and the type of ion states accessible on ionization is based on the use of Molecular orbitals (MOs). In each orbital of an atom or molecule, the electrons have a characteristic binding energy and, according to Koopmans' theorem, the negative of the energy of an occupied orbital from a theoretical calculation is equal to the vertical ionization energy due to the removal of an electron from that orbital [48]. This theorem, which is a good and very useful approximation, translates into the fact that the PE spectrum of a molecule is a direct representation of the molecular orbital energy diagram. In order to find a first and clear relationship between PE spectra and molecular electronic structure, it is possible to use two approximate rules [2]. The first is that each band in the spectrum corresponds to ionization from a single MO; the second is that each occupied MO of binding energy less than hν gives rise to a single band in the spectrum. These rules represent, however, a simplification because, in a spectrum, one can observe more bands with respect to the number of valence orbitals in the

molecule. This evidence is due to the fact that there are several mechanisms that lead to additional bands. These can stem, firstly, from the ionization of one electron with simultaneous excitation of a second electron to an unoccupied excited orbital. This is referred to as a two-electron process. Furthermore, additional bands can be generated by the ionization from a degenerate occupied orbital, as well as from molecules which have unpaired electrons, such as O_2 or NO. In these illustrated cases, the inadequacy of the Koopmans' theorem is evident.

Line intensities represent the second source of information in a PE spectrum. Band intensities, contrary to ionization energies, vary with photon energy. The use of the synchrotron radiation, characterized by continuous tunable radiation, has permitted one to carry out more extensive studies of PE band intensities. While the absolute intensities of different peaks in the spectrum are very difficult to control because they depend on a number of experimental variables (such as intensity of incident radiation, type of energy analyser, sensitivity of the electron detector and so on), the relative intensities represents the relative probabilities of photoionization to different states of the ion, called *partial ionization cross-sections*. In addition to the wavelength of the light used, relative bands intensities and their vibrational structures depend also on the nature of the molecular orbitals. The changes in molecular geometry can occur when one electron is ejected from an orbital and they can be analysed by observing the detailed form of the bands. These changes furnish information about the character of the orbitals, namely whether they are bonding, anti-bonding or non-bonding.

The quantity which is measured in a PE experiment is the ionization energy. This is defined as the minimum energy required to move to infinity an electron from the atom or molecule isolated in free space and in its ground electronic state. This quantity is also called ionization potential (IP). The ionization energies observed in PE spectroscopy are the energy differences between the ground state of the molecule and the electronic states of the molecular ion. A prior knowledge of the energies and the character of the occupied orbitals in the molecule, as well as a theoretical determination of the IPs, are necessary in order to analyse correctly a spectrum and exploit the information contained in it. The IPs can be calculated, at first approximation, using total energies calculated in the Hartree-Fock (HF) scheme [49–51] or within more sophisticated methods, such as Configuration-interaction (CI) [52]. In order to obtain reliable values for the IPs, the initial and final state energies have to be calculated to a very high degree of accuracy. In

particular, great care must be taken to ensure that the correlation in both the initial and the final states is considered.

1.3 Basic observables

For each final ionic state, the basic measurable quantities which can be obtained from a PE experiment, and, at the same time, which can be predicted theoretically, are cross sections, asymmetry parameters and *Molecular Frame Photoelectron Angular Distributions* (MFPADs). In this section we highlight their meaning, together with their main characteristics. A more exhaustive study of these observables will be done in Chapter 2.

1.3.1 Cross section

One of the main aims of photoionization is the determination of cross sections. The cross section is proportional to the probability of photoionization to an ionic state [53]. This observable permits us to have a clear knowledge about electronic structure of atoms and molecules. In the course of time, the cross sections calculations have become increasingly accurate. The first PE studies were restricted to determine the line positions in the spectrum and in deriving electron binding energies. Progressively the attention began to concentrate on line intensities as well. The first measurements of partial photoionization cross sections were made using discrete photon sources (VUV and X-ray), until the advent of monochromatized synchrotron radiation. The use of discrete photon sources prevented the investigation of the photon-energy dependent partial cross section behaviour. At the same time, the theory made several advances in the calculation of behaviour of partial cross section, predicting characteristic features, such as shape resonances, Cooper minima [54] and 'many-electron' effects [55].

A more specific and informative quantity, rather than the total cross section which corresponds to the sum of all emitted photoelectrons, is the partial cross section [55], which is given by

$$\sigma_{if}(h\nu) = \frac{4\pi^2 \alpha a_0^2}{3} h\nu \sum_{lm} |\bar{M}_{iflm}|^2 \tag{1.1}$$

where α is the fine-structure constant, a_0 the Bohr radius, and $h\nu$ the photon energy. The matrix element M_{iflm} describes, in the dipole approximation [56], the dipole transition between the initial state i and the final state f:

$$|\bar{M}_{iflm}|^2 = |\langle flm| \sum_{\mu} \bar{r}_{\mu} |i\rangle|^2 \tag{1.2}$$

with $\sum_{\mu} \bar{r}_{\mu}$ being the dipole operator of the n-electron system. The photoionization is, then, a dipole transition between the initial and final states and the transition probability is controlled by the above defined dipole transition moment.

1.3.2 Asymmetry Parameter

When the monochromatized photon beam of energy $h\nu$ interacts with an atom or a molecule, the detection of electrons emitted towards the entrance slit of the electron spectrometer will give an angle-resolved signal and yield information on the spatial distribution of the photoelectrons when the spectrometer is set at different positions in space. In general, the emission pattern of photoelectrons is not isotropic in space, but possesses a characteristic angular distribution. The angle-resolved measurements, through the study of the angular distribution of photoelectrons, provide a further step towards a detailed understanding of the photoionization process and the nature of the states involved in photoelectron transitions. These measurements, over wide energy ranges, permit one to determine the so-called angular distribution asymmetry parameter β, which represents the angular distribution of electrons emitted after photoionization. The asymmetry parameter takes its name from the fact that, in the early days, the angular distribution was studied at a high photon energy where the dipole approximation breaks down and there is a forward/backward asymmetry with respect to the direction of an unpolarized photon beam. The characterization of orbitals according to their asymmetry parameters β and an understanding of the variation of β with photon energy can yield useful information about ionic states.

This characteristic quantity is expressed in the expression of the differential partial cross section, which for linearly polarized light is [57]

$$\frac{d\sigma_{if}(h\nu)}{d\Omega}(\theta) = \frac{\sigma_{if}(h\nu)}{4\pi}[1 + \beta_{if}(h\nu)P_2(cos\theta)] \tag{1.3}$$

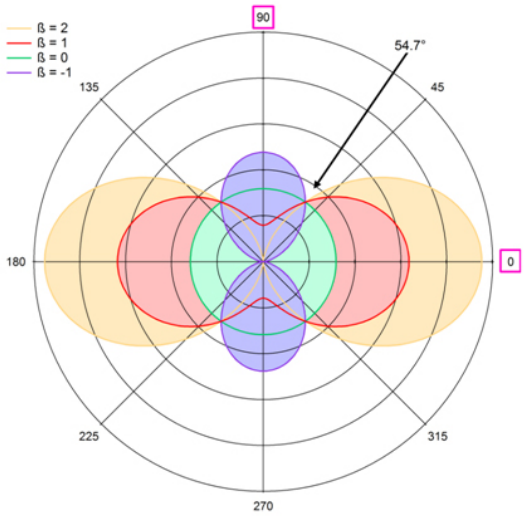

FIGURE 1.2: Polar plots of the photoelectron differential cross section with four different values of β. The polar angle β is the angle between the polarization vector of light and the electron velocity vector (axis of the electron detector). The arrow points to an angle of 54.7^o, at which the cross sections are the same independently of β (this angle is so important in electron spectroscopy that it is called a magic angle).

with θ being the angle between the electric vector of the photon beam and the direction of the outgoing electron, and $P_2(cos\theta)$ the Legendre polynomial of second degree. At the so-called 'magic angle' $\theta = 54.7^o$ (assuming 100% linear polarization), this polynomial becomes zero and therefore the differential partial cross section becomes proportional to the integral partial cross section. The shape of the angular distribution pattern is determined from the numerical value of β. In the particular case of photoionization of an s-electron and for negligible spin-orbit effects, the β parameter has the energy-independent value β=2. This case applies, for example, to 1s photoionization in helium. In the general case, the β parameter varies between 2 and -1 because different amplitudes contribute to the photoionization process (Fig. 1.2).

1.3.3 MFPADs

Gas-phase free molecules are randomly oriented in space and then it needs introduce an anisotropy parameter that describes the photoelectron angular distributions (PADs) in the laboratory frame. However, especially from a theoretical perspective, is more natural to consider molecular photoionization by using a molecular frame [58, 59]. The molecular frame PADs (MFPADs) may be used

to extract further information about the target molecule. Measuring PADs from fixed-in-space molecules has been a goal for researchers since the 1970s when it was first proposed by Dill [60] to be a *"much richer source of information on photoionization dynamics, being able to probe details "washed out" by the freely tumbling molecules of typical gas phase experiments"*. In the last decade, significant experimental efforts have been directed to MFPAD measurements. An important progress in the MFPAD measurements has been brought by the use of the position sensitive detectors [61–64]. By employing these detectors, one can extract three-dimensional momentum from the information about the detected position and arrival time for each of the charged particles recorded in coincidence.

1.4 Outline

The first part of this manuscript is dedicated to the theory of photoionization processes (Chapter 2), by illustrating the approximations and mathematical procedures used to express the differential cross sections and the boundary conditions for ionization processes. The different approximations for the expression of the final wavefunction will be detailed, with particular attention paid to the effects of electronic correlation. In Chapter 3 an overview of the standard quantum methods used in our study is presented. This overview is followed by a discussion of the multicenter B-spline static-exchange DFT method (Chapter 4), employed to obtain the first part of the results. Then Chapter 5 is devoted to the treatment of the correlated single channel approach, in particular to the exposition of Dyson orbitals. The second part of the thesis is introduced by an overview (Chapter 6) related to the results obtained studying the interference and diffraction patterns for different systems (from Chapter 7 to Chapter 12). Finally, Chapter 13 will present the results obtained with the correlated single channel approach.

Part I

Theory

Chapter 2

Theory

2.1 The photoionization processes

When an atomic or molecular system absorbs electromagnetic radiation of sufficiently high frequency, the final state may lie in the continuum and one or more electrons will be ejected from it. This process is known as *photoionisation*. The *electronic continuum* of the system is defined as the collection of all states of the system in which one electron is free and the residual system is in a state of definite energy. The study of continuum states is generally more complex than that of bound states. The analysis of the structure and properties of continuum states is treated by *scattering theory* [65]. The results of scattering experiments are usually expressed in terms of cross section, which is used to measure the probability of a certain collision event. Both classical and quantum mechanical scattering are characterized by this quantity. Before turning to quantum scattering, let us consider the scattering process in a classical picture. This will allow us to obtain a simple expression of cross section.

2.1.1 The classical cross section

Let us consider the scattering of a particle by a fixed target. We can measure the momentum of the projectile before and after collision. From a single passage of the projectile, we can know only if it hit the target or not. Repeating the experiment many times with the same incident momentum, $\mathbf{k}_0$, but with random

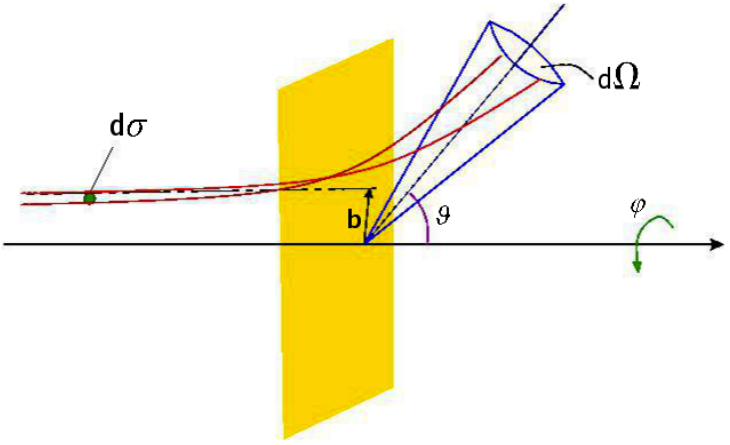

FIGURE 2.1: Schematic illustration of the scattering process. b is the impact parameter, contained in the plane perpendicular to the particles flux. $d\sigma$ is the area crossed by the particles scattered into the solid angle $d\Omega$.

impact parameters [1], we can consider the number n_{inc} of projectiles incident per unit area perpendicular to $\mathbf{k}_0$ (Fig. 2.1). Then the relation between the total number of scattered particles N_{scat} and n_{inc} is given by

$$N_{scat} = n_{inc}\sigma, \tag{2.1}$$

where σ is the cross-sectional area of the target normal to $\mathbf{k}_0$. This quantity can be, at this point, simply found by measuring N_{scat} and n_{inc}, or equivalently the fluxes $j_{scat} = \frac{N_{scat}}{\Delta t}$ and $j_{inc} = \frac{n_{inc}}{\Delta t}$, where the flux corresponds to the number of particles crossing the unit area in the unit of time.

Considering scattering in any given direction, we can write an analogous relation by taking into account the number of particles scattered into the solid angle $\Delta\Omega$. Then we have the relation:

$$N_{scat}(\Delta\Omega) = n_{inc}\sigma(\Delta\Omega), \tag{2.2}$$

where $\sigma(\Delta\Omega)$ represents the cross section of that part of the target which scatters into $\Delta\Omega$. The cross section is proportional to $\mathrm{d}\Omega$ in the limit of a small solid angle. One can then write:

$$\sigma(d\Omega) = \frac{d\sigma(\Omega)}{d\Omega} d\Omega, \tag{2.3}$$

where $\mathrm{d}\sigma/\mathrm{d}\Omega$ is called the *differential cross section* and represents the measurable quantity in scattering experiments.

[1] the impact parameter is defined as the distance of the center of the target from the incident trajectory

2.1.2 Differential cross section

In Quantum Mechanics, the photoionization process is a transition from an initial bound state, Ψ_0^N, to a final state characterized by a well defined bound state of the ion, Ψ_I^{N-1}, and a photoelectron with a well defined asymptotic momentum, $\mathbf{k}$. Hence the final state, $\Psi_{I\mathbf{k}}^{(-)}$, is characterized by the quantum numbers I and the momentum $\mathbf{k}$ and by the boundary condition of incoming wave (indicated by the symbol $(-)$) which describes the physical process and that will be discussed in the following section 2.1.3. In the weak field limit, it corresponds to the absorption of one photon caused by the dipole operator and leads to the expression for the differential cross section

$$\frac{d\sigma_I}{d\mathbf{k}} = 4\pi^2\alpha\omega|\langle\Psi_{I\mathbf{k}}^{(-)}|D|\Psi_0\rangle|^2, \tag{2.4}$$

where ω is the energy of the photon and α is the dimensionless fine-structure constant, in atomic units (a.u.). This expression, derived by first order *Time Dependent Perturbation Theory* (TDPT), is analogous to a bound-bound transition and we shall take it as a starting point. So, basically, the task amounts to the calculation of the final wavefunction $\Psi_{I\mathbf{k}}^{(-)}$ (the calculation of Ψ_0^N is much easier) and the evaluation of the dipole matrix elements:

$$D_{I\mathbf{k}}^{(-)} = \langle\Psi_{I\mathbf{k}}^{(-)}|D|\Psi_0^N\rangle, \tag{2.5}$$

Note that in Eq. (2.4) the continuum wavefunction is assumed to be normalized to a Dirac delta function with respect to the energy.

2.1.3 Boundary condition for ionization processes

Let us start by considering a one particle scattering by a fixed short range potential, i.e. a potential $V(\mathbf{r})$ that decays sufficiently fast at infinity. The exact condition is

$$V(\mathbf{r}) \xrightarrow[\mathbf{r}\to\infty]{} 0, \tag{2.6}$$

but, for simplicity, let us assume $V(r) = 0$ for $r > R_0$.

If one considers the time evolution of a wavepacket, which itself can be represented as a linear combination of stationary states, we can describe an experiment

where ionisation occurs. But, in the current case, we actually consider the mathematically simpler exact eigenstates $\varphi_{\mathbf{k}}^{(-)}(\mathbf{r})$ rather than a mixed-state. These states represent the final-state electron wavefunction in a photoionization process and satisfy the incoming-wave boundary condition.

Let us consider first a spherically symmetric potential $V(r)$. The positive energy eigenstates of the Hamiltonian

$$H = \frac{p^2}{2m} + V(r), \tag{2.7}$$

$$H\varphi_{\mathbf{k}} = E_k \varphi_{\mathbf{k}}, \tag{2.8}$$

characterized by a well defined asymptotic momentum $\mathbf{k}$ of the photoelectron ($E_k = k^2/2$) have the following asymptotic behaviour:

$$\varphi_{\mathbf{k}}^{(-)}(\mathbf{r}) \xrightarrow[r\to\infty]{} \frac{1}{(2\pi)^{\frac{3}{2}}}[e^{i\mathbf{k}\cdot\mathbf{r}} + f^{(-)}(k,\hat{k},\hat{r})\frac{e^{-ikr}}{r}]. \tag{2.9}$$

This expression is derived from scattering theory and indicates that, at large r, the wavefunction has the form of a plane wave plus incoming spherical waves. The quantity $f^{(-)}(k,\hat{k},\hat{r})$ is called the *scattering amplitude* and its dimensions are of length (ref, indicate e guarda appunti foglio sulla normalizzazione). Like the plane wave, $\varphi_{\mathbf{k}}^{(-)}(\mathbf{r})$ is normalized in momentum

$$\langle\varphi_{\mathbf{k}}^{(-)}(\mathbf{r})|\varphi_{\mathbf{k}'}^{(-)}(\mathbf{r})\rangle = \delta(\mathbf{k}\mathbf{k}'). \tag{2.10}$$

Computationally it is generally convenient to work in the basis of angular momentum states instead of linear momentum $\varphi_{\mathbf{k}}$. In general, any function $f(x,y,z)$ can be represented, in polar coordinates, as an expansion over spherical harmonics $Y_{lm}(\vartheta,\varphi)$, as

$$\Psi(x,y,z) \equiv \Psi(r,\vartheta,\varphi) = \sum_{lm} R_{lm}(r)Y_{lm}(\vartheta,\varphi), \tag{2.11}$$

which is called an *expansion in partial waves*. Each contribution $R_{lm}(r)Y_{lm}(\vartheta,\varphi)$, a product of a radial function times a spherical harmonic, is called a *partial wave* (of angular momentum l,m). In particular, the plane wave $e^{i\mathbf{k}\cdot\mathbf{r}}$ admits a well known partial wave representation:

$$e^{i\mathbf{k}\cdot\mathbf{r}} = \sum_l i^l(2l+1)P_l(cos\theta)j_l(kr) = 4\pi\sum_{lm} i^l j_l(kr)Y_{lm}^*(\hat{k})Y_{lm}(\hat{r}), \tag{2.12}$$

where θ is the angle between the vectors $\mathbf{k}$ and $\mathbf{r}$. The spherical Bessel function, $j_l(kr)$, which appears in the above equation, is regular at the origin (i.e., $rj_l(kr) \xrightarrow[r\to 0]{} 0$) and has the asymptotic behaviour:

$$j_l(kr) \xrightarrow[r\to\infty]{} \frac{sin(kr - l\pi/2)}{kr} = \frac{e^{i(kr-l\pi/2)} - e^{-i(kr-l\pi/2)}}{2ikr}. \tag{2.13}$$

If we now consider the left side of Eq. (2.9), the exact solution $\varphi_{\mathbf{k}}^{(-)}(\mathbf{r})$ can also be expanded in terms of partial waves:

$$\varphi_{\mathbf{k}}^{(-)}(\mathbf{r}) = \sum_{lm} C_{lm} R_{El}(r) Y_{lm}(\vartheta, \varphi), \tag{2.14}$$

where the function $\mathrm{R}_{El}(\mathrm{r})$ is an eigenstate of definite angular momentum of the radial Schrödinger equation relative to

$$H\varphi_{Elm} = E\varphi_{Elm}, \qquad E = \frac{k^2}{2m}. \tag{2.15}$$

The asymptotic behaviour of this function can be written as a linear combination of regular and irregular spherical Bessel functions:

$$R_{El}(r) \xrightarrow[\mathbf{r}\to\infty]{} A_l j_l(kr) + B_l n_l(kr) = A_l(k)\,[j_l(kr) + K_l n_l(kr)], \tag{2.16}$$

which defines the K-matrix (which is diagonal for a spherical potential) and the associated phase shift $\tan\delta_l = K_l$, where $\mathrm{A}_l(\mathrm{k})$ is a normalization factor. This wave-phase shift is a measure of the asymptotic amplitude of the spherical Bessel function $n_l(\mathrm{kr})$. This function is irregular at the origin (i.e., $n_l(kr) \xrightarrow[r\to 0]{} \infty$) and does not contribute to $\mathrm{R}_{El}(\mathrm{r})$ when the central potential is absent. The asymptotic behaviour of the irregular solution is given by

$$n_l(kr) \xrightarrow[\mathbf{r}\to\infty]{} \frac{cos(kr - l\pi/2)}{kr}, \tag{2.17}$$

so that asymptotically $R_{kl}(r)$ has the form:

$$R_{El}(r) \propto \frac{sin(kr - l\pi/2 + \delta_l)}{kr}. \tag{2.18}$$

The set of expansion coefficients C_{lm} in the expression (2.14) can be obtained by comparing the asymptotic forms of the partial wave expansions of Eqs. (2.9) and (2.14). To fix the normalization of the computed solutions let us define the energy

normalized regular and irregular radial functions

$$f_l(kr) \xrightarrow[r\to\infty]{} \sqrt{\frac{2}{\pi k}}\frac{1}{r}\sin\theta_l, \qquad g_l(kr) \xrightarrow[r\to\infty]{} \sqrt{\frac{2}{\pi k}}\frac{1}{r}\cos\theta_l, \tag{2.19}$$

with

$$\theta_l(kr) = kr - l\frac{\pi}{2}. \tag{2.20}$$

Then the unnormalized radial functions (2.16) obtained from the solution of the Schrödinger equation (2.15) are fitted in the asymptotic region (for $r = R_{max}$) to the linear combination

$$R_{El}(r) = A_l\, f_l(kr) + B_l\, g_l(kr), \tag{2.21}$$

and, dividing by A_l, one gets the final K-matrix normalized solutions

$$R_{El}(r) = f_l(kr) + K_l\, g_l(kr), \tag{2.22}$$

with

$$K_l = B_l A_l^{-1}. \tag{2.23}$$

From Eq. (2.9), Eq. (2.12) and Eq. (2.13), expanding

$$f^{(-)}(k,\hat{k},\hat{r}) \equiv f^{(-)} = 4\pi\sum_{lm} f_{lm} Y^*_{lm}(\hat{\mathbf{k}})Y_{lm}(\hat{\mathbf{r}}), \tag{2.24}$$

we have

$$\begin{aligned}\varphi^-_{\mathbf{k}}(\mathbf{r}) \xrightarrow[r\to\infty]{} &\frac{4\pi}{(2\pi)^{\frac{3}{2}}}\left[i^l\frac{e^{i\theta_l}-e^{-i\theta_l}}{2ikr} + f_{lm}\frac{e^{-i\theta_l}e^{-il\frac{\pi}{2}}}{r}\right]Y^*_{lm}(\hat{\mathbf{k}})Y_{lm}(\hat{\mathbf{r}}) = \\ &= \sqrt{\frac{2}{\pi}}\frac{i^l}{2ikr}\sum_{lm}[e^{i\theta_l} - (1-2ikf_{lm}i^{-2l})e^{-i\theta_l}]Y^*_{lm}(\hat{\mathbf{k}})Y_{lm}(\hat{\mathbf{r}}).\end{aligned} \tag{2.25}$$

Normalizing to a $\delta(E-E')$ and by multiplying by $\sqrt{\frac{k}{m}}$ we obtain:

$$\varphi^-_{\mathbf{k}}(\mathbf{r}) \xrightarrow[r\to\infty]{} \sqrt{\frac{1}{2\pi km}}\frac{i^l}{ir}\sum_{lm}[e^{i\theta_l} - (1-2ikf_{lm}i^{-2l})e^{-i\theta_l}]Y^*_{lm}(\hat{\mathbf{k}})Y_{lm}(\hat{\mathbf{r}}). \tag{2.26}$$

The K-normalized radial functions R_{kl} (2.21) have the asymptotic behaviour:

$$\begin{aligned} R_{kl} \xrightarrow[r\to\infty]{} \sqrt{\frac{2}{\pi k}}\frac{1}{r}\left[\frac{e^{i\theta_l}-e^{-i\theta_l}}{2i}+K_l\frac{e^{i\theta_l}+e^{-i\theta_l}}{2}\right] = \\ = \sqrt{\frac{2}{\pi k}}\frac{1}{2ir}\left[e^{i\theta_l}(1+iK_l)-e^{-i\theta_l}(1-iK_l)\right]. \end{aligned} \tag{2.27}$$

It can be brought to so called S^+-matrix normalization by multiplying by $(1+iK_l)^{-1}$

$$R_{kl}^{(-)} \Rightarrow R_{kl}(1+iK_l)^{-1} \xrightarrow[r\to\infty]{} \sqrt{\frac{1}{2\pi k}}\frac{1}{ir}\left[e^{i\theta_l}-S_l^+e^{-i\theta_l}\right], \tag{2.28}$$

with

$$S_l = (1+iK_l)(1-iK_l)^{-1}, \qquad S^+ = (1-iK_l)(1+iK_l)^{-1} = S^{-1}. \tag{2.29}$$

Then expressing

$$\varphi_{\mathbf{k}}^-(\mathbf{r}) = \sum_{lm} C_{lm}R_{kl}^{(-)}Y_{lm}(\hat{\mathbf{r}}) \xrightarrow[r\to\infty]{} \sum_{lm} C_{lm}\sqrt{\frac{2}{\pi k}}\frac{1}{ir}\left[e^{i\theta_l}-S^+e^{-i\theta_l}\right]Y_{lm}(\hat{\mathbf{r}}). \tag{2.30}$$

Comparing with Eq. (2.26) one obtains

$$C_{lm} = \frac{1}{\sqrt{m}}i^lY_{lm}^*(\hat{\mathbf{k}}). \tag{2.31}$$

So finally:

$$\varphi_{\mathbf{k}}^-(\mathbf{r}) = \frac{1}{\sqrt{m}}\sum_{lm} i^lR_{El}^{(-)}(r)Y_{lm}^*(\hat{\mathbf{k}})Y_{lm}(\hat{\mathbf{r}}). \tag{2.32}$$

This is the partial wave expansion for the continuum wavefunction which, in this case, depends only on the angle θ between $\mathbf{k}$ and $\mathbf{r}$. It can be also written as

$$\varphi_{\mathbf{k}}^-(\mathbf{r}) = \frac{1}{4\pi m^{1/2}}\sum_{l} i^l(2l+1)P_l(cos\theta)R_{El}^{(-)}(r), \tag{2.33}$$

employing the standard expansion for the Legendre polynomials

$$P_l(cos\theta) = \frac{4\pi}{2l+1}\sum_{m} Y_{lm}^*(\hat{\mathbf{k}})Y_{lm}(\hat{\mathbf{r}}). \tag{2.34}$$

In the partial wave expansion each term $R_{El}^{(-)}(r)Y_{lm}(\hat{\mathbf{r}})$ is the energy-normalized single-electron wavefunction corresponding to the angular momentum state (l,m). The spherical harmonic $Y_{lm}^*(\hat{\mathbf{k}})$ gives the probability amplitude for an electron in

the angular momentum state (l, m) to have the direction $\hat{\mathbf{k}}$.

2.1.4 Coulomb asymptotic potential

We have thus far considered an electron moving in a short-range potential. This is correct in the photoionization of anion systems (photodetachment) where the final bound state is neutral. However, in the case of photoionization of a neutral molecular system (or a positive ion), the photoelectron wave must be solution of the scattering Schrödinger equation where the potential in the scattering Hamiltonian is given by:

$$V(r) \xrightarrow[r\to\infty]{} -\frac{Z_{ion}}{r}. \tag{2.35}$$

This is the long-range Coulomb potential, where Z_{ion} is the residual charge of the ion. This potential modifies the single-channel final-state wavefunction $\varphi_{\mathbf{k}}^{(-)}(\mathbf{r})$. Therefore, the partial wave expansion of Coulomb wave becomes:

$$\varphi_{\mathbf{k}}^{(-)}(\mathbf{r}) = \frac{1}{(2\pi)^{3/2}}\frac{1}{kr}\sum_{l}(2l+1)i^l e^{-i\sigma_l}F_l(k,r)P_l(cos\theta), \tag{2.36}$$

where θ is the angle between $\hat{\mathbf{r}}$ and $\mathbf{k}$, and $F_l(k,r)$ is the spherical Coulomb function which is regular at $r = 0$.

As before, it is useful to consider a second linear independent solution, the irregular Coulomb function $G_l(k,r)$. Their asymptotic forms are given by

$$\begin{aligned} &F_l(k,r) \xrightarrow[r\to\infty]{} \sin\theta_l(kr), \\ &G_l(k,r) \xrightarrow[r\to\infty]{} \cos\theta_l(kr), \\ &f_l = \sqrt{\frac{2}{\pi k}}\frac{1}{r}F_l, \qquad g_l = \sqrt{\frac{2}{\pi k}}\frac{1}{r}G_l, \end{aligned} \tag{2.37}$$

where

$$\theta(kr) = kr - l\frac{\pi}{2} - \eta log2kr + \sigma_l, \qquad \eta = -\frac{Z_{ion}}{k}, \tag{2.38}$$

and

$$\sigma_l = arg\Gamma(l+1+i\eta). \tag{2.39}$$

The final-state wavefunction $\varphi_{\mathbf{k}}^{(-)}(\mathbf{r})$, on the other hand, may always be expanded as:

$$\varphi_{\mathbf{k}}^{(-)}(\mathbf{r}) = \sum_{lm} C_{lm}R_{El}(r)Y_{lm}(\hat{r})), \tag{2.40}$$

where $\mathrm{R}_{El}(\mathrm{r})$ has the asymptotic form (K-matrix normalized)

$$R_{El}(r) \xrightarrow[r\to\infty]{} f_l(kr) + K_l\, g_l(kr). \tag{2.41}$$

By the same substitutions, the final expression for the energy normalized continuum wavefunction is

$$\varphi^{(-)}_{\mathbf{k}}(\mathbf{r}) = \frac{1}{\sqrt{m}} \sum_{l,m} i^l e^{-i\sigma_l} R^{(-)}_{El}(r) Y_{lm}(\hat{\mathbf{r}}) Y^*_{lm}(\hat{\mathbf{k}}). \tag{2.42}$$

This function is thus of the same form as the corresponding wavefunction in the absence of the Coulomb potential as given by Eq. (2.32). Furthermore, each term in the partial wave expansion in Eq. (2.42) has the same interpretation as the terms in Eq. (2.32). The two major differences between the two expressions are, firstly, the different radial wave functions and, secondly, in Eq. (2.42) the Coulomb phase-shift σ_l enters into the normalization factor.

So, in general, we define regular and irregular asymptotic radial solutions as (f_l, g_l) in both cases, with appropriate definition of θ_l.

2.1.5 Non-spherically symmetric potential

If $V(\mathbf{r})$ is not spherically symmetric, we can expand the solution in terms of partial waves:

$$\varphi_{Elm} = \sum_{l'm'} R_{El'm'lm} Y_{l'm'}. \tag{2.43}$$

The Hamiltonian is given by

$$\begin{aligned} h &= h_0 + V(\mathbf{r}), \\ h_0 &= \frac{p^2}{2m} = -\frac{1}{2m}\left(\frac{1}{r}\frac{\partial}{\partial r} r \frac{\partial}{\partial r}\right) + \frac{L^2}{2mr^2}. \end{aligned} \tag{2.44}$$

If one projects the Schrödinger equation

$$h\varphi_{Elm} = E\varphi_{Elm},$$

onto spherical harmonics $Y_{l''m''}$, we then obtain the coupled equations for the radial functions:

$$\langle Y_{l''m''}, H\sum_{l'm'} R_{El'm'lm}Y_{l'm'}\rangle = E\langle Y_{l''m''}, \sum_{l'm'} R_{El'm'lm}Y_{l'm'}\rangle,$$

and

$$\begin{aligned} &-\frac{1}{2m}\frac{1}{r}\frac{\partial}{\partial r}r\frac{\partial}{\partial r}R_{El''m''lm} + \frac{l''(l''+1)}{2mr^2}R_{El''m''lm} + \\ &+\sum_{l'm'} V_{l''m''l'm'}(r)R_{El'm'lm}(r) = ER_{El''m''lm}, \end{aligned} \tag{2.45}$$

where $V_{l''m''l'm'}(r) = \langle Y_{l''m''}|V(\mathbf{r})|Y_{l'm'}\rangle$. The functions $R_{El'm'lm}$ are coupled by the non-spherical components of the potential, $V_{l''m''l'm'}$. At large distances, the radial functions become a linear combination of the free-particle solutions

$$R_{El'm'lm}(r) \xrightarrow[r\to\infty]{} f_{l'}(kr)A_{l'm'lm} + g_{l'}(kr)B_{l'm'lm}, \tag{2.46}$$

which defines the matrices $\mathbf{A}$ and $\mathbf{B}$. We then obtain a set of solutions, $\{R_{El'm'lm}\}$, relative to the same energy E and whose number corresponds to that of the angular momenta included in the expansion. Hence it is possible to linearly combine them through an invertible transformation so as to obtain a set of equivalent solutions.

Defining $R_{EL'L} \equiv R_{El'm'lm}$, where $(l,m) \equiv L$, we can write

$$R_{EL'L} \xrightarrow[r\to\infty]{} f_{l'}(kr)A_{L'L} + g_{l'}(kr)B_{L'L}. \tag{2.47}$$

We then obtain a set of solutions

$$\varphi_{EL} = \sum_{L'} R_{EL'L}Y_{L'} \xrightarrow[r\to\infty]{} \sum_{L'}(f_{L'}A_{L'L} + g_{L'}B_{L'L})Y_{L'}. \tag{2.48}$$

Transforming to K-matrix normalization

$$\varphi_{EL} \longrightarrow \varphi^{(K)}_{EL} = \sum_{L''}\varphi_{EL''}A^{-1}_{L''L} \xrightarrow[r\to\infty]{} \sum_{L'}(f_{L'}\delta_{L'L} + g_{L'}K_{L'L})Y_{L'}, \tag{2.49}$$

where $\mathbf{K} = \mathbf{BA}^{-1}$, it is easy to further transform to incoming wave (S-matrix) normalization

$$\varphi^{(-)}_{EL} = \sum_{L''}\varphi^{(K)}_{L''}(1+iK)^{-1}_{L''L}. \tag{2.50}$$

The corresponding S-matrix incoming wave solution is

$$R^{(-)} = R(1 + iK)^{-1}, \tag{2.51}$$

with the asymptotic behaviour

$$R^{(-)}_{EL'L} \xrightarrow[r\to\infty]{} \sqrt{\frac{2}{\pi k}}\frac{1}{r}(\delta_{L'L}e^{i\theta'_l} + S^{+}_{L'L}e^{-i\theta'_l}). \tag{2.52}$$

A further transformation gives the linear momentum wavefunction

$$\varphi^{(-)}_{\mathbf{k}} = \sum_L C_L \varphi^{(-)}_{EL}, \tag{2.53}$$

with

$$C_L = \frac{1}{\sqrt{m}} i^l e^{-i\sigma_l} Y^*_L(\hat{k}), \tag{2.54}$$

as before ($\sigma_l = 0$ in the case of short range potential). The wavefunction $\varphi^{(-)}_{\mathbf{k}}$ so obtained corresponds to the proper normalization and asymptotic boundary condition for the calculation of the photoionization cross section.
Finally, if the molecular hamiltonian is invariant under a symmetry group G, its matrix is diagonal over different symmetry irreducible representations (λ, μ). It is then advantageous to work in a symmetry adapted angular basis, making a unitary transformation from the spherical harmonic basis $\{Y_{lm}\}$ to the angular basis

$$X_{lh\lambda\mu} = \sum_m Y_{lm} b_{mlh\lambda\mu}, \tag{2.55}$$

with $b^+ = b^{-1}$ and

$$Y_{lm} = \sum_{h\lambda\mu} X_{lh\lambda\mu} b^*_{mlh\lambda\mu}. \tag{2.56}$$

Here h counts the number of linearly independent functions $X_{lh\lambda\mu}$ corresponding to a given l. Then

$$\varphi_{Elm} \xrightarrow[r\to\infty]{} \varphi_{Elh\lambda\mu} = \sum_{l'h'} R_{l'h'lh\lambda} X_{l'h'\lambda\mu}, \tag{2.57}$$

and the $\mathbf{K}$, $\mathbf{S}$ matrices are diagonal on λ and independent on μ, i.e. $K^{\lambda}_{l'h'lh}$, $S^{(-)\lambda}_{l'h'lh}$.

2.1.6 Convergence of the partial wave expansion

The expansion considered are formally exact in the limit of an infinite number of partial waves. The convergence of partial waves is very fast at low energies, but becomes slower at higher energies. A simple classical picture of scattering shows that with momentum k and maximum impact parameter a, the corresponding angular momentum is $L = ak \sim l$, so that the maximum l required increases linearly with electron momentum. In general, the expansion of the photoelectron wavefunction over a large number of partial waves constitutes a computational problem. For this reason, the partial waves development is a convenient method at low energies, but very demanding at high energies.

2.1.7 The multichannel continuum wavefunction

Let us now suppose a number of final ionic states (channels) are open at a given photon energy ω, with wavefunction Ψ_I^{N-1}, and corresponding energies

$$E_I^{N-1}, \qquad IP_I = E_I^{N-1} - E_0^N < \hbar\omega, \qquad E = E_0^N + \hbar\omega, \tag{2.58}$$

$$k_I = \sqrt{2(E - E_I^{N-1})} = \sqrt{2(\omega - IP_I)}. \tag{2.59}$$

Although their number may be infinite, in practical calculations only a finite number of the most interacting channels will be retained. Again scattering theory dictates the form of asymptotic boundary conditions, which is a simple generalization of that already considered in the single particle case, i.e. a plane wave associated with the final channel considered plus incoming spherical waves in all channels:

$$\Psi_{I\mathbf{k}}^{(-)}(r^{N-1}, r) \xrightarrow[r\to\infty]{} \frac{1}{(2\pi)^{\frac{3}{2}}} \left[\Psi_I^{N-1} e^{i\mathbf{k_I}\cdot\mathbf{r}} + \sum_{I'}^{nop} \Psi_{I'}^{N-1} \frac{e^{-ik_{I'}r}}{r} \right], \tag{2.60}$$

where *nop* is the number of open channels at ω and $\Psi_{I'}^{N-1}$ are the wavefunctions that describe the ionic states I'.
Employing a partial wave expansion for the continuum electron, the wavefunction assumes the form

$$\Psi_{EIL} = \sum_{I'L'} \Psi_{I'}^{N-1} R_{EI'L'IL}(r) Y_{L'}(\hat{r}), \tag{2.61}$$

with

$$R_{EI'L'IL}(r) \xrightarrow[r\to\infty]{} f_{l'}(k_I r)A_{I'L'IL} + g_{l'}(k_I r)B_{I'L'IL}. \tag{2.62}$$

Again, multiplying by $\mathbf{A}^{-1}$ leads to K-matrix normalization

$$\Psi^{(K)}_{EIL} = \sum_{I'L'} \Psi_{EI'L'} A^{-1}_{I'L'IL}, \qquad \mathbf{K} = \mathbf{B}\mathbf{A}^{-1}, \tag{2.63}$$

and further transformation to S^+ boundary condition

$$\Psi^{(-)}_{EIL} = \sum_{I'L'} \Psi^{(K)}_{EI'L'}(1 + iK)^{-1}_{I'L'IL}. \tag{2.64}$$

Finally, transformation from angular momentum to linear momentum conditions gives

$$\Psi^{(-)}_{I\mathbf{k}} = \sum_{L} C_{L\mathbf{k}} \Psi^{(-)}_{EIL}, \tag{2.65}$$

with

$$C_{Lk} = \frac{1}{\sqrt{m}} i^l e^{-i\sigma_l} Y^*_L(\hat{k}). \tag{2.66}$$

2.2 Photoionization cross section

Given the final state wavefunction, one can compute the differential cross section. In the present treatment we work in the fixed nuclei representation and disregard nuclear motion, by considering the molecule as a classical rigid body. We shall discuss two limiting cases, corresponding to two different experimental situations. The most common situation is a randomly oriented molecular sample, typical of gas phase experiments. The cross section is then obtained by averaging over all possible molecular orientations. The second situation corresponds to a completely fixed orientation of the molecule in space. That can be achieved in a variety of experimental settings and gives rise to a more complex angular distribution of the photoelectrons, known as *Molecular Frame Photoelectron Angular Distribution* (MFPAD).

To treat this situation one needs two reference systems [66]. The first one is called Laboratory Frame (LF, with axes X', Y', Z' and in general primed coordinate) and is defined by the photon beam and the detection apparatus. The second one is the Molecular Frame (MF, with axes X, Y, Z and unprimed coordinates), which is fixed with respect to the molecule. Let us define $\Omega = (\alpha, \beta, \gamma)$ the Euler angles

relative to the rotation that carries MF into LF. Then β and α are the polar angles which define photon orientation in MF.

Initially the wavefunctions are computed in the MF. So also the photon orientation is converted in the MF and the electron momentum vector $\mathbf{k}$ is defined in the MF. This gives directly the MFPAD cross section, for fixed orientation Ω. To obtain the unoriented cross section in LF, one has to transform the electron momentum vector $\mathbf{k}$ from the MF to $\mathbf{k}'$ in the LF and then further average over all molecular orientations (Ω).

We shall consider only electric dipole transitions and assume the LF Z' axis defined by the electric vector $\mathbf{E}$ in the case of linearly polarized light (LP) or by the photon propagation vector in the case of circularly polarization (Left or Right circularly polarized, LCP and RCP, respectively). The corresponding one electron dipole operator (in the length gauge) is then

$$d_{1m_r} = \sqrt{\frac{4\pi}{3}} r Y_{1m_r}, \tag{2.67}$$

with $m_r = 0$ for LP, and $m_r = +1$, $m_r = -1$ for LCP and RCP.
In general, the angular distribution of the cross section can be expanded in angular momentum components. In the case of one photon absorption in the dipole approximation, if the molecule is unoriented, very general symmetry considerations limit the angular momentum expansion of the differential cross section to a maximum l value of 2 (given the absorption of a photon of spin = 1)

$$\frac{d\sigma}{d\hat{k}} = \frac{\sigma_0}{4\pi}[1 + \beta_2 P_2(\cos\theta)], \qquad m_r = 0, \tag{2.68}$$

$$\frac{d\sigma}{d\hat{k}} = \frac{\sigma_0}{4\pi}[1 \pm \beta_1 \cos\theta + \frac{1}{2}\beta_2 P_2(\cos\theta)], \qquad m_r = \pm 1, \tag{2.69}$$

where $\sigma_0(I,\omega)$, $\beta_1(I,\omega)$, $\beta_2(I,\omega)$ completely characterize the photoionization process. Actually, $\beta_1 \neq 0$ only for circularly polarized light and chiral molecules. For linearly polarized light, $\beta_1 = 0$ and θ is the angle between the electric field vector and the electron momentum, i.e. the cross section has cylindrical symmetry around the electric vector. Instead, in the case of MFPAD, in the general case, all angular momenta up to $2L_{max}$ contribute to the cross section, where L_{max} is the maximum l value included in the continuum

$$\frac{d\sigma}{d\hat{k}} = \sum_{LM} A_{LM} Y_{LM}(\hat{k}), \tag{2.70}$$

where the coefficients $A_{LM}(k,\Omega)$ depend of the orientation of the photon beam in the MF.

2.2.1 Cross section in the molecular frame

The dipole matrix elements computed from the continuum wavefunction φ_{EL} (2.49) or, in general, Ψ_{EIL} (2.61), are given by

$$D_{EIL\gamma} = \langle \Psi_{EIL} | D_{1\gamma} | \Psi_0 \rangle, \tag{2.71}$$

and are transformed to the linear momentum asymptotic boundary conditions by the same transformations of the wavefunction

$$\Psi_{EIL} \longrightarrow \Psi^{(K)}_{EIL} \longrightarrow \Psi^{(-)}_{EIL} \longrightarrow \Psi^{(-)}_{I\mathbf{k}}, \tag{2.72}$$

So

$$D^{(K)}_{EIL\gamma} = \sum_{I'L'} D_{EI'L'\gamma} A^{-1}_{I'L'IL}, \tag{2.73}$$

$$D^{(-)}_{EIL\gamma} = \sum_{I'L'} D^{(K)}_{EI'L'\gamma} (1 - iK)^{-1}_{I'L'IL}, \tag{2.74}$$

$$D^{(-)}_{I\mathbf{k}\gamma} = \sum_{L} C^{*}_{L\mathbf{k}} D^{(-)}_{EIL\gamma}, \qquad \text{with } C_{L\mathbf{k}} = \frac{1}{\sqrt{m}} i^l e^{-i\sigma_l} Y^{*}_{L}(\hat{k}). \tag{2.75}$$

Actually, calculations are best performed employing full point group symmetry and symmetry adapted angular functions $X_{lh\lambda\mu}$, so that in (2.73) L $\equiv lh\lambda\mu$, and there is a further transformation to the angular momentum basis Y_{lm}

$$D^{(K)}_{EIlm\gamma} = \sum_{h\lambda\mu} D^{(K)}_{EIlh\lambda} b_{mlh\lambda\mu}. \tag{2.76}$$

To simplify expressions, let us include the $\frac{1}{\sqrt{m}} i^l e^{-i\sigma_l}$ factors in the dipole matrix elements, defining

$$\mathcal{D}^{(-)}_{EIL\gamma} = \frac{1}{\sqrt{m}} i^l e^{-i\sigma_l} D^{(-)}_{EIL\gamma}, \tag{2.77}$$

so that

$$D^{(-)}_{I\mathbf{k}\gamma} = \sum_{lm} Y_{lm}(\hat{k}) \mathcal{D}^{(-)}_{EIlm\gamma}. \tag{2.78}$$

Finally, in the expression for the dipole matrix elements

$$D^{(-)}_{I\mathbf{k}m_r} = \langle \Psi^{(-)}_{I\mathbf{k}} | D_{1m_r} | \Psi_0 \rangle, \tag{2.79}$$

the dipole operator in LF has to be expressed through its MF components $D_{1\gamma}$, by employing a rotation matrix $R^1_{\gamma m_r}(\Omega)$

$$D_{1m_r} = \sum_{\gamma} D_{1\gamma}\, R^1_{\gamma m_r}. \tag{2.80}$$

One can now expand the differential cross section in the MF as:

$$\begin{aligned} \frac{d\sigma_I(\omega)}{d\mathbf{k}d\Omega} &= 4\pi^2\alpha\omega |\langle \Psi^{(-)}_{I\mathbf{k}} | D_{m_r} | \Psi_0 \rangle|^2 = \\ &= 4\pi^2\alpha\omega \sum_{lm\gamma l'm'\gamma'} Y_{lm}(\hat{k}) Y^*_{l'm'}(\hat{k}) R^{(1)}_{\gamma m_r}(\Omega) R^{(1)*}_{\gamma' m_r}(\Omega) \mathcal{D}^{(-)}_{lm\gamma} \mathcal{D}^{(-)*}_{l'm'\gamma'}. \end{aligned} \tag{2.81}$$

Recoupling

$$Y_{lm} Y^*_{l'm'} = (-1)^m \sum_L \sqrt{\frac{(2l+1)(2l'+1)(2L+1)}{4\pi}} \begin{pmatrix} l' & l & L \\ m' & -m & M \end{pmatrix} \begin{pmatrix} l' & l & L \\ 0 & 0 & 0 \end{pmatrix} Y_{LM}(\hat{k}), \tag{2.82}$$

where $M = m - m'$, and

$$R^{(1)}_{\gamma m_r} R^{(1)*}_{\gamma' m_r} = (-1)^{\gamma - m_r} \sum_J (2J+1) \begin{pmatrix} 1 & 1 & J \\ \gamma' & -\gamma & \gamma - \gamma' \end{pmatrix} \begin{pmatrix} 1 & 1 & J \\ m_r & -m_r & 0 \end{pmatrix} R^{(J)}_{\gamma-\gamma',0}(\Omega), \tag{2.83}$$

and

$$R^J_{M0}(\alpha\beta\gamma) = (-1)^M \sqrt{\frac{4\pi}{2J+1}} Y_{J,-M}(\beta, \alpha), \tag{2.84}$$

one obtains

$$\frac{d\sigma_I(\omega)}{d\mathbf{k}d\Omega} = 4\pi^2\alpha\omega(-1)^{m_r} \sum_{LM} A_{LM} Y_{LM}(k), \tag{2.85}$$

with $A_{LM} = A_{LM}(k, m_r, \Omega)$, namely

$$\begin{aligned} A_{LM} = & \sum_{lm\gamma, l'm'\gamma'} (-1)^m \sqrt{\frac{(2l+1)(2l'+1)(2L+1)}{4\pi}} \begin{pmatrix} l' & l & L \\ m' & -m & M \end{pmatrix} \begin{pmatrix} l' & l & L \\ 0 & 0 & 0 \end{pmatrix} \mathcal{D}^{(-)}_{lm\gamma} \mathcal{D}^{(-)*}_{l'm'\gamma'} \\ & (-1)^{\gamma} \sum_J (2J+1) \begin{pmatrix} 1 & 1 & J \\ \gamma' & -\gamma & \gamma - \gamma' \end{pmatrix} \begin{pmatrix} 1 & 1 & J \\ m_r & -m_r & 0 \end{pmatrix} (-1)^{\gamma - \gamma'} \sqrt{\frac{4\pi}{2J+1}} Y_{J,\gamma'-\gamma}(\beta, \alpha) = \\ & = \sum_{lm\gamma, l'm'\gamma'} (-1)^{m+\gamma'} \hat{l}\hat{l}'\hat{L}\hat{J} \begin{pmatrix} l' & l & L \\ m' & -m & M \end{pmatrix} \begin{pmatrix} l' & l & L \\ 0 & 0 & 0 \end{pmatrix} \mathcal{D}^{(-)}_{lm\gamma} \mathcal{D}^{(-)*}_{l'm'\gamma'} \\ & \sum_J \begin{pmatrix} 1 & 1 & J \\ \gamma' & -\gamma & \gamma - \gamma' \end{pmatrix} \begin{pmatrix} 1 & 1 & J \\ m_r & -m_r & 0 \end{pmatrix} Y_{J\gamma'-\gamma}(\beta, \alpha), \end{aligned} \tag{2.86}$$

where $\hat{l} = \sqrt{2l+1}$.

One can note that the only "dynamical" part (that is, depending on ω) is in the $\mathcal{D}_{lm\gamma}$ terms. These terms depend, in turn, on the initial and final states and on the Coulombic phase shift σ_l. All the other terms consist of geometrical factors. Since the calculation of $\frac{d\sigma}{d\hat{k}}$ has been done in the MF, the propagation direction $\hat{\mathrm{k}}$ of the photoelectron is defined with respect to the molecule. This situation describes the experiments with oriented molecules where both the polarization of the photoelectron and its emission direction are related to the frame of reference of the molecule. For linear molecules, the angle β is that between the photon polarization and the molecular axis. The two most common orientations are $\parallel$ (parallel, β=0) and $\perp$ (perpendicular, β=90^o).

The integral cross section is obtained by integrating over all emission directions $\hat{\mathrm{k}}$. Recalling

$$\int Y_{LM}(\hat{k}) d\hat{k} = \delta_{L0}\delta_{M0}\sqrt{4\pi}, \tag{2.87}$$

from which we can derive the total cross section

$$\sigma(\Omega) = \int \frac{d\sigma}{d\mathbf{k}} d\hat{k} = 4\pi^2 \alpha\omega (-1)^{m_r} \sqrt{4\pi} A_{00}, \tag{2.88}$$

then the total cross section for randomly oriented molecules is obtained by averaging over Ω. We can see that the result is the same both in the LF and in the MF. From

$$\frac{1}{8\pi^2} \int R^j_{m'm}(\Omega) d\Omega = \delta_{j0}\delta_{m'm}, \tag{2.89}$$

then averaging $A_{00}(\Omega)$ gives a $\delta_{J0}\delta_{\lambda\lambda'}$ in the sum

$$\frac{1}{8\pi} \int A_{00}(\Omega) d\Omega \longrightarrow \delta_{J0}\delta_{\lambda\lambda'}, \tag{2.90}$$

and

$$\begin{pmatrix} l & l & 0 \\ m & -m & 0 \end{pmatrix} \begin{pmatrix} l & l & 0 \\ 0 & 0 & 0 \end{pmatrix} \sqrt{\frac{(2l+1)^2}{4\pi}} = (-1)^{l-m}(-1)^l \frac{1}{\sqrt{4\pi}} = \frac{(-1)^m}{\sqrt{4\pi}}, \tag{2.91}$$

$$\begin{pmatrix} 1 & 1 & 0 \\ \lambda & -\lambda & 0 \end{pmatrix} \begin{pmatrix} 1 & 1 & 0 \\ m_r & -m_r & 0 \end{pmatrix} = (-1)^{1-\lambda}(-1)^{1-m_r} \frac{1}{3} = \frac{(-1)^{\lambda+m_r}}{3}. \tag{2.92}$$

From which

$$\sigma = \frac{4}{3}\pi^2 \alpha\omega \sum_{lm\gamma} |\mathcal{D}^{(-)}_{lm\gamma}|^2 = \frac{4}{3}\pi^2 \alpha\omega \sum_{lh\lambda\mu\gamma} |D^{(-)}_{lh\lambda\mu\gamma}|^2. \tag{2.93}$$

2.2.2 Cross section in the laboratory frame

Let us start from the formula of the differential cross section in the MF (2.85) in order to express the differential cross section in the LF. Once the orientation of the vector $\hat{\mathrm{k}}$ in the LF has been re-expressed through the rotation matrices, we can average over all molecular orientations Ω. The $Y_{LM}(\hat{k})$ in the MF is expressed as

$$Y_{LM'}(\hat{k}) = \sum_M Y_{LM}(\hat{k}') R^L_{MM'}(-\Omega) = \sum_M Y_{LM}(\hat{k}') R^{L*}_{M'M}(\Omega), \tag{2.94}$$

and recoupling

$$R^L_{M'M}(\Omega)^* R^J_{\gamma-\gamma',0}(\Omega) = (-1)^{\gamma-\gamma'} \sum_{KQQ'} (2K+1) \begin{pmatrix} L & J & K \\ M' & \gamma'-\gamma & Q' \end{pmatrix} \begin{pmatrix} L & J & K \\ M & 0 & Q \end{pmatrix} D^K_{Q'Q}(\Omega), \tag{2.95}$$

with $M' + \gamma' - \gamma + Q' = 0$ and $Q = -M$. From expressions (2.85) and (2.86) we can obtain:

$$(-1)^{m_r} \sum_{LM'} A_{LM'}(k,\Omega) Y_{LM'}(\hat{k}) = (-1)^{m_r} \sum_{LM} \bar{A}_{LM}(k,\Omega) Y_{LM}(\hat{k}'), \tag{2.96}$$

with

$$\begin{aligned} \bar{A}_{LM} = \sum_{M'} A_{LM'} R^{L*}_{M'M}(\Omega) = \sum_{\substack{lm\gamma \\ l'm'\gamma'}} (-1)^{m+\gamma} \sum_{M'} \begin{pmatrix} l' & l & L \\ m' & -m & M' \end{pmatrix} \begin{pmatrix} l' & l & L \\ 0 & 0 & 0 \end{pmatrix} \\ \sqrt{\frac{(2l+1)(2l'+1)(2L+1)}{4\pi}} \mathcal{D}^{(-)}_{lm\gamma} \mathcal{D}^{(-)*}_{l'm'\gamma'} \sum_J (2J+1) \begin{pmatrix} 1 & 1 & J \\ \gamma' & -\gamma & \gamma-\gamma' \end{pmatrix} \begin{pmatrix} 1 & 1 & J \\ m_r & -m_r & 0 \end{pmatrix} \\ (-1)^{\gamma-\gamma'} \sum_K (2K+1) \begin{pmatrix} L & J & K \\ M' & \gamma'-\gamma & Q' \end{pmatrix} \begin{pmatrix} L & J & K \\ M & 0 & -M \end{pmatrix} D^K_{Q',-M}(\Omega), \end{aligned} \tag{2.97}$$

with $M' = m - m'$ and $Q' = \gamma - \gamma' - M'$.
Then we can write

$$\bar{A}_{LM}(k,\Omega) = \sum_{\substack{lm\gamma \\ l'm'\gamma'}} (-1)^{m+\gamma} \begin{pmatrix} l' & l & L \\ m' & -m & M \end{pmatrix} \begin{pmatrix} l' & l & L \\ 0 & 0 & 0 \end{pmatrix} \sqrt{\frac{(2l+1)(2l'+1)(2L+1)}{4\pi}} \mathcal{D}^{(-)}_{lm\gamma} \mathcal{D}^{(-)*}_{l'm'\gamma'} \sum_{JK} (2J+1)(2K+1) \begin{pmatrix} 1 & 1 & J \\ \gamma' & -\gamma & \gamma - \gamma' \end{pmatrix} \begin{pmatrix} 1 & 1 & J \\ m_r & -m_r & 0 \end{pmatrix} \begin{pmatrix} L & J & K \\ m - m' & \gamma' - \gamma & Q \end{pmatrix} \begin{pmatrix} L & J & K \\ M & 0 & -M \end{pmatrix} D^K_{Q,-M}(\Omega). \tag{2.98}$$

In order to obtain $\frac{d\sigma}{d\mathbf{k}}$ for randomly oriented molecules, we have to average over all the orientations Ω, then:

$$\begin{aligned} &\frac{1}{8\pi^2} \int \bar{A}_{LM}(k,\Omega) d\Omega = \bar{A}_{L0}(k) \equiv A_L(k) = \\ &= \sum_{\substack{lm\gamma \\ l'm'\gamma'}} (-1)^{m+\gamma'} \begin{pmatrix} l & l' & L \\ -m & m' & M \end{pmatrix} \\ &\begin{pmatrix} l & l' & L \\ 0 & 0 & 0 \end{pmatrix} \sqrt{\frac{(2l+1)(2l'+1)(2L+1)}{4\pi}} \mathcal{D}^{(-)}_{lm\gamma} \mathcal{D}^{(-)*}_{l'm'\gamma'} (2L+1) \\ &\begin{pmatrix} 1 & 1 & L \\ -\gamma & \gamma' & \gamma - \gamma' \end{pmatrix} \begin{pmatrix} 1 & 1 & L \\ -m_r & m_r & 0 \end{pmatrix} \begin{pmatrix} L & L & 0 \\ m - m' & \gamma' - \gamma & 0 \end{pmatrix} \begin{pmatrix} L & L & 0 \\ 0 & 0 & 0 \end{pmatrix} = \\ &= \sqrt{\frac{2L+1}{4\pi}} \sum_{\substack{lm\gamma \\ l'm'\gamma'}} (-1)^{m+\gamma} \begin{pmatrix} l' & l & L \\ -m & m' & M \end{pmatrix} \\ &\begin{pmatrix} l & l' & L \\ 0 & 0 & 0 \end{pmatrix} \sqrt{(2l+1)(2l'+1)} \mathcal{D}^{(-)}_{lm\gamma} \mathcal{D}^{(-)*}_{l'm'\gamma'} \\ &\begin{pmatrix} 1 & 1 & L \\ -\gamma & \gamma' & \gamma - \gamma' \end{pmatrix} \begin{pmatrix} 1 & 1 & L \\ -m_r & m_r & 0 \end{pmatrix}, \end{aligned} \tag{2.99}$$

with $m - m' = \gamma - \gamma'$

$$A_L(k) Y_{L0} = \sqrt{\frac{2L+1}{4\pi}} A_L(k) P_L(cos\theta). \tag{2.100}$$

Then finally we can obtain

$$\frac{d\sigma}{d\mathbf{k}} = \pi\alpha\omega(-1)^{m_r} \sum_L A_L P_L(cos\theta'), \tag{2.101}$$

where θ' is referred to the laboratory system and with

$$A_L(k) = (2L+1)\begin{pmatrix} 1 & 1 & L \\ m_r & -m_r & 0 \end{pmatrix} \sum_{\substack{lm\gamma \\ l'm'\gamma'}} (-1)^{m+\gamma} \sqrt{(2l+1)(2l'+1)} \begin{pmatrix} l & l' & L \\ 0 & 0 & 0 \end{pmatrix} \begin{pmatrix} l & l' & L \\ -m & m' & m-m' \end{pmatrix} \begin{pmatrix} 1 & 1 & L \\ \gamma' & -\gamma & \gamma-\gamma' \end{pmatrix} \begin{pmatrix} 1 & 1 & L \\ -m_r & m_r & 0 \end{pmatrix} \mathcal{D}^{(-)}_{lm\gamma} \mathcal{D}^{(-)*}_{l'm'\gamma'}. \tag{2.102}$$

From the term $\begin{pmatrix} 1 & 1 & L \\ m_r & -m_r & 0 \end{pmatrix}$ we can see that $0 \leq L \leq 2$, that is L can be only $L = 0, 1, 2$. Furthermore, for linearly polarized light $m_r = 0$ and the term $\begin{pmatrix} 1 & 1 & L \\ 0 & 0 & 0 \end{pmatrix}$ is non-zero only for even values of L [67]. As a result, only the terms A_0 and A_2 survive in the sum (2.101).
By integrating Eq. (2.101), the only non-zero term is for P_0. For $P_0 = 1$, we can obtain [68]

$$\begin{aligned} \sigma &= \int \frac{d\sigma}{dk} sin\theta d\theta d\varphi = \pi\alpha\omega(-1)^{m_r} A_0 \int 1 \cdot sin\theta d\theta d\varphi = \\ &= 4\pi^2 \alpha\omega(-1)^{m_r} A_0 \Longrightarrow \frac{\sigma}{4\pi} = \pi\alpha\omega(-1)^{m_r} A_0, \end{aligned} \tag{2.103}$$

$$\frac{d\sigma}{dk} = \pi\alpha\omega(-1)^{m_r} A_0 \left(1 + \frac{A_1}{A_0} cos\theta + \frac{A_2}{A_0} P_2(cos\theta)\right), \tag{2.104}$$

and by defining

$$\beta_1 = \frac{A_1(m_r = 1)}{A_0} \qquad \beta = \frac{A_2(m_r = 0)}{A_0}, \tag{2.105}$$

we can obtain

$$\frac{d\sigma}{dk} = \frac{\sigma}{4\pi}[1 + m_r \beta_1 cos\theta + \left(-\frac{1}{2}\right)^{m_r} \beta P_2(cos\theta)]. \tag{2.106}$$

2.3 Expression of the wave function: different approximations

The problem of calculating photoionization cross-sections is related to the calculation of matrix elements in expression (2.4). Hence it is necessary to specify the initial and final states of the system. The methods of calculation differ on the choice of the bound and continuum states. While the calculation of the initial

state wavefunction is straightforward, the accurate calculation of the final state wavefunction is, on the contrary, extremely difficult and requires several approximations. In this section we want to illustrate the approximations that we used to express the final wavefunction. Each of these methods considers correlation to a greater or lesser degree and some methods do not consider it at all.

We will now start discussing the consequences of correlation.

2.3.1 Correlation effects

If we consider the Hamiltonian operator for a system, the problem for the corresponding Schrödinger equation lies in the term which describes the coulombian interaction between electrons. The Schrödinger equation is not analytically solvable because of this *correlation* term. As a consequence, the basic approximation for many-electron systems is the *mean-field approximation*. This is based on the independent particle model, in which each particle moves on the mean field created from the other particles. In general, the term "electron correlation" is related to all the effects not included in the mean field approximation.

The *one-electron picture* is the basic description of the ionic states created in photoionization. For example, within this approximation, in the most simple case of closed shell atoms, it is possible to associate each line, in a PE spectrum, to an orbital. For the molecular case, the rotational and vibrational excitations determine more complex bands but these broadened bands can be associated, in any case, to an individual molecular orbital. The main photoelectron peaks or bands observed in the spectrum are connected to those final electronic states of the ion, which can be described as single hole configurations (1h) with respect to the ground-state.

Although it represents a first level of PE spectrum interpretation, the one particle approach is insufficient to provide a complete description in the general case. This is a consequence of the many-electron nature of most targets. Then it is necessary to take into account the interelectron interaction which leads to dependent/correlated motion of electrons.

Electron correlation together with relaxation effects lead to additional bands in a PE spectrum. Relaxation effects are connected to the orbital's change in response to the creation of a hole. These extra structures, called *shake-up* or *satellite bands*, correspond to excitation processes occurring simultaneously with the ionization processes. Indeed, if more than one electron participates in the transition,

the PE spectrum will contain satellite lines in addition to the generally strong main line which represents the direct single photoionization. The experimental evidence of these structures has been named as the *breakdown of the independent-particle picture* of electronic structure [5]. The simple theoretical interpretation is that the extra features in the ionization spectra appear, in addition to those expected from the one-electron picture, because of the strong interaction between single-hole configurations and two-hole, one-particle configurations. The interaction between a single-hole configuration and a multiply-excited configurations leads to a mixing of the configurations that redistributes the intensity amongst many states of the same symmetry. Experimentally this mixing redistributes the intensity between main peaks associated with main states expected from the simple Koopmans' theorem picture and satellite peaks associated with correlation states.

Correlation effects in photoionization can be usefully subdivided into two classes [69]. The first one is correlation within the bound states relative to the initial state (often called initial state configuration interaction, ISCI) and final ionic state (FISCI). ISCI and FISCI refer to discrete bound electron systems, N-electrons and N-1 electrons, respectively. The second one comprises interaction between continuum channels (interchannel coupling, IC), or between a discrete state (or closed channel) and the continuum (autoionization resonances, also resonant Auger). Correlation effects in the bound states have been extensively investigated using several many-body approaches like Configuration Interaction (CI), Perturbation Theory (PT), Green's function (GF),[5, 70–73] and are the major source of correlation effects in photoelectron spectra.

2.3.2 General expression of the wavefunction

In photoionization, *open channels* are defined as target states accessible at the given energy E and which satisfy the relation:

$$IP_I = E_I^{N-1} - E_0^N < h\nu. \tag{2.107}$$

In the current case, eigenstates in the continuum of N-particles correspond to bound states of N-1 particles (target states) plus one particle in the continuum. The continuum wavefunctions satisfy the Schrödinger equation:

$$H^N \Psi_{E\alpha}^N = E\Psi_{E\alpha}^N, \tag{2.108}$$

where $\alpha \equiv I$ collectively indicates all additional quantum numbers necessary to uniquely label the solution.

This solution, $\Psi_{E\alpha}^N$, can be formally expressed in the so called Close-Coupling form:

$$\Psi_{EIL}^N = \sum_{I'L'} \Psi_{I'}^{N-1} \phi_{EI'LIL} + \sum_K \Phi_K^N C_{E\alpha K}. \tag{2.109}$$

The first sum runs over all open channels and comprises antisymmetrized products of the bound state wavefunctions for the final ionic states Ψ_I^{N-1} and single particle wavefunctions $\phi_{EI'L'IL}$ describing the continuum electrons (see Sec. 2.1.7) and automatic satisfies the boundary conditions in the continuum. The reminder, which is square integrable, can be represented by the second sum, involving only bound state wavefunctions Φ_K^N, which can be described with the typical methods of Quantum Chemistry such as CI and takes also into account orthogonality conditions. This is analogous to a CI expansion for the bound states. It is in principle convergent, as the set of Φ_K^N becomes complete. It may be a computationally convenient form to get approximate solutions, by selecting basis functions and then truncating the sums to a finite number of terms. This can still satisfy any required asymptotic form and boundary conditions.

At long range, this solution has to reduce asymptotically to a linear combination of products of target states multiplied by single particle continuum functions

$$\Psi_{E\alpha}^N \xrightarrow[r_N \to \infty]{} \sum_{I'} \Psi_{I'}^{N-1} \phi_{E\alpha I'}, \tag{2.110}$$

relative to all open channels I'. The "channel function" index $\alpha = Ilm$ counts all the possible products of target states I multiplied by all angular momenta lm of the continuum particle which are degenerate.

2.3.2.1 First approximation

At the single channel level, the final continuum wavefunction is approximated as an antisymmetrized product:

$$\Psi_{EIL}^{N} = A\Psi_{I}^{N-1}\varphi_{\varepsilon IL}, \tag{2.111}$$

where Ψ_{I}^{N-1} is a final ionic state wavefunction and $\varphi_{\varepsilon} \equiv \varphi_{\varepsilon IL}$ is a continuum orbital describing the outgoing photoelectron. We also note that A is the antisymmetrizer, ε is the photoelectron kinetic energy ($\mathrm{E} = \mathrm{E}_{I}^{N-1} + \varepsilon$). The continuum orbitals satisfy the K-matrix boundary conditions which were defined in the previous section.

In our approach, in the independent particle approximation (IPA), the wavefunction associated to the ionic state is expressed as a product of single particle functions

$$\Psi_{i}^{N-1} = |\varphi_1, ..., \varphi_{i-1}, \varphi_{i+1}, ..., \varphi_N\rangle\,. \tag{2.112}$$

The wavefunction of the final state is a single determinant

$$\Psi_{EiL}^{N} = |\varphi_1, ..., \varphi_{\varepsilon}, ..., \varphi_N\rangle\,, \tag{2.113}$$

where the i-th function is substituted with the φ_{ε}, the function related to the photoelectron. This wavefunction corresponds to a single particle excitation, in which the i-th orbital has been ionized and an electron excited to the continuum state φ_{ε}.

Once the initial and final wavefunctions are defined, we can concentrate on the calculation of transition matrix elements to find the differential cross section. At this level (frozen orbitals), in the N-particle transition matrix element there is only the contribution from the wavefunction of the photoelectron. This is because the contribution from the other electrons will integrate out to unity. Then the calculation of the transition dipole moments reduces to:

$$\langle\Psi_{EI}|D|\Psi_0\rangle = \langle\varphi_{\varepsilon}|d|\varphi_i\rangle\,. \tag{2.114}$$

Since the dipole transition operator is a one-particle operator, only single transitions $\varphi_i \longrightarrow \varphi_\varepsilon$ are permitted. Within this approximation, the Koopmans' theorem is valid.

At this level, one can use two different approximations: Hartree-Fock (HF) and Kohn-Sham Density Functional Theory (KS DFT). If the initial state is represented by a Hartree-Fock determinant, the residual ionic state can be taken as the Koopmans' frozen state, by removing the relevant one-electron orbital from the determinant. Therefore, in the calculation of dipole transition moments, the φ_i orbital will be represented by an HF orbital or, in the DFT case, by a DFT orbital.

On the one hand, at this level of approximation, one can describe cross section and asymmetry parameter oscillations, dichroism in chiral molecules, direct photoionization from molecules fixed in space, non-dipolar effects and vibrationally resolved cross-sections. Furthermore, one-electron theories include the effects of shape resonances and Cooper minima [53]. But on the other hand, calculations based on these approximations do not include autoionization [53]. So the one-electron description represents only a first-level approximation to the photoionization process. This approach is unable to describe processes where the remaining electrons are simultaneously excited as the photoelectron leaves the ion. Multi-electrons processes have to be described by means of other approximations.

2.3.2.2 Second approximation

The second approximation consists in coupling of single particle excitations, namely in considering several single excited determinants. The continuum wavefunction is expressed as:

$$\Psi_{Ej}^{N} = \sum_i C_{ij} \left|\varphi_1, ..., \varphi_{Ei}, ..., \varphi_N\right\rangle = \sum_i \Phi_i^{N-1} \varphi_{Eij}. \tag{2.115}$$

Hence, the final state wavefunction is a mixing of the previous independent particle functions. The effects included, that is the effects that it can gain respect to those described from first approximation, are:

- interchannel coupling effects (which transfers intensity fron one channel to another)

- singly excited autoionizations (and Super Coster Kronig (SCK) giant resonances) [74] autoionization resonances due to discrete single excitations
- correlation effects due to the mixing of singly-excited configurations (channel mixing)

At this level, it is possible to use the *Time-dependent density functional theory* (TDDFT) within the linear response approximation. This method has been shown to provide accurate results for large systems and permits to introduce couplings between the treated photoionization channels and some single excitation transitions. The interchannel mixing is visible in the cross section by the presence of relatively sharp structures at photon energies corresponding to the coupled single-excitations. TDDFT and, in general, this second type of approximation do not consider:

- correlations due to multiple excitations
- autoionizations due to doubly excited states
- description of satellite states

These effects are partially considered in a third approach, explained in the next session.

2.3.2.3 Third approximation

One can stay at the single channel level, but employ highly-correlated bound state wavefunctions for the initial Ψ_I^N and final ionic states Ψ_F^{N-1}

$$\Psi_{EIL}^N = A\Psi_I^{N-1}\varphi_{\varepsilon IL}. \tag{2.116}$$

At the HF or DFT level, the dipole matrix elements between the initial wavefunction, Ψ_0^N, and the final one, Ψ_{Ek}^N, reduce to one particle matrix elements $\langle\varphi_k \,|\, d \,|\, \varphi_i\rangle$ between the initial orbital φ_i from which the electron is emitted, and the final orbital φ_k describing the electron in the continuum. This approach can be extended to the use of fully correlated the bound states, Ψ_I^N and Ψ_F^{N-1}, by substituting to

φ_i the orbital ϕ^d_{IF}, called Dyson orbital.

The Dyson orbitals are defined as:

$$\phi^d_{IF}(1) = \sqrt{N} \int \Psi^N_I(1, ..., N)\Psi^{N-1}_F(2, ..., N)d2...dN. \tag{2.117}$$

They represent the superposition between the initial neutral state wavefunction (N-electron system), Ψ^N_I, and the final ionic state wavefunction (N-1 electrons system), Ψ^{N-1}_F. A more extensive discussion of these orbitals will be in Chapter 5.

At this level, all correlation effects present in the bound states (ISCI and FISCI) are completely described by the single Dyson orbital. The IP's are not calculated simply by Koopmans' theorem but by using the relation $\mathrm{IP}_I = \mathrm{E}^{N-1}_I - E^N_0$ (correction to KT). As a consequence, we can speak about *breakdown of Koopmans' theorem* or, equivalently, *breakdown of one-particle picture*. In this way it is possible to consider the presence of satellite states.

More specifically, dipole matrix elements can be exactly reduced to one particle matrix elements, through the definition of direct and conjugate amplitudes, χ_{Ik} and η_{Ik} respectively, defined as:

$$\chi_{Ik} = \left\langle \Psi^{N-1}_I \,\middle|\, a_k \,\middle|\, \Psi^N_0 \right\rangle, \quad \eta_{Ik} = \left\langle \Psi^{N-1}_I \,\middle|\, Da_k \,\middle|\, \Psi^N_0 \right\rangle, \tag{2.118}$$

where D is the many particle dipole operator (x, y, z component) and a_k is the annihilation operator relative to orbital φ_k. Then one can write:

$$\begin{aligned} \left\langle \Psi^{N-1}_F \varphi_{\epsilon j} \,\middle|\, D \,\middle|\, \Psi^N_I \right\rangle &= \textstyle\sum_k \langle \varphi_{\epsilon j} \,|\, d \,|\, \varphi_k \rangle \chi_{Ik} + \sum_k \langle \varphi_{\epsilon j} \,|\, \varphi_k \rangle \eta_{Ik} = \\ &= \langle \varphi_{\epsilon j} \,|\, d \,|\, \chi_I \rangle + \langle \varphi_{\epsilon j} \,|\, \eta_I \rangle, \end{aligned} \tag{2.119}$$

where it has defined Dyson orbitals χ_I and η_I as

$$\chi_I = \sum_k \chi_{Ik}\varphi_k, \quad \eta_I = \sum_k \eta_{Ik}\varphi_k. \tag{2.120}$$

The second term, which is called conjugate, is deemed of minor importance, especially far from threshold, and it is neglected in our study. It is associated with a dipole transition within the bound states and can populate final ionic states which are symmetry-forbidden by the first (direct) mechanism.

Chapter 3

Methods

3.1 Hartree-Fock Method

In the Hartree-Fock approach it is assumed, according to the independent-particle approximation and the Pauli exclusion principle, that the N-electron wavefunction is a *Slater determinant*, i.e. an antisymmetric product of individual electron spin-orbitals [75, 76].
This wavefunction can be then expressed as:

$$\Phi = \hat{A}[\phi_1(1)\phi_2(2)\dots\phi_N(N)] = \hat{A}\Pi, \tag{3.1}$$

where Â is the antisymmetrizing operator and Π is the diagonal product. The operator Â can be expanded as a sum of permutations and is defined as:

$$\hat{A} = \frac{1}{\sqrt{N!}}\sum_P (-1)^p \hat{P}, \tag{3.2}$$

where Î is the identity operator, the sum over $\hat{\mathrm{P}}_{ij}$ generates all possible permutations of two electron coordinates, while the sum over $\hat{\mathrm{P}}_{ijk}$ generates all possible permutations of three electron coordinates etc.

The Hamiltonian operator can be written as:

$$\hat{H} = \sum_i^N \hat{h}_i + \sum_{j>i}^N \hat{g}_{ij} + \hat{V}_{nn}, \tag{3.3}$$

where

$$\hat{h}_i = \frac{1}{2}\nabla_i^2 - \sum_a^{N_{nuclei}} \frac{Z_a}{|\mathbf{R}_a - \mathbf{r}_i|}, \tag{3.4}$$

describes the motion of electron i in the field generated by the nuclei, while the two-electron operator

$$\hat{g}_{ij} = \frac{1}{|\mathbf{r}_i - \mathbf{r}_i|}, \tag{3.5}$$

expresses the electron-electron repulsion. Finally, the term

$$V_{nn} = \sum_a^{N_{nuclei}} \sum_{b>a}^{N_{nuclei}} \frac{Z_a Z_b}{|\mathbf{R}_a - \mathbf{R}_b|}, \tag{3.6}$$

is the nuclear-nuclear repulsion which is a constant for a given nuclear geometry.

The expectation value of the energy can be written as:

$$E = \langle\Phi|\hat{H}|\Phi\rangle = \langle\hat{A}\Pi|\hat{H}|\hat{A}\Pi\rangle = \sqrt{N!}\,\langle\Pi|\hat{H}|\hat{A}\Pi\rangle = \sum_p (-1)^p \langle\Pi|\hat{H}|\hat{P}\Pi\rangle\,. \tag{3.7}$$

While for the one-electron operator only the identity operator can give a non-zero contribution, for the two-electron operator, non-zero contributions are given by the identity and the $\hat{\mathrm{P}}_{ij}$ operators. The identity operator is responsible for the term:

$$\begin{aligned}\langle\Pi|\hat{g}_{12}|\Pi\rangle &= \langle\phi_1(1)\phi_2(2)...\phi_N(N)|\hat{g}_{12}|\phi_1(1)\phi_2(2)...\phi_N(N)\rangle \\ &= \langle\phi_1(1)\phi_2(2)|\hat{g}_{12}|\phi_1(1)\phi_2(2)\rangle\,...\,\langle\phi_N(N)|\phi_N(N)\rangle \\ &= \langle\phi_1(1)\phi_2(2)|\hat{g}_{12}|\phi_1(1)\phi_2(2)\rangle = J_{12},\end{aligned} \tag{3.8}$$

where the J_{12} matrix element is the *Coulomb integral* which represents the classical repulsion between two charge distributions. The other term, which stems from the $\hat{\mathrm{P}}_{ij}$ operator, is given by

$$\begin{aligned}\langle\Pi|\hat{g}_{12}|\hat{P}_{12}\Pi\rangle &= \langle\phi_1(1)\phi_2(2)...\phi_N(N)|\hat{g}_{12}|\phi_1(1)\phi_2(2)...\phi_N(N)\rangle \\ &= \langle\phi_1(1)\phi_2(2)|\hat{g}_{12}|\phi_2(1)\phi_1(2)\rangle\,...\,\langle\phi_N(N)|\phi_N(N)\rangle \\ &= \langle\phi_1(1)\phi_2(2)|\hat{g}_{12}|\phi_2(1)\phi_1(2)\rangle = K_{12},\end{aligned} \tag{3.9}$$

where the K_{12} matrix element is the *exchange integral* and has no classical analogue. As a result, the energy can be written in terms of Coulomb and exchange

operators as

$$E = \sum_{i}^{N} \langle \phi_i | \hat{h}_i | \phi_i \rangle + \frac{1}{2} \sum_{ij}^{N} (\langle \phi_j | \hat{J}_i | \phi_j \rangle - \langle \phi_j | \hat{K}_i | \phi_j \rangle) + V_{nn}. \tag{3.10}$$

With this expression, the aim is to determine a set of orthogonal and normalized MOs that minimize the energy.

The Lagrange function for the system is given by

$$L = E - \sum_{ij}^{N} \lambda_{ij} (\langle \phi_i | \phi_j \rangle - \delta_{ij}),$$

The energy minimization can be done by using Lagrange multipliers with the condition that a small change in the orbitals should not change the Lagrange function:

$$\delta L = \delta E - \sum_{ij}^{N} \lambda_{ij} (\langle \delta\phi_i | \phi_j \rangle - \langle \phi_i | \delta\phi_j \rangle) = 0. \tag{3.11}$$

The variation of energy can be written as:

$$\begin{aligned} \delta E &= \sum_{i}^{N} (\langle \delta\phi_i | \hat{h}_i | \phi_i \rangle + \langle \phi_i | \hat{h}_i | \delta\phi_i \rangle) + \sum_{ij}^{N} (\langle \delta\phi_i | \hat{J}_j - \hat{K}_j | \phi_i \rangle + \langle \phi_i | \hat{J}_j - \hat{K}_j | \delta\phi_i \rangle) = \\ &= \sum_{i}^{N} (\langle \delta\phi_i | \hat{F}_i | \phi_i \rangle + \langle \phi_i | \hat{F}_i | \delta\phi_i \rangle), \end{aligned} \tag{3.12}$$

where the Fock operator is defined as:

$$\hat{F}_i = \hat{h}_i + \sum_{j}^{N} (\hat{J}_j - \hat{K}_j). \tag{3.13}$$

This operator describes the kinetic energy of a specific electron and the nuclei-electron attraction as well as the repulsion of all the other electrons (through the $\hat{\mathrm{J}}$ and $\hat{\mathrm{K}}$ operators). Thus, the variation of the Lagrange function becomes

$$\delta L = \sum_{i}^{N} (\langle \delta\phi_i | \hat{F}_i | \phi_i \rangle + \langle \phi_i | \hat{F}_i | \delta\phi_i \rangle) - \sum_{ij}^{N} \lambda_{ij} (\langle \delta\phi_i | \phi_j \rangle + \langle \phi_i | \delta\phi_j \rangle). \tag{3.14}$$

According to the variational principle, the desired orbitals are those that make $\delta L = 0$. Using the complex conjugate properties, we have that

$$\delta L = \sum_{i}^{N} \langle \delta\phi_i | \hat{F}_i | \phi_i \rangle - \sum_{ij}^{N} \lambda_{ij} \langle \delta\phi_i | \phi_i \rangle + \sum_{i}^{N} \langle \delta\phi_i | \hat{F}_i | \phi_i \rangle^* - \sum_{ij}^{N} \lambda_{ij} \langle \delta\phi_i | \phi_i \rangle^* = 0. \tag{3.15}$$

The variation of either $\langle \delta\phi |$ or $\langle \delta\phi^* |$ should make δL $= 0$, i.e. the first two terms in the above equation must cancel, and the last two terms must cancel. Taking the complex conjugate of the last two terms and subtracting them from the first two, we obtain:

$$\sum_{ij}^{N} (\lambda_{ij} - \lambda_{ij}^*) \langle \delta\phi_i | \phi_j \rangle = 0. \tag{3.16}$$

Hence the Lagrange multipliers are elements of a Hermitian matrix ($\lambda_{ij} = \lambda_{ji}^*$). The final set of Hartree-Fock equations may be written as

$$\hat{F}_i \phi_i = \sum_{j}^{N} \lambda_{ij} \phi_j. \tag{3.17}$$

The equations may be simplified by choosing a unitary transformation that makes the matrix of Lagrange multipliers diagonal. These particular molecular orbitals (ϕ') are called the canonical MOs and they transform Eq. (3.17) into a set of pseudo-eigenvalue equations:

$$\hat{F}_i \phi_i' = \varepsilon_i \phi_i'. \tag{3.18}$$

The complexity with solving Eq. (3.18) lies in the fact that the Fock operator depends on the Fock orbitals. Hence, the system of Hartree-Fock equations are solved by iteration. Starting from an initial guess set of orbitals, one can use these orbitals to construct the Fock operator that is used, in turn, to solve for a new set of orbitals. This procedure is repeated until no significant change in the orbital energies occurs. As a consequence, the solution of Eq. (3.18) is self-consistent, and the method is called the *Self-Consistent Field* (SCF) method.

3.1.1 Koopmans' Theorem

Let us consider the energy of an N-electron system and the corresponding system with one electron removed from orbital k. Furthermore, we assume that the MOs

are the same for the two systems. The energy of the N-electron system is given by

$$E_N = \sum_i^N h_i + \frac{1}{2}\sum_i^N \sum_j^N (J_{ij} - K_{ij}) + V_{nn}, \tag{3.19}$$

while that of the (N-1)-electron system is given by

$$E_{N-1} = \sum_i^{N-1} h_i + \frac{1}{2}\sum_i^{N-1} \sum_j^{N-1} (J_{ij} - K_{ij}) + V_{nn}. \tag{3.20}$$

Subtracting the two total energies gives

$$E_N - E_{N-1} = h_k + \sum_i^N (J_{ik} - K_{ik}) = \varepsilon_k, \tag{3.21}$$

where ε_k is exactly the orbital energy. This quantity then represents approximately the necessary energy to remove an electron from the orbital ϕ_k, or the *ionization energy* of electron k. This result is known as *Koopmans' theorem* [48].

3.2 Configuration Interaction

The HF energy of a given state and the corresponding HF wavefunction are only approximations to the exact energy and the exact wavefunction. The HF wavefunction usually gives $\sim 99\%$ of the correct energy and the difference between the exact energy and HF energy is known as the *correlation energy* [76, 77]. Correlation effects can be calculated by using the variational method with a wavefunction that is a linear combination of Slater determinants. These determinants correspond to electronic configurations in which electrons are promoted into virtual orbitals. Hence, they represent excited states whose contribution to the total wavefunction of the ground state generally decreases with the order of excitation.

This is the *Configuration Interaction* (CI) approach [52] and the corresponding wavefunction can be written as

$$\Psi_{CI} = a_0\Phi_{HF} + \sum_S a_S\Phi_S + \sum_D a_D\Phi_D + \sum_T a_T\Phi_T + ... = \sum_i a_i\Phi_i, \tag{3.22}$$

where subscripts S, D, T, etc. indicate determinants that are singly, doubly, triply, etc., excited relative to the HF configuration.

Exploiting the symmetry properties of the system, the linear combination in Eq. (3.22) can be reduced to a basis of states with the same spatial and spin symmetry. Such linear combinations of determinants are called *Configurational State Functions* (CSFs). If the expansion Eq. (3.22) includes all possible CSFs of the appropriate symmetry, it represents a *full CI* procedure which exactly solves the electronic Schrödinger equation in the given basis.

3.3 MCSCF

The *Multi-Configuration Self-Consistent Field* (MCSCF) methods represent a series of computational methods which include only a few number of determinants in Eq. (3.22). The MCSCF methods provide a general approach for describing chemical systems in which a single-electron configuration does not permit an adequate description of the electronic structure. In particular, they can be considered as a CI where both the coefficients in front of the determinants in Eq. (3.22) and the MOs used for constructing the determinants are variationally optimized [78]. This is distinct from the regular CI case where only the coefficients are optimized.

For the wavefunction Ψ_k in the MCSCF expansion:

$$\Phi_{MCSCF} = \sum_k A_k \Psi_k, \tag{3.23}$$

we can use a single determinant, a linear combination of determinants or CSFs.

MCSCF treatments are generally designed to correct the HF energy by including the static part of the correlation. This contribution, known as the *near-degeneracy effect*, is mainly due to the existence of different degenerate solutions and refers to the inadequacy of a single reference in describing a given molecular state. The remaining dynamical contribution is associated with the instantaneous correlation between electrons. This term can be included in several ways. One approach is by using a perturbative treatment which will be subsequently illustrated 3.4.

The main problem in MCSCF methods is in choosing the most important configurations to describe the property of interest. There exist several implementations of this approach based on different choices of the Ψ_k and of the optimization methods. One of these will be illustrated in the next section 3.3.1.

3.3.1 CASSCF

One of the most famous multideterminantal approaches is the *Complete Active Space Self-Consistent Field* (CASSCF) method, which has been popularized by Roos et al. [79]. In this approach, the initial molecular orbital space, which may be taken from a HF calculation, is partitioned into *inactive* and *active* spaces. The inactive space is composed of the doubly occupied orbitals in all CSFs that are used to build the multiconfigurational wavefunction. Meanwhile, the active space includes both occupied and virtual orbitals. These orbitals will typically include some of the highest occupied and some of the lowest unoccupied MOs from a HF calculation. We include all determinants which are allowed for a particular choice of active orbitals. These determinants contribute to the expansion in Eq. (3.23). The orbitals in the resulting wavefunction can have a fractional occupation (typically from 1.999 to 0.001). The wavefunction tends to easily converge with respect to the general MCSCF methods.

A common notation to indicate the procedure is [n,m]-CASSCF, which means that n electrons are distributed in all possible ways in m orbitals. Once the active space has been adequately chosen, the CASSCF wavefunction will include the most important CSFs in the full CI wavefunction. This means that a full CI is performed within the active MOs.

The choice of the correct active space represents the chief difficulty in the CASSCF method. Indeed, there do not exist unequivocal rules to guarantee that the orbital space is correctly partitioned. The subdivision between active and inactive orbitals depends on the target system and on its properties of interest. One wishes to consider those orbitals whose occupations change during the chemical process. In the optimal case, these orbitals are included in the active space.

Furthermore, it is essential to take into account the intrinsic limit of the method represented by the computational expense. Indeed, in practice, it is impossible to include in an active space of more than 15 electrons in 15 orbitals. This restriction depends on memory and disk storage in the available software packages. The CASSCF model is then inapplicable to systems where a larger active space is chemically necessary.

In relation to the computational expense, a key factor in CASSCF calculations is scaling the method with system size. There is a factorial dependence on both the number of active electrons and on the number of active orbitals. The

number of Slater determinants in a full configuration interaction calculation is

$$n_{Slater} = \binom{M}{N_\alpha}\binom{M}{N_\beta}, \tag{3.24}$$

where M is the number of active orbitals, N_α and N_β are the numbers of active electrons with α-spin and β-spin, respectively, and the quantities in parentheses are binomial coefficients:

$$\binom{a}{b} = \frac{a!}{b!(a-b)!}. \tag{3.25}$$

If spin adapted CSFs are used, then the number of configurations is given by the Weyl-Robinson formula [78]:

$$n_{CSFs} = \frac{(2S+1)}{M+1}\binom{M+1}{M-N/2-S}\binom{M+1}{N/2-S}, \tag{3.26}$$

where S is the total spin and N the total number of active electrons. Further reduction is obtained by use of special symmetry, generally restricted to the abelian groups.

3.4 NEVPT2

Perturbation theory is one of the affordable methods used to treat dynamic correlation. This contribution is essential to generate quantitatively accurate results.

In particular, *n-electron valence state perturbation theory* (NEVPT) is a perturbative treatment which can be applied to a multireference CASSCF wavefunction. It means that one can first performs a CASSCF calculation which takes into account static correlation and then uses the NEVPT2 to include a part of the dynamic correlation.

Roughly, in the NEVPT2 method, the orbital space is divided into three orbital subspaces of inactive orbitals with occupations of 2, active orbitals with variable occupations, and virtual orbitals with zero occupation. A certain number of classes of spaces are generated by the action of excitation operators. These classes are characterized by a different number of electrons promoted to and from the CAS space. Different numbers of perturbing functions are chosen for these spaces by further subdividing them into various categories: strongly contracted spaces and partially contracted spaces [80–82].

3.5 Density Functional Theory

> *"The birth of Density Functional Theory as a formal subject took place in 1964 with P. Hohenberg and W. Kohn serving as midwives. [...] The baby was beautiful - and surprisingly compact for a child who had been causing labor pangs for over half a century. The first prenatal kicks, associated with the Drude model of metals, came around the turn of the century. These were followed by ever-increasing activity: the Thomas-Fermi atom, Slater's approximate treatment of exchange and the $X\alpha$ method, then countless applications of various approximate DFT methods to specific atoms, molecules and solids.*
>
> *DFT is now a teenager, still a bit uncertain of its roots and its place in society, but able, if provoked, to do an honest day's work."*
>
> *D. R. Salahub*

Since the complexity of the many-particle wave functions grows factorially with the number of particles (see CI before), many approaches have been developed to find approximate solutions for the multielectron case. Among the various approaches, wavefunction based methods such as Hartree-Fock (HF) or *post*-HF are very sophisticated but computationally expensive for large systems.

Using *Density Functional Theory* (DFT) in many-body problems provides an enormous simplification because the basic variational object is represented by the electron density instead of a many-particle wavefunction. Indeed, the many-body wavefunction is a very complex function in a 3N-dimensional space, on the contrary the density is a simple function that depends solely on 3 variables, x, y and z. Considering the computational time, while the traditional methods scales extremely poorly with the number of atoms N, DFT grows much less rapidly. As a consequence, DFT is the only available method for the very large systems. In addition to its capability to treat relatively big systems, DFT is also characterized by high accuracy in structure calculations such as calculations of geometries, interatomic distances and vibrational frequencies. Although DFT is computationally very similar to the HF method, it has become very popular because it includes the correlation energy in the Hamiltonian in a simple way and provides results that give a better representation of the multielectron structure [83, 84].

The idea of describing the molecular energy as a functional of the electron density started with Thomas [85, 86], Fermi [87–89] and Dirac [90]. They initially formulated an approximate theory of electronic structure depending only on

the total electronic density. However, this theory was unable to self-consistently reproduce atomic shell structure and the resulting energies had errors of around 10%. The aims of Thomas, Fermi and Dirac were not achievable until later when P. Hohenberg and W. Kohn [83] proved that there is a unique functional of the electron density which gives the exact ground state energy of the system. Hohenberg and Kohn theorems, however, do not offer a way to calculate an actual ground state. The existence of modern DFT methods is based on the further work of Kohn and L. J. Sham [84]. They proposed a method in which self-consistent equations must be solved for an auxiliary set of orbitals used for representing the electron density. In these equations, a rather small fraction of the total energy, the exchange-correlation (XC) energy, must be given in terms of electron density and represents the only unknown functional. In practical calculations the goal of DFT is to approximate the XC contribution. As a consequence, the accuracy of the calculations depends on the quality of this approximation.

3.5.1 Schrödinger Equation

A system of N interacting electrons is described, within the Born-Oppenheimer approximation [91], by the nonrelativistic Schrödinger equation [92]:

$$\hat{H}\Psi(\mathbf{r}_1, ..., \mathbf{r}_N) = E\Psi(\mathbf{r}_1, ..., \mathbf{r}_N). \tag{3.27}$$

The wavefunction Ψ completely describes the state of the system [93–95].

The many-body Hamiltonian operator is given by

$$\hat{H} = \hat{T} + \hat{V} + \hat{U} = \left[-\frac{1}{2}\sum_i \nabla_i^2 + \sum_i V_i(\mathbf{r}_i) + \frac{1}{2}\sum_{i<j} U(\mathbf{r}_i\mathbf{r}_j) \right], \tag{3.28}$$

where $\hat{\mathrm{T}}$, $\hat{\mathrm{V}}$ and $\hat{\mathrm{U}}$ are, respectively, the kinetic energy, the external potential, i.e. the attraction potential created by the nuclei, and the electron-electron interaction operators. The solution of this 3N-dimensional differential equation is complicated by the presence of the interelectronic potential in the Hamiltonian.

We can reformulate Eq. (3.27) by calculating the expectation value of the

total energy:

$$\begin{aligned} E &= \langle\Psi|\hat{H}|\Psi\rangle = \langle\Psi|\hat{T}+\hat{V}+\hat{U}|\Psi\rangle = \\ &= -\frac{1}{2}\int d\mathbf{r}\nabla^2\rho(\mathbf{r}) + \int d\mathbf{r}v(\mathbf{r})\rho(\mathbf{r}) + \iint d\mathbf{r}_1 d\mathbf{r}_2 \frac{\rho(\mathbf{r}_1,\mathbf{r}_2)}{r_{12}}, \end{aligned} \tag{3.29}$$

where $\rho(\mathbf{r})$ is the electron density defined as

$$\rho(\mathbf{r}) = N\int d\mathbf{r}_2 ... d\mathbf{r}_N \Psi^*(\mathbf{r}_1,...,\mathbf{r}_N)\Psi(\mathbf{r}_1,...,\mathbf{r}_N), \tag{3.30}$$

and $\rho(\mathbf{r}_1,\mathbf{r}_2)$ is the two-particle density function given by

$$\rho(\mathbf{r}_1,\mathbf{r}_2) = N(N-1)\int d\mathbf{r}_3 ... d\mathbf{r}_N \Psi^*(\mathbf{r}_1,...,\mathbf{r}_N)\Psi(\mathbf{r}_1,...,\mathbf{r}_N). \tag{3.31}$$

DFT is founded on the idea that the ground state electronic energy of the system can be expressed and calculated as a *functional* of the electron density, without having to calculate its full wave function. By extension, any observables are a functional of the ground state electron density.

Comparing with the wavefunction-representation approach, the energy functional can be divided into three parts:

$$E[\rho] = T[\rho] + V[\rho] + U[\rho]. \tag{3.32}$$

In Eq. (3.29) we can express the operator $\hat{\mathrm{U}}$ as the classical Coulombian self-interaction of a charge distribution:

$$\langle\Psi|\hat{U}|\Psi\rangle = J[\rho] = \frac{1}{2}\iint d\mathbf{r}_1 d\mathbf{r}_2 \frac{\rho(\mathbf{r}_1)\rho(\mathbf{r}_2)}{r_{12}}, \tag{3.33}$$

but by using this approximation we do not consider the particle self-interaction and the exchange interaction which stem from the antisymmetry of the wavefunction with respect to coordinate exchange for fermions (Pauli principle). Then we introduce a pair correlation function $h_{xc}(\mathbf{r}_1,\mathbf{r}_2)$ that includes non-classical effects. We can write the two-particle density function as

$$\rho(\mathbf{r}_1,\mathbf{r}_2) = \rho(\mathbf{r}_1)\rho(\mathbf{r}_2)[1+h_{xc}(\mathbf{r}_1,\mathbf{r}_2)]. \tag{3.34}$$

This probability is called the *exchange-correlation hole*. The exchange part of h_{xc} is called the *Fermi hole*, while the dynamical correlation gives rise to the *Coulomb*

hole. The expectation value of $\hat{U}$ then becomes

$$\begin{aligned}\langle\Psi|\hat{U}|\Psi\rangle &= J[\rho] + \frac{1}{2}\iint d\mathbf{r}_1 d\mathbf{r}_2 \rho(\mathbf{r}_1)\rho(\mathbf{r}_2)\frac{h_{xc}(\mathbf{r}_1,\mathbf{r}_2)}{r_{12}} = \\ &= J[\rho] + \frac{1}{2}\int d\mathbf{r}_1 \rho(\mathbf{r}_1) v_{xc}(\mathbf{r}_1),\end{aligned} \tag{3.35}$$

where $v_{xc}(\mathbf{r}_1)$ is a local potential that takes into account correlation and exchange effects, defined as

$$v_{xc}(\mathbf{r}_1) \doteq \int d\mathbf{r}_2 \rho(\mathbf{r}_2)\frac{h(\mathbf{r}_1,\mathbf{r}_2)}{r_{12}}. \tag{3.36}$$

The accuracy of DFT is determined by the accuracy of the description of v_{xc}.

3.5.2 Hohenberg-Kohn Theorems

P. Hohenberg and W. Kohn in 1964 [83] formulated the two following theorems:

- **Theorem I**: for a non degenerate ground state, the external potential $\hat{\mathrm{V}}$, and hence the total energy, is a unique functional of the electron density ρ.
- **Theorem II**: the density ρ that minimizes the total energy $E[\rho]$ is the exact ground state density.

Proof I Let us assume that two different potentials, $\hat{V}^{(1)}$ and $\hat{V}^{(2)}$, give rise to the same ground state density $\rho(\mathbf{r})$. These potentials belong to two distinct Hamiltonian operators $\hat{H}^{(1)}$ and $\hat{H}^{(2)}$ with respective ground-state eigenstates $\Psi^{(1)}(\mathbf{r})$ and $\Psi^{(2)}(\mathbf{r})$ and eigenvalues $E^{(1)}$ and $E^{(2)}$. According to the variational principle:

$$E^{(1)} < \langle\Psi^{(2)}|\hat{H}^{(1)}|\Psi^{(2)}\rangle = \langle\Psi^{(2)}|\hat{H}^{(2)}|\Psi^{(2)}\rangle + \langle\Psi^{(2)}|\hat{H}^{(1)} - \hat{H}^{(2)}|\Psi^{(2)}\rangle\,, \tag{3.37}$$

$$E^{(1)} < E^{(2)} + \langle\Psi^{(2)}|\hat{V}^{(1)} - \hat{V}^{(2)}|\Psi^{(2)}\rangle = E^{(2)} + \int \rho(\mathbf{r})[v^{(1)}(\mathbf{r}) - v^{(2)}(\mathbf{r})]d\mathbf{r}. \tag{3.38}$$

Exchanging labels in the above equation, we obtain:

$$E^{(2)} < E^{(1)} + \langle\Psi^{(1)}|\hat{V}^{(2)} - \hat{V}^{(1)}|\Psi^{(1)}\rangle = E^{(1)} + \int \rho(\mathbf{r})[v^{(2)}(\mathbf{r}) - v^{(1)}(\mathbf{r})]d\mathbf{r}. \tag{3.39}$$

Adding Eq. (3.38) and Eq. (3.39), we have

$$E^{(1)} + E^{(2)} < E^{(2)} + E^{(1)}, \tag{3.40}$$

which is clearly an *absurdum*. It means that the initial assumption was wrong and it must be:

$$\rho^{(1)}(\mathbf{r}) \neq \rho^{(2)}(\mathbf{r}). \tag{3.41}$$

As a consequence, the electron density uniquely determines the external potential and all the properties of the system.

We can write the general form for the exact energy of the ground state as:

$$E[\rho_0] = T[\rho_0] + V[\rho_0] + U_{ee}[\rho_0], \tag{3.42}$$

where T is the kinetic energy, V is the potential created by the nuclei:

$$V[\rho_0] = -\sum_{\alpha=1}^{M} \int \frac{Z_\alpha}{|\mathbf{r} - \mathbf{R}_\alpha|} \rho_0(\mathbf{r}_i) d\mathbf{r}_i, \tag{3.43}$$

and the bielectronic term U_{ee} is given by

$$\begin{aligned} U_{ee}[\rho_0] &= \frac{1}{2} \iint \frac{\rho_0(\mathbf{r}_i, \mathbf{r}_j)}{|\mathbf{r}_i - \mathbf{r}_j|} d\mathbf{r}_i d\mathbf{r}_j = \\ &= \underbrace{\frac{1}{2} \iint \frac{\rho_0(\mathbf{r}_i)\rho_0(\mathbf{r}_j)}{|\mathbf{r}_i - \mathbf{r}_j|} d\mathbf{r}_i d\mathbf{r}_j}_{J[\rho_0]} + \underbrace{\frac{1}{2} \iint \frac{\rho_0(\mathbf{r}_i) h_{XC}(\mathbf{r}_i, \mathbf{r}_j)}{|\mathbf{r}_i - \mathbf{r}_j|} d\mathbf{r}_i d\mathbf{r}_j}_{E_{xc}[\rho_0]}, \end{aligned} \tag{3.44}$$

where the term E_{xc} represents the non-classical contribution to the electron-electron interaction and is unknown. Rewriting the equation for any density ρ, we obtain:

$$E[\rho] = F_{HK} + \int \rho(\mathbf{r}) v(\mathbf{r}) d\mathbf{r}, \tag{3.45}$$

with

$$F_{HK} = T[\rho] + U_{ee}[\rho]. \tag{3.46}$$

F_{HK} is the universal Hohenberg-Kohn functional which can be expressed by the sum of classical terms, that is kinetic, coulombian and non-classical terms.

Proof II In the ground state of the system, the energy is defined by the unique ground state density $\rho^{(1)}(\mathbf{r})$:

$$E^{(1)} = E[\rho^{(1)}] = \langle \Psi^{(1)} | \hat{H}^{(1)} | \Psi^{(1)} \rangle . \tag{3.47}$$

According to the variational principle, a different density $\rho^{(2)}(\mathbf{r})$ will give a higher energy:

$$E^{(1)} = E[\rho^{(1)}] = \langle \Psi^{(1)} | \hat{H}^{(1)} | \Psi^{(1)} \rangle < \langle \Psi^{(2)} | \hat{H}^{(1)} | \Psi^{(2)} \rangle = E^{(2)}. \tag{3.48}$$

Then if one minimizes the total energy of the system written as a functional of $\rho(\mathbf{r})$ with respect to $\rho(\mathbf{r})$, it is possible to find the total energy of the ground state. The correct density that minimizes the energy is then the ground state density.

3.5.3 The Kohn-Sham Equations

The foundation for the use of DFT methods in computational chemistry is the introduction of orbitals as suggested by Kohn and Sham [96]. They made use of a fictitious non-interacting system where its ground-state density was exactly the same as that of some interacting system of interest. The ground-state wavefunction associated with this non-interacting system can be represented with a single Slater determinant of orthonormal orbitals, ψ_i. Thus, the expression of the electronic density becomes

$$\rho(\mathbf{r}) = \sum_i |\psi_i(\mathbf{r})|^2. \tag{3.49}$$

The problem for the pure DFT approach lies in the lack of accurate approximations for the kinetic energy functional. Nevertheless, if we consider a non-interacting system, the total kinetic energy can be calculated from an auxiliary set of orbitals used for representing the electron density (ref KS):

$$T_0 = -\frac{1}{2} \sum_i \int d\mathbf{r} \psi_i^*(\mathbf{r}) \nabla^2 \psi_i(\mathbf{r}). \tag{3.50}$$

In reality, the electrons are interacting and so the above equation does not truly provide the total kinetic energy. However, the difference between the exact kinetic energy and that calculated by assuming a non-interacting system is small and the remaining kinetic energy is absorbed into an exchange-correlation term.

The equations of KS theory are derived by partitioning the ground state energy functional as

$$E_{KS}[\rho] = T_0[\rho] + J[\rho] + \int d\mathbf{r} \rho(\mathbf{r}) v(\mathbf{r}) + E_{XC}[\rho], \tag{3.51}$$

where T_0 and J are given by exact expressions, while E_{XC} is the exchange-correlation energy functional and represents the unknown functional. It is a rather small fraction of the total energy.

By equating this energy to the exact energy Eq. (3.45), we can find an expression for E_{XC}:

$$E_{XC}[\rho] = T[\rho] - T_0[\rho] + U_{ee}[\rho] - J[\rho]. \tag{3.52}$$

The E_{XC} term is then composed of both kinetic and potential energies. By applying the variational principle for the energy to the functional $E[\rho]$ for arbitrary variations of the density, one obtains the Kohn-Sham differential equations:

$$-\frac{1}{2}\nabla^2\psi_i + v_{KS}\psi_i = \varepsilon_i\psi_i, \tag{3.53}$$

where v_{KS} is given by:

$$v_{KS} = v_{ext} + \frac{\delta J}{\delta\rho} + \frac{\delta E_{XC}}{\delta\rho} = v_{ext} + v_{ee} + v_{xc}. \tag{3.54}$$

According to the KS equations, electrons in atoms, molecules and solids behave as independent particles moving in the effective potential v_{KS}.

Although DFT is in principle exact, it requests two kind of approximations in its practical application. The first approximation concerns the XC energy functional and, as a consequence, the XC potential; the second one refers to Kohn-Sham equations which need to be solved using some computational scheme. Self-consistent procedure consists of starting with an initial guess distribution, $\rho^{(i)}$, used to build the external potential V, the Coulomb potential J and the exchange-correlation potential V_{XC}. The single terms are then summed to obtain the effective potential $v_{KS}^{(i)}$. The corresponding Kohn-Sham equation is solved for $\{\psi_j^{(i)}\}$ to update ρ and v_{KS}. Then Kohn-Sham equation is solved again and the procedure is carried on until the difference between two consecutive v_{KS} is below a predetermined accuracy threshold.

To implement the Kohn-Sham scheme, the exchange-correlation functional must to be approximated. There exist different classes of functionals, depending on the kind of the approximation. In the next sessions, the two most important classes of these functionals will be briefly illustrated.

3.5.3.1 Local Density Approximation

The history of XC functionals in ground-state DFT starts with the *Local Density Approximation* (LDA) [96]. In this approximation it is assumed that the exchange-correlation potential depends only on the value of the charge density at the same point:

$$E_{XC}^{LDA} = \int \rho(\mathbf{r})\varepsilon_{XC}[\rho(\mathbf{r})]d\mathbf{r}, \tag{3.55}$$

where $\varepsilon_{XC}(\rho)$ is the exchange-correlation energy of a homogeneous electron gas [97–100] having the local value $\rho(\mathbf{r})$ of the density. The LDA potential is local, i.e., the value of the potential at position $\mathbf{r}$ depends solely on the value of the spin densities at the very same point. It is a reasonable first approximation, for atoms as well as molecules, certainly good when the density is a slowly varying function. It provides atomic and molecular total ground-state energies within 1-5% of the exact value, and molecular equilibrium distances and geometries within about 3% [101]. However, it presents also some shortcomings: among these, the asymptotic behaviour. The XC potential goes to zero exponentially fast and not as $-1/r$ and, as a consequence, the Kohn-Sham energy eigenvalues are too low in magnitude.

3.5.3.2 Generalized Gradient Approximation

LDA can be improved by including a dependence also on gradients of the density. This permits one to define a new generation of functionals, the *Generalized Gradient Approximations* (GGA) [102]. The XC energy density has then the following form:

$$E_{XC}^{GGA} = \int d\mathbf{r}\rho(\mathbf{r})\varepsilon_{XC}(\rho(\mathbf{r}), \nabla\rho(\mathbf{r})). \tag{3.56}$$

Among the most famous GGA functionals, there are the B88 exchange functional [103], the LYP correlation functional [104] and the PBE functional [105]. Their improvements has progressively led to the development of the *hybrid functionals*, which include the exact Hartree-Fock exchange functional. The most popular is B3LYP [98, 104, 106].

3.6 Time-dependent density functional theory

Time-dependent density-functional theory (TDDFT) extends the basic ideas of ground-state DFT to the treatment of time-dependent phenomena and excited states. This generalization of DFT includes the calculation of photoabsorption spectra, as well as dynamical polarizability [107]. Analogously to the static case, the many-body time-dependent Schrödinger equation can be replaced by a set of time-dependent Kohn-Sham (TDKS) equations whose orbitals yield the same time-dependent density [108].

If the time-dependent potential is weak, it is possible to use the linear-response theory to study the target system [109, 110]. In particular, within this approximation, TDDFT yields predictions for electronic excitations and it has become, in this research area, a standard tool. On the other hand, if the time-dependent potential is strong, a full solution of the Kohn-Sham equations is required.

3.6.1 Basic concepts

Let us consider a system of N electrons which obeys the time-dependent Schrödinger equation

$$i\frac{\partial}{\partial t}\Psi(\mathbf{r},t) = \hat{H}(\mathbf{r},t)\Psi(\mathbf{r},t). \tag{3.57}$$

The one-electron density obtained from the wavefunction $\Psi(\mathbf{r},t)$ gives the probability of finding the electrons in position $\mathbf{r}$:

$$\rho(\mathbf{r},t) = N\int d^3\mathbf{r}_2\cdots d^3\mathbf{r}_N|\Psi(\mathbf{r},\mathbf{r}_2\cdots\mathbf{r}_N,t)|^2, \tag{3.58}$$

normalized at all times to the total number of electrons, N.
The Hamiltonian operator can be written as:

$$\hat{H}(\mathbf{r},t) = \hat{T}(\mathbf{r}) + \hat{W}(\mathbf{r}) + \hat{V}_{ext}(\mathbf{r},t), \tag{3.59}$$

where the first term is the kinetic energy of the electrons

$$\hat{T}(\mathbf{r}) = -\frac{1}{2}\sum_{i=1}^{N}\nabla_i^2, \tag{3.60}$$

the second term $\hat{\mathrm{W}}$ accounts for the Coulomb repulsion between the electrons

$$\hat{W}(\mathbf{r}) = \frac{1}{2}\sum_{i\neq j}^{N}\frac{1}{|\mathbf{r}_i - \mathbf{r}_j|}, \tag{3.61}$$

and, finally, the third term is the time-dependent potential, $\hat{V}_{ext}(\mathbf{r}, t)$, which includes the fixed nuclear potential.

If we consider a system interacting with a laser beam which we treat classically, the additional $\hat{\mathrm{V}}_{ext}$ in the length gauge and within the dipole approximation [56] is expressed as:

$$\hat{V}_{ext}(\mathbf{r}, t) = Ef(t)sin(\omega t)\sum_{i=1}^{N}\mathbf{r}_i \cdot \boldsymbol{\alpha}, \tag{3.62}$$

where $\boldsymbol{\alpha}$, ω and E are, respectively, the polarization, the frequency and the amplitude of the laser. The function $f(t)$ is an envelope that describes the temporal shape of the laser pulse.

3.6.2 The Runge-Gross theorem

The Runge-Gross theorem [111] represents the time-dependent extension of the Hohenberg-Kohn theorem [83]. It proves that there is a one-to-one correspondence between the external time-dependent potential and the electronic density for many-body systems evolving from a fixed initial state. Hence, analogously to time-independent case, knowing the density of a system permits to find the external potential which, in turn, permits to solve the time-dependent Schrödinger equation and obtain all properties of the system. The proof of the Runge-Gross theorem is considerably more involved than the proof of the ordinary Hohenberg-Kohn theorem and it will do not consider here.

Given the Runge-Gross theorem, the next step consists in determining the fictitious non-interacting system (i.e., the Kohn-Sham system) which has the same density as the interacting system of interest. In the static case, a minimization of the energy functional yields the ground-state density and thus all other ground-state observables. On the contrary, in time-dependent systems the ground state can not be determined through the minimization of the total energy functional, because the total energy is not a conserved quantity. However, it is possible to introduce a quantity analogous to the energy, the quantum mechanical action,

given by

$$A[\Phi] = \int_{t_0}^{t_1} dt \, \langle \Phi(t) | i\frac{\partial}{\partial t} - \hat{H}(t) | \Phi(t) \rangle \, , \tag{3.63}$$

where $\Phi(t)$ is a N-body function.

In their original paper, Runge and Gross [111] offered a derivation of the Kohn-Sham equation starting from the action (3.63). However, it was later discovered that this formulation encompasses some fundamental problems [107] which were solved by van Leeuwen in 1998 [112].

3.6.3 Time-dependent Kohn-Sham equations

The Runge-Gross theorem, analogously to the Hohenberg-Kohn theorem, does not permit to calculate the electronic density. However, starting from the assertion offered by Runge-Gross theorem, it is fairly straightforward to construct a time-dependent Kohn-Sham scheme. As a consequence, we consider an auxiliary system of noninteracting electrons subject to an external local potential v_{KS}. This potential is chosen such that the density of the Kohn-Sham electrons is the same as the density of the interacting system. These Kohn-Sham electrons obey the time-dependent Schrödinger equation

$$i\frac{\partial}{\partial t}\varphi_i(\mathbf{r},t) = \left[-\frac{\nabla^2}{2} + v_{KS}(\mathbf{r},t)\right]\varphi_i(\mathbf{r},t), \tag{3.64}$$

which have the form of a one-particle equation.

It is worth noting that the Kohn-Sham equation is not a mean-field approximation. Indeed, if we knew the exact Kohn-Sham potential, v_{KS}, we would obtain from Eq. (3.64) the exact Kohn-Sham orbitals, and from these the correct density of the system.

The density of the interacting system can be obtained from the time-dependent Kohn-Sham orbitals

$$\rho(\mathbf{r},t) = \sum_{i}^{N} |\varphi_i(\mathbf{r},t)|^2, \tag{3.65}$$

The Kohn-Sham potential, which gives the density of the interacting system, is given by the sum of three terms

$$v_{KS}(\mathbf{r},t) = v_{ext}(\mathbf{r},t) + v_H(\mathbf{r},t) + v_{xc}(\mathbf{r},t). \tag{3.66}$$

The first term is the external potential, the second one is the Hartree potential which accounts for the classical electrostatic interaction between the electrons, i.e.

$$v_H(\mathbf{r},t) = \int d\mathbf{r}' \frac{\rho(\mathbf{r},t)}{|\mathbf{r}-\mathbf{r}'|}. \tag{3.67}$$

Finally, the xc potential takes into account all the non-trivial many-body effects and is usually approximated by means of the *Adiabatic Local Density Approximation* (ALDA).

3.6.4 Exchange-correlation functionals: adiabatic approximation

While in the stationary DFT many functionals are available to approximate the v_{xc} potential, within the TDDFT approximations to v_{xc}(**r**,t) are still in their infancy. The first and simplest of these is the ALDA, which approximates the XC potential at point **r** and time t by that of a ground-state uniform electron gas of density $\rho(\mathbf{r},t)$. This is clearly accurate when the density varies sufficiently slowly in time and space, but works surprisingly well beyond that limit for many systems and properties, just as LDA does for most ground-state problems.

Considering that $\tilde{\mathrm{v}}_{xc}[\rho]$ is an approximation to the ground-state xc density functional, an adiabatic time-dependent xc potential can be written as

$$v_{xc}^{adiabatic}(\mathbf{r},t) = \tilde{v}_{xc}[\rho](\mathbf{r})|_{\rho=\rho(t)}, \tag{3.68}$$

where we employ the same functional form but evaluated at each time with the density ρ(**r**,t). The adiabatic approximation works only in cases where the temporal dependence is small, i.e., when our time-dependent system is locally close to equilibrium.

By inserting the LDA functional [96] in Eq. (3.68), we can obtain the ALDA:

$$v_{xc}^{ALDA}(\mathbf{r},t) = v_{xc}^{HEG}(\rho)|_{\rho=\rho(\mathbf{r},t)}. \tag{3.69}$$

This approximation assumes that the xc potential at the point **r** and time t is equal to the xc potential of a homogeneous-electron gas (HEG) of density $\rho(\mathbf{r},t)$.

The ALDA has the same problems present in the LDA. Amongst these, there is the erroneous asymptotic behaviour of the LDA potential: for neutral finite

systems, the exact xc potential decays as $-1/r$, whereas the LDA xc potential falls of exponentially. Furthermore, most of the generalized-gradient approximations (GGAs) have asymptotic behaviours similar to the LDA.

3.6.5 Linear response theory

Let us consider the case in which the system responds to a small time-dependent perturbation. As a consequence, we will focus on the linear change of the density.

Let us assume that for $t < t_0$ the system is subject only to the nuclear potential, $v^{(0)}$, and it is in its ground-state with ground-state density, $\rho^{(0)}$. At t_0 we turn on the perturbation, $v^{(1)}$, which induces a change in the density. The total external potential is now $v_{ext} = v^{(0)} + v^{(1)}$.

It is possible to express the density in a perturbative series

$$\rho(\mathbf{r}, t) = \rho^{(0)}(\mathbf{r}) + \rho^{(1)}(\mathbf{r}, t) + \rho^{(2)}(\mathbf{r}, t) + ... \tag{3.70}$$

where $\rho^{(1)}$ is the component of $\rho(\mathbf{r}, t)$ that depends linearly on $v^{(1)}$, $\rho^{(2)}$ depends quadratically etc. If the perturbation is weak, we only consider the linear term, $\rho^{(1)}$. In frequency space it becomes:

$$\rho^{(1)}(\mathbf{r}, \omega) = \int d\mathbf{r}' \chi(\mathbf{r}, \mathbf{r}', \omega) v^{(1)}(\mathbf{r}', \omega). \tag{3.71}$$

The quantity χ is the linear density-density response function of the system. The evaluation of χ through perturbation theory is a very demanding task (ref). We can use the TDDFT to simplify this process.

We can calculate the linear change of density using the Kohn-Sham system

$$\rho^{(1)}(\mathbf{r}, \omega) = \int d\mathbf{r}' \chi_{KS}(\mathbf{r}, \mathbf{r}', \omega) v^{(1)}_{KS}(\mathbf{r}', \omega). \tag{3.72}$$

It means that the response function in Eq. (3.72), χ_{KS}, is the density response function of a system of non-interacting electrons. In terms of the unperturbed stationary Kohn-Sham orbitals we have

$$\chi_{KS}(\mathbf{r}, \mathbf{r}', \omega) = lim \xrightarrow[\eta \to 0^+]{} \sum_{jk}^{\infty} (f_k - f_j) \frac{\varphi_j(\mathbf{r}) \varphi_j^*(\mathbf{r}') \varphi_k(\mathbf{r}') \varphi_k^*(\mathbf{r})}{\omega - (\epsilon_j - \epsilon_k) + i\eta}, \tag{3.73}$$

where f_m is the occupation number of the m orbital in Kohn-Sham ground-state and η is a positive infinitesimal. The Kohn-Sham potential, v_{KS}, includes all powers of the external perturbation due to its non-linear dependence on the density. The potential in Eq. (3.72) is just the *linear* change of v_{KS}, i.e. $v^{(1)}_{KS}$. This latter quantity can be calculated explicitly from the definition of the Kohn-Sham potential

$$v^{(1)}_{KS}(\mathbf{r},t) = v^{(1)}(\mathbf{r},t) + v^{(1)}_{Hartree}(\mathbf{r},t) + v^{(1)}_{xc}(\mathbf{r},t). \tag{3.74}$$

The variation of the external potential is simply $v^{(1)}$, while the change in the Hartree potential is

$$v^{(1)}_{Hartree}(\mathbf{r},t) = \int d\mathbf{r}' \frac{\rho^{(1)}(\mathbf{r}',t)}{|\mathbf{r}-\mathbf{r}'|}. \tag{3.75}$$

Finally the third term,$v^{(1)}_{xc}(\mathbf{r},t)$, is the linear part in $\rho^{(1)}$ of the functional $v_{xc}[\rho]$, given by:

$$v^{(1)}_{xc}(\mathbf{r},t) = \int dt' \int d\mathbf{r}' \frac{\delta v_{xc}(\mathbf{r},t)}{\delta\rho(\mathbf{r}',t)}\rho^{(1)}(\mathbf{r}',t). \tag{3.76}$$

It is useful to introduce the exchange-correlation kernel, f_{xc}, defined by

$$f_{xc}(\mathbf{r}t,\mathbf{r}'t') = \frac{\delta v_{xc}(\mathbf{r},t)}{\delta\rho(\mathbf{r}',t')}. \tag{3.77}$$

Combining the previous results, and transforming to frequency space we arrive at:

$$\begin{aligned}\rho^{(1)}(\mathbf{r},\omega) = &\int d\mathbf{r}'\chi_{KS}(\mathbf{r},\mathbf{r}',\omega)v^{(1)}(\mathbf{r}',\omega)+ \\ &\int d\mathbf{x}\int d\mathbf{r}'\chi_{KS}(\mathbf{r},\mathbf{x},\omega)\left[\frac{1}{|\mathbf{x}-\mathbf{r}'|}+f_{xc}(\mathbf{x},\mathbf{r}',\omega)\right]\rho^{(1)}(\mathbf{r}',\omega).\end{aligned} \tag{3.78}$$

From Eq. (3.71) and Eq. (3.78) trivially follows the relation

$$\begin{aligned}\chi(\mathbf{r},\mathbf{r}',\omega) = &\chi_{KS}(\mathbf{r},\mathbf{r}',\omega)+ \\ &\int d\mathbf{x}\int d\mathbf{x}'\chi(\mathbf{r},\mathbf{x},\omega)\left[\frac{1}{|\mathbf{x}-\mathbf{x}'|}+f_{xc}(\mathbf{x},\mathbf{x}',\omega)\right]\chi_{KS}(\mathbf{x}',\mathbf{r}',\omega).\end{aligned} \tag{3.79}$$

This equation gives a formally exact representation of the linear density response. It means that if we possessed the exact Kohn-Sham potential, a self-consistent solution of (3.79) would yield the response function, χ, of the interacting system. The key ingredient of Eq. (3.79) is then the xc kernel, f_{xc}. The simplest

approximation to f_{xc} is the ALDA kernel, which in linear response reads:

$$f_{xc}ALDA(\mathbf{r}t, \mathbf{r}'\omega) = \delta(\mathbf{r} - \mathbf{r}') \left(\frac{dV_{xc}^{LDA}}{d\rho} \right)_{\rho=\rho_0}. \tag{3.80}$$

In practical implementation, Eq. (3.78) is solved with respect to $\rho^{(1)}(\mathbf{r}, \omega)$, then the photoabsorption spectrum is calculated from the imaginary part of the complex dynamical polarizability:

$$\sigma(\omega) = \frac{4\pi\omega}{c} \mathcal{I} \int z\rho^1(\mathbf{r}, \omega) d\mathbf{r}. \tag{3.81}$$

Chapter 4

Multicenter B-spline static-exchange DFT method

4.1 The B-spline functions

B-splines, originally introduced by I. J. Schoenberg [113, 114], constitute an excellent basis set which became, in the last few decades, a powerful tool in atomic and molecular physics [115]. Their widespread usage in this field is mainly due to the publication of the monograph by de Boor [116]. B-spline functions are defined as piecewise polynomials and they bridge the gaps left by the standard basis functions, such as *Slater Type Orbitals* (STOs) or *Gaussian Type Orbitals* (GTOs), in the treatment of specific molecular problems. In particular, with respect to our purpose, the description of the continuum states requires basis sets which could obey to the peculiar continuum boundary conditions and could reproduce the oscillating behaviour of the wavefunction to infinity. Traditional GTO and STO functions are not adequate to represent the rapidly oscillating continuum states, since numerical linear dependencies rapidly come up as the basis set increases. B-splines, on the contrary, are very flexible functions and can describe accurately both bound and continuum states without running into numerical dependencies. They produce smooth curves with continuous derivatives at every point. Since B-splines are defined in a restricted space, usually referred to as a box, one has to define a certain knot sequence, depending on the target system. The continuum wavefunctions can be correctly reproduce by using a linear grid of points and a sufficient density of B-splines.

4.1.1 Mathematical definition

Let us introduce some mathematical definitions to properly describe the B-spline functions [115]:

- the order k (maximum degree $k-1$) which defines the polynomial:

$$p(x) = a_0 + a_1 x + ... + a_{k-1} x^{k-1}$$

- the interval $I = [a, b]$, divided in l subintervals $I_j = [\xi_j, \xi_{j+1}]$, where the $l+1$ *breakpoints* $\{\xi_j\}$ are in strict ascending order:

$$a = \xi_1 < \xi_2 < \cdots < \xi_{l+1} = b$$

- the class $\mathcal{C}^n$ which specifies the maximum derivation order n for which the derivative function f^n is still continuous over a specified interval

- another sequence of points constituted by the knots $\{t_i\}$, in ascending order, not necessarily distinct:

$$t_1 \leq t_2 \leq \cdots \leq t_m$$

and associated with ξ_j and ν_j as follows:

$$\begin{aligned}
&t_1 = t_2 = \cdots = t_{\mu_1} = \xi_1 \\
&t_{\mu_1+1} = t_{\mu_1+2} = \cdots = t_{\mu_1+\mu_2} = \xi_2 \\
&\cdots \\
&t_{\mu_1+\mu_2+\cdots+\mu_{i-1}+1} = \cdots = t_{\mu_1+\cdots+\mu_i} = \xi_i \\
&\cdots \\
&t_{\mu_1+\cdots+\mu_i+\cdots+\mu_l+1} = \cdots = t_{\mu_1+\cdots+\mu_{l+1}} = \xi_{l+1}
\end{aligned}$$

where μ_j is the multiplicity of the knots t_i at ξ_j and is given by the relation $\mu_j = k - \nu_j$ which implies that $\mu_1 = \mu_{l+1} = k$ and defines the continuity at the knots which is $\mathrm{C}^{k-\mu_j-1}$. In particular at the end points $\mu_1 = \mu_{l+1} = k$

The most common choice for knot multiplicity at inner breakpoints is unity. This choice corresponds to the maximum continuity C^{k-2} in the interval $I =]a, b[$. Then,

the number of B-splines is given by:

$$n = l + k - 1 \tag{4.1}$$

Once these definitions have been introduced, we can express any function f in a B-spline basis set over an interval $[a, b]$:

$$f(x) = \sum_{i=1}^{n} c_i B_i^k(x) \tag{4.2}$$

Hence f is a linear combination of B-splines, made of l polynomial pieces of order k, one for each subinterval I_j . Such a function is conventionally called a *piecewise polynomial function* (pp-function).

4.1.2 The B-spline basis set

A single B-spline $B_i^k(x)$, defined by the order $k > 0$ and a set of $k + 1$ knots, has the following properties:

- $B_i^k(x)$ is a pp-function of order k over $[t_i, t_{i+k}]$
- $B_i^k(x) > 0$ for $x \in]t_i, t_{i+k}[$
- $B_i^k(x) = 0$ for $x \notin]t_i, t_{i+k}[$
- $B_i^k(x) \in C^{k-1-\mu_j}$ for $x = \xi_j$
- $B_j^k(x) \neq 0$ over $]t_i, t_{i+1}[$ for $j = i - k + 1, \cdots, i$ which implies that there are exactly k non-zero B-splines on each interval I_j and:

$$B_i^k(x) \cdot B_j^k(x) = 0 \quad \text{for} \quad |i - j| \geq k \tag{4.3}$$

- the previous property reduces the number of expansion terms to k:

$$f(x) = \sum_{j=1}^{n} c_j B_j^k(x) = \sum_{j=1-k+1}^{i} c_j B_j^k(x) \quad \text{for} \quad x \in]t_i, t_{i+1}[\tag{4.4}$$

- the B-splines are normalized

$$\sum_i B_i^k(x) = 1 \quad \text{over the whole interval} \quad [t_k, t_{n+1}] \tag{4.5}$$

- for simple equidistant knots, each $B_i^k(x)$ is just a translation by one interval of the previous one. If the knots are not equidistant there is a smooth change in the shape

- the index i of each B-spline corresponds to the index of the left knot of the interval $I_j = [\xi_j, \xi_{j+1}] = [t_i, t_{i+1}]$

- Since the B-splines are defined positive and own a minimal support (i.e. an interval $]t_i, t_{i+k}[$ where $B_j^k(x) > 0$), the expansion coefficients of an arbitrary function f are close to the function values at the knot. The main consequence is that wild oscillations in the coefficients are avoided, cancellation errors are minimal and numerical stability maximal

- the B-splines satisfy the recursion relation:

$$B_i^k(x) = \frac{x - t_i}{t_{i+k-1} - t_i} B_i^{k-1}(x) + \frac{t_{i+k} - x}{t_{i+k} - t_{i+1}} B_{i+1}^{k-1}(x) \tag{4.6}$$

  From the last relation it is possible to construct recursively all of the k B-splines of order k from a former one of order $k = 1$ at a specific x. The former B-spline of order $k = 1$ is defined by:

$$B_i^1(x) = \begin{cases} 1, & \text{for } t_i \leq x < t_{i+1}, \\ 0, & \text{otherwise} \end{cases} \tag{4.7}$$

It is worth recalling that for each x, we obtain k non-zero B-splines and their sum equal to 1. The choice of the first and the last k points is completely free but it has to fulfill the increasing order condition:

$$t_1 \leq \cdots t_k \leq \xi_1 \quad \text{and} \quad \xi_{l+1} \leq t_{n+1} \leq \cdots t_{n+k} \tag{4.8}$$

Although it affects only the first and last k B-spline functions, it is generally adopted to use the following sequence:

$$t_1 = \cdots = t_k = \xi_1 \quad \text{and} \quad \xi_{l+1} = t_{n+1} = \cdots = t_{n+k} \tag{4.9}$$

This choice is very convenient because it imposes to all B-splines to cancel outside of the interval $I = [a, b]$. Furthermore, only the first $B_1(x)$ and the last B_n B-splines are respectively discontinuous at $x = a$ and $x = b$. In this context, the boundary conditions can be easily implemented removing B_1 and B_n to satisfy

$f(a) = 0$ and $f(b) = 0$.

In practice calculations, the stable evaluation of B-splines is accomplished by a recursion algorithm efficiently implemented in subroutine BSPLVP [116]. By giving as input values the spline order, the knot sequence, the value of the abscissa and the index of the 'left knot' t_i, this subroutine evaluates the k B-splines that are non-zero at x. Another subroutine, called BSPLVD, can also be used in order to obtain their derivatives which are needed in most of the quantum mechanical applications.

4.2 B-spline static-exchange DFT method

The present method [117] is based on the use of B-spline functions associated to a particularly simple least-squares formulation for the determination of eigenvectors in the continuum spectrum.
It consists of three different steps:

1. Standard DFT calculation (by means of the ADF program) to generate the ground state electron density.
2. Construction of the Hamiltonian matrix in the *Linear Combination of Atomic Orbitals* (LCAO) basis set, followed by a generalized diagonalization for bound states and application of Galerkin approach for continuum states.
3. Dipole transition moment calculation to obtain photoionization observables.

Let us illustrate each single step of this procedure.

4.2.1 Initial guess

A standard LCAO-DFT calculation of the ground state of the molecule represents the first step of the method. This can be done through the program *Amsterdam Density Functional* (ADF) [118], by using, in our case, a double zeta plus polarization (DZP) basis set centered on each atom and a LB94 or LDA functional to describe exchange and correlation effects. This allows to generate the Kohn-Sham

orbitals for the ground state. They are a linear combination of STOs:

$$\phi^{STO}_{nlm\zeta}(\mathbf{r}) = R^{STO}_{n\zeta}(r)Y_{lm}(\theta,\phi), \tag{4.10}$$

where $Y_{lm}(\theta,\phi)$ are the spherical harmonics and the radial part is defined as:

$$R^{STO}_{n\zeta}(r) = Nr^{n-1}e^{-\zeta r}. \tag{4.11}$$

In the above expressions n is the principal quantum number, l the azimuthal quantum number, m the magnetic quantum number and ζ the nuclear effective charge.
The calculated STOs permit to express the ground state density as:

$$\rho_0(\mathbf{r}) = \sum_{i=1}^{N} \varphi_i^*(\mathbf{r})\varphi_i(\mathbf{r}), \tag{4.12}$$

where the Kohn-Sham orbitals are defined as

$$\varphi_i(\mathbf{r}) = \sum_{j}^{Natoms} \sum_{nlm} a_{nlm}\phi^{STO}_{nlm\zeta}(\mathbf{r}_j). \tag{4.13}$$

This density is used as initial guess to build the hamiltonian matrix in a new basis set.

4.2.2 Construction of the LCAO basis set

In the present method the wavefunction is expanded in a basis set obtained as a product of radial B-spline functions [116] and real spherical harmonics adapted to the symmetry [119]. The first implementation was based on a *One Center Expansion* (OCE), where the functions are centered on a single origin. The subsequent step consisted in adding off-center functions, located at non-equivalent nuclei, to the B-spline expansion. This multicenter approach permits to improves dramatically the convergence of the calculation for most molecules [117]. Since the basis set is built on many centers, we indicate the employed basis set as LCAO. Traditionally LCAO basis set is constituted by GTO or STO functions that yield fast convergence for the lowest bound states with a limited number of basis functions. Increasing the basis represents a difficult task because, as already mentioned, numerical linear dependencies rapidly come up. This is due to the large overlap

between functions on different centers. One of the advantages of using spherical B-spline functions lies on the fact that their local nature permits to control the overlap between functions and avoid numerical linear dependence problems [115].

The radial and angular parts of the basis set are expanded over several suitable centers to correctly describe bound and continuum states. These centers are:

- The centre of mass of the molecule, marked by superscript O, associated with a large sphere of radius R^O_{max} to correctly describe the long range behaviour of the continuum wavefunctions.
- The position occupied by each nucleus, marked by the superscript $i > 0$, associated with a small sphere of radius R^i_{max} to comply with the Kato's cusp condition [120]. The radius is generally quite small ($\approx 1 a.u.$) in order to avoid significant overlap with expansion performed on neighbouring centers.

In particular, the OCE is located on a chosen origin and the functions are given by

$$\chi^O_{nlh\lambda\mu} = \frac{1}{r_O} B_n(r_O) X_{lh\lambda\mu}(\vartheta_O, \varphi_O), \tag{4.14}$$

where B_n is the nth B-spline monodimensional function and

$$X_{lh\lambda\mu}(\theta, \phi) = \sum_m Y^R_{lm}(\vartheta, \varphi) b_{lmh\lambda\mu}, \tag{4.15}$$

are symmetry adapted linear combination of real spherical harmonics $Y^R_{lm}(\vartheta, \varphi)$ [117]. The indices have the following meaning: l and m are the usual angular momentum quantum numbers, λ indicates the irreducible representation (IR) of the molecular point group under consideration, μ the subspecies in case of degenerate IR and h distinguishes amongst different elements with the same $\{l, \lambda, \mu\}$ set.
The further off-center functions are given by:

$$\chi^i_{nlh\lambda\mu} = \sum_{j \in Q_i} \frac{1}{r_j} B_n(r_j) \sum_m b_{lmh\lambda\mu j} Y^R_{lm}(\vartheta_j, \varphi_j), \tag{4.16}$$

where i is an index which runs over the non-equivalent nuclei, Q_i is the set of equivalent nuclei, j runs over the equivalent nuclei and gives the origin of the off-center spherical coordinates, r_j, ϑ_j, φ_j. The coefficients $b_{lmh\lambda\mu}$ and $b_{lmh\lambda\mu j}$ are determined by symmetry.

B-splines are built over different radial intervals: $\left[0; R^O_{max}\right]$ for the set $\{\chi^O_{nlh\lambda\mu}\}$

and $[0; R^i_{max}]$ for the set $\{\chi^i_{nlh\lambda\mu}\}$. Furthermore, $R^0_{max} \gg R^i_{max}$. Each shell i comprises a different number of B-splines N^i_b.
These functions, as already highlighted, are completely defined by their order k and by the grids of knots. In our calculation, k has been fixed to 10 and the grids defined linearly with a specific density for each shell.
The cost and the accuracy of the calculation are due to:

- the point group symmetry of the molecule
- the B-spline parameters: k, R^O_{max}, R^i_{max} and N^i_b
- the maximum value of the angular momentum L_0 used in the OCE

4.2.3 Construction of the Hamiltonian matrix

Once the self-consistent electron density has been obtained by the ADF calculation, it is possible to build the Hamiltonian matrix. The present method is called *static-exchange DFT*, by reference to static-exchange in Hartree-Fock method. It has the advantage to provide directly orthogonal bound and continuum states.

In the LCAO basis, each elements of the matrix is given by:

$$\mathbf{H}^{\lambda}_{ijmnhh'll'} = \int B^i_m(r_i) X^i_{lh\lambda\mu}(\vartheta_i, \varphi_i) \hat{h}_{KS} B^j_n(r_j) X^j_{l'h'\lambda\mu}(\vartheta_j, \varphi_j). \tag{4.17}$$

By definition, the hamiltonian matrix $\mathbf{H}$ is totally symmetric. As a consequence, it is block-diagonal with the quantum numbers λ and independent on μ and can be partitioned into blocks for each λ value. The off-center spheres do not overlap and then the only non-zero blocks are diagonal blocks $\mathbf{H}_{ii}$ connecting basis functions from the same set $\left\{\chi^i_{\lambda\mu hl}\right\}$ and off-diagonal blocks $\mathbf{H}_{i0}$ and $\mathbf{H}_{0i}$ connecting basis functions from two different sets $\left\{\chi^O_{nlh\lambda\mu}\right\}$ and $\left\{\chi^i_{nlh\lambda\mu}\right\}$. The Hamiltonian matrix has then the following structure:

$$\hat{H} = \begin{pmatrix} \hat{H}_{00} & \hat{H}_{01} & \cdots & \hat{H}_{0i} & \cdots & \hat{H}_{0\kappa} \\ \hat{H}_{10} & \hat{H}_{11} & \cdots & 0 & \cdots & 0 \\ \vdots & \vdots & \vdots & 0 & \vdots & \vdots \\ \hat{H}_{i0} & 0 & \cdots & \hat{H}_{ii} & \cdots & 0 \\ \vdots & \vdots & \vdots & 0 & \vdots & \vdots \\ \hat{H}_{\kappa 0} & 0 & \cdots & 0 & \cdots & \hat{H}_{\kappa\kappa} \end{pmatrix}. \tag{4.18}$$

Since multicentric electronic integrals between B-splines are not analytical, the largest computational effort is due to the calculation of the non-diagonal block elements H_{i0} ($H_{0i} = H_{i0}^T$). A numerical three-dimensional Gauss-Legendre scheme is used to carry out the integration: the weights and points are distributed in spherical coordinates around the jth off-center nucleus, with polar axis rotated and passing through the origin of the large OCE. This rotation of the coordinate framework permits to reduce the integration to two variables (r and ϑ). Within this new framework only the molecular potential must be numerically integrated over φ also.

4.2.4 Solutions of the KS equations

The one-electron orbitals are obtained as the solutions of the KS equations

$$H_{KS}\varphi_i = \varepsilon_i\varphi_i, \qquad i = 1, ..., n, \tag{4.19}$$

where the KS Hamiltonian is given by

$$H_{KS} = -\frac{1}{2}\nabla^2 - \sum_N \frac{Z_N}{|\mathbf{r} - \mathbf{R}_N|} + \int \frac{\rho_0(\mathbf{r}')d\mathbf{r}'}{|\mathbf{r} - \mathbf{r}'|} + V_{XC}[\rho_0(\mathbf{r})]. \tag{4.20}$$

The density obtained from the ADF program is used to build the hamiltonian (4.20) in the new basis, which will take the form (4.18). One can evaluate separately each term:

- the kinetic energy term and the Coulomb attraction potential can be easily integrated in the LCAO basis set used
- the solution of the Poisson equation, $\nabla^2 V_H = -4\pi\rho(\mathbf{r})$, in the same basis, provides the classical electrostatic Hartree potential, represented by the third term in Eq. (4.20)
- depending on the target system, one can choose among several exchange-correlation potentials, $V_{XC}\left[\rho_0(\mathbf{r})\right]$. In particular, for small molecules, LB94 and LDA(VWN) functionals reproduce quite well the photoelectron spectra [121].

Through a generalized diagonalization of the Hamiltonian one can solve the KS equations and the resulting Kohn-Sham orbitals are expanded on the full basis set.

Since the LCAO basis set is larger than the DZP one, the bound states obtained are expected to be more accurate than those obtained in the initial ADF calculation, notably in the long range region, which appreciably affects the transition moments to the continuum.

In order to correctly describe both bound and continuum states near the nuclear positions, it is essential to use a dense knot grid around the nuclei. However, these states do not have the same properties and then we must consider different elements for the parametrization of the basis:

- since the bound states spread spatially with the increasing of the principal quantum number, the description of higher bound states needs a bigger box size
- the variation of the continuum states at large scales implies the use of a box bigger than for the case of bound states
- since the asymptotic period of radial oscillations associated to the continuum wavefunctions decreases linearly with the square root of the energy, the description of higher continuum states requires a denser knot grid

4.2.5 The continuum

The spectrum of the static-exchange DFT Hamiltonian is constituted by a bound eigenvalues spectrum below zero electron energy and by a continuum eigenvalues spectrum above. These continuum states can be obtained with a correct normalization by using the Galerkin (or least-squares) approach.

4.2.6 Galerkin method

This method represents a generalization of the Ritz-Galerkin method originally developed to extract bound states. Within this approach, the continuum states do not vanishes at R^O_{max} and are obtained for specific energies in a fixed basis set [122]. For the traditional Galerkin approach, one considers the traditional algebraic eigenvalue problem (secular equation):

$$(\mathbf{H} - E\mathbf{S})\mathbf{c} = 0. \tag{4.21}$$

For the continuous spectrum, such equation does not admit non-trivial solutions $\mathbf{c} \neq 0$ and the energy ε of the photoelectron is fixed. However, we can equivalently find approximate solutions by calculating the coefficients that minimize the residual vector, $Hc - \varepsilon Sc$, with $c \neq 0$. In order to do this, we solve the following eigenvalue problem instead of (4.21):

$$\mathbf{A}(\varepsilon)\mathbf{c} = a\mathbf{c}, \tag{4.22}$$

where $\mathbf{A}(\varepsilon) = \mathbf{H} - \varepsilon\mathbf{S}$. Fischer et al. [123] proposed to solve this equation by taking as approximate solutions the values of c that correspond to the eigenvalues closest to zero. Of course, for exact solutions of the KS equation, a should be zero. This can not be exactly satisfied in a finite basis. However, the minimum modulus eigenvalues a of $\mathbf{A}$ corresponding to the required number of the independent solutions (open channels) are well separated from the others when the basis set is sufficiently dense and flexible to provide accurate solutions. The matrix $\mathbf{A}$ is not Hermitian, because there are not boundary conditions, and the eigenvalues a and eigenvectors $\mathbf{c}$ are generally complex. Meanwhile, $\mathbf{A}$ is real, and they necessarily occur by conjugate pairs (a, c) and (a^*, c^*). If all these solutions are associated to the same energy ε, it is possible to avoid complex representations by taking R(c) and I(c) as independents solutions. Once known the eigenvalues, it is possible to obtain eigenvectors by block inverse iteration [124]. These constitute a complete and independent set of stationary solutions. From these states, one can build continuum states that are normalized and which satisfy required boundary conditions. Actually, it has been later found that a better stability is obtained solving the modified equation

$$A^T Ac = ac, \tag{4.23}$$

which is an hermitian problem.

4.2.7 TDDFT

The static-exchange DFT method might be unsuitable when the coupling between different photoionization channels is significant. The TDDFT level results, in such a situation, are expected to be improved with respect to the simpler KS. The response of the electrostatic potential due to a first order variation in the electronic density can be consider, according to Zangwill and Soven [125], in a self consistent way, by taking into account a total perturbing potential Φ^{SCF}, which

results from two contributions: the external potential Φ^{EXT} and the Coulomb and exchange-correlation terms due to the screening of electrons. The deriving expression is:

$$\Phi^{SCF}(\mathbf{r},\omega) = \Phi^{EXT}(\mathbf{r},\omega) + \int \frac{\delta\rho(\mathbf{r},\omega)d\mathbf{r}'}{|\mathbf{r}-\mathbf{r}'|} + \left.\frac{\partial V_{XC}}{\partial\rho}\right|_{\rho(\mathbf{r})} \delta\rho(\mathbf{r},\omega), \tag{4.24}$$

where $\delta\rho(\mathbf{r},\omega)$ is the induced density and the adiabatic local density approximation (ALDA) to the exchange-correlation kernel is employed. The induced density is obtained from the KS dielectric susceptibility (χ) and the SCF potential:

$$\delta\rho(\mathbf{r},\omega) = \int \chi(\mathbf{r},\mathbf{r}',\omega)\Phi^{SCF}(\mathbf{r}',\omega)d\mathbf{r}'. \tag{4.25}$$

So we have to solve the two coupled equations, (4.24) and (4.25). In order to do this, it is possible to use different algorithms. Iterative algorithms, for example, consist in starting with the initial guess $\Phi^{SCF} = \Phi^{EXT}$ and then alternatively solve (4.25) and (4.24) until convergence is met for Φ^{SCF}. However, since the two equations are linear in Φ^{SCF}, one can avoid the iterative procedure and use a direct (noniterative) algorithm. By substituting (4.25) in (4.24) we can obtain the equation:

$$\Phi^{SCF}(\mathbf{r},\omega) = \Phi^{EXT}(\mathbf{r},\omega) + \iint K(\mathbf{r},\mathbf{r}')\chi(\mathbf{r}',\mathbf{r}'',\omega)\Phi^{SCF}(\mathbf{r}'',\omega)d\mathbf{r}'\mathbf{r}'', \tag{4.26}$$

where K indicates the Coulomb and the ALDA exchange-correlation kernel:

$$K(\mathbf{r},\mathbf{r}') = \frac{1}{|\mathbf{r}-\mathbf{r}'|} + \delta(\mathbf{r}-\mathbf{r}') \left.\frac{\partial V_{XC}}{\partial\rho}\right|_{\rho(\mathbf{r})}. \tag{4.27}$$

If the integral (4.26) is solved with respect to Φ^{SCF}, the TDDFT problem can be recast avoiding the SCF procedure. Once Φ^{SCF} is obtained, all the parameters which describe the photoionization process are calculated through transition moments using Φ^{SCF} instead of dipole operator in the conventional expressions [125, 126].

4.2.7.1 Resolution of the direct TDDFT equation

If Eq. (4.26) is represented over the LCAO B-spline basis set, we can indicate with $\mathbf{K}$ and $\boldsymbol{\chi}$ the matrix representation of the kernel and dielectric susceptibility,

respectively, with $\mathbf{\Phi}^{SCF}$ and $\mathbf{\Phi}^{EXT}$ the vector of the coefficients of the unknown SCF and the known external dipole potential, respectively. Solving with respect to $\mathbf{\Phi}^{SCF}$ the following algebraic linear system is obtained:

$$(\mathbf{K}\boldsymbol{\chi} - 1)\mathbf{\Phi}^{SCF} = -\mathbf{\Phi}^{EXT}. \tag{4.28}$$

If a method is given to build the two matrices which appear in (4.28) over the basis set, the TDDFT problem is recast to a linear set of algebraic equations, and the SCF procedure is avoided.

The K matrix is energy independent, and gives the potential generated in first order by a charge density $\delta\rho$

$$\delta\Phi = K\delta\rho = \delta V_c + \delta V_{xc}, \tag{4.29}$$

$$\delta V_{xc} = -4\pi\Delta^{-1}\delta\rho, \tag{4.30}$$

where Δ is the matrix of the Laplacian (Poisson equation) and $\delta V_c = \frac{\partial V_{xc}}{\partial\rho}|_{\rho_0(\mathbf{r})}\delta\rho$. Employing $\delta\rho = \tau_j$, a basis functions, both matrices are easily evaluated. The linear response is instead energy (ω) dependent and gives the density response to a potential perturbation. Again the idea is to employ a single basis functions τ_j as a potential perturbation, and to compute the induced density $\delta\rho_j = \chi\tau_j$. Then $\chi_{kj}(\omega) = \langle\tau_k, \chi\tau_j\rangle = \langle\tau_k, \delta\rho_j\rangle$. In order to solve the linear response equations, we can employ the *Modified Sternheimer Approach* (MSA) [127]. In this formalism, the generic induced density $\delta\rho_j$ can be obtained from the perturbation of the KS orbitals $\varphi_{ij}^{(1,\pm)}$:

$$\delta\rho_j(\mathbf{r},\omega) = \sum_i n_i(\varphi_i^*\varphi_{ij}^{(1,\pm)} + \varphi_i\varphi_{ij}^{(1,\mp)*}), \tag{4.31}$$

where n_i are the occupation numbers and $\varphi_{ij}^{(1,\pm)}$ are extracted from the solution of the inhomogeneous equation:

$$[H_{KS} - \varepsilon_i \pm \omega]\varphi_{ij}^{(1,\pm)} = -\hat{P}\tau_j\varphi_i, \tag{4.32}$$

where the generic basis element τ_j has been substituted to the Ψ^{SCF} of the inhomogeneous equation [128], ω indicates the photon energy and $\hat{P}$ is a projector which orthogonalizes with respect to the occupied orbitals.

Equation (4.32) can be represented in the LCAO basis set, obtaining a system of linear algebraic equations, where the left-hand side matrix is built from the

unperturbed KS Hamiltonian and the overlap matrix, while the right-hand side consists in integrals between two basis elements and an occupied molecular orbital properly orthogonalized [129]. More precisely this equation can be solved with standard Lower-Upper (LU) decomposition for each photon energy. The adequate outgoing boundary conditions for the photoelectron wave functions are also imposed. The integrals between the two basis elements and an occupied molecular orbital are calculated with the same numerical integration scheme employed in the construction of the KS Hamiltonian. Once Eq. (4.32) has been solved, the coefficients $\varphi_{ij}^{(1,\pm)}$ are obtained and from them $\delta\rho_j$ and $\chi_{kj}(\omega)$. Once the solution vector $\mathbf{\Phi}^{SCF}$ of the coefficients is obtained, the integrals between an initial occupied orbital, the SCF potential and the continuum orbital, necessary to calculate the cross section and the asymmetry parameters, are calculated from the integrals between the occupied orbitals and the two basis functions, by performing two summations running over both continuum and SCF potential coefficients.

Chapter 5

Correlated single channel approach

5.1 Bound states calculation

In the correlated single channel approach, the initial and final bound states are computed at the CASSCF level, with Molpro package [130]. The first step of the procedure is the choice of a suitable active space for the target system. This is followed by a CASSCF calculation of the ground state of the molecule and then a CASSCF calculation of the ionic state of interest. The obtained CASSCF wavefunctions are then employed to compute the relative Dyson orbitals. This is done through a code set up in collaboration with the theoretical chemistry group of the University of Ferrara. This code is based on the direct evaluation of the overlap between the CASSCF wavefunctions separately optimized for the ion and for the neutral molecule.

5.2 Transition moment from the Dyson orbitals

Let us consider two given wavefunctions for an initial N particle system, Ψ_I^N, and for the $N-1$ system, Ψ_F^{N-1}. The Dyson orbital is uniquely defined as

$$\phi_{IF}^d(1) = \sqrt{N} \int \Psi_I^N(1,...,N)\Psi_F^{N-1}(2,...,N)d2...dN. \tag{5.1}$$

Let us introduce an orthonormal basis $\{\phi_p\}$ and the associated creation and annihilation operators $\{a_p^+, a_p\}$. Then the Dyson orbital can be expanded as

$$\phi^d = \sum_p \gamma_p \phi_p, \tag{5.2}$$

where the amplitudes γ_p are given by

$$\gamma_q = \langle \Psi_F^{N-1} | a_q | \Psi_I^N \rangle \,. \tag{5.3}$$

At high energy, the final wavefunction corresponding to a given ionic state, described by a bound $N-1$ particle wavefunction, Ψ_F^{N-1}, and a photoelectron of kinetic energy ε (neglecting additional quantum numbers), ϕ_ε, can be written as an antisymmetrized product

$$A(\Psi_F^{N-1}\phi_\varepsilon) = a_\varepsilon^+ \Psi_F^{N-1}, \tag{5.4}$$

where a_ε^+ is the creation operator relative to the photoelectron wavefunction ϕ_ε. By following the Arneberg's derivation [131], one can express the photoelectron wavefunction as

$$\phi_\varepsilon = \sum_p \phi_p \langle \phi_p | \phi_\varepsilon \rangle \,, \tag{5.5}$$

from which one can also obtain the relations:

$$\begin{aligned} a_\varepsilon^+ &= \sum_p a_p^+ \langle \phi_p | \phi_\varepsilon \rangle \\ a_\varepsilon &= \sum_p a_p \langle \phi_\varepsilon | \phi_p \rangle \,, \end{aligned} \tag{5.6}$$

and

$$[a_p, a_q^+] = \delta_{pq}, \qquad [a_\varepsilon, a_q^+]_+ = \langle \phi_\varepsilon | \phi_q \rangle \,. \tag{5.7}$$

Let us also write the transition (dipole) operator T in second quantized form as

$$T = \sum_{pq} t_{pq} a_p^+ a_q. \tag{5.8}$$

Therefore the dipole transition moment between the initial wavefunction and the final one is defined as

$$D_{FI} = \langle a_\varepsilon^+ \Psi_F^{N-1} | T | \Psi_I^N \rangle = \langle \Psi_F^{N-1} | a_\varepsilon T | \Psi_I^N \rangle \,. \tag{5.9}$$

By calculating

$$\begin{aligned} a_\varepsilon T &= \sum_{pq} t_{pq} a_\varepsilon a_p^+ a_q = \sum_{pq} t_{pq} \langle \phi_\varepsilon | \phi_p \rangle a_q - \sum_{pq} t_{pq} a_p^+ a_\varepsilon a_q = \\ &= \sum_p \sum_q \langle \phi_\varepsilon | \phi_p \rangle \langle \phi_p | t | \phi_q \rangle a_q + \sum_{pq} t_{pq} a_p^+ a_q a_\varepsilon = \\ &= \sum_q \langle \phi_\varepsilon | t | \phi_q \rangle a_q + T a_\varepsilon = \sum_q \langle \phi_\varepsilon | t | \phi_q \rangle a_q + T \sum_q \langle \phi_\varepsilon | \phi_q \rangle a_q, \end{aligned} \tag{5.10}$$

we can obtain:

$$D_{FI} = \sum_q \langle \phi_\varepsilon | t | \phi_q \rangle \langle \Psi_F^{N-1} | a_q | \Psi_I^N \rangle + \sum_q \langle \phi_\varepsilon | \phi_q \rangle \langle \Psi_F^{N-1} | T a_q | \Psi_I^N \rangle , \tag{5.11}$$

$$D_{FI} = \sum_q \langle \phi_\varepsilon | t | \phi_q \rangle \gamma_q + \sum_q \langle \phi_\varepsilon | \phi_q \rangle \eta_q, \tag{5.12}$$

where one has defined the amplitudes

$$\begin{aligned} \gamma_q &= \langle \Psi_F^{N-1} | a_q | \Psi_I^N \rangle \\ \eta_q &= \langle \Psi_F^{N-1} | T a_q | \Psi_I^N \rangle . \end{aligned} \tag{5.13}$$

In this expression, originally derived by Martin and Shirley [70], the first term is called the direct term and the second one the conjugate term. At high energy (or simply if the photoelectron wavefunction is considered orthogonal to all bound orbitals included in the expansion of the initial state, Ψ_I^N) the conjugate term is negligible and only the first term survives.

Moreover, we have already seen that in a basis of one-particle states $\{\phi_p\}$ the Dyson orbital can be expanded as

$$\phi^d = \sum_p \gamma_p \phi_p.$$

The dipole transition moment is then expressed as

$$D_{FI} = \sum_p \langle \phi_\varepsilon | t | \phi_p \rangle \gamma_p = \langle \phi_\varepsilon | t | \phi^d \rangle , \tag{5.14}$$

namely it is reduced to the dipole transition moment between the Dyson orbital and the photoelectron wavefunction.

Finally, at the independent particle level (unrelaxed Hartree-Fock configurations)

$\gamma_p = 1$ for the primary ionic states

$$\Psi_F^{N-1} = a_p \Phi_0^N, \tag{5.15}$$

and $\gamma_p = 0$ otherwise (Φ_0^N is the HF initial state), so only those final states are allowed, and the relative Dyson orbitals are just the canonical occupied HF orbitals ϕ_p, of unitary norm.
The norm of the Dyson orbital, defined as

$$\|\phi^d\|^2 = \sum_p |\gamma_p|^2 = R_F, \tag{5.16}$$

is often called *spectral strength* (or *pole strength*, or *spectroscopic factor*) of the final state Ψ_F^{N-1}. Correlation lowers the spectral strengths of the primary ionic states and, at the same time, gives intensity to additional states, i.e. satellite or shake-up states, characterized by further electronic excitations. The usual values for the outermost primary states (outer valence) are about $0.8 - 1.0$. The effects become especially strong for the inner valence region mainly because of the mixing with $2h - 1p$ configurations relative to outer excitations and the spectral strength can spread over many final states of low intensity. Another important effect is represented by the mixing of different canonical MOs in the Dyson orbital, namely a rotation of the occupied orbitals upon ionization.

5.3 Projection onto the B-spline basis

In Molpro, as in most quantum chemistry programs, MOs are approximated by Gaussian basis functions, since the required integrals can be computed very quickly in this basis. Actually, the basis functions are constituted by linear combination of gaussian primitives. Such a basis functions will have their coefficients and exponents fixed. These linear combinations, called contractions, are defined *Contracted Gaussian Type Orbitals* (CGTO).

Once the *ab initio* orbitals have been obtained, the first task in our procedure consists in expanding these orbitals expressed in Gaussian basis functions onto the B-spline basis by projection. This is related to the ease of evaluating one particle dipole matrix elements. The calculation of dipole matrix elements is the only part, in the present formulation, where mixed Gaussian/spline integrals are

needed. This has the advantage of decoupling the calculation of Dyson orbitals from that of continuum dipole matrix elements, and can be easily adapted to any calculation of the former.

In practice, in order to express the bound states monoelectronic wavefunctions, we can choose MOs coefficients which result from a HF calculation or, indeed, from a CASSCF calculation. Once the *ab initio* calculation of the ground state of the target system is performed, we can dump the current geometry, the basis functions and the MOs coefficients in a Molden file. Molden is a package for displaying molecular density from several *ab initio* packages and the Molden format can be easily handled. The MOs orbitals contained in this file, which is suitably modified, are then projected onto the B-spline basis through a specific implemented subroutine.

In the case of Dyson orbitals, we first obtain these orbitals as linear combination of CASSCF orbitals with suitable coefficients obtained from the previous calculation and then we can do the projection onto the B-spline basis.
In particular, within our procedure, each MO is expressed as:

$$\varphi_k = \sum_{j=1}^{n} c_{jk}\phi_j, \tag{5.17}$$

where $\{\phi_j\}$ is the CGTO set. The MOs orbitals so obtained are used to express the ith Dyson orbital as:

$$\varphi^D_{i,\lambda,\mu} = \sum_k \varphi_{k,\lambda,\mu} C^D_{k,i,\lambda}, \tag{5.18}$$

where k runs over the number of orbitals in each symmetry, λ is the active symmetry index, μ stands for the symmetry degeneracy and the coefficients $C^D_{k,i,\lambda}$ are obtained by the matrix elements:

$$C^D_{k,i,\lambda} = \langle \Psi^N | a^+_{k\lambda\mu} | \Psi^{N-1}_i \rangle \,. \tag{5.19}$$

The projection of the MOs φ_k is obtained by computing the scalar products with the B-spline basis

$$b_{nk\lambda} = \langle \chi_{n\lambda\mu} | \varphi_{k\lambda\mu} \rangle \,, \tag{5.20}$$

by the same numerical integration algorithms employed for the calculation of other matrix elements. Then it is easy to obtain the coefficients in the expansion

$$\varphi_{k\lambda\mu} = \sum_n a_{nk\lambda}\chi_{n\lambda\mu}, \tag{5.21}$$

by solving the linear system

$$\sum_n S^{\lambda}_{mn} a_{nk\lambda} = b_{mk\lambda}. \tag{5.22}$$

The accuracy of the expansion is monitored by the norms of the projected orbitals, which are extremely close to 1. The projected orbitals are in any case renormalized. The expansion coefficients for the Dyson orbitals are obtained in the same way.

5.4 Test case

We carried out some tests to verify the accuracy of our procedure and the size of the basis set required to reach the convergence. The test case was represented by a simple molecule: H_2^+. The results obtained have been compared with those of the standard DFT procedure fully converged with respect to the B-spline basis in Fig. 5.1. We tested several basis sets for both cases. These basis sets are reported in the table 5.1, with the corresponding number of basis functions. The results obtained both for the cross sections and for the asymmetry parameters show that it is necessary, at least in the case of asymmetry parameters, to use an extremely large basis set to reach the convergence with the CGTO basis. This is due to the extension of the B-spline basis with respect to the Gaussian basis set. In particular, only by using the d-aug-cc-pV5Z basis set reported in Fig. 5.2, the curves have a good match. The excellent agreement between the calculated values proves the correctness of the current implemented procedure.

Basis set	**Number of CGTOs**
cc-pVTZ	17
aug-cc-pVTZ	27
d-aug-cc-pVTZ	37
d-aug-cc-pVQZ	77
d-aug-cc-pV5Z	143

TABLE 5.1: Number of CGTOs associated to each basis set.

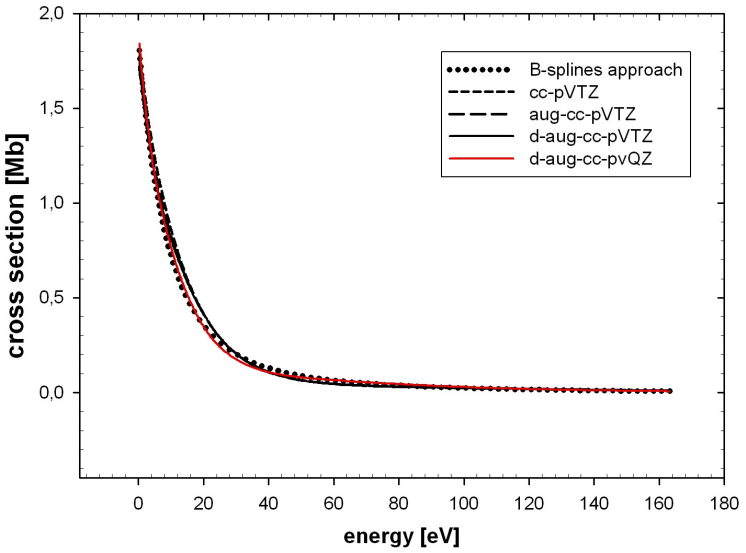

(a) Cross section of H_2^+

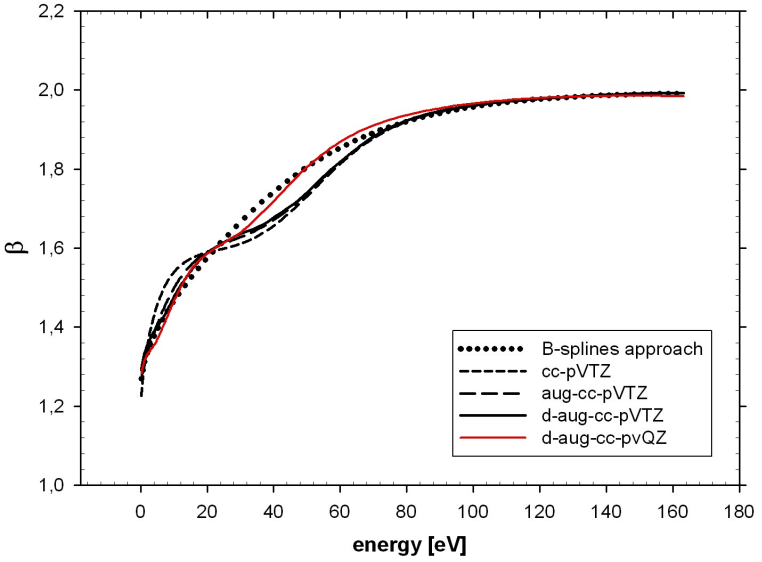

(b) Asymmetry parameter of H_2^+

FIGURE 5.1: Cross section and asymmetry parameters of H_2^+ calculated with different basis sets and compared to the B-splines approach.

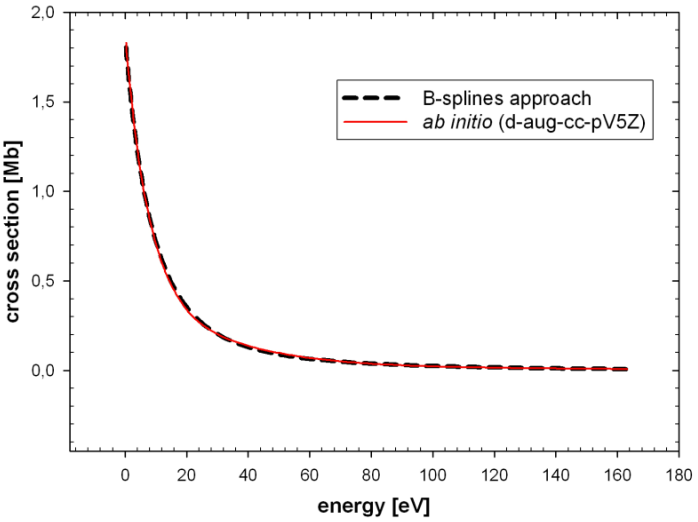

(a) Cross section of H_2^+

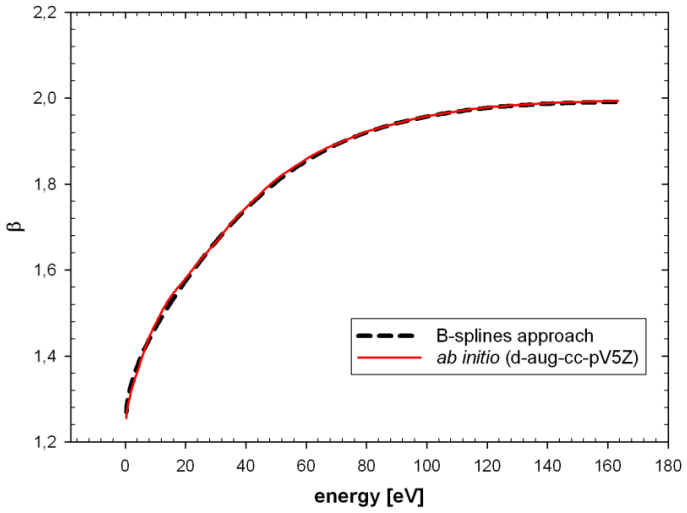

(b) Asymmetry parameter of H_2^+

FIGURE 5.2: Cross section and asymmetry parameters of H_2^+ calculated with d-aug-cc-pV5Z and compared to the B-splines approach.

Part II

Results

Chapter 6

Introduction

The high energy behaviour of cross sections in molecular photoemission has received scant attention up till now. This is due to the difficulty of observing rapidly decreasing cross sections over a wide energy range. Moreover it was tacitly assumed that all molecular features die after approximately 50–100 eV, so that only flat and dull behaviour would be observed due to the sum of atomic cross sections. Development of latest-generation synchrotron radiation has extended the accessible energetic range in photoelectron spectroscopy and it has instead been seen that there are structures at high energy in cross section profiles due to diffraction and interference effects. As the wavelength of the emitted electron becomes comparable to the size of interatomic distances, diffraction and interference phenomena appear in the spectra as a result of wave propagation. This gives rise to an oscillatory behaviour superimposed on the fast declining atomic cross section. So, far from being an exceptional feature of the spectra, confined to peculiar systems, it is expected that such oscillations represent a universal phenomenon, present in all polyatomic targets, from diatomics to complex non-symmetrical molecules and from the deep core to the outer valence shell. Besides the general qualitative understanding the observed features may differ considerably in the details. This points to the richness of potential chemical information, about both geometrical and electronic structure, but complicates the interpretation, such that a more careful analysis is needed. Ultimately, the full reconstruction of the observed patterns may require accurate theoretical modelling and a least squares retrieval of interesting information from fitting the simulated profiles to the experimental ones. At the outset however two quite separate mechanisms can be distinguished: interference due to direct emission from equivalent centres, and diffraction due

to secondary waves scattered from adjacent inequivalent centres. These effects, related to electron waves emitted by photoionization, are a manifestation of the wave particle duality at the heart of Quantum Mechanics. They have been observed and understood long ago [132] and have been revived in more recent times to become the widespread EXAFS technique [133] which is of routine application in the determination of the geometry of molecules, solids and surfaces. Photoelectron interference due to coherent emission from equivalent centers, also known as Young's type interference, had been also predicted in 1966 by H. D. Cohen and U. Fano (CF) [27], from a model calculation on H_2^+. However, it laid dormant until quite recently, when it became possible to observe the predicted features in the ionization of core orbitals in N_2 [134–136] and C_2H_2 [137, 138] and also in related collision experiments [139, 140].

The original idea of Cohen and Fano consists in considering that the nuclei could act as two-center emitters. The results of this interaction are waves that interfere like in a typical Young's double slit experiment. As a consequence, fingerprints of these interferences are expected in the photoionization cross sections. Within this picture, the photoelectron is supposed to be coherently emitted from the two atomic centers when the wavelength is comparable to the internuclear distance. This can be considered valid for quite localized initial MOs such as core MOs. Actually, this assumption can be done also in the case of valence shell photoionization for small molecular systems such as N_2 and CO. The CF formula for oscillation in the total cross section is given by:

$$\sigma(k) = \sigma^*(k)\frac{1}{1+S}\left[1 + \frac{sinkR}{kR}\right] \tag{6.1}$$

where k is the photoelectron momentum, S the overlap integral, R the interatomic distance and σ^* an effective atomic cross section. The above formula, although capturing the basic mechanism involved, fails to quantitatively describe the actual interference patterns as it has been verified by accurate calculations on H_2, H_2^+ [141] and in some early experiments [134, 135]. This is basically due to the inadequacy of the plane wave description of the continuum employed by CF, and the corresponding phase shifts, especially at low energy, where the molecular potential gives rise to a quite structured continuum.

The reason that most investigations have concentrated in the core region is due to the simple nature of the relevant MOs, $1\sigma_g$ and $1\sigma_u$, which correspond to the symmetric and antisymmetric combinations of 1s AOs. Experimentally their study

requires resolving the two individual ionization channels. This is because oscillations appear exactly out of phase in the two channels and cancel in the unresolved cross section. In practice this restricts investigation to the already mentioned N_2 and C_2H_2 molecules, which have a larger $1\sigma_g$-$1\sigma_u$ separation of about 100 meV because of the short interatomic distance, caused by the triple bond, just at the limits of experimental feasibility. Indeed, commonly, the g/u splitting of core orbitals is too small to be observable; generally well below lifetime broadening and vibrational excitation.

In general, oscillations induced by interference are difficult to observe directly as they are a tiny modulation over a strongly decreasing background. A clear way of revealing them experimentally is by taking cross section ratios between different channels. Since cross sections from gerade and ungerade states originating from 1s orbitals on equivalent centers have fully out of phase oscillations, interference is clearly revealed in taking $1\sigma_g$ / $1\sigma_u$ ratios.
The investigation on diatomic and small polyatomic molecules has shown the ubiquitous appearance of interference and diffraction effects, not only in the partial cross sections, but in angular distributions [142, 143] and vibrational branching ratios (v-ratios) as well [29, 138, 144, 145].

Since the spectrally unresolved splitting of core orbitals does not permit the study of interferences in most systems, an interesting possibility is constituted by taking into account the ionization of inner-valence orbitals deriving from the C 2s AOs. Indeed, they have a much larger splitting due to the stronger bonding interaction that can be experimentally resolved. Although ionizations of 2s-derived MOs are often influenced by very strong many-body effects which prevent the observation of the primary line, a direct study of the interference effects is possible at least in many hydrocarbon molecules [146]. Even though the C 2s-derived orbitals are mixed with AOs of neighbouring atoms, they remain mainly localized on the equivalent centers, so that well-developed interference patterns are expected.

In a recent study [146] the possibility of investigating the same phenomenon in the inner valence orbitals originating from the C 2s AO was considered. Indeed, the relevant MOs present are split by a few eV and therefore can be easily investigated. This has allowed us to consider interference in the three simplest hydrocarbons C_2H_2, C_2H_4 and C_2H_6, with the aim to investigate the expected dependence of interference pattern on the bond length. This was indeed observed and it was shown that accurate theoretical simulations of the interference patterns are potentially able to recover the geometric information from the experimental

data with high accuracy. It also turned out that the pattern was more complex, due to partial delocalization of the inner valence MOs on the full molecule and to the presence of many-body effects. This in turn made the study of such structures a potential source of important information about the electronic structure of the target.

As well as in simple molecules, these features can appear under favourable circumstances in the outer valence shell of very complex molecules. This has been long known in C_{60} [30–32, 37] and other fullerenes, as well in other very symmetrical molecules like $MgCp_2$ [147]. Indeed, a strong and rather short period oscillation in the partial cross sections relative to HOMO and HOMO-1 ionizations was previously discovered in the outer valence photoionization of C_{60} [30]. Since oscillations appear in antiphase in the two channels, the effect can be magnified, as already highlighted, by taking the ratio of the two cross sections. This ratio has been accurately measured both in the gas phase [31] and in the solid state [32]. A number of models have been put forward to explain the phenomenon, including quantization in a spherical box [33], diffraction from its edges [34] and various spherical models [35]. Our interpretation [36, 37], also followed by [32], is that their origin is in the interference of electron waves emitted from equivalent centres and is just another manifestation of the interference effects predicted and observed in diatomic molecules. Analogous structures have also been uncovered in deeper channels [38, 39] and in the non-dipole parameters [40]. The whole range of effects has been quantitatively reproduced and this has also permitted the ability to predict analogous effects in a number of different situations. This clarifies the interplay of interference (coherent emission from equivalent centers) and scattering (EXAFS structures) from neighbouring centers, as well as the role of the electronic structure of the orbitals involved [146, 148–151]. In fact, while emission from core orbitals is essentially atomic-like, strongly localized and can be well assimilated to a point source, in contrast the emission from valence orbitals is generally delocalized. This valence emission also mixes orbitals from different atomic species. As a consequence, different amplitudes emerge from different regions of space and so the resulting interference pattern is less regular and significantly more complex, although it is still accurately described by the theoretical model.

In next chapters we will illustrate the effects just described in the photoionization profiles at high energy for several systems. In the core region, we have analysed the oscillations in the intensity ratio C2,3/C1,4 in the carbon 1s photoelectron spectrum for 2-butyne, which will be the first result to be presented

(Chapter 7).

In the inner valence shell region, the interference effects in the photoionization spectra of simple polyatomic molecules (propane, butane, isobutane, cis/trans-2-butene) were studied. All the experiments on these systems were carried out by an experimental group at the Soleil synchrotron in Paris and the results from the theory and experiment are presented in Chapter 8.

Furthermore, we analysed the effect due to coherent emission from equivalent centers and diffraction from neighbouring non-equivalent atoms in core and valence photoelectron spectra. We investigated mono and disubstituted fluoro- and iodo-acetylenes, compared to the simple acetylene system. These results are presented in Chapter 9.

In the outer valence shell, we have investigated interference effects in the outer valence ionization cross sections of simple hydrocarbons, C_2H_2, C_2H_4, C_2H_6 and we found that they are comparable to those observed in core and inner valence ionizations as outlined in Chapter 10. In the same region, another class of compounds which has been examined is that of Mg and Be metallocenes. The influence of geometrical structure on their photoionization profiles is studied by varying metal-ring distance in the permethylated compounds $MgCp_2^*$ and $BeCp_2^*$ as well as in non-permethylated $MgCp_2$ (Chapter 11).

Finally, in the inner valence shell region, we considered the photoionization profiles for the case of ArC_{60}. The results are compared with data already available in literature and with a previous study on the C_{60} molecule in Chapter 12.

All these results have been analysed in terms of the model based on the DFT method combined with the use of a B-spline basis (Chapter 4). This method gives a good description of the energy dependence of the intensity ratios.

Chapter 7

Intensity oscillations in the carbon 1s ionization cross sections of 2-butyne

7.1 Introduction

The energy-dependent modulations of inner-shell cross sections well above threshold were predicted theoretically for carbon 1s ionization in a number of molecules [152] and observed experimentally by Söderström et al. in chlorine-substituted ethanes [150]. In this work it was found that the oscillations were associated with the chlorinated carbon atom and that the degree of oscillation increased with the number of chlorine atoms attached to the ionized carbon. These results were interpreted as arising from EXAFS-type scattering of the outgoing photoelectron from the attached chlorine atoms and it was shown that they could be accounted for quantitatively by a multiple-scattering EXAFS calculation using the FEFF codes [153, 154]. The geometrical information is currently retrieved in EXAFS studies by accurate fitting and background subtraction of the absorption signal. In this respect photoemission is much richer of information content, because of the ability to disentangle individual ionization channels which are superimposed in the total absorption cross section, e.g the possibility of distinguishing several inequivalent sites, to analyze also valence and inner valence photoemission, and to obtain additionally electronic structure information. However extraction of the features from the photoemission signal is more difficult, and an appealing possibility, when

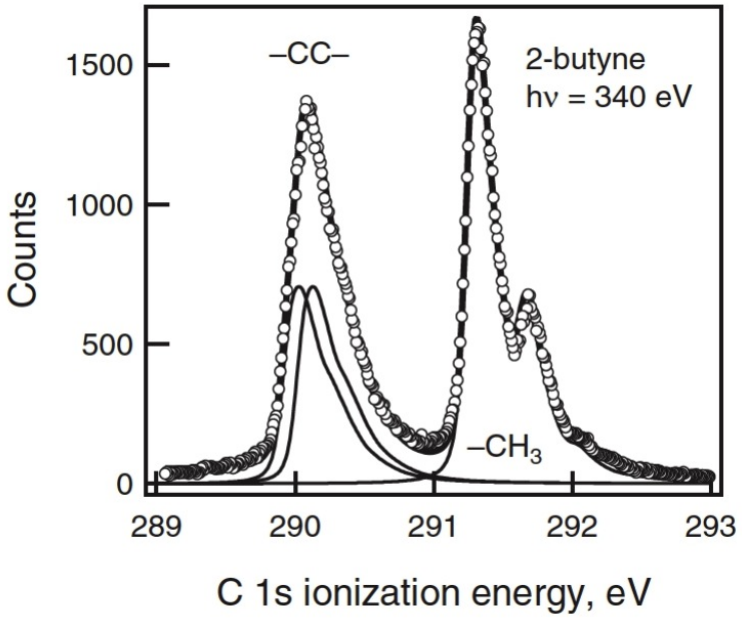

FIGURE 7.1: Carbon 1s photoelectron spectrum of 2-butyne taken at photon energy of 340 eV. Open circles show the data. Solid lines show the overall fits and the contribution from individual components.

missing an internal reference given by the ratio of two similar channels, is to use a mixture with a reference compound against which to normalise the cross section. While it may be reasonable to expect pronounced scattering effects in the presence of heavy atoms such as chlorine, it might not be anticipated that such effects would also play a significant role in molecules containing only first-row atoms. Guided by some preliminary observations of non-stoichiometric intensity ratios in 2-butyne ($CH_3C{=}CCH_3$), we have investigated the carbon 1s photoelectron spectra of 2-butyne over a range of photon energies from threshold to 150 eV above threshold. Over this energy range we see oscillations in the intensity ratio (C2,3/C1,2) that range from 0.8 to 1.15, indicating that nonstoichiometric cross section ratios will be found even when there is no high-Z scattering center.

7.2 Results and Discussion

Gas-phase carbon 1s photoelectron spectrum for 2-butyne, shown in Fig. 7.1, was measured at photon energies from 295 eV to 450 eV using beamline I411 of the MAX II synchrotron [155]. For the two triply bonded carbon atoms in 2-butyne, C2 and C3, there are two core orbitals separated by approximately 100 meV resulting

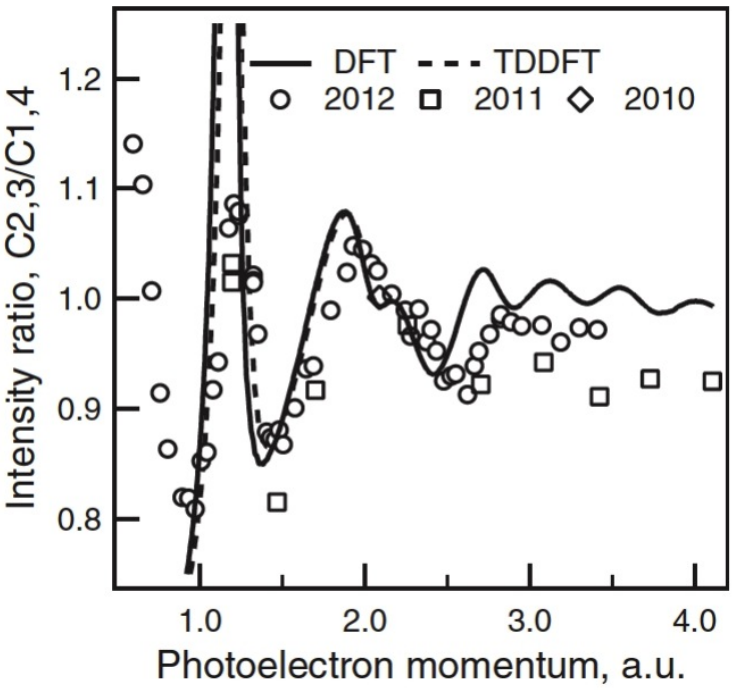

FIGURE 7.2: Comparison between density-functional calculations and experimental values for the intensity ratios (C2,3/C1,4) for the carbon 1s photoelectron spectra of 2-butyne. The solid line represents the results of the DFT methods and the dashed line represents the results from the TDDFT method.

from the bonding and antibonding combinations of the two atomic 1s orbitals. The intensities for photoemission from the two different carbon atoms are obtained from the areas under the peaks. The intensity ratio, C2,3/C1,2, as a function of the average momentum of the photoelectron is shown in Fig. 7.2. It is apparent from Fig. 7.2 that there are energy dependent oscillations of the cross section ratio. These are similar to those reported by Söderström et al. [150] for chlorinated ethanes, and, specifically, comparable in magnitude to those for 1,1-dichloroethane (CH_3CHCl_2). In the chloroethanes these oscillations have been interpreted as arising from EXAFS-like scattering of the outgoing electrons from the chlorine substituents. This view is supported by the observation that the magnitude of the oscillations increases with the number of chlorine substituents and by theoretical calculations that take this scattering into account. In 2-butyne what appears to be a similar phenomenon must arise from scattering of the photoelectrons by the carbon atoms, primarily those adjacent to the ionized carbon. Since the two central carbon atoms each have two nearest neighbours and the terminal carbon atoms have only one, we expect that this scattering effect will be larger for the central atoms than it is for the terminal ones.

For the density-functional calculations the multicentric B-spline code has been employed with asymptotic angular expansion up to $L_{max} = 24$, which ensures complete convergence of the calculated cross sections. Two sets of calculations have been made. One is based on DFT and the other on TDDFT. In Fig. 7.2 we compare the experimental intensity ratios with the predictions of the two density-functional theoretical models. There is a good agreement between theory and experiment. Both show a sharp peak in the intensity ratio for k slightly greater than 1 a.u., but the theoretical results predict a much higher ratio (1.8-2.0) than is observed (about 1.1). An observed dip in the intensity ratio at k $\approx$ 1.5 a.u. is reproduced accurately by the theory. A second peak at k $\approx$ 2 a.u. is reproduced by the theory, which predicts the position, height, and structure of this peak reasonably well. Beyond k $\approx$ 2.5 a.u. the theory shows another peak approximately where one is observed in the data. Overall, the theory predicts the peaks at slightly lower values of k than they are observed in the experimental data, and this trend increases with increasing k. There is little difference between the DFT and TDDFT predictions. If the energy scale for the theoretical calculations is shifted to higher energies by about 3 eV (with a corresponding shift in the values of the momentum) the agreement between theory and experiment is improved. The need for such a shift arises because the exchange-correlation potential employed in the calculation is slightly too attractive, and shifts the calculated profiles towards threshold. A more detailed look at the theoretical calculations shows that the strong peak at k $\approx$ 1 a.u. arises from ionization of the $2a'_1$ molecular orbital, which is equivalent to a σ_g orbital made from the gerade combination of the two 1s orbitals of the triply bonded central carbon atoms. This is similar to the behaviour seen in ethyne, where the $1\sigma_g$ ionization shows a broad peak in the cross section at a photon energy of about 310 eV (k = 1.2 a.u.) [156]. By contrast ionization of the $2a''$ orbital in 2-butyne shows a monotonically decreasing cross section in this energy region, which is similar to the behavior seen for ionization of the $1\sigma_u$ orbital in ethyne. A strong shape resonance at k $\approx$ 1 a.u. is predicted to be a common feature for substituted ethyne molecules such as FCCH, $FCCCH_3$, and FCCCN [152]. The origin of this feature is the presence of a continuum σ_u^* resonance, associated with the ionization of the σ C2C3 antibonding orbital, similar to that seen in the core ionization of N_2. Such a feature also appears in the $1a'_1$ ionization, but with much reduced intensity, because of the smaller dipole transition moment from the adjacent methyl C1s orbital.

7.3 Conclusions

The experimental results show that the intensities of the peaks in the photoelectron spectrum of 2-butyne do not necessarily reflect the exact stoichiometry of the molecule, but may differ from this expectation by as much as 20%. Moreover, the intensity ratio oscillates with the photon energy (or momentum of the photoelectron). This behaviour is similar to that seen for chloroethanes [150], where the chlorine substituents provide strong scattering centers. The current results show that such oscillations and nonstoichiometric intensity ratios can be expected also in cases where there is no strong scattering center. These results have important consequences for the use of photoelectron spectroscopy as an analytical tool. Comparison of the experimental results with predictions of the theoretical approach shows that our method accounts well for the overall structure seen in the energy-dependence of the cross-section ratios. In detail, the theoretical models overestimate the magnitude of these effects near threshold. This overestimate is particularly noticeable for the peak at k $\approx$ 1 a.u. As noted, this peak arises from the presence of a shape resonance near threshold and it is commonly observed that this level of calculation predicts the profiles of shape resonances to be sharper and more intense than is experimentally observed.

Chapter 8

Interference and diffraction in molecular photoionization: isomer discrimination

8.1 Introduction

A recent study on the inner-valence MOs of a series of simple hydrocarbons with two centers has shown that the interference in coherent emission of photoelectrons from these equivalent centers represents the microscopic analogy of the Young's double-slit experiment [146]. This type of interference is related to both electronic and geometrical structure. By considering the electronic structure, even if inner-valence MOs remain basically atomic, they are mixed with AOs of neighbouring atoms and a certain amount of delocalization is always present. This complicates the interpretation of the interference patterns. In particular, the most important effect will be the amount of H 1s orbital participation, which will generally give a change in the value of the cross-section ratio considered due to the rapidly decreasing hydrogen cross section at high energies. Furthermore, the geometrical dependence of the interference patterns can offer a method to accurately determine molecular geometries, especially when photoemission is the chief investigative tool. In particular, the potential of such structures for accurate determination of interatomic distances has been put forward [146].

In collaboration with an experimental group of the Soleil synchrotron in Paris on the Pléiades beamline, we have explored the feasibility of examining interference

in photoemission from 2s-derived orbitals in simple hydrocarbon molecules with two or more pairs of chemically equivalent carbon atoms: propane, cyclopropane, butane, isobutane and 2-butene. This permitted us to verify the existence of oscillations in interference profiles which depend on the internuclear distance, on the electronic structure and on the orbital composition. In particular, given the great interest in isomer discrimination we propose a new investigation specifically aimed at distinguishing different isomers by the change in the interference pattern expected on the basis of the different distance between the centers in cis- and trans-dimethylethene (2-butene) that are not directly bonded. Since in this case the molecular geometry is rigid, we expect comparisons between theory and experiment to be more straightforward and lead us to better understand the potential for conformation discrimination in the case of more flexible molecules.

In the results that we will illustrate, we have taken into account *branching ratios* and cross section ratios instead of simple cross section profiles in order to emphasize the interference effects. The branching ratio is defined as the ratio between a specific cross section and the sum of all considered cross sections, i.e.

$$BR_i = \frac{\sigma_i}{\sigma_{tot}}. \tag{8.1}$$

The second possibility to enhance the differences between different cross section profiles is constituted by the intensity ratios between single bands, namely:

$$R_{ij} = \frac{\sigma_i}{\sigma_j}. \tag{8.2}$$

Let us now to examine the different target systems.

8.2 Results and discussion

8.2.1 Propane

The most simple system with more than two centers is propane, C_3H_8. Fig. 8.1 shows the inner-valence spectrum taken at a photon energy of 105 eV for this molecule. Experimentally, once the peak areas are obtained, their ratios can be derived. The ionization of three inner-valence orbitals, $3a_1$, $2b_2$ and $4a_1$, originating from C 2s AOs are well separated and experimentally resolved, in contrast with the small separation between C 1s orbitals (almost 0.13 eV) [157]. The corresponding

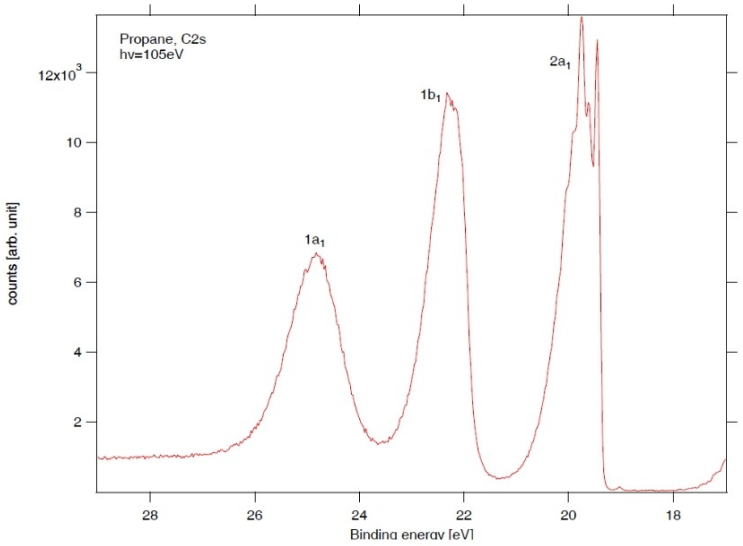

FIGURE 8.1: Valence-electron spectrum of propane.

eigenvalues obtained both by an ADF calculation and from the B-splines/DFT method are reported in Tab. 8.1 and they match quite well with the experimental ionization potentials.

	ADF	**B-spline**
$3A_1$	23.99	23.93
$2B_2$	21.45	21.42
$4A_1$	19.10	19.06

TABLE 8.1: Inner-valence MOs eigenvalues [eV] of propane.

In order to obtain these values, the large one center basis with maximal expansion up to $L_{max} = 24$, with a range $R_{max} = 25$ a.u. and step size $h = 0.2$ is supplemented by expansions around the carbon and hydrogen atoms with $l_{max} = 2$, $r_{max} = 0.6$ for carbon and $l_{max} = 1$, $r_{max} = 0.6$ for hydrogen. We note that this basis affords a very accurate solution of discrete DFT orbitals as well as continuum orbitals. Moreover, the excellent agreement between ADF eigenvalues and those calculated with the B-spline/DFT method indicates the convergence of the chosen basis.

The molecular structure of propane with non-equivalent atoms labelled with different numbers and a scheme of 2s-derived MOs are reported in Fig. 8.2. The

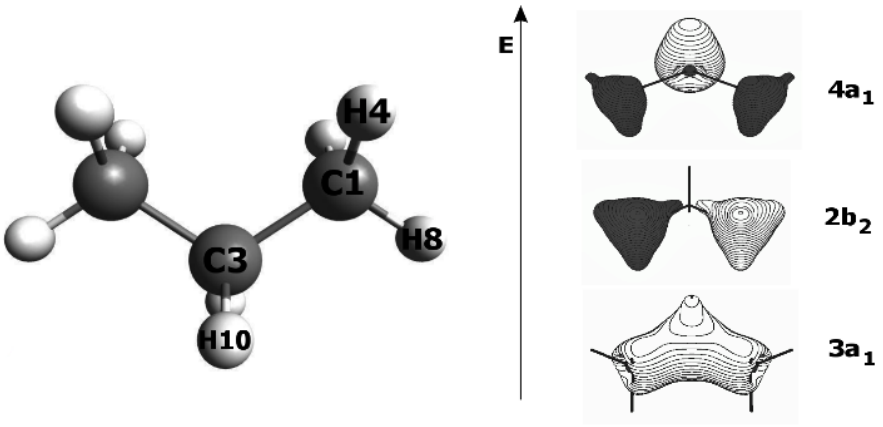

FIGURE 8.2: Propane molecule and MOs deriving from C2s AOs.

corresponding percentage composition of each orbital, obtained by an ADF calculation, is shown in Tab. 8.2. Here the non-equivalent atoms are labelled with the same convention used in Fig. 8.2.

	C1		**C3**		**H4**	**H8**	**H10**
	2s	2p	2s	2p	1s	1s	1s
$3A_1$	35.23%	3.41% (p_y)	35.46%	1.52% (p_z)	13.00%	6.27%	10.67%
$2B_2$	53.89%	//	//	8.70% (p_y)	22.65%	14.12%	//
$4A_1$	16.65%	8.53% (p_z)	22.94%	5.60% (p_z)	17.72%	5.49%	17.86%

TABLE 8.2: Orbital composition of inner-valence MOs of propane.

The percentages less than 1% have been neglected, so the total percentage is not 100%. This choice has been made for all the molecules considered.
In order to emphasize the oscillations characterizing the interference profiles, we considered the branching ratio values instead of simple cross sections. In Fig. 8.3, we illustrate the experimental and calculated branching ratios related to the three inner-valence orbitals as a function of photon energy. The shape and the absolute values of the theoretical curves are matched extremely well by the experimental points. As one can note, strong oscillations are present in the branching ratio values, corresponding to a complex and irregular structure. In general, irregularities in the oscillations are directly informative of the nature and atomic composition of the inner-valence MOs. Indeed, these orbitals include not only contributions from C 2s but also from C 2p and H 1s as one can see from the Tab. 8.2. By considering all three profiles, the oscillations for the inner-valence orbitals are far from being

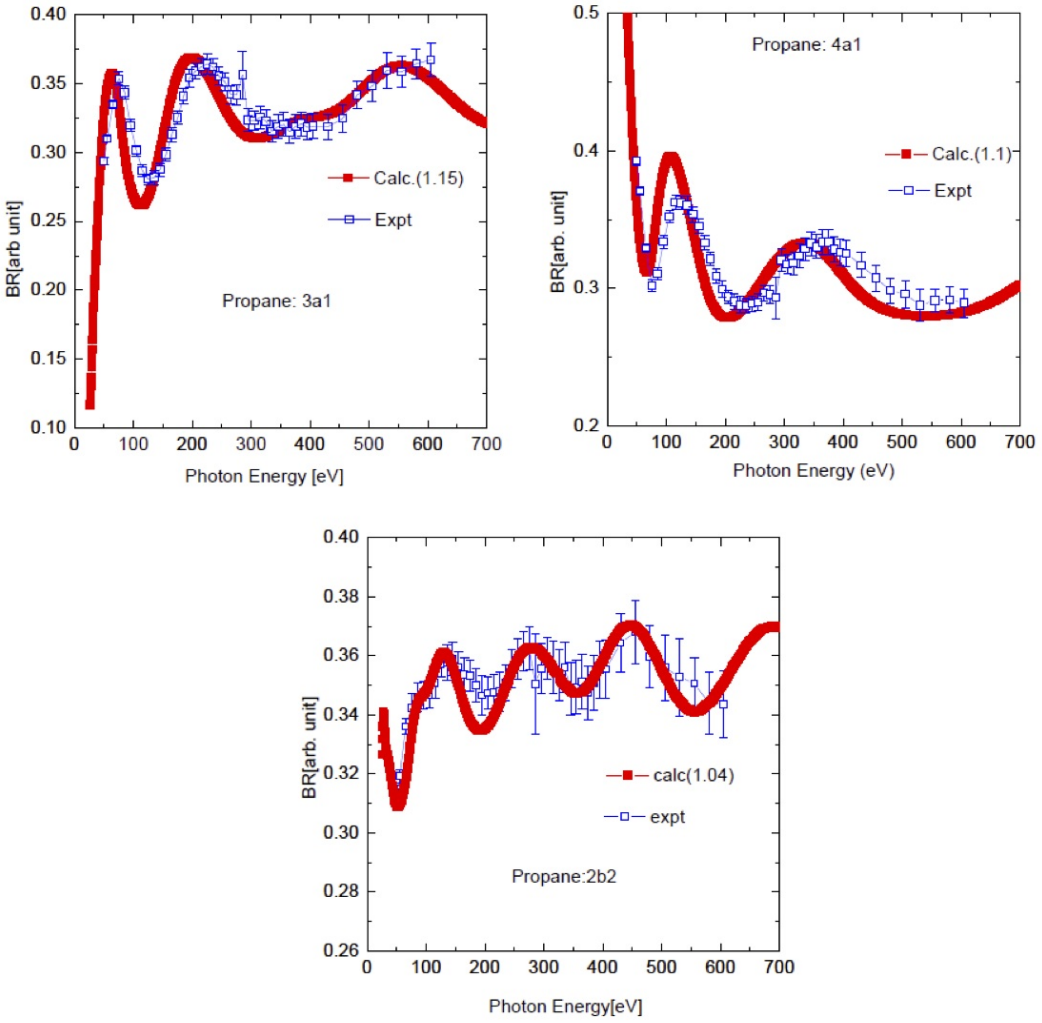

FIGURE 8.3: Branching ratios associated to $3a_1$, $2b_2$ and $4a_1$ inner-valence orbitals of propane.

regular around a mean value but they diverge quite rapidly at high photon energies. This is essentially due to the different MO composition in terms of AOs. Let us examine in detail the composition of each orbital. 70% of the deepest orbital, $3a_1$, is composed of C 2s AOs from both terminal and central atoms. Thus, it can be considered as an in-phase sum of terminal and central atom contributions. Meanwhile, the second orbital, $2b_2$, has a strong contribution from terminal carbon 2s AOs together with a large contribution from the H 1s AOs bonded to them. Finally, the $4a_1$ orbital has a composition more closely related to that of $3a_1$ because it includes C 2s contributions from both types of carbon atoms, although it has a noticeably large contribution from the central carbon atom. By comparison, of the branching ratio curves associated to two orbitals of symmetry a_1, one can

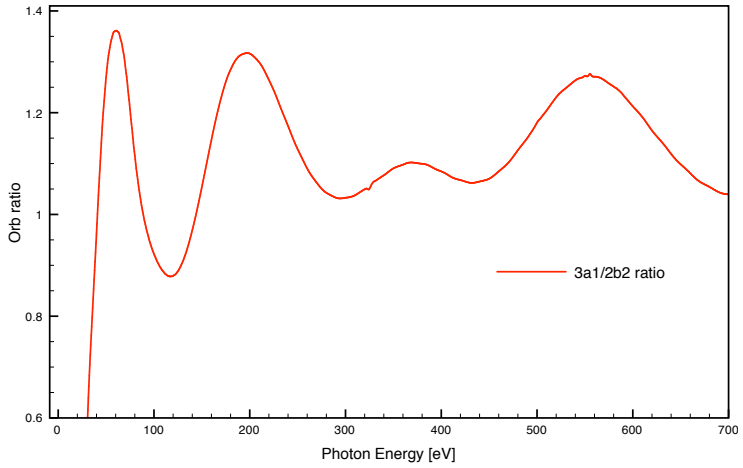

FIGURE 8.4: A selected orbital ratio for propane molecule.

note that they present anti-phase interference structures. This is related to their different nodal structure, +++ for $3a_1$ and -+- for $4a_1$, reported in the scheme 8.2. It is interesting to note that the branching ratio associated with the $2b_2$ orbital exhibits a structure with a shorter period and a frequency which is almost double with respect to the other two curves. This is due to the relationship between interference and distance between emission centers: the larger the distance, the smaller the period of the oscillations. In this case, the interference is exclusively due to the emission from the two C terminals which are characterized by a distance which is double that of the terminal-center separation. The period of oscillation is almost half with respect to that of the two other orbitals. Furthermore, since the atomic cross sections of C 2s orbitals at high energy decay slower than C 2p and H 1s, the branching ratio at high energy increases with the C 2s contribution in the corresponding orbital. As a consequence, one can expect the following behaviour in the branching ratios: BR $3a_1$ > BR $2b_2$ > BR $4a_1$.

One can consider the ratios between single cross sections if one is interested in highlighting oscillations in the interference patterns. In particular, the relevant ratio between the orbitals $3a_1$ and $2b_2$ is reported in Fig. 8.4. A very clear interference pattern emerges, indicating that it is mostly dominated by the different C 2s contribution of the two orbitals and not by the details of their composition.

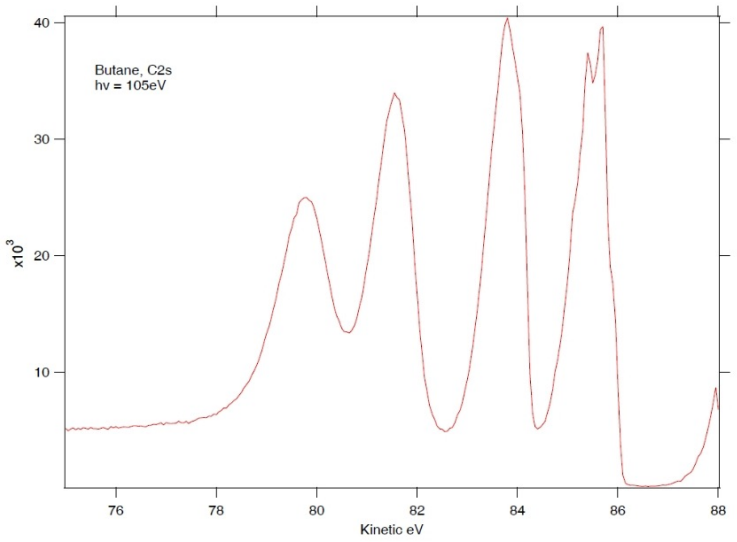

FIGURE 8.5: Valence-electron spectrum of n-butane.

8.2.2 Butane

The great potential of the technique for accurate determination of molecular conformers in the gas phase emerges by considering the case of butane. Indeed, in the beginning, investigations of emission from C 2s-derived MOs of butane had shown some disagreement with theoretical simulations. This disagreement was traced back to the neglect of the gauche isomer in the theoretical treatment; the isomer was expected to be thermally populated. In Fig. 8.5, we show the inner-valence spectrum taken at a photon energy of 105 eV for n-butane. The inner-valence shell is constituted by four orbitals, $3a_g$, $3b_u$, $4a_g$ and $4b_u$, originating from C 2s AOs of the anti-conformer. Their ionization peaks which appear well separated in the spectrum can be experimentally resolved (Fig. 8.5). The same applies to the gauche-conformer: the ionizations derive from $3a$, $3b$, $4a$ and $4b$ orbitals. The corresponding eigenvalues obtained both by an ADF calculation and the B-splines/DFT method are reported in Tab. 8.3. Also in this case, they match quite well with the experimental ionization potentials. In order to obtain these values, as for the propane case, we have used the large one center basis, with maximal expansion up to $L_{max} = 26$, with a range $R_{max} = 25$ a.u., and step size $h = 0.2$ together with, for the anti-conformer, expansions around the C ans H atoms, with $l_{max} = 2$, $r_{max} = 0.4$ (central carbon), $l_{max} = 2$, $r_{max} = 1.0$ (terminal carbon) and $l_{max} = 1$, $r_{max} = 1.0$ (H). For the gauche-conformer, the parameters are just a bit different: $l_{max} = 2$, $r_{max} = 0.5$ (central carbon), $l_{max} = 2$, $r_{max} = 0.8$ (terminal

	Anti butane			**Gauche butane**	
	ADF	B-splines		ADF	B-splines
$3A_g$	24.467	24.382	3A	24.464	24.394
$3B_u$	22.852	22.498	3B	22.395	22.360
$4A_g$	20.085	20.045	4A	20.393	20.373
$4B_u$	18.798	18.773	4B	18.499	18.491

TABLE 8.3: Inner-valence MOs eigenvalues [eV] of butane.

carbon) and $l_{max} = 1$, $r_{max} = 0.8$ (H). This choice provides a very accurate solution of discrete DFT orbitals. The excellent agreement between ADF eigenvalues and those calculated with B-spline basis indicates the convergence of basis used. Fig. 8.6 shows the molecule where non-equivalent atoms are labelled by different numbers and a scheme of MOs deriving from C2s AOs. The percentage composition of each MO deriving from C2s AOs of anti-conformer and gauche-conformer is reported in Tab. 8.4 and 8.5, respectively. These percentages have been obtained by an ADF calculation.

	C1		**C3**		**H5**	**H9**	**H11**
	2s	2p	2s	2p	1s	1s	1s
$3A_g$	55.30%	2.42% (p_x)	19.44%	3.13% (p_y)	15.66%	3.40%	7.34%
$3B_u$	16.04%	9.25% (p_y)	46.54%	//	4.05%	9.10%	16.16%
$4A_g$	14.72%	7.85% (p_y)	34.29%	3.78% (p_y)	6.10%	11.33%	19.26%
$4B_u$	29.04%	17.03% (p_x)	6.42%	8.49% (p_x)	27.75%	1.34%	9.10%

TABLE 8.4: Orbital composition of inner-valence MOs of anti butane.

As in the previous case, the non-equivalent atoms are labelled with the same criterion of Fig. 8.6. From the analysis of the percentage composition, one can infer that even if the 2s-derived MOs are partially involved in the bonding and they are mixed with AOs of neighbouring atoms, such orbitals are still predominantly localized on the equivalent centers. As such, well-developed interference patterns are expected. Let us now examine the composition for each MO. The $3A_g$ orbital

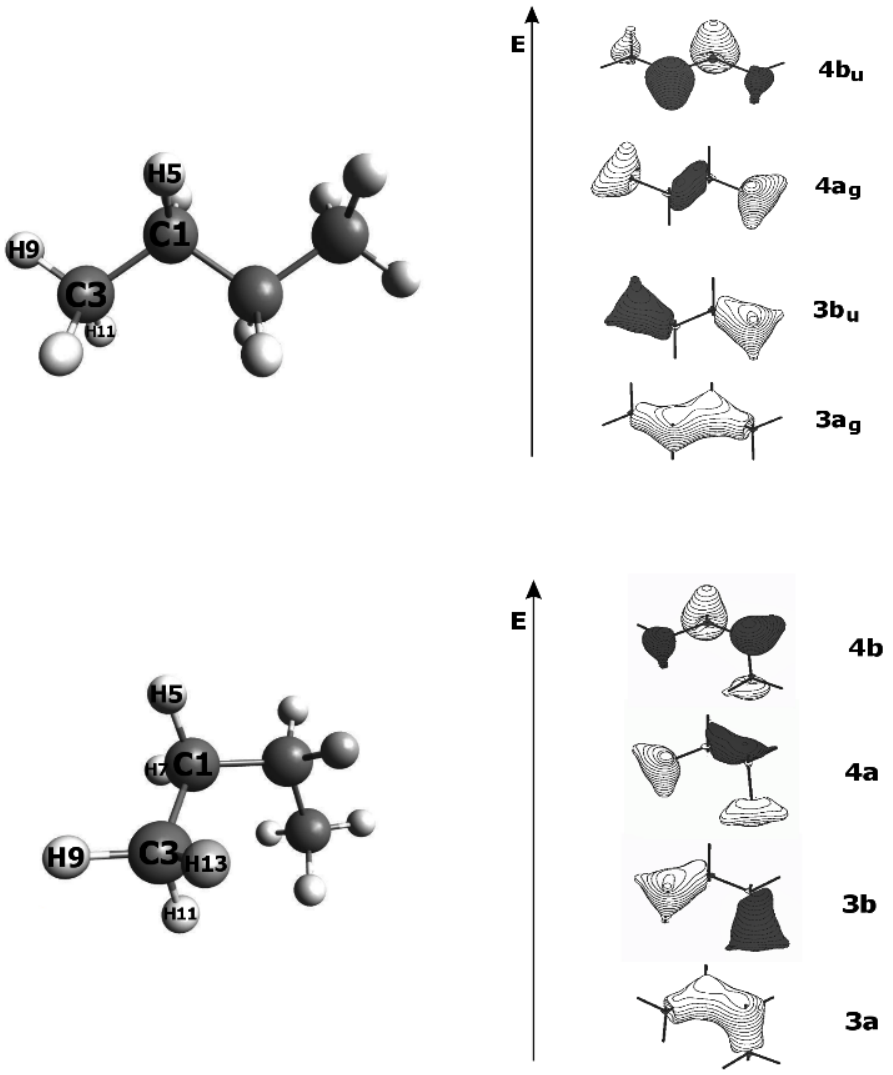

FIGURE 8.6: Butane molecule and MOs deriving from C2s AOs: anti-conformer (upper panel) and gauche-conformer (lower panel).

of the anti-conformer and the $3A$ orbital of the gauche-conformer constitute almost 75% of the C 2s AOs contribution and are essentially localized on the central carbon atoms. The contributions deriving from the H 1s AOs exceeds 10% only in the case of the anti-conformer. The other MOs, $4B_u$ (anti) and $4B$ (gauche), are mainly localized on the central carbon atoms, although the total percentage of C 2s AOs is less than the $3A_g/3A$ case and there is a large contribution deriving both from the C 2p AOs and H 1s AOs. For this reason we would expect a less pronounced oscillation with respect to those associated with the orbitals $3A_g/3A$. We consider the other two orbitals, $3B_u/3B$ and $4A_g/4A$, which are essentially localized on the terminal carbon atoms even if with different percentages: in the first case the localization is more prominent with respect to the second. As already

	C1		**C3**		**H5**	**H7**	**H9**	**H11**	**H13**
	2s	2p	2s	2p	1s	1s	1s	1s	1s
3A	52.84%	1.46% (p_z)	21.27%	1.72% (p_y)	7.83%	7.66%	3.16%	4.14%	3.85 %
3B	18.00%	6.15% (p_y)	44.48%	//	3.17%	2.47%	9.78%	6.70%	7.92 %
4A	16.61%	7.63% (p_z)	31.96%	2.18% (p_z)	5.27%	3.41%	8.99%	11.15%	7.95 %
4B	27.54%	8.76% (p_x)	8.75%	5.51% (p_z)	9.50%	15.59%	2.85%	3.88%	7.54 %

TABLE 8.5: Orbital composition of inner-valence MOs of gauche butane.

highlighted, the differences in the composition of the MOs are directly reflected in the interference patterns. In order to verify this, let us consider the branching ratio values of the different ionization events.

If we only consider the anti-conformer, Fig. 8.7, the experimental and calculated BR values are in reasonable agreement for the ionizations deriving from $3A_g$, $4A_g$ and $4B_u$ but not for the $3B_u$ orbital. In Fig. 8.8, the experimental and calculated branching ratios related to the four inner-valence orbitals as a function of photon energy are illustrated. By mixing the contribution of both conformers, one can obtain an excellent agreement between theory and experiment. The oscillations observed are not regular around a mean value because of different orbital composition. They diverge quite rapidly at high photon energy. Firstly, if one considers the ionization cases which derive from the MOs which are mainly localized on the central carbon atoms, namely $3A_g/3A$ and $4B_u/4B$, one can observe that they present anti-phase oscillations due to their different nodal structure which is reported in the scheme 8.6. The oscillations related to the $3A_g/3A$ branching ratios are somewhat more evident with respect to those of $4B_u/4B$ because of a higher percentage of C 2s AOs: in particular, 55.4% for $3A_g$ against 29.4% for $4B_u$ in the case of the anti-conformer and 52.8% for $3A$ against 27.5% for $4B$ in the case of the gauche-conformer. By considering the ionization cases due to the MOs mainly localized on the terminal carbon atoms, the profiles exhibit different periods and frequencies of oscillation with respect to the profiles which are related to the central carbon atoms. This is a consequence of the dependence on the distance between the slits. Then, as already highlighted for the case of propane, the emission linked to the terminal atoms generates an oscillation with smaller period and, consequently, larger frequency. This is true both for $3B_u/3B$ and $4A_g/4A$ but it is more pronounced for $3B_u/3B$ because of a larger percentage of C 2s contributions.

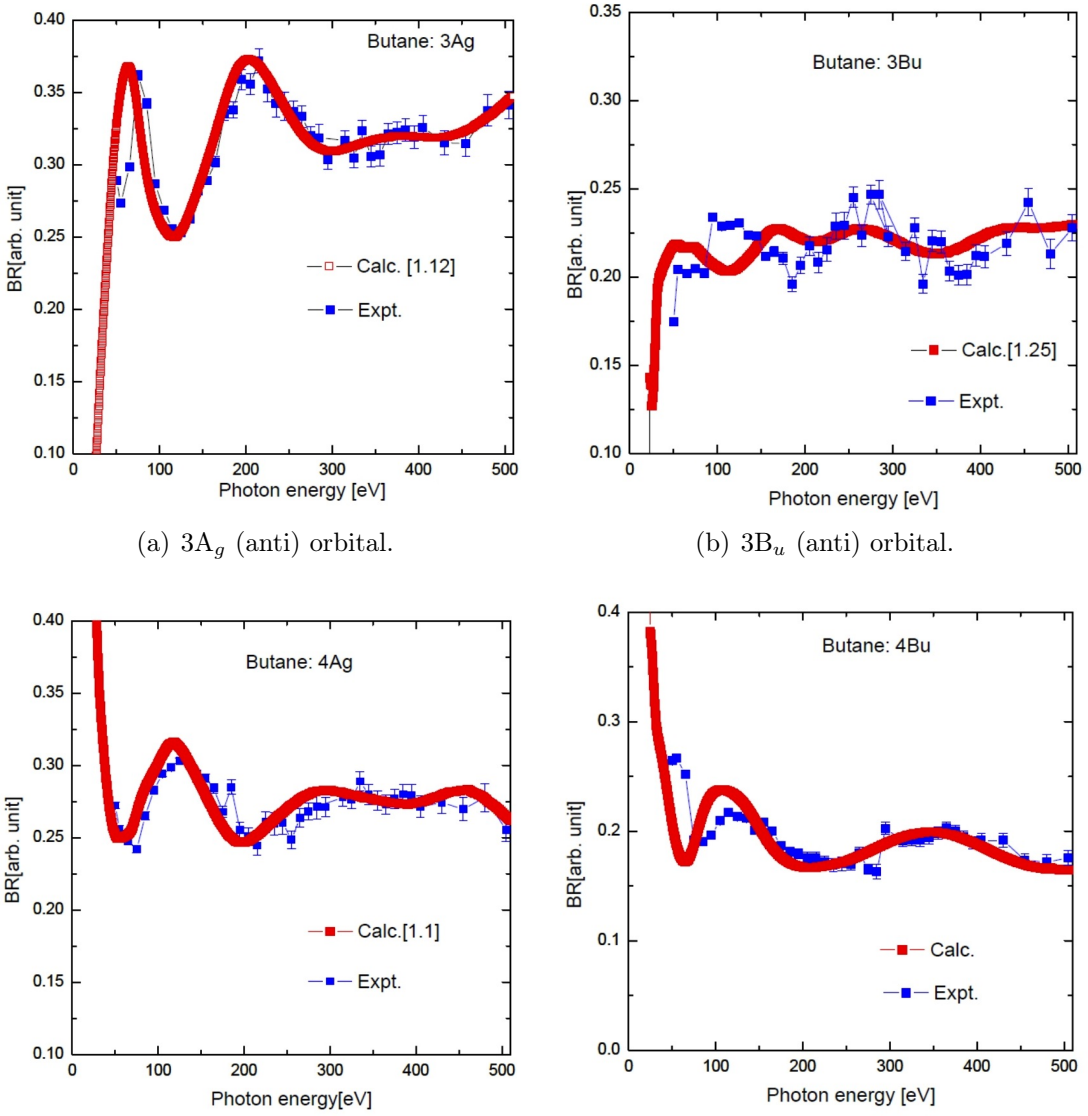

(a) $3A_g$ (anti) orbital.

(b) $3B_u$ (anti) orbital.

(c) $4A_g$ (anti) orbital.

(d) $4B_u$ (anti) orbital.

FIGURE 8.7: Branching ratios associated to $3a_g$, $3b_u$, $4a_g$ and $4b_u$ inner-valence orbitals of anti butane.

8.2.3 Isobutane and cyclopropane

In this series of hydrocarbon molecules we have also considered the cylcopropane and isobutane. However, the analysis of current experimental data is still in progress then only our theoretical results are available. The inner-valence shell of cyclopropane is constituted by two orbitals, $2a_1'$ and $2e_1'$, originating from C 2s AOs. The corresponding eigenvalues obtained both by an ADF calculation and by the B-splines/DFT method are reported in Tab. 8.6.

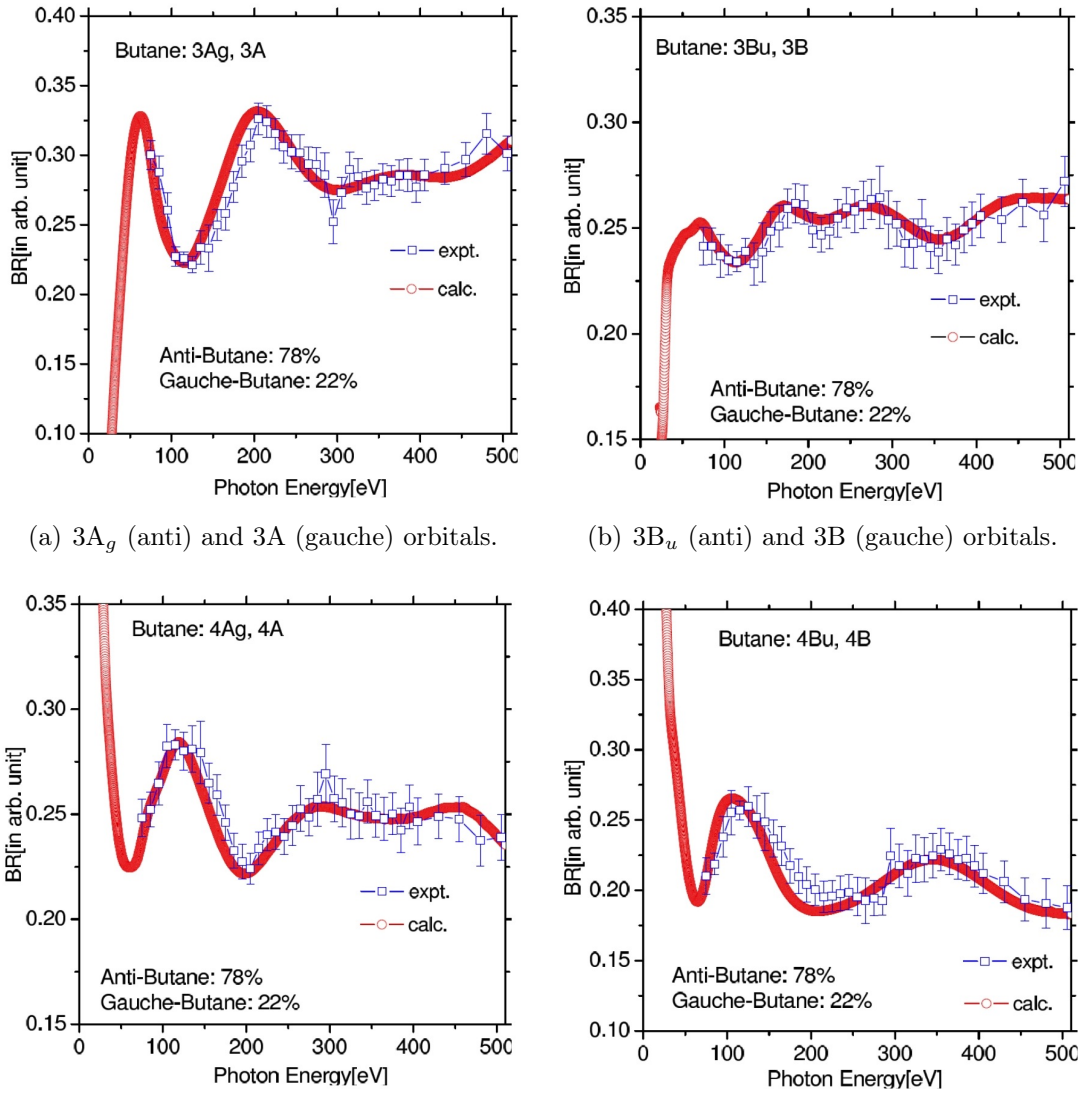

(a) $3A_g$ (anti) and 3A (gauche) orbitals.

(b) $3B_u$ (anti) and 3B (gauche) orbitals.

(c) $4A_g$ (anti) and 4A (gauche) orbitals.

(d) $4B_u$ (anti) and 4B (gauche) orbitals.

FIGURE 8.8: Branching ratios associated to $3a_g/3a$, $3b_u/3b$, $4a_g/4a$ and $4b_u/4b$ inner-valence orbitals of anti/gauche butane.

As for the previous cases, in order to obtain these values, the large one center basis, with maximal expansion up to $L_{max} = 20$, with a range $R_{max} = 25$ a.u., and step size $h = 0.2$ is supplemented by expansions around the C ans H atoms, with $l_{max} = 2$, $r_{max} = 0.5$ (C), $l_{max} = 1$ and $r_{max} = 1.0$ (H). Fig. 8.9 shows the molecule where not equivalent atoms are labelled by different numbers and a scheme of MOs deriving from C2s AOs. In Tab. 8.7 the percentage compositions of MOs deriving from C2s AOs are reported. They have been obtained by ADF calculation. As in the previous cases, the non-equivalent atoms are labelled with the same numbers of Fig. 8.9.

	ADF	**B-spline**
$2A_1'$	25.790	25.798
$2E_1'$	19.306	19.336

TABLE 8.6: Inner-valence MOs eigenvalues of cyclopropane.

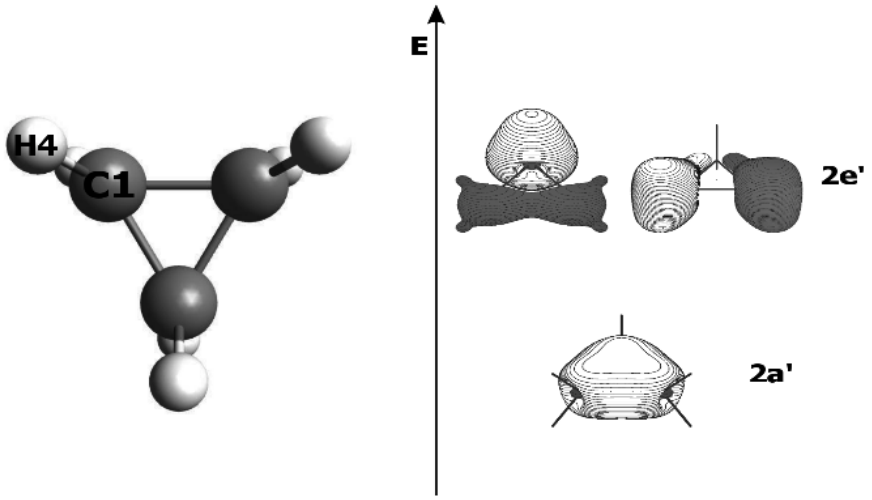

FIGURE 8.9: Molecular structure of cyclopropane and scheme of MOs deriving from C2s AOs.

	C1		**H4**
	2s	2p	1s
$2A_1'$	73.42%	18.84% (p_x)	13.64%
$2E_1'$	50.99%	12.60% (p_x)	37.04%

TABLE 8.7: Orbital composition of inner-valence MOs of cyclopropane.

One can consider the ratios between the two single cross sections to highlight oscillations in the interference pattern. The ratio between the orbitals $2a_1'$ and $2e_1'$ is reported in Fig. 8.10. The very clear interference pattern that emerges indicates that it is mostly dominated by the different C 2s contribution of the two orbitals and not by the other details of their composition.

In Fig. 8.11, we show the inner-valence spectrum taken at a photon energy of 105 eV for isobutane. Three ionizations of inner-valence $3a_1$, $2e_1$ and $4a_1$ orbitals originating from C 2s AOs of isobutane are well separated and experimentally

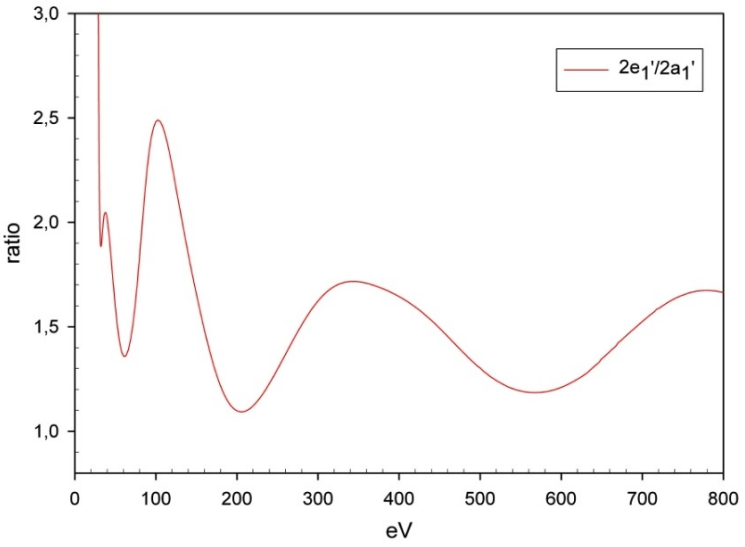

FIGURE 8.10: Ratio between the orbitals $2a_1'$ and $2e_1'$ of cyclopropane.

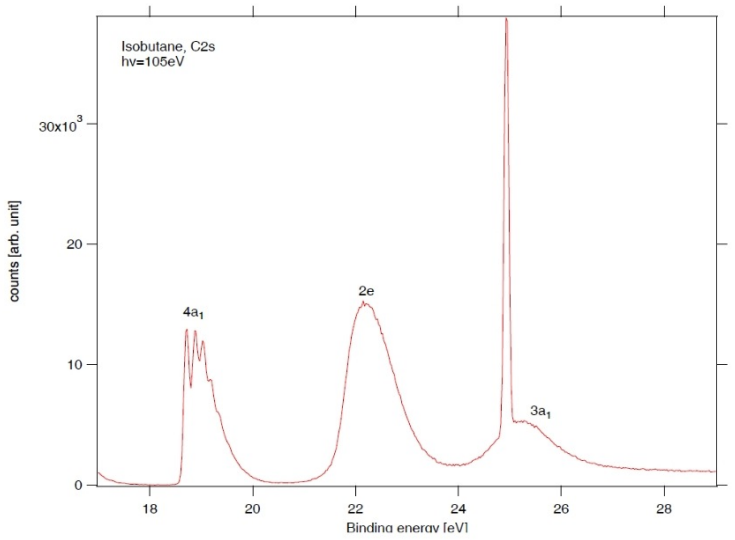

FIGURE 8.11: Valence-electron spectrum of isobutane.

resolved. The corresponding eigenvalues obtained both by ADF calculation and by B-splines/DFT method are reported in Tab. 8.8.

As for the previous cases, in order to obtain these values, we have used the large one center basis, with maximal expansion up to $L_{max} = 24$, with a range $R_{max} = 25$ a.u., and step size $h = 0.2$. Further expansions around the C ans H atoms, with $l_{max} = 2$, $r_{max} = 1.0$ (C), $l_{max} = 1$ and $r_{max} = 0.8$ (central hydrogen) and $l_{max} = 1$ and $r_{max} = 1.0$ (H) have been employed. This choice provides a very accurate solution of discrete DFT orbitals. Fig. 8.12 shows the molecule where non-equivalent atoms are labelled by different numbers and a scheme of MOs

	ADF	**B-spline**
$3A_1$	24.703	24.616
$2E_1$	21.428	21.396
$4A_1$	18.382	18.364

TABLE 8.8: Inner-valence MOs eigenvalues of isobutane.

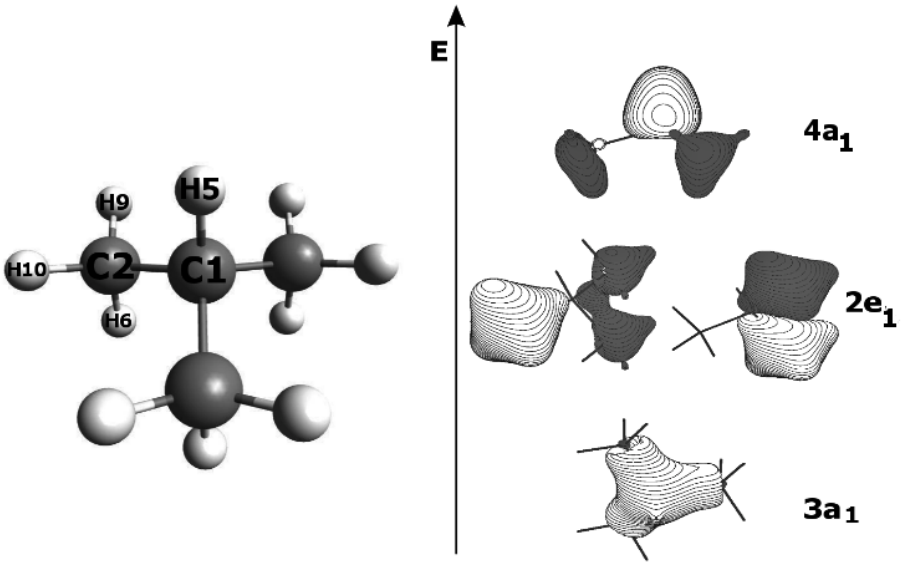

FIGURE 8.12: Molecular structure of isobutane and MOs deriving from C2s AOs.

deriving from C2s AOs. In Tab. 8.9 the percentage compositions of MOs deriving from C2s AOs are reported. They have been obtained by an ADF calculation.

	C1		**C2**		**H5**	**H6**	**H9**	**H10**
	2s	2p	2s	2p	1s	1s	1s	1s
$3A_1$	39.98%	//	36.95%	6.19% (p_x)	4.87%	7.04%	12.12%	//
$2E_1$	//	10.74%(p_x,p_y)	53.09%	1.83% (p_x)	//	10.26%	8.41%	16.05%
$4A_1$	22.48%	6.85%(p_z)	13.78%	10.54% (p_z)	10.75%	13.91%	11.89%	//

TABLE 8.9: Orbital composition of inner-valence MOs of isobutane.

By taking into account the composition of three orbitals, one can note that while the $2E_1$ orbital is essentially localized on the three equivalent carbon atoms with a non-negligible contribution from the C1 2p AO, the orbitals of symmetry

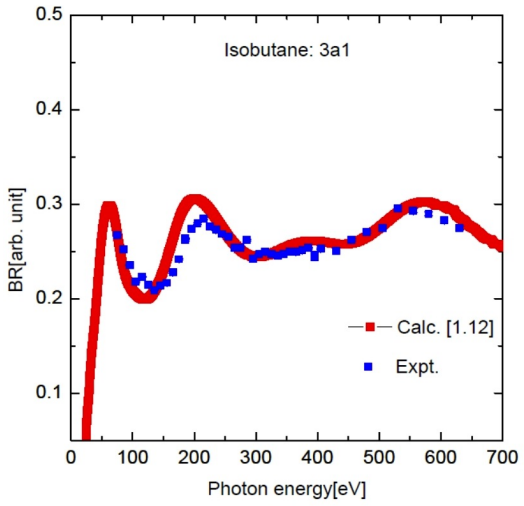

(a) $3A_1$ orbital.

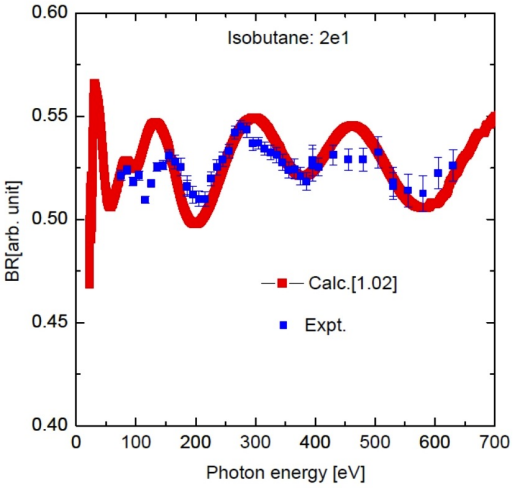

(b) $2E_1$ orbital.

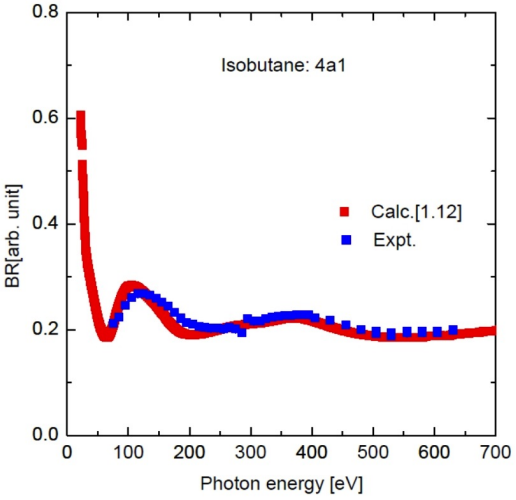

(c) $4A_1$ orbital.

FIGURE 8.13: Branching ratios associated to $3a_1$, $2e_1$ and $4a_1$ inner-valence orbitals of isobutane.

A_1 are delocalized on both type of carbon atoms, although for the $4A_1$ orbital the percentage of the 2s AO is more relevant for the C1 atom. Consequently, we can expect shorter period oscillations for the $2E_1$ ionization with respect to other (Fig. 8.13(b)). Further, a quite similar behaviour for the $3A_1$ (Fig. 8.13(a)) and $4A_1$ (Fig. 8.13(c)) ionizations occurs, although with a more pronounced oscillation for the $3A_1$ orbital because of a more significant C 2s percentage. Finally, there is an anti-phase oscillation between the $3A_1$ (Fig. 8.13(a)) and $4A_1$ (Fig. 8.13(c)) orbitals because of different nodal structures, as one can verify from the scheme (8.12). As before, the irregularity in the interference profiles is typically due to the contribution of H 1s AOs.

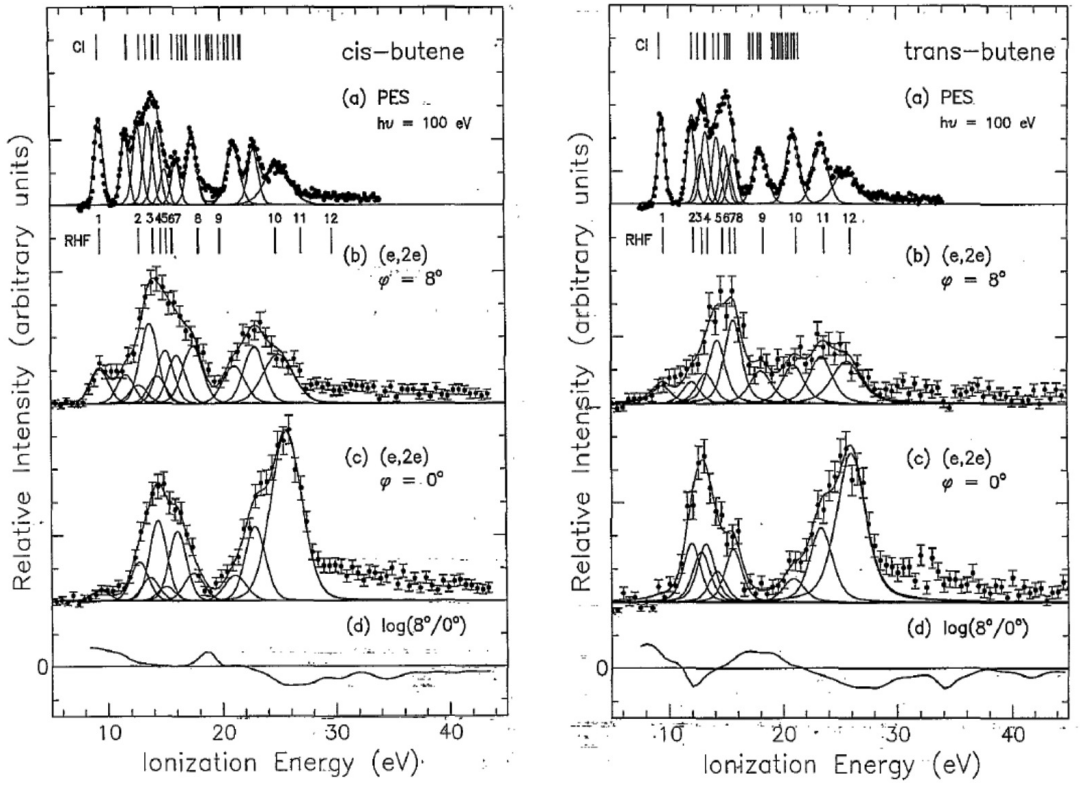

(a) Cis-2-butene (b) Trans-2-butene

FIGURE 8.14: PE spectrum of cis/trans-2-butene.

8.2.4 2-butene

In this section, we examine the interference patterns in ionization of inner-valence orbitals originating from C2s AOs of the two cis/trans isomers of 2-butene. Cross section profiles for the inner-valence region for the two systems have been obtained in the photon energy range of 0.27-700 eV and different cross section ratios have been derived. The experimental data has recently been collected at the Synchrotron Soleil of Paris but, unfortunately, they have not yet been available for the comparison with theoretical results in this thesis. As for the cases previously analysed, this study permitted us to investigate the dependence of the interference patterns on the bond-length as well as on the electronic structure. Our study aims to verify the sensitivity of the interference patterns to the different configurations of the two isomers, in particular with respect to the distance between the two terminal methyl groups. The PE spectrum of both molecules [158], shown in the Fig. 8.14, exhibits four sufficiently resolved bands which are those expected for the MOs deriving from the C2s AO. The inner-valence shell is constituted by four orbitals, $3a_g$, $3b_u$, $4a_g$ and $4b_u$, originating from C 2s AOs of the trans-isomer. The

same applies to the cis-isomer: the ionizations derive from $3a_1$, $3b_1$, $4a_1$ and $4b_1$ orbitals. The corresponding eigenvalues obtained both by an ADF calculation and from a B-splines/DFT method are reported in Tab. 8.10 and they match quite well with the experimental ionization potentials.

	Cis-2-butene			**Trans-2-butene**	
	ADF	B-splines		ADF	B-splines
$3A_1$	24.227	24.208	$3A_g$	24.165	24.122
$3B_1$	22.311	22.292	$3B_u$	22.574	22.520
$4A_1$	20.654	20.652	$4A_g$	20.226	20.195
$4B_1$	17.288	17.307	$4B_u$	17.852	17.868

TABLE 8.10: Inner-valence MOs eigenvalues of 2-butene.

In order to obtain these values, as for the previous cases, we have used the large one center basis, with maximal expansion up to $L_{max} = 26$, with a range $R_{max} = 25$ a.u., and step size $h = 0.2$ together with, both for the cis-isomer and for the trans-isomer, expansions around the C ans H atoms, with $l_{max} = 2$, $r_{max} = 0.4$ (central carbon), $l_{max} = 2$, $r_{max} = 1.0$ (terminal carbon) and $l_{max} = 1$, $r_{max} = 1.0$ (H). This choice provides a very accurate solution of discrete DFT orbitals. Fig. 8.15 and Fig. 8.16 show the two isomers where non-equivalent atoms are labelled by different numbers and, for each isomer, a scheme of MOs deriving from C2s AOs. The percentage composition of each MO deriving from C2s AOs of cis-isomer and trans-isomer is reported in Tab. 8.12 and 8.11, respectively. These percentages have been obtained by an ADF calculation.

	C1		**C3**		**H5**	**H7**	**H9**
	2s	2p	2s	2p	1s	1s	1s
$3A_g$	60.27%	1.73% (p_x)	22.68%	//	6.01%	4.81%	7.42%
$3B_u$	13.29%	5.81% (p_y)	49.93%	//	1.22%	9.35%	18.98%
$4A_g$	21.08%	11.49% (p_x)	31.70%	2.47% (p_x)	2.73%	7.36%	19.74%
$4B_u$	28.04%	13.62% (p_y)	2.86%	13.06% (p_y)	24.90%	7.34%	1.25%

TABLE 8.11: Orbital composition of inner-valence MOs of trans-2-butene.

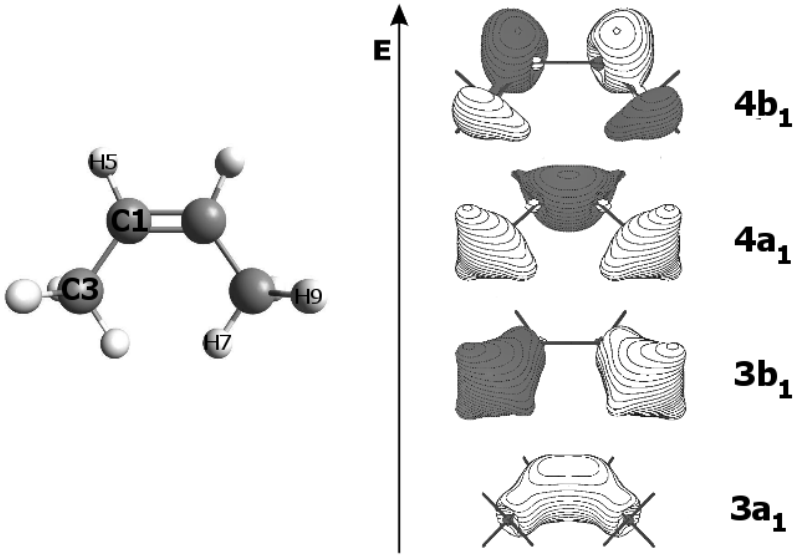

FIGURE 8.15: Cis-2-butene and MOs deriving from C2s AOs.

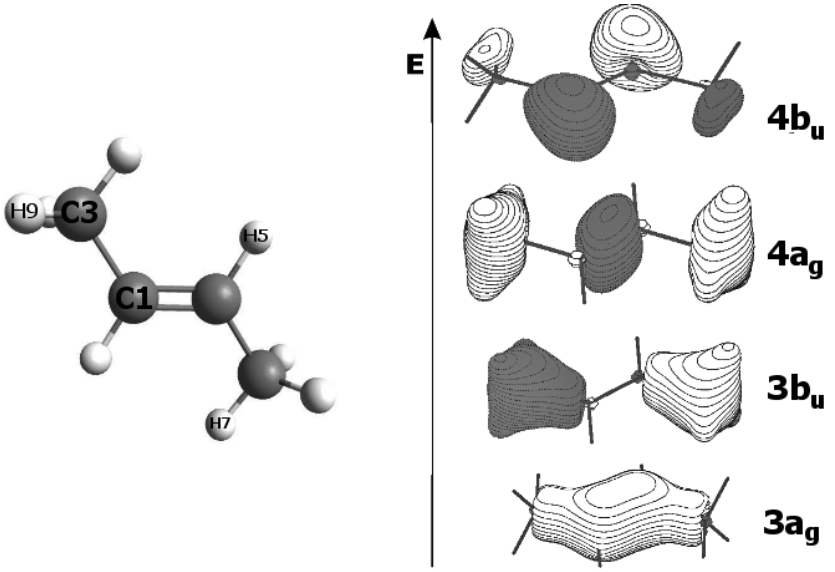

FIGURE 8.16: Trans-2-butene and MOs deriving from C2s AOs.

As in the previous cases, the non-equivalent atoms are labelled with the same criterion of Fig. 8.2. Fig. 8.17 shows, in the upper panel, the cross sections relative to the $3a_g$ and $3a_1$ ionizations of trans and cis-2-butene, respectively. Meanwhile, in the lower panel, the cross sections relative to the $4a_g$ and $4a_1$ ionizations are also shown. The first set of cross sections indicate the in-phase combination of the C 2s AOs of the central atoms. They are almost indistinguishable because the electronic structures and bond distances of the atoms are approximately the same. On the contrary, in the second case it is possible to distinguish small oscillations characterized by a different periodicity in the two conformers. This behaviour is

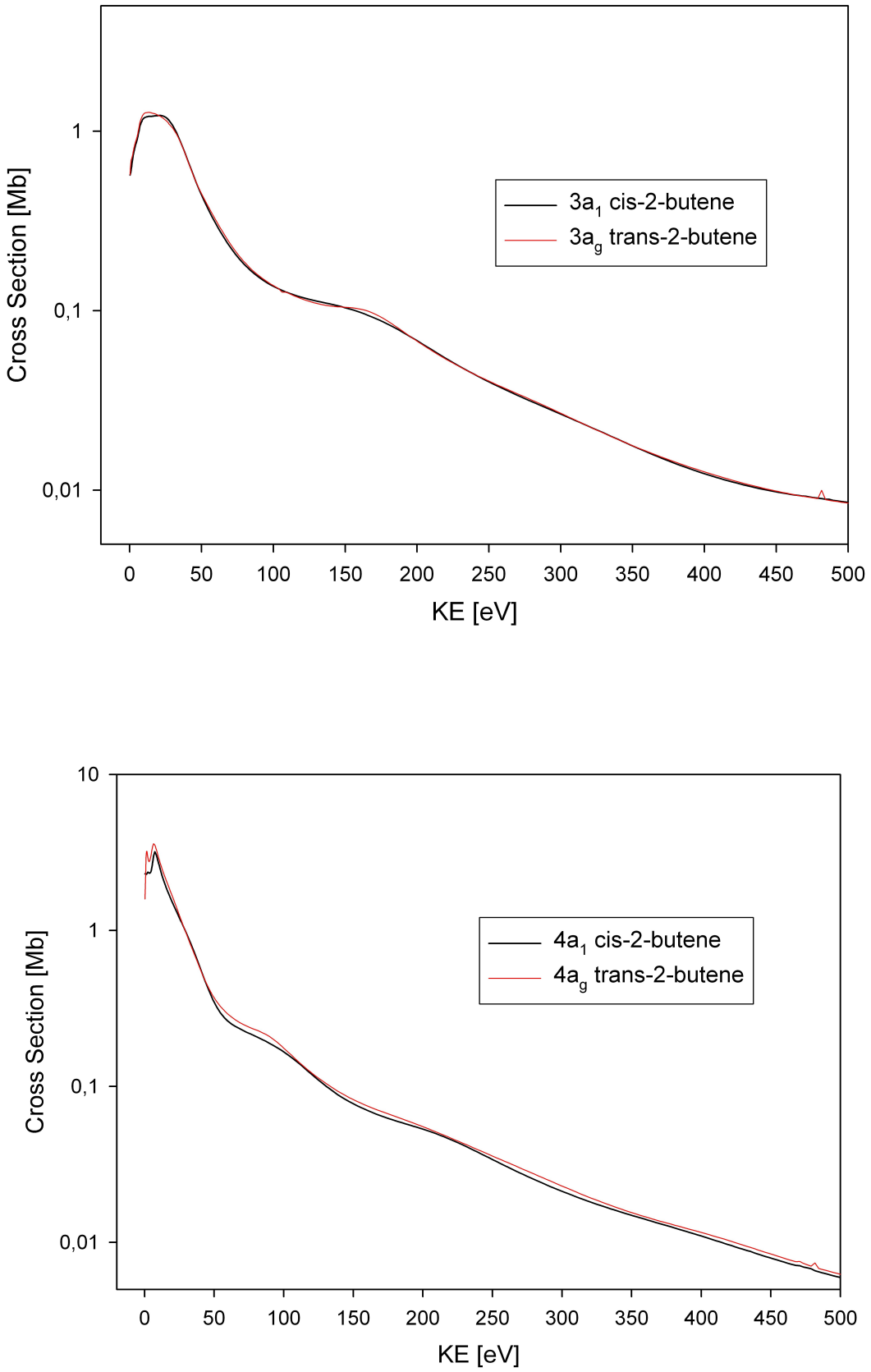

FIGURE 8.17: Theoretical cross sections relative to the $3a_g$ and $3a_1$ ionizations (upper panel) and to the $4a_g$ and $4a_1$ ionizations (lower panel) of trans and cis-2-butene.

	C1		**C3**		**H5**	**H7**	**H9**
	2s	2p	2s	2p	1s	1s	1s
$3A_1$	58.03%	1.95% (p_z)	24.49%	1.71% (p_x)	6.08%	5.29%	6.77%
$3B_1$	14.84%	5.23% (p_x)	49.77%	//	1.74%	7.45%	20.12%
$4A_1$	21.68%	9.46% (p_x)	29.78%	1.36% (p_z)	6.20%	9.98%	15.12%
$4B_1$	32.08%	9.80% (p_x)	5.04%	16.86% (p_z)	18.65%	5.40%	7.46%

TABLE 8.12: Orbital composition of inner-valence MOs of cis-2-butene.

mainly due to the significant change in the distance between the two terminal methyl groups. Nevertheless, it is also clear that these structures are very difficult to observe from a direct measure of the cross section because the quantity quickly diminishes. Hence they can be highlighted by taking into account suitable cross sections ratios of the same conformer. In this way, indeed, the effect of the decrease of the cross section is deleted since it is practically identical for MOs which derive from the same AOs. We can separately consider the two ratios relative to 3A and 4B ionizations and those relative to 4A and 4B ionizations. The first ratios are relative to the orbitals predominantly localized on the central carbon atoms and they are reported in Fig. (8.18). While they show relatively small changes in the two conformers, a more evident change is present in the second case and for the ionization relative to the orbital 3B, Fig. (8.19). 3B is the orbital which is mainly localized on the terminal carbon atoms. In particular, it is worth noting that the period of oscillation is clearly different in the two isomers. Hence it represents the more suitable property for one to experimentally distinguish between the two conformations.

As already mentioned, it is possible to emphasize the oscillation patterns by considering single orbital ratios. Let us examine three of these ratios. The first one is the 4A/3A ratio, reported in Fig. 8.20(a). It exhibits only small changes although it involves orbitals with rather different composition: the 4A orbital is distributed on the whole molecule while the 3A orbital is mainly localized on the C=C group. We partially anticipated this behaviour since orbitals with the same parity, corresponding to in-phase combination of AOs, exhibit in-phase oscillations which tend to cancel each other out in terms of the ratio. The second ratio, namely ratio 3B/3A shown in Fig. 8.20(b), contains large differences, in particular there are large displacements between minima and maxima associated

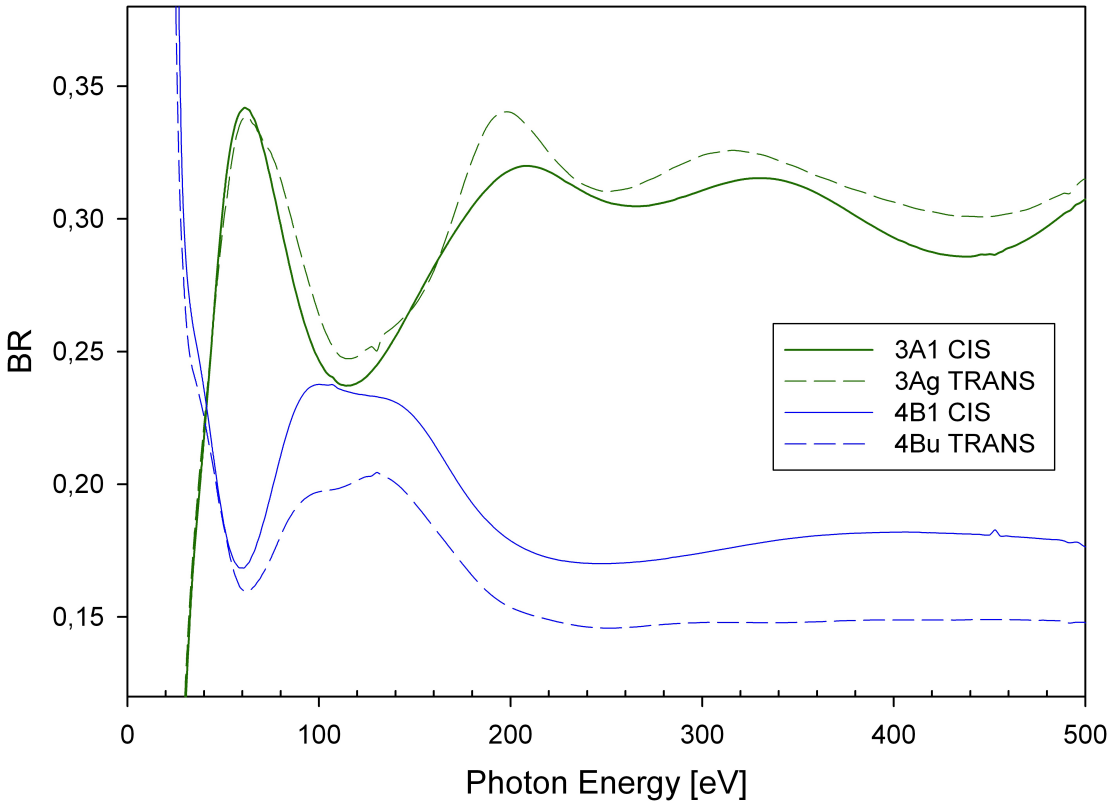

FIGURE 8.18: Cross section ratio relative to 3A and 4B ionizations of trans and cis-2-butene.

with the two conformers. This ratio can then be used to distinguish between the different conformations. The last ratio is the 3B/4A ratio, shown in Fig. 8.20(c). Although we do note significant differences between the two conformers, they are not so clear as in the previous cases. This is true even though these ionizations formally correspond to two orbitals with different parity. These orbitals originate from C2s AOs localized on the terminal methyl groups. This is an indication of the complex and delocalized nature of the orbitals, in particular of the 4A orbital at higher energy.

Summarizing, the differences between the interference patterns associated to the different isomers are quite large and constitute an unambiguous signature of two conformers. This makes possible to do, at least in the simple cases, a conformational analysis of more than two conformers with the relative populations by the accurate comparison amongst the experimental and theoretical interference patterns.

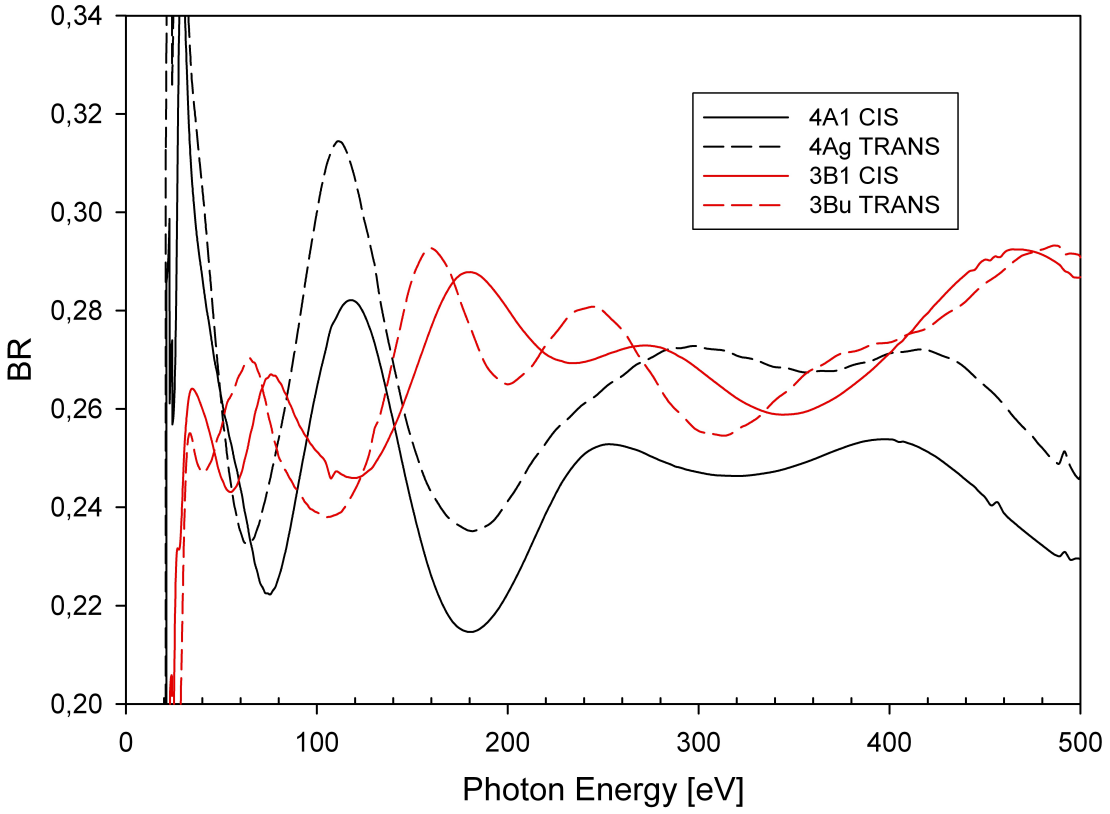

FIGURE 8.19: Cross section ratio relative to 4A and 4B ionizations of trans and cis-2-butene.

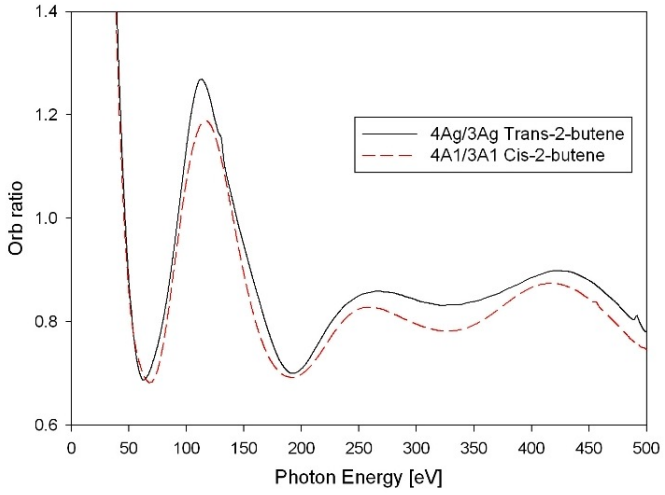

(a) 4A/3A ratio

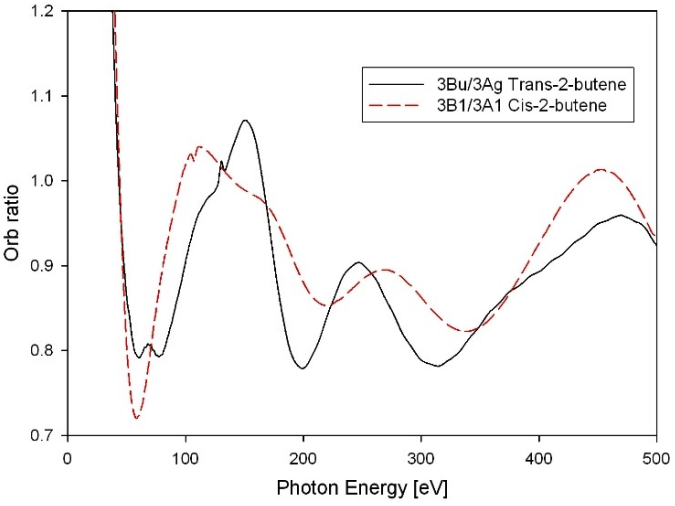

(b) 3B/3A ratio

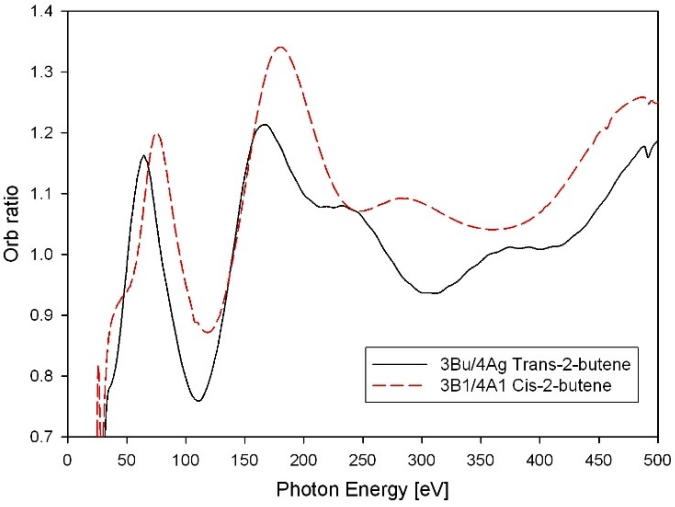

(c) 3B/4A ratio

FIGURE 8.20: Selected orbital ratios of cis/trans-2-butene.

Chapter 9

Interference and diffraction in photoelectron spectra

9.1 Introduction

An effect due to diffraction from neighbouring inequivalent atoms has been known for a long time [132, 133] and is at the basis of EXAFS oscillations observed in core X-ray photoabsorption spectra, which should obviously stem from the same underlying features in photoemission. In this case, considering again a single localized core orbital for simplicity, there is a single origin of photoelectron waves, which are however rescattered by the potential wells generated by the adjacent atoms, like a wave hitting an obstacle, giving rise to a reflected wave that interferes with the original one. A clear signature of the difference is the oscillation period, as now the path covered by the wave is twice the internuclear distance, giving a sin(2kR) modulation. Moreover, as the scattered wave is much less intense than the primary one,it is expected that the amplitude of the oscillations is significantly weaker than in the case of Young type interference. This diffraction pattern has escaped attention until very recently, probably because of the experimental difficulty of accurately observing photoemission over an extended energy range. A beautiful set of EXAFS type oscillations has been observed in the chloroethanes [150], and even in the light atom only molecule dimethylacetylene [151]. Also in this case a neat observation of the diffraction pattern is possible by taking ratios of cross sections from inequivalent atom C 1s ionizations, eliminating

the strong damping due to the cross section decrease. The geometrical information is currently retrieved in EXAFS studies by accurate fitting and background subtraction of the absorption signal. In this respect photoemission is much richer of information content, because of the ability to disentangle individual ionization channels which are superimposed in the total absorption cross section, e.g. the possibility of distinguishing several inequivalent sites, to analyse also valence and inner valence photoemission, and to obtain additionally electronic structure information. However extraction of the features from the photoemission signal is more difficult, and an appealing possibility, when missing an internal reference given by the ratio of two similar channels, is to use a mixture with a reference compound against which to normalize the cross section. One interesting issue is now the interplay of interference due to coherent emission from equivalent centres and diffraction due to backscattering from neighbouring atoms, their relative importance and their disentangling. Actually the distinction becomes blurred in the case of valence orbitals, which in complex molecules are often delocalized, with several centres and different atomic species, contributing to the cross section with unequal amplitudes. It may be worth recalling that the degree of localization is basically determined by the ratio between the energy difference of the relevant atomic orbitals, possibly shifted by the different substituents, and their mutual interaction, which is proportional to their overlap. For core orbitals interaction is very small, and even a small perturbation can completely localize the molecular orbitals on a single centre. In the valence shell interaction is much stronger, and localization due to substituents is generally modest, unless the two sites involved are not directly connected.In the simple hydrocarbons, diffraction from the neighbouring hydrogens is negligible, due to the smallness of electron density. To explore the interplay of interference and diffraction we have performed a series of calculations on the fluorine and iodine substituted acetylenes, both core C 1s and inner valence C 2s ionizations,with the same approach that has been shown to be very accurate in describing such features, so that the results reported should rep-resent a close description of the phenomena. In the case of HCCF and HCCI the equivalence of the two carbon atoms is lost, and only diffraction is at play in C 1s ionizations, but not in C 2s, because,although skewed, the relevant orbitals remain largely delocalized. Because of the large chemical shifts, the predicted features should be amenable to experimental verification.In the case of the disubstituted compounds, C_2F_2 and C_2I_2, symmetry is restored, and both interference

and diffraction are atwork, because of the bulky substituents. In this case experimental verification becomes hardly possible due to the tiny separation of the core levels. Still diffraction should appear even without resolving the core states. To reveal it we consider the ratio of C 1s cross section of C_2F_2 and C_2H_2, and show that diffraction pattern emerges very clearly. To confirm that diffraction is detectable even in the smallest systems, we have considered the CO molecule, and compared C 1s and O 1s ionizations to those of CH_4 and H_2O respectively. The emergence of a well defined diffraction pattern shows that the proposed approach is general, and experimentally feasible.

9.2 Results and discussion

9.2.1 HCCF, HCCI

As already mentioned the loss of inversion symmetry causes complete localization of C 1s orbitals on each one of the two inequivalent sites. Instead of the two $1\sigma_g$, $1\sigma_u$ orbitals here one has 2σ, the lower lying, localized on the carbon bound to the electronegative fluorine, and 3σ, localized on the other site. Interference is then completely lost, and only diffraction is expected. It is very informative to compare the C 1s cross ratio $3\sigma/2\sigma$ to the $1\sigma_g/1\sigma_u$ ratio in C_2H_2 [146] reported in Fig. 9.1, where basically a pure interferenceeffect is present. As expected, there is a dramatic drop in the amplitude of oscillations, confirming that diffraction effects are much weaker than interference ones and also the damping is much more pronounced. There is however a clear oscillatory structure, more complex than in the pure interference case, with a kind of bimodal structure, one with a similar period as the interference pattern,with a superimposed short period oscillation. Actually, neglecting the H atom, one can expect three frequencies coming into play,one associated to the C-C distance, equal for the two centres, and two different ones associated with the two different C-F distances,which show up in the cross section ratio. These qualitative features are completely borne out by the calculations, which show also stronger shape resonant features at low energy. A comparison of the C 1s ionization ratio in HCCF and HCCI is reported in Fig. 9.2. A much stronger scattering amplitude could have been expected from the bulky iodine substituent. Actually this is not apparent at low energy, but the oscillations become of shorter period, due to the longer C-I distance, and are much more persistent

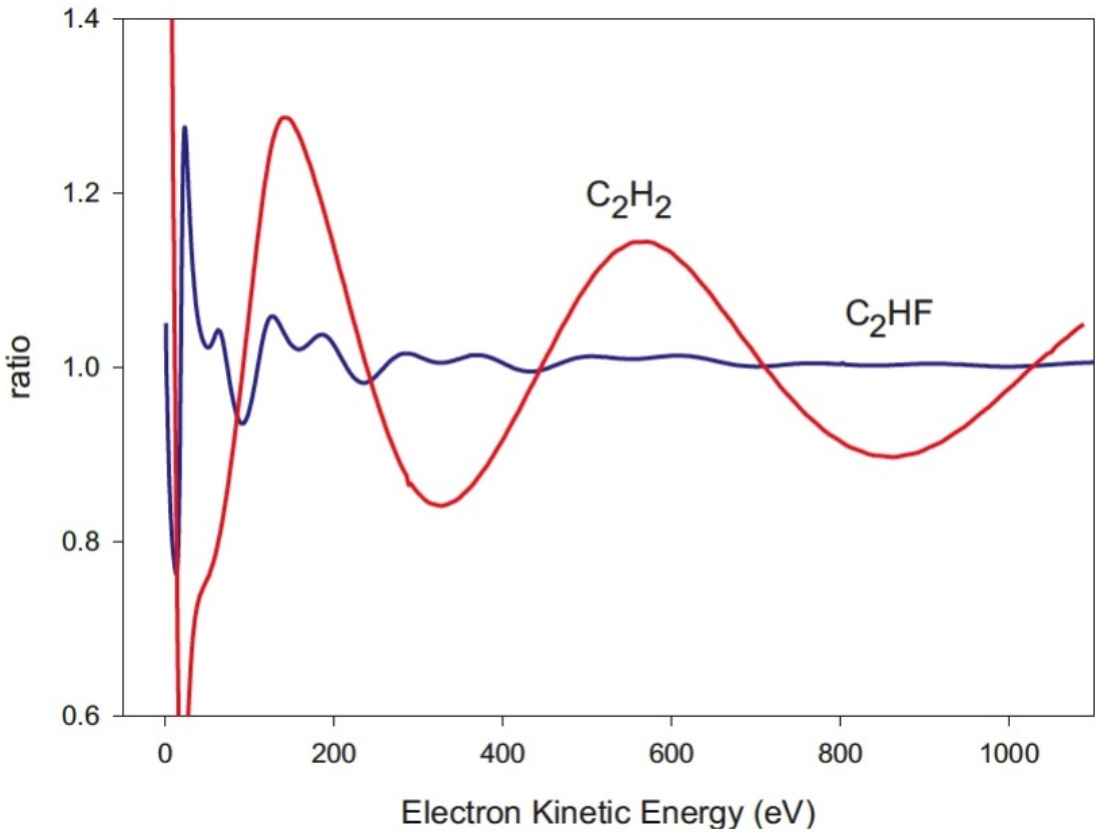

FIGURE 9.1: Theoretical cross section ratios as a function of electron kinetic energy in C 1s-derived orbital ionizations of C_2H_2 ($1\sigma_g/1\sigma_u$) and C_2HF ($3\sigma/2\sigma$). Pure interference effects in C_2H_2 are compared with pure diffraction in C_2HF.

at higher energy. One can speculate that due to a harder inner core iodine keeps a strong scattering power even towards high energy electrons, while F becomes almost transparent. The results relative to oscillations originating from the C 2s dominated molecular orbitals ($2\sigma_g$, $2\sigma_u$ in C_2H_2; 5σ, 6σ in C_2HF and 12σ, 13σ in C_2HI) are reported in Fig. 9.3. Already in C_2H_2 the pattern is less regular due to the delocalized nature of the inner valence orbitals, and the admixture of atomic orbitals of the H atoms, which is different and much stronger in the higher lying $2\sigma_u$ orbital. Going to the C_2HF and C_2HI, there is a drastic decrease in the ratio, and a more irregular pattern. This is due to the interplay of interference,which, at variance with the core is only partly lost, as the two C 2s orbitals do not localize strongly, and participate to both orbitals, and diffraction from the halogen atom. The decrease in the ratio is basically due to a more even participation of the two C 2s orbitals to both molecular orbitals, as well as to the comparable cross section of halogen orbitals admixed, which render the high energy ratio much closer to the ideal limit of 1, as is very accurately verified in the case of core ionization [146], where two pure C 1s cross sections are involved. So the valence ratios, in addition

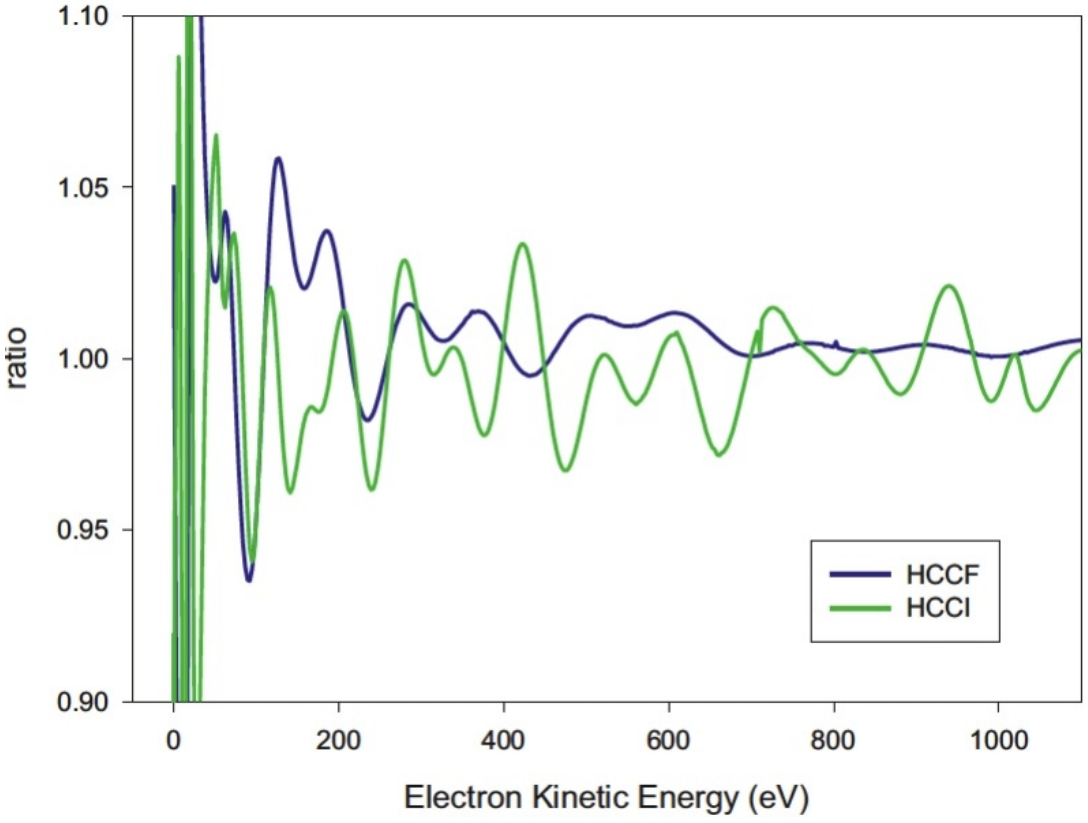

FIGURE 9.2: Theoretical cross section ratios as a function of electron kinetic energy in C 1s-derived orbital ionizations of C_2HF ($3\sigma/2\sigma$) and C_2HI ($7\sigma/8\sigma$). Comparison between the scattering amplitudes of the F and I substituents.

to the geometrical structure, contain further information on the AO composition, i.e.the electronic structure, of the relevant MOs, although the latter can be obtained only through a theoretical model and a simulation of the spectra. It must be reminded that also in the case of core spectra, the high energy limit ratio of 1 is obtained in the present simulation by employing a Koopmans' theorem like formulation, and that many body effects neglected can affect the different holes to different extent, causing the asymptotic ratio to deviate significantly from the statistical ratio. This has been experimentally seen most clearly in a recent study of diffraction patterns in the C1s coreionization of chlorinated ethanes [150], where it was significantly dependent on the degree of substitution. Looking at Fig. 9.3 it appears that the amplitude of the oscillation is significantly reduced in C_2HF and C_2HI compared to C_2H_2. In part this may be amplified as percentage by the larger value of the ratio in the latter, but it is also a sign of reduced interference effects due to the partial localization ("unequal slits") of the C 2s AOs due to the substituent. In this case the situation is intermediate with respect to the C1s case, where the drop in amplitude is very strong.

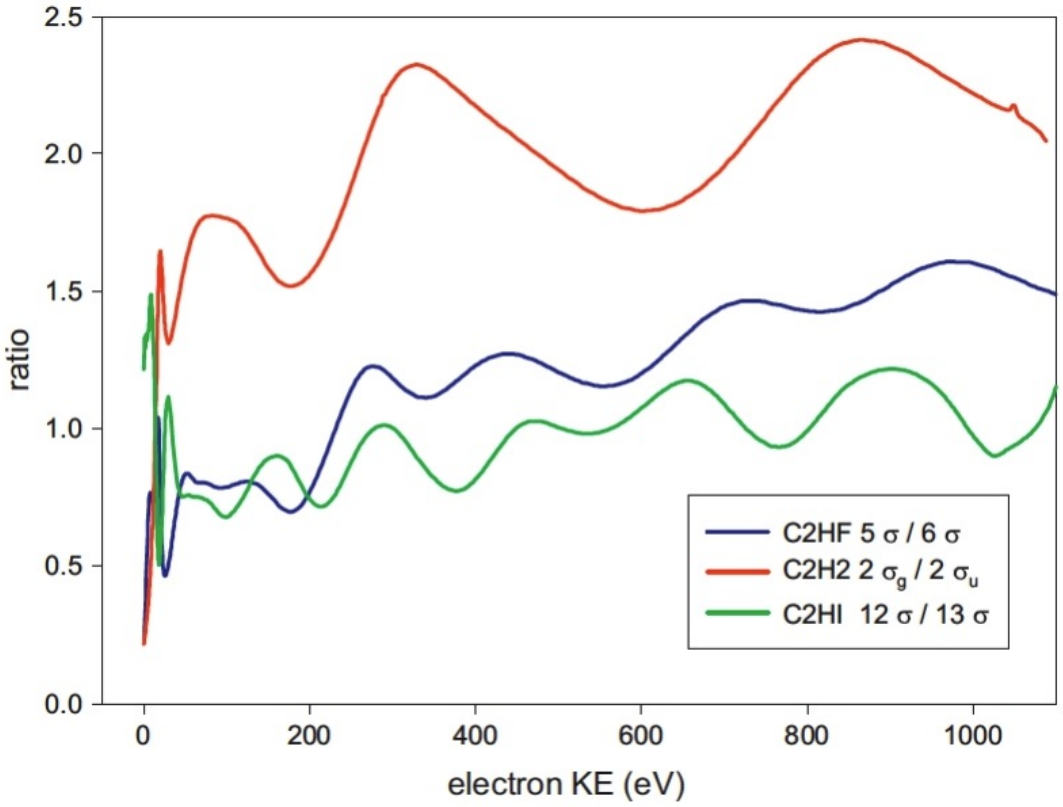

FIGURE 9.3: Theoretical cross section ratios as a function of electron kinetic energy in C 2s-derived orbital ionizations of C_2H_2 ($2\sigma_g/2\sigma_u$), C_2HF ($5\sigma/6\sigma$) and C_2HI ($12\sigma/13\sigma$) molecules. Both interference and diffraction are apparent in the valence shell. Electronic structure change is responsible of the decrease of the ratio in the substituted acetylenes.

9.2.2 C_2F_2, C_2I_2

In this case symmetry is restored and full interference is expected again, compounded however with non-negligible diffraction due to the substituents. Again it is very instructive to compare the results with those obtained for acetylene. The comparison between C_2H_2 and C_2F_2 C 1s cross sections ratio is reported in Fig. 9.4. The anticipation is fully confirmed, C_2F_2 shows an interference oscillation very close, in period and amplitude (the C-C bond length is very similar), with smaller superimposed oscillations due to diffraction from the neighbouring fluorines, of shorter period and quite strongly damped. The pattern repeats for C_2I_2, which is added in Fig. 9.5, where it is seen that in this case, as happens also in C_2HI, the diffraction oscillations have a significantly shorter period, and persist at higher energies. The diffraction oscillations are in general more complex, as there are two inequivalent C-X distances. The results for the inner valence orbitals are reported in Fig. 9.6. The situation is further complicated in the case of C_2I_2,

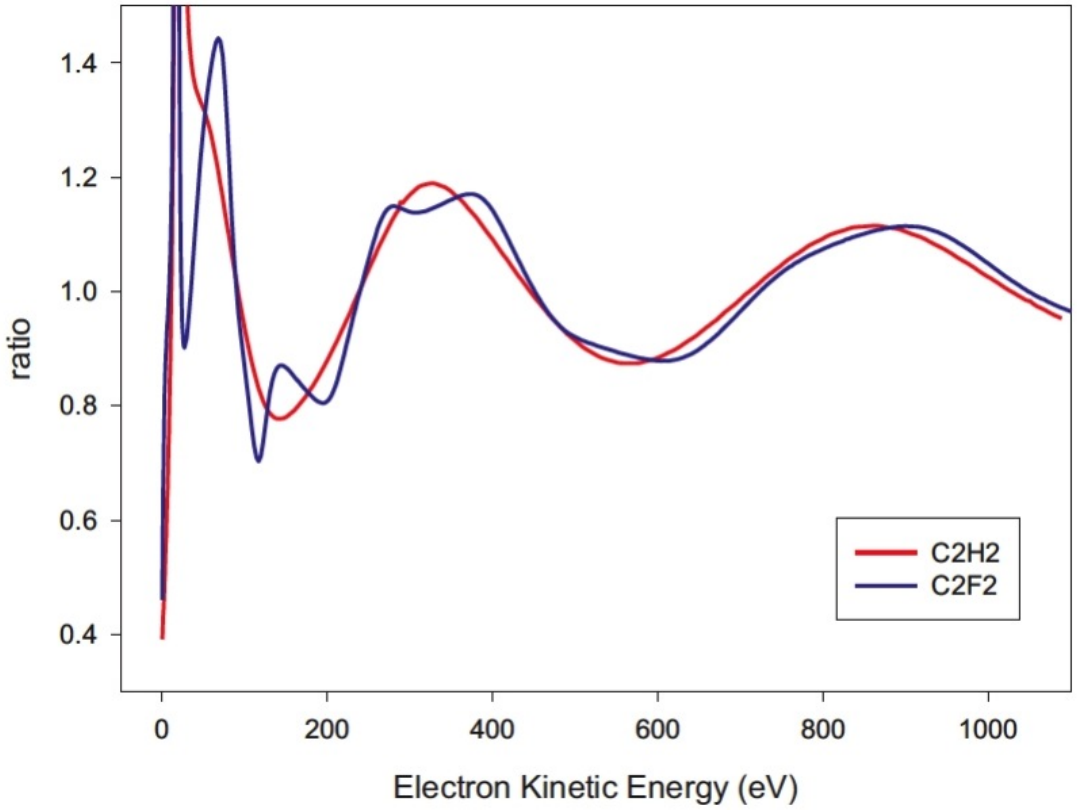

FIGURE 9.4: Theoretical cross section ratios as a function of electron kinetic energy in C 1s-derived orbital ionizations of C_2H_2 ($1\sigma_g/1\sigma_u$) and C_2F_2 ($2\sigma_g/2\sigma_u$). C_2F_2 shows interplay of interference, very similar to that in C_2H_2, and diffraction, due to the additional substituents.

because 5s AO mixes in heavily with C 2s, and there are two σ_g orbitals, $11\sigma_g$ and $12\sigma_g$ which have significant C 2s participation, so that we have considered both ratios with respect to $11\sigma_u$. Actually, although quite different in detail, both show analogous features. Overall, the general behaviour is similar to that found in the mono-substituted compounds. Curiously, oscillations appear significantly reduced in the case of C_2F_2, possibly because of some destructive interplay of interference from equivalent centres and diffraction effects. While the situation is very neat in the case of core ionization, unfortunately experimental verification is unlikely because of the difficulty of resolving the very small σ_g/σ_u splitting. In the case of different sets of equivalent atoms, it is still possible to reveal diffraction pattern (not the interference) by taking ratio of the cross sections of the two inequivalent channels. This has been indeed observed in the case of dimethylacetylene, CH_3CCCH_3 [151], by taking the ratio of acetylenic and methyl C 1s cross sections. In the case of a single equivalent set of atoms, like C_2F_2, this is no longer possible, but it can be experimentally feasible to analyse a mixture of two compounds, one

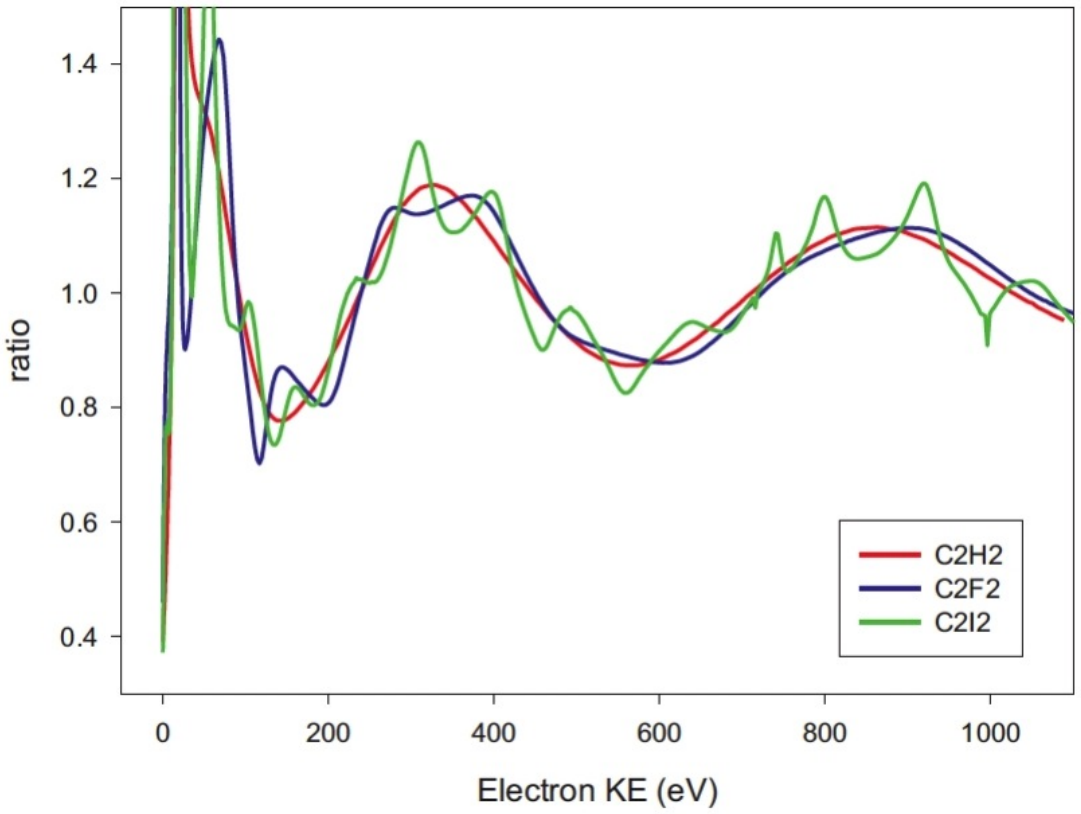

FIGURE 9.5: Theoretical cross section ratios as a function of electron kinetic energy in C 1s-derived orbital ionizations of C_2H_2 ($1\sigma_g/1\sigma_u$), C_2F_2 ($2\sigma_g/2\sigma_u$) and C_2I_2 ($7\sigma_g/7\sigma_u$). The effects of different subtituents on the diffraction pattern are shown. Shorter oscillation period in C_2I_2 is due to the longer bond length.

chosen as an external reference, taking the ratios of the two photoemission lines (it is easy to correct for non 1:1 molar ratio). Indeed examination of Fig. 9.4 suggests that this could be the case for the couple C_2F_2/C_2H_2, and the ratio of the two unresolved σ_g, σ_u C1s ionizations is reported in Fig. 9.7. As can be seen the diffraction pattern emerges strongly and could be easily detected and analysed. To further test this approach we have considered the simplest case of the CO molecule. In a previous investigation we unsuccessfully attempted to reveal a diffraction pattern by taking the ratio of C1s/O1s cross sections [159]. Actually, since the same diffraction pattern appears, as we shall verify, in both ionizations, it basically cancels out. In any case, given the large energy separation of C1s and O1s ionizations,measuring an accurate value of this ratio could be experimentally difficult.In the present case we have employed two different external standards, CH_4 for C 1s and H_2O for O 1s. The ratios of C1s and O1s cross sections of CO to the two standards are reported in Fig. 9.8. Even in this small molecule of first row atoms, a diffraction pattern is clearly revealed, even if relatively weak, and

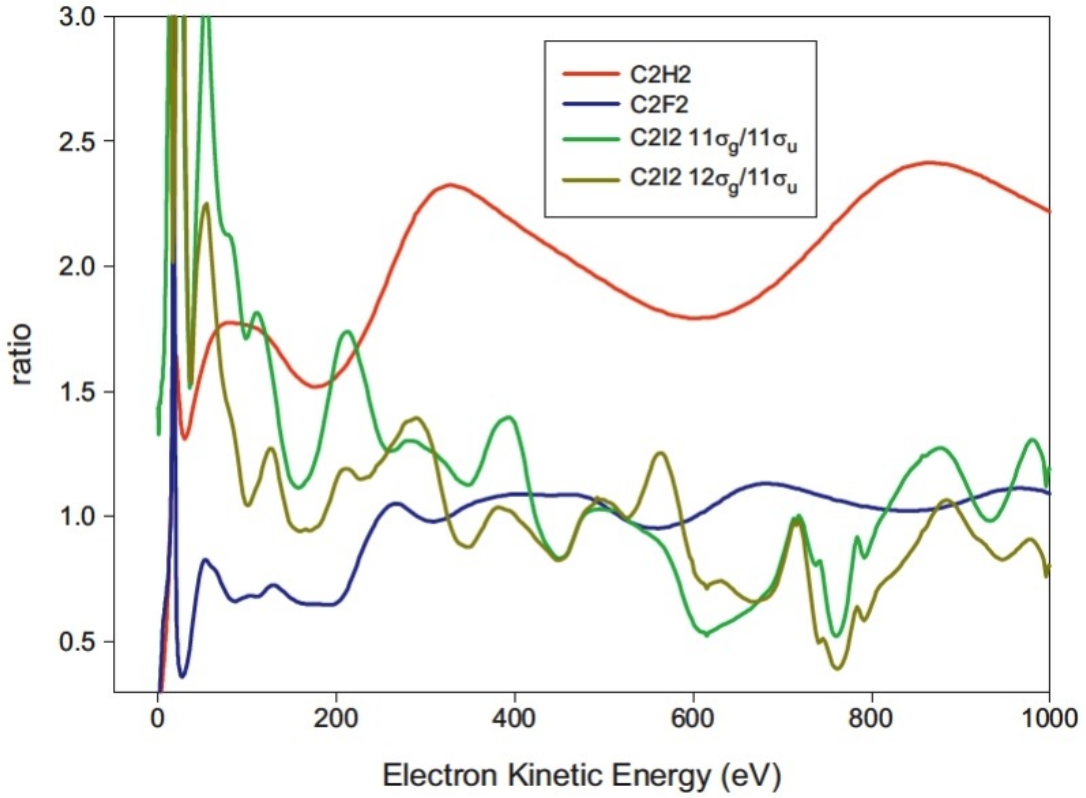

FIGURE 9.6: Theoretical cross section ratios as a function of electron kinetic energy in C 2s-derived orbital ionizations of C_2H_2 ($2\sigma_g/2\sigma_u$), C_2F_2 ($4\sigma_g/4\sigma_u$) and C_2I_2 ($11\sigma_g/11\sigma_u$, $12\sigma_g/12\sigma_u$). The more complex pattern in the valence shell is due to the interplay of interference and diffraction. Two σ_g orbitals with strong C 2s participation are available in C_2I_2 due to mixing with I 5s AO

as expected the pattern is very similar, given the unique interatomic distance. Of course each separate molecule will have a separate diffraction pattern, and so the one measured with reference to a standard is really a ratio of two different patterns, although in the case of the pure hydrides like CH_4 and H_2O the diffraction is expected to be tiny. Indeed diffraction effects have been clearly revealed in CH_4 as embodied in the cross section ratios of the individual vibrational components, the so-called v-ratios [144]. Ideally one would employ purely atomic cross sections, but this is not experimentally feasible. It does not mean however that the patterns obtained with reference to an external standard are meaningless, since the quantitative extraction of the information content embodied in the diffraction pattern, geometrical as well as electronic structure, will require comparison with the simulated pattern and leastsquares fitting, while qualitative information will be often available by simple analysis of trends obtained in classes of related compounds.

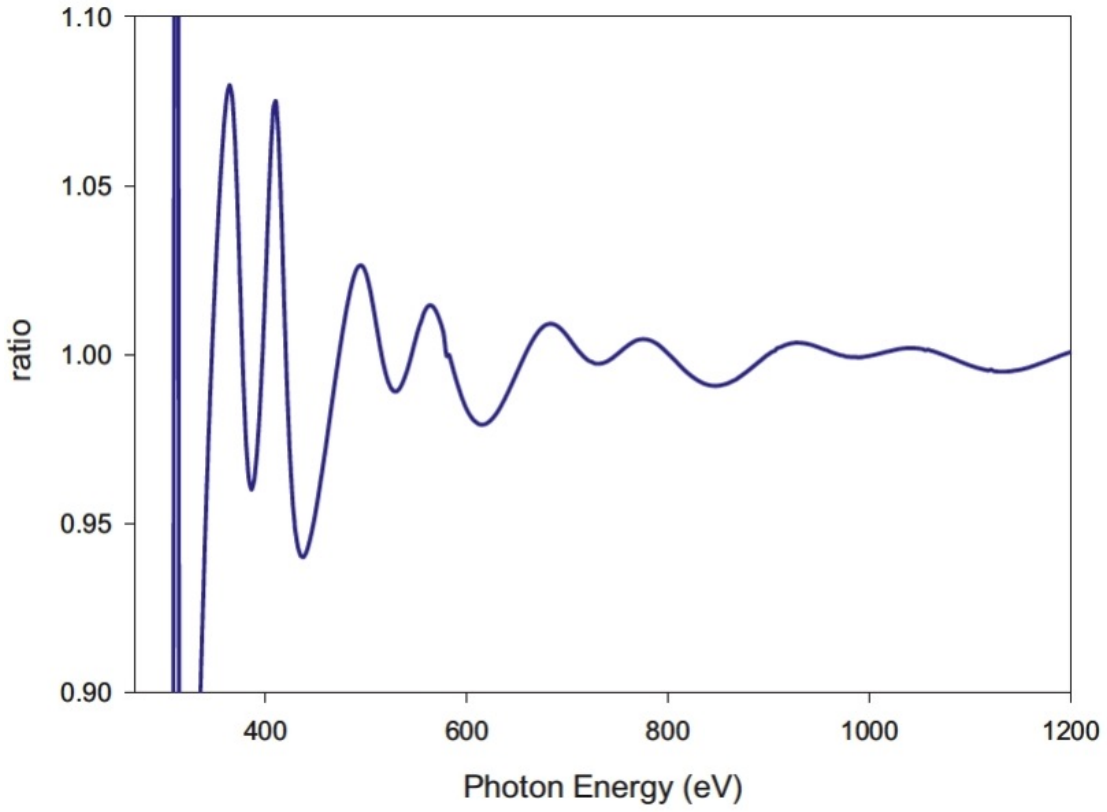

FIGURE 9.7: Ratio of the two unresolved σ_g, σ_u C 1s cross section ratio for C_2F_2 ($2\sigma_g$+$2\sigma_u$) and C_2H_2 ($1\sigma_g$+$1\sigma_u$). Although interference pattern is lost, diffraction is clearly revealed.

9.3 Conclusions

The different behaviour of interference due to the coherent emission from equivalent centres and diffraction from neighbouring inequivalent atoms has been clearly revealed in the analysis of core ionization of simply (asymmetric) and doubly (symmetric) substituted haloacetylenes, as well as their interplay.Both effects participate with different extent in photoionization of valence orbitals, giving rise to a more complex oscillatory pat-tern which although carrying important geometric and electronic structure information is more difficult to analyse in simple terms. Diffraction patterns in the core region are very clear and can be easily detected by taking cross section ratios with respect to a reference standard molecule mixed with the sample under examination.In this respect the simple hydrides appear very convenient. Previous experience suggests that the static-exchange DFT approach presently employed can be profitably employed for an accurate and cost effective simulation of the spectra, and as a means of extracting quantitative information via least squares fitting.

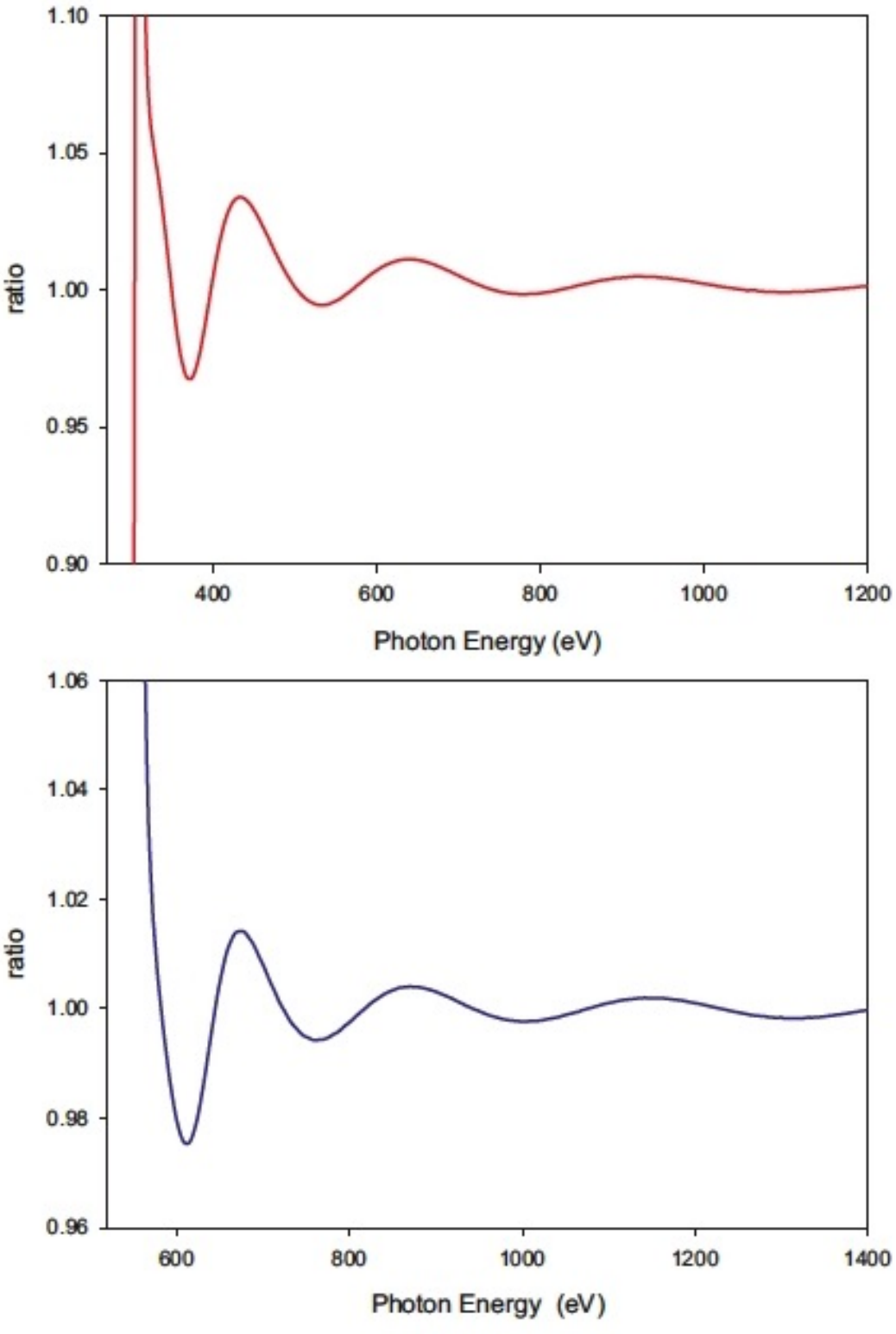

FIGURE 9.8: C 1s cross section ratio for CO/CH_4 (upper panel) and O 1s cross section ratio for CO/H_2O (lower panel). Diffraction effects show clearly, and are very similar in the two ratios.

Chapter 10

Interference effects in the valence shell ionization of simple hydrocarbons

10.1 Introduction

A full delocalization is expected in the outer valence shell, which could be expected to wash out completely the interference structure. On the other side, outer valence ionization is very rich, as it comprises several orbitals, including those most responsible of the bonding and chemical properties of the compound. Although in complex molecules the full valence spectrum may become very crowded and often unresolved, typically a few ionization show up as well resolved isolated bands, or even resolved composite bands can be analyzed, giving a wealth of opportunities for application. To investigate such possibility in this chapter we report structures in the outer valence shell cross section of the four molecules C_2H_2, C_2H_4, C_2H_6 and C_3H_8. All cross sections have been computed at the static density functional level, employing the LCAO B-spline approach previously developed, which has been shown to produce interference structures in excellent agreement with the experiment [138, 146].

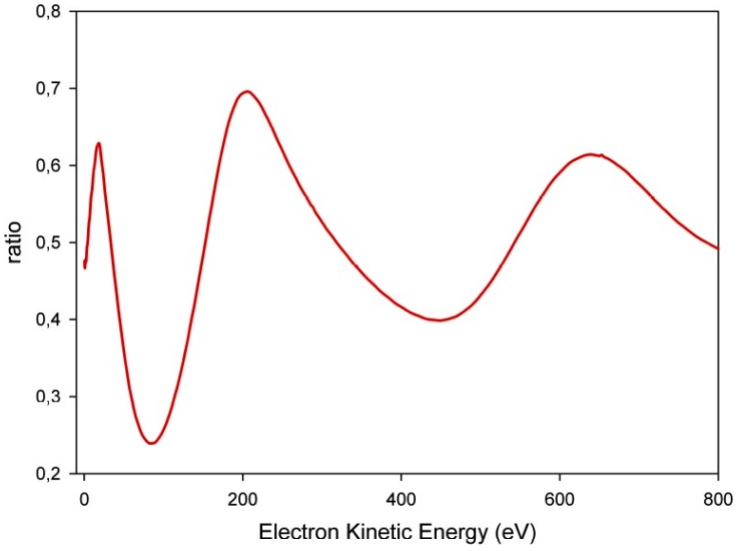

FIGURE 10.1: $3\sigma_g/1\pi_u$ cross section ratio for C_2H_2

10.2 Results and discussion

10.2.1 C_2H_2

In this case the outer valence shell only comprises two orbitals: the $3\sigma_g$ (HOMO) and the $1\pi_u$ (HOMO-1). $1\pi_u$, in a minimal LCAO picture, is purely localized on the two carbons, being composed of symmetric and antisymmetric combination of C 2p orbitals, while the $3\sigma_g$ is fully delocalized and contains an important contribution from H 1s. The relevant cross section ratio is reported in Fig. 10.1. Despite the different nature, a very clear interference pattern emerges, indicating that it is mostly dominated by the different g, u symmetry of the two orbitals, and not by the details of their composition. The average cross section ratio is close to the statistical ratio of 0.5.

10.2.2 C_2H_4

In this case the outer valence shell comprises four different ionizations, $1b_{3u}$ (HOMO), $1b_{3g}$, $3a_g$, $1b_{2u}$, all well resolved, and an ample choice of cross section ratios to investigate. We have chosen the ratio of HOMO (π) to the three higher lying orbitals (σ), which are reported in Fig 10.2. Well developed interference patterns are apparent in all three ratios. The two peaks, around 70 and 400 eV, quite similar in all ratios, are therefore probably attributed to patterns in HOMO, while

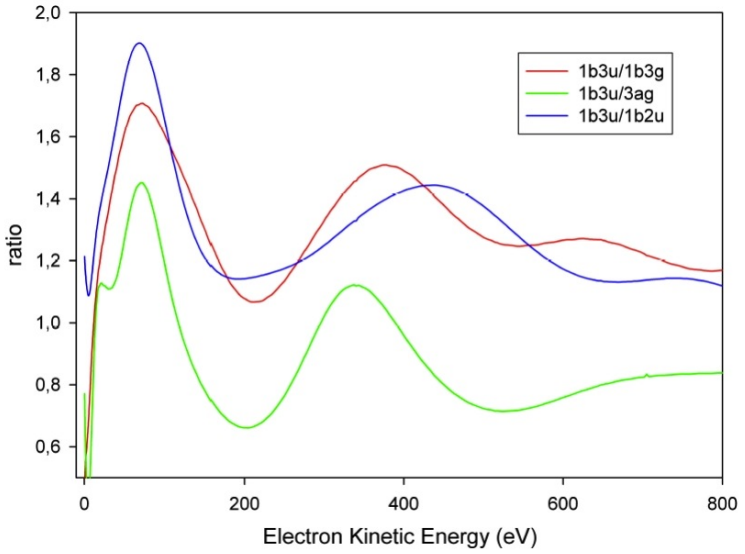

(a) $1b_{3u}$ (HOMO) versus $1b_{3g}$, $3a_g$, $1b_{2u}$ ionizations

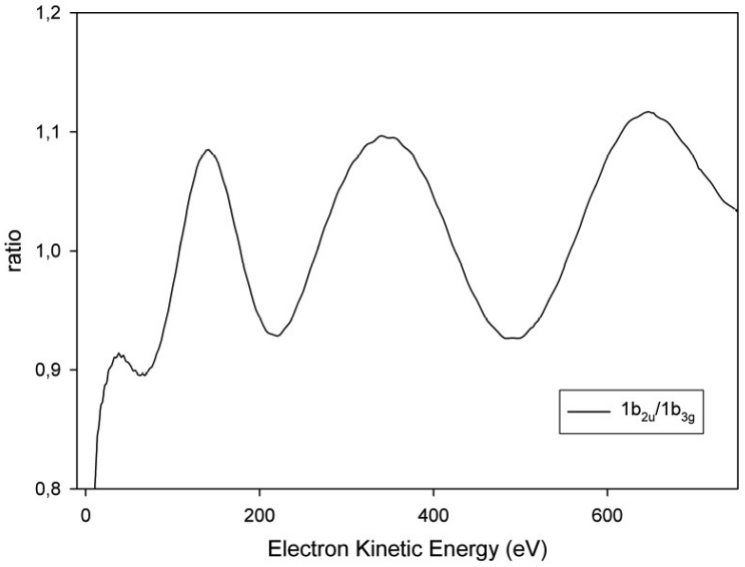

(b) $1b_{2u}/1b_{3g}$ ratio

FIGURE 10.2: Cross section ratios for C_2H_4

the profiles of the two ratios $1b_{3u}/1b_{3g}$ and $1b_{3u}/1b_{2u}$ show an additional relative oscillatory pattern, with smaller period. To see it more clearly, we have plotted the ratio $1b_{2u}/1b_{3g}$ in Fig. 10.2 where their structure appears very clearly. It is interesting that $1b_{2u}$ and $1b_{3g}$ have basically opposite composition, $1b_{2u}$ is 64% C $2p_y$ + 34% H 1s, and the composition is reversed in $1b_{3g}$. These opposite parity, delocalized orbitals, extending over the whole molecule, originate the regular, short period interference pattern, that would be otherwise unexpected, given the single short C-C internuclear distance in C_2H_4.

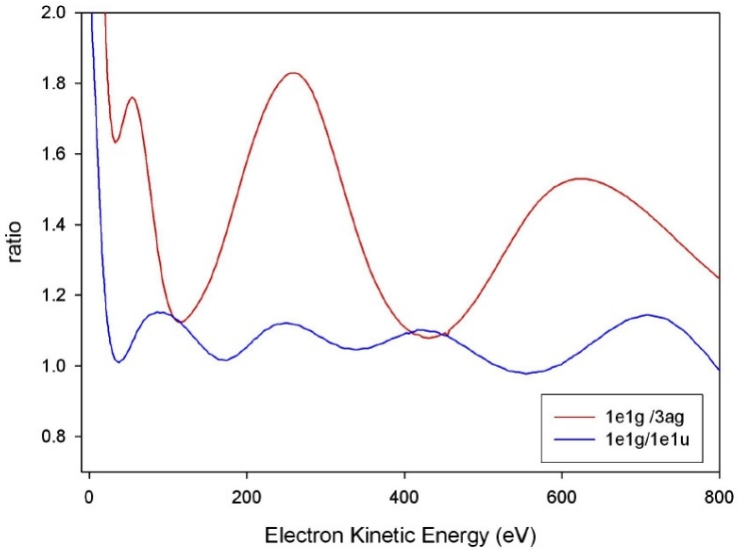

FIGURE 10.3: Cross section ratio for C_2H_6: $1e_{1g}/3a_g$ ratio and $1e_{1g}/1e_{1u}$ ratio

10.2.3 C_2H_6

In this case, because of the higher symmetry, only three outer valence ionizations are present: $1e_{1g}$ (HOMO), $3a_g$ and $1e_{1u}$. We have considered HOMO/$3a_g$ and HOMO/$1e_{1u}$ cross section ratios reported in Fig. 10.3. While the former displays well developed oscillations, the latter shows a flatter and less regular pattern, with shorter oscillation period, like in the $1b_{2u}/1b_{3g}$ case in C_2H_4, again a sign of the delocalized nature of the orbitals involved. So in this case, more than the u/g difference, it is the specific nature of the MOs that dominates the pattern.

10.2.4 C_3H_8

This serves as an example of a congested outer valence region. There are seven ionizations, spanning 6-7 eV, which cannot be resolved, but give rise to three well separated composite bands I: $2b_2$, $6a_1$, $4b_1$; II : $1a_2$, $3b_2$; III: $5a_1$, $1b_1$ [160]. To give an idea of the complexity we have rather arbitrarily plotted (Fig. 10.4) the ratios of all cross sections relative to the $1a_2$ one, chosen because of its simple and localized nature, about 50% C $2p_x$, 43% H 1s on the terminal CH_3 groups. One can observe a very regular oscillatory pattern in the $1b_1/1a_2$ ratio, together with many strong but irregular features. An alternative, experimentally feasible, is to consider ratios of the composite bands, which are also reported in Fig. 10.4. Although many details are lost, and interpretation may be more difficult, significant interference

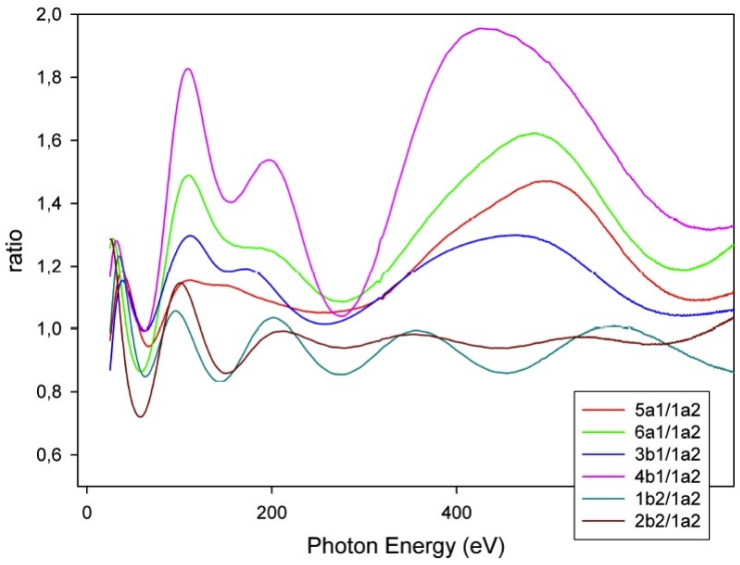

(a) Cross section ratio of all valence orbitals with respect to the $1a_2$ ionization

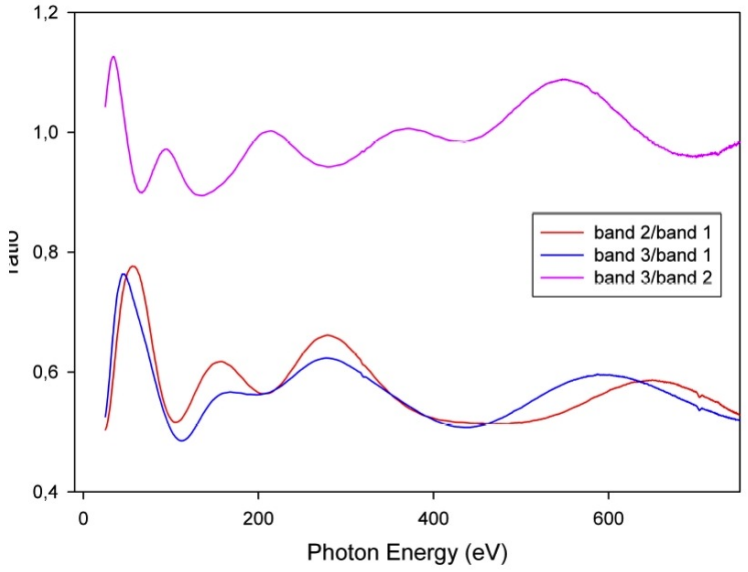

(b) Ratios of the composite bands resolved in the outer valence spectrum, band 1 ($2b_2$, $6a_1$, $4b_1$), band 2 ($1a_2$, $3b_2$), band 3 ($5a_1$, $1b_1$)

FIGURE 10.4: Cross section ratio for C_3H_8.

patterns still survive, and may yield sufficient information in combination with a theoretical simulation.

10.3 Conclusions

We have shown that well developed interference patterns emerge from cross section ratios in the outer valence shell of simple hydrocarbons. They contain important information both on the geometrical and electronic structure of the molecule. Strong evidence of the sensitivity of the interference pattern to molecular orbital delocalization over the full molecular skeleton is given by oscillation period shorter than expected on the basis of C-C bond distance. Also in the case of unresolved ionizations, ratios of composite bands still show significant interference pattern and convey useful information.

Chapter 11

Photoelectron interference in metallocenes

11.1 Introduction

As already highlighted, emission from valence orbitals is generally delocalized and, since it involves also mixing of orbitals from different atomic species, the resulting interference patterns are characterized by more complex profiles with respect to those related to the emission from core orbitals. The ubiquitous appearance, and the complexity, carry however an important reward in the form of the richness of information contained in the diffraction patterns, which concerns foremost the geometrical structure of the target, but also the detailed composition of the molecular orbitals probed. Indeed the ability of photoeelectron spectroscopy to select individual orbital ionizations allows to maximize the information required. Actually, in the course of an investigation on the electronic structure and photoemission properties of transition metallocenes, some high energy structures that emerged prompted to investigate the simpler Magnesocene, where strong oscillations in the HOMO/HOMO-1 ratios, qualitatively similar to those observed in C_{60}, although quite different in detail, were predicted and subsequently observed [147].

The recent emphasis on the suitability of photoelectron diffraction patterns to obtain quantitative geometrical parameters, also in complex molecules, prompted us to reconsider the metallocene case, with the purpose of investigating the sensitivity of the patterns to molecular geometry. To this end we have performed

theoretical investigations by arbitrarily changing the metal-ring distance in bis-cyclopentadienyl-magnesium ($MgCp_2$), a procedure that has been shown able to retrieve the experimental C-C distance to better than 0.01 Å in the simple case of acetylene [146]. Moreover we have computed diffraction patterns in the bis-decamethyl-cyclopentadienyl compounds of Mg and Be ($MgCp_2^*$ and $BeCp_2^*$). In the former, metal-ring distance is very similar to that in $MgCp_2$, and offers then an opportunity to investigate the change, if any, of the diffraction pattern induced by the additional methyl groups. While their influence on the geometrical parameters is very limited, it is known that their electronic donor properties affect significantly the electronic structure and the chemical properties of the metallocenes. In particular the inductive donor effect of methyl groups causes a growth of electronic density along metal-$CpMe_5$ bond axis [161]; this phenomenon might be connected to the profiles of the photoionization dynamical observables. On the other hand the large change in the metal-ring distance brought about by the Be substitution, due to its much smaller ionic radius, is expected to reflect in a dramatic change of the oscillation period in the interference patterns, in addition to specific changes due to subtler electronic structure effects. Although no experimental data are available, the excellent agreement with experiments obtained in a number of cases including $MgCp_2$ makes us confident in the basic soundness of the results reported and the conclusions drawn, which in any case are readily amenable to experimental verification.

Last it is worth recalling the great varieties of geometries, coordination modes and electronic structures of metal sandwich compounds, which span the entire periodic table [162, 163]. In a previous study the difference of the photoelectron diffraction pattern in $MgCp_2$ with those of $FeCp_2$ and $Cr(C_6H_6)_2$ was traced to metal d participation into the relevant orbitals [147]. On the other hand the bonding and geometry in $BeCp_2$ is still not settled [164], in $CaCp_2^*$ the rings become tilted, and a variety of coordination patterns is present in other compounds. This will challenge the capabilty of the diffraction pattern to reproduce them, in turn paving the way to establish this observable as a general and viable tool for structural and electronic information on complex systems.

11.2 Method

For V_{XC} we have employed the exchange-correlation potential LB94 [165]. The SCF initial electronic density of the ground state is obtained by means of the ADF program [166], employing a DZP basis set for H and C (TZP for Mg and Be), taken from the otpimized database included in the ADF package. For V_{XC} we have employed the exchange-correlation potential LB94 [165]. The basis comprises a long-range one-center expansion, with large angular momenta, plus a set of short range expansions centered on all nuclei. This allows an accurate treatment of both the bound states and the oscillating long range continuum functions, up to the asymptotic limit. The convergence of the calculation is mainly determined by the largest L value employed in the long range expansion, called L_{max}. Both the geometrical size of the molecule and the maximum energy in the continuum increase the number of angular continuum channels which become open at high energy, and influence the value of L_{max} needed to reach convergence. While convergence in $MgCp_2$ up to 300 eV photoelectron energy is obtained already at $L_{max} = 30$, a larger $L_{max} = 40$ is needed for the more spatially extended $MgCp^*_2$ and $BeCp^*_2$ molecules, as illustrated in Fig. 11.3. One can notice convergence with $L_{max} = 30$ up to about 150 eV in the case of $MgCp^*_2$, and a little higher for $BeCp^*_2$, a reflection of the slightly smaller molecular size.

11.3 Results and discussion

The permethylated metallocenes geometry has been otpimized with the ADF code employing the VWN exchange-correlation potential. Optimized bond lenghts for $MgCp_2$, $MgCp^*_2$ and $BeCp^*_2$, compared to some available experimental parameters, are shown in Tab. 11.1. The geometry optimization of the complexes was carried out with the Cp^* rings staggered with respect to each other (D_{5d} symmetry). Indeed calculations showed that the D_{5h} and D_{5d} forms are nearly degenerate.

We have studied the two outermost valence ionizations of $MgCp_2$, $MgCp^*_2$ and $BeCp^*_2$, HOMO and HOMO-1. The percentages of the contributions of atomic orbitals to the molecular orbitals involved in the ionizations are summarized in Tab. 11.2, and the HOMO/HOMO-1 orbitals plots are shown in Fig. 11.2. Both in the case of $MgCp^*_2$ and in that of $BeCp^*_2$, the main contribution to the HOMO and

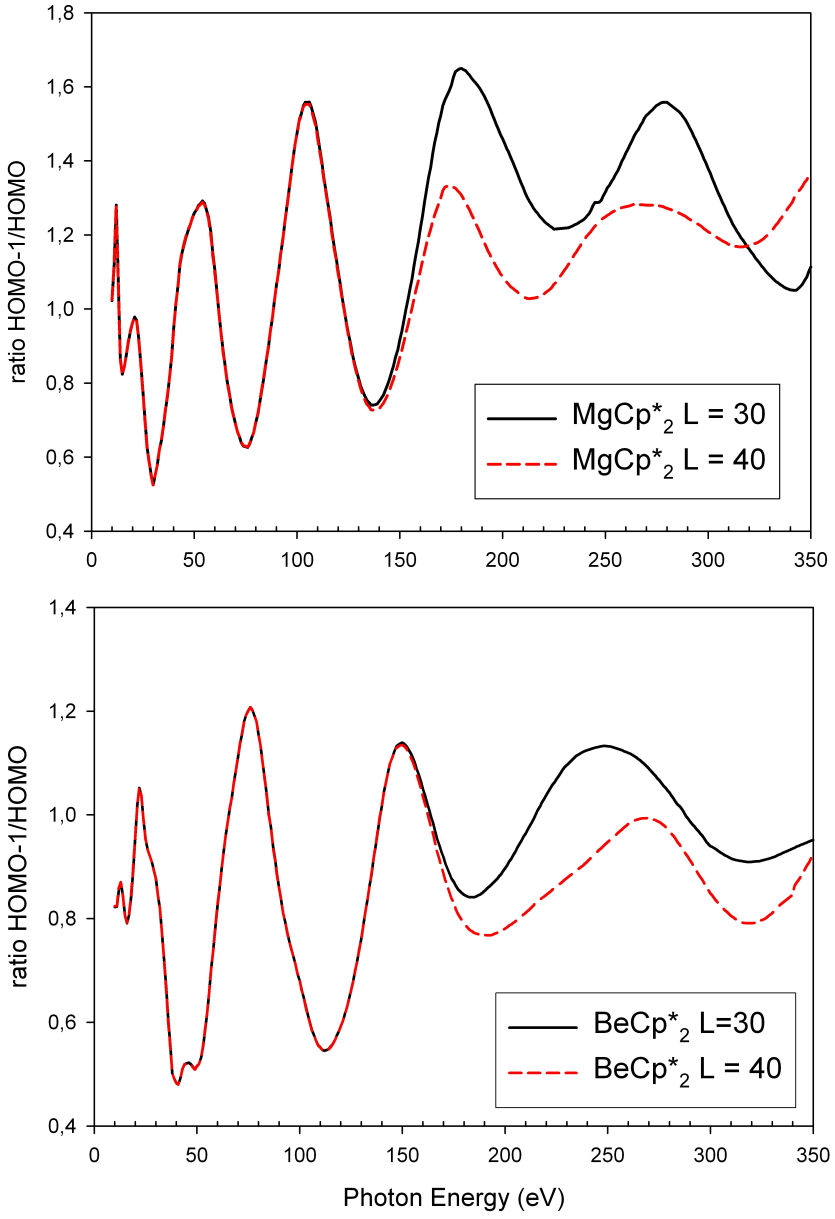

FIGURE 11.1: HOMO-1/HOMO cross section ratio calculated with L = 30 and L = 40.

	$MgCp_2$	$MgCp_2$ exp	$MgCp^*_2$	$MgCp^*_2$ exp	$BeCp^*_2$	$BeCp^*_2$ exp
r(C-C)	1.411		1.419		1.415	
r(C-CH_3)	//		1.479		1.476	
r(C-H)	1.089		1.104		1.104	
r(Me-C)	2.326	2.339[a]	2.295	2.341[b], 2.305[d]	2.011	1.969-2.114[c]
r(Me-ring)	1.992	2.008[a]	1.952	2.011[b]	1.611	1.655[c]

TABLE 11.1: Optimized values of bond lengths (Å); *a*: [167]; *b*: [168]; *c*: [169] ; *d*: [170]

	HOMO	HOMO-1
$MgCp_2$	90% p_z C + 3.6 % d_{xy} Mg	85% p_z C + 9% p_x Mg
$MgCp^*_2$	76% p_z C + 9% s H + 3% d_{yz} Mg	70% p_z C + 9% s H + 8% p_x Mg
$BeCp^*_2$	80.6% p_z C + 9% s H + 1.2% d_{yz} Be	62% p_z C + 10% s H +9.9% p_x Be

TABLE 11.2: Percentages of the contributions of atomic orbitals to HOMO and HOMO-1 orbitals.

HOMO-1 orbitals is given by p_z orbital of carbon of the ring. The percentages of metal d orbital and metal p orbital, respectively in HOMO and HOMO-1 orbitals, were negligible. The bonding of the Cp^* ligand to the s-block elements (groups 1,2) is generally considered to be mainly ionic, while complexes of the p-block elements should be predominantly covalent. The two lowest ionizations arise from the e_{1g} (HOMO) and e_{1u} (HOMO-1) orbitals in D_{5d} symmetry. These are the symmetric and antisymmetric combinations of the outermost orbital, e_{1u} (π), of the $(C_5Me_5)^-$ ring. It is interesting to observe the large reduction of C $2p_z$ ring population in the case of permethylated compounds, and the opposite trend for HOMO and HOMO-1 obtained for the Mg and Be compounds. This is brought about by the significant delocalization of these orbitals over the methyl groups. The reduction is however comparable for both HOMO and HOMO-1, and therefore expected to have a minor effect on their cross section ratio. The calculated HOMO and HOMO-1 cross sections, evaluated at the DFT level, are reported in Fig. 11.3, both for $MgCp^*_2$ and $BeCp^*_2$. They show the typical oscillations due to diffraction

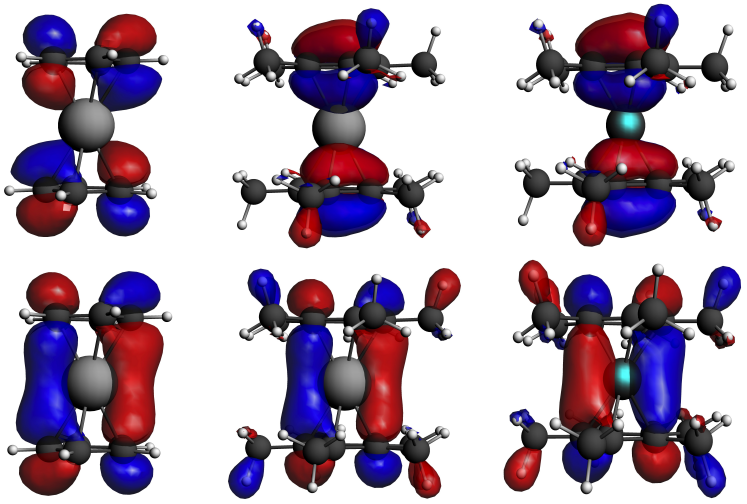

FIGURE 11.2: HOMO orbitals (upper panel) and HOMO-1 orbitals (lower panel) for $MgCp_2$, $MgCp_2^*$ and $BeCp_2^*$.

effects, analogous to those obtained in C_{60}, rather strong up to 200 eV, and then progressively damped. They are in antiphase for the two HOMO and HOMO-1 orbitals, characteristic of opposite parity combinations of the constituent atomic orbitals. It is also interesting to compare the HOMO orbital cross sections in all three compounds, which are shown in Fig. 11.4. One may observe a noticeable similarity between cross sections of $MgCp_2$ and $MgCp_2^*$, apart from a clear dephasing of the oscillations due to the slightly different period, and the surprising fact that the absolute cross section is appreciably larger in the permethylated compound. On the contrary the $BeCp_2^*$ profile is significantly different, more clearly in the lower energy range, an indication of differences in electronic structure due to the different metal atom. To test the sensitivity of the diffraction pattern to a change in the metal-ring distance, we have computed the diffraction pattern relative to the HOMO-1/HOMO cross section ratio by changing the distance by $\pm 5\%$. The results are shown in Fig. 11.5 , where it is seen the large change obtained in the profiles, which points out the high sensitivity of the approach to geometrical parameters. The most obvious change is in the positions of the maxima and minima, which reflect the shortening of the period with the increase of the distance between the rings, as expected from the well known inverse relationship between interference fringes and slit separation. For instance sets of 3 maxima appear at (93.4, 102.4, 112.6) and (150.2, 166.6, 187.6) eV, and corresponding minima at (68.8, 76.9, 85.0) and (120.7, 132.5, 146.8) eV, so that the distance between the minima are about (51, 56, 62) eV and between maxima (57, 64, 75) eV, a large difference which is easily appreciated. Moreover large changes are apparent also in

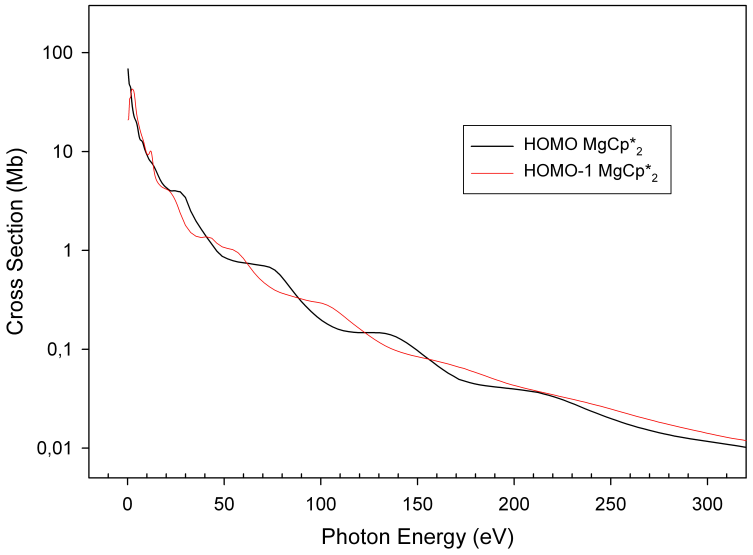

(a) $MgCp_2^*$

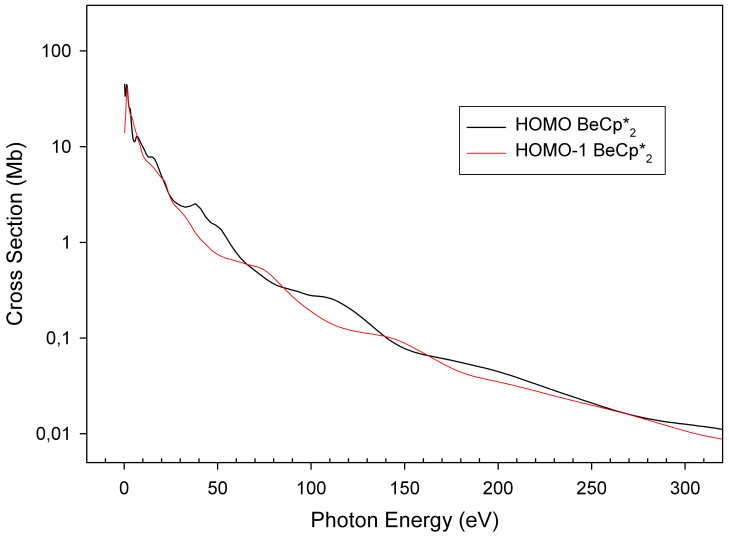

(b) $BeCp_2^*$

FIGURE 11.3: HOMO and HOMO-1 cross sections.

the shape of the profiles at lower energies: the height of the first shape resonance, and its shoulder, as well as an analogous change in the shape of the maxima around 50 eV. Also in this more complex system the sensitivity of the diffraction pattern to changes in geometrical parameters is quite high, and by careful least squares adjustment of the calculated spectra on the experimental one could provide an estimate of the relevant structural parameter, in this case the metal-ring distance, to better than 1%. This is already a quite interesting information. In fact, as it is seen in Tab. 11.1, two different determinations of metal-ring distances in $MgCp_2^*$

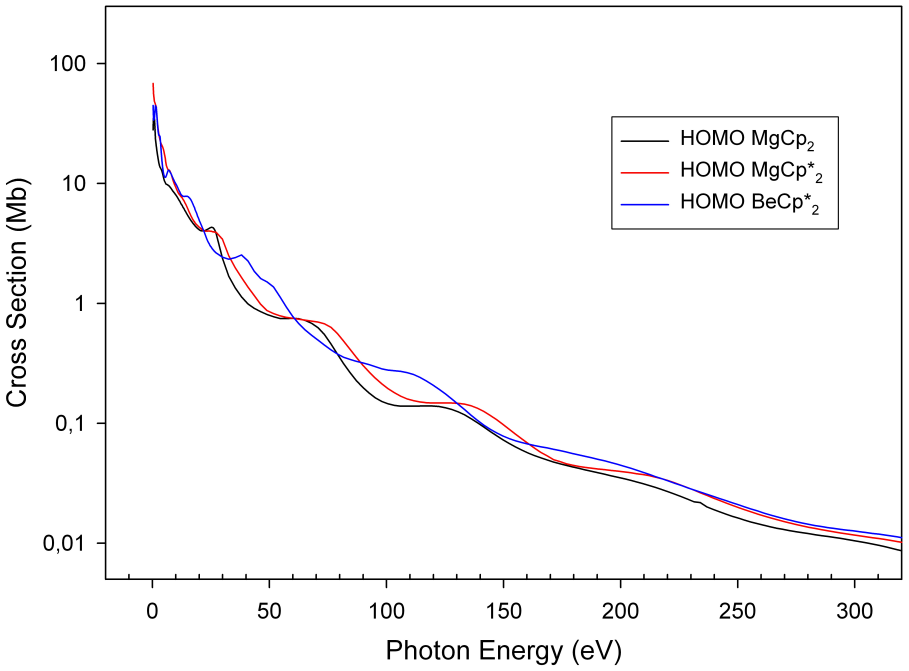

FIGURE 11.4: Cross sections of HOMO ionizations.

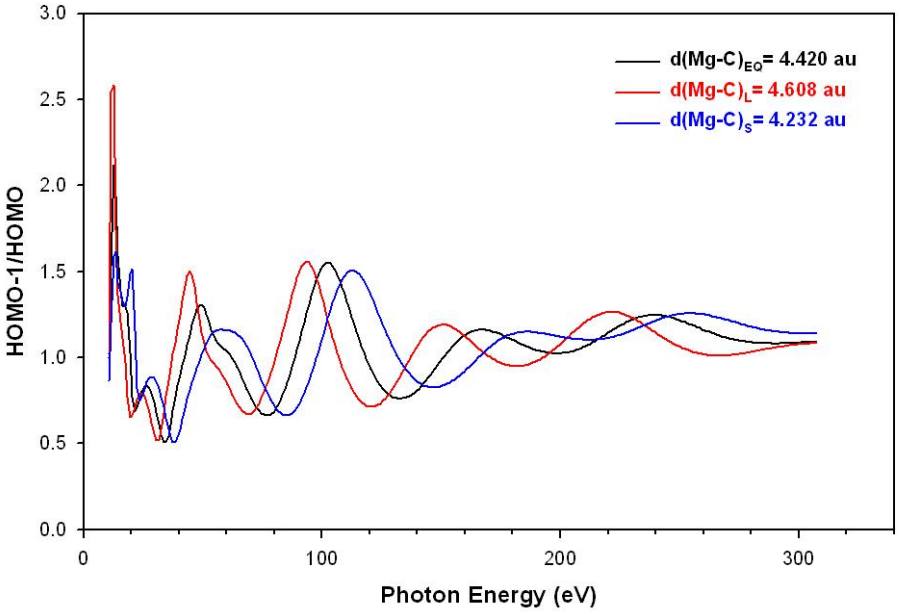

FIGURE 11.5: HOMO-1/HOMO cross section ratio for $MgCp_2$ at different Mg-ring distances.

vary quite significantly, by about 2%. In fact the DFT calculation agrees with the most recent one, that shows some shrinking of the metal-ring distance with permethylation, despite the possible increase in sterical hindrance brought about by the latter. So it is argued that a comparison of accurate experimental profiles should be able to distinguish easily between the two possibilities, and give an accurate value for those distances, and even more accurately for their difference. In the absence of sure data, we employed then the geometrical parameters afforded by DFT optimization, with the metal-ring distances collected in Tab. 11.3.

	Me-ring distance
$MgCp_2$	1.992
$MgCp_2^*$	1.952
$BeCp_2^*$	1.611

TABLE 11.3: Calculated values (Å) of metal-ring distance.

Finally, a comparison of the calculated HOMO-1/HOMO cross section ratios is reported in Fig. 11.6 for the couples $MgCp_2$, $MgCp_2^*$ and $BeCp_2^*$, $MgCp_2^*$. In the former case the most apparent feature is still a clear difference in the oscillation period, with the largest one associated with $MgCp_2^*$. This is basically a reflection of the shorter Mg-ring distance employed in the calculation. Other differences are the shapes and heights of the maxima, and the apparent drift to higher values of the ratio at higher energy in $MgCp_2^*$. While this underlines once more the high sensitivity of the profile to the Mg-ring distance, it is difficult to ascertain the influence of further electronic differences due to permethylation. That might be revealed by investigating different orbital ionization ratios, despite the difficulties associated with the congestion of the photoelectron spectrum at higher ionization energies. On the other hand, the change in the profiles between $MgCp_2^*$ and $BeCp_2^*$ is dramatic, as expected, because of the large change in the metal-ring distance. In addition the average ratio in the Be compound is significantly lower than in the Mg one, which is seen in the height of the maxima, and especially in the much lower value of the profile at high energy, which averages around 0.8, compared with the value above 1.2 in the Mg compound. This is a typical signature of electronic effects. For a pure $\pi_1 \pm \pi_2$ combination of two π ring orbitals, one would expect the ratio to oscillate at high energy around a value of 1, this is indeed very well observed, as well as computed, for the $1\sigma_u/1\sigma_g$ ratio in diatomics [134, 135, 146].

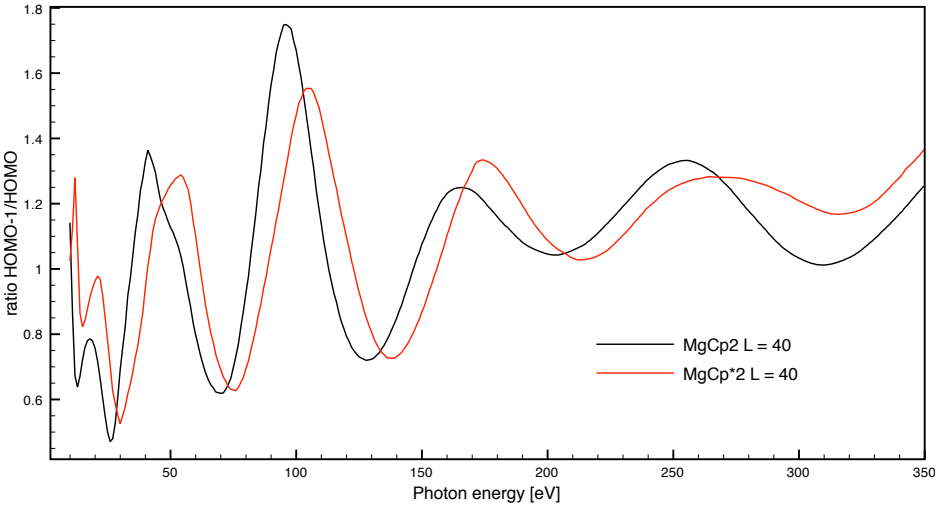

(a) $MgCp_2$ and $MgCp_2^*$

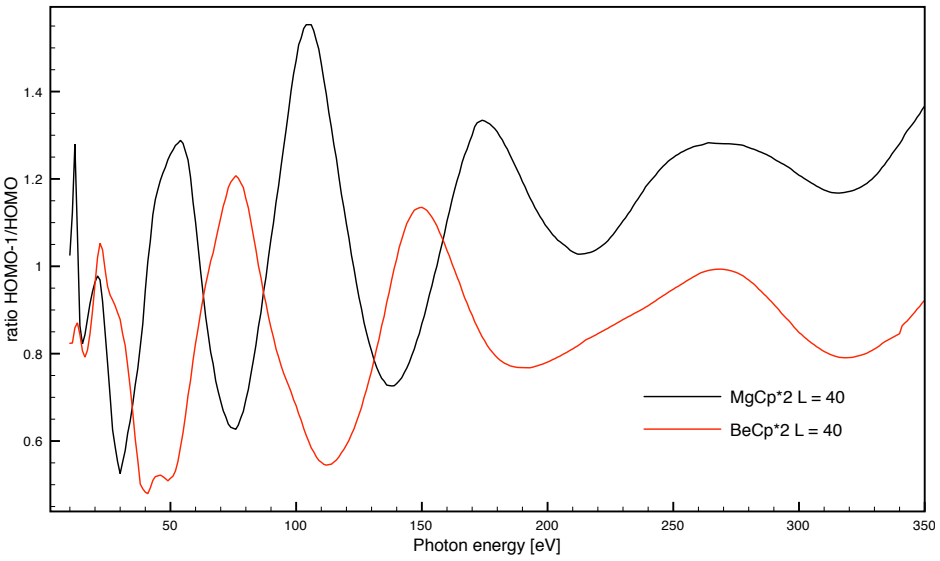

(b) $BeCp_2^*$ and $MgCp_2^*$

FIGURE 11.6: HOMO-1/HOMO cross section ratio.

So this large deviation points out to a different amount of delocalization of the two HOMO and HOMO-1 orbitals in the two compounds, as actually suggested by the simple Mulliken population analysis reported in Tab. 11.2, which shows different behaviour in the two compounds. Again it is seen that even rather modest changes give rise to pretty large differences in the cross section ratios, another interesting piece of information available from this observable. A further source of deviation in the ratios predicted at the one particle level is the presence of different many-body effects in the orbitals involved, as already observed both in the core [150] and inner valence [146] ionizations.

11.4 Conclusions

In conclusion, the long range oscillations in the molecular photoemission cross sections are a general phenomenon, which can give important information about geometric and electronic structure of the target. Convergent results at the DFT level can be easily obtained also for rather complex molecules. A computational experiment changing the Mg-ring distance in $MgCp_2$ shows the high sensitivity of the cross section ratio profile considered to the geometrical parameter, and is expected to allow its determination to better than 1% by comparison with the experiment. The results obtained for the case of $MgCp_2$ are compared to the analogous results for the two methyl-subtituted cyclopentadienyl compounds, $MgCp_2^*$ and $BeCp_2^*$. The main effect is again due to the geometrical change, and an experimental determination should allow to resolve the discrepancy in the literature concerning the relative Mg-ring distance in the the normal and permethylated compound. Subtler effects due to small differences in electronic structure are also imprinted in the profiles, notably in the low energy shapes, relative height of the maxima, and especially high energy average value. This is particularly shown in the large effect on the asymptotic ratios in $MgCp_2^*$ and $BeCp_2^*$, attributed to an opposite, but rather minor, change in the delocalization of HOMO and HOMO-1 orbitals over the methyl groups in the two compounds.

Chapter 12

Interchannel coupling and confinement resonance effects in the inner Ar 2p subshell of $Ar@C_{60}$

12.1 Introduction

Starting from its discovery in 1985, many photoionization studies have been focused on fullerene (C_{60}) [171–173]. The interest in this molecule is mainly due to its particular and extremely stable structure. Among fullerenes' derivatives, the endohedral compounds $M@C_{60}$ constitute a special class [174] and over the past decade or so they have been the subject of a large number of studies. These compounds are characterized by the presence of a dopant agent (M) embedded in the C_{60} cage, where M can be an atom or a small molecule. When an atom is encapsulated inside a hollow spherical carbon buckyball, the complex is called an *endofullerene*. Theoretically, if the atom is an unreactive noble gas like xenon, it should be centered within the cage. This particular conformation allows one to probe the variations of the properties both of the dopant and the cage. Indeed, they represent an exceptionally clean and stable "laboratory" to study the effects of confinement upon the properties on the encapsulated atom and to understand how the confinement alters the static and dynamic properties of the atom. There exist many possible applications of endohedral atoms, such as quantum computing [175], drug delivery [176], photovoltaics [177] and hydrogen storage [178].

Of the many extant photoionization studies, the overwhelming majority are

theoretical, due to the difficulties in the fabrication of endohedral systems in large enough quantities to investigate experimentally, although some experimental photoionization work has been reported. The first system of this type to be discovered was La@C_{60} [174] and after its detection many experiments to encapsulate many other atoms inside C_{60} have been done [179–184]. Among these atoms, noble gas has been considered. Recently, experimental photoabsorption of the Xe@C_{60} [185] showed the existence of an oscillatory behaviour in the total cross-section, known as confinement oscillations or confinement resonances (CR), which is related to the superposition or interference of the electron wavepacket scattered by the spherical shell of the C_{60} cage. From the theoretical perspective, confinement oscillations were predicted by using simplified spherical potential models, such as the jellium potential. Endohedral systems were then approximated by an atom surrounded by a spherically symmetric potential [186–189]. The few studies considering the full molecular potential have been at the DFT (central field) [36, 190, 191] or static-exchange (Hartree-Fock) level [192]. Thus, there are no reports of calculations which include both molecular structure and correlation; such calculations are, however, important to provide some notion of the qualitative and quantitative accuracy of the previous calculations. This is needed owing to the relative scarcity of experimental results. We have performed calculations of photoionization of Ar@C_{60}, which has been the subject of a number of earlier studied [192–195], including both the molecular structure of the target and correlation. The correlation is included through the use of TDDFT [129]. Within this study, we have focused on two questions: the first one is how confinement resonances are affected by the inclusion and interaction of both the molecular structure and correlation; the second one is how the inclusion of the C 1s channels of C_{60}, and the interchannel coupling with these channels, affects the inner-shell atomic photoionization channels. We consider the Ar 2p cross section to explore these questions. Ar 2p was chosen because it is an inner shell (no hybridization and negligible interaction with the confining shell) so that we could focus on the effects of the confining environment and correlation on the final state continuum wave function which results in the changes to the cross section.

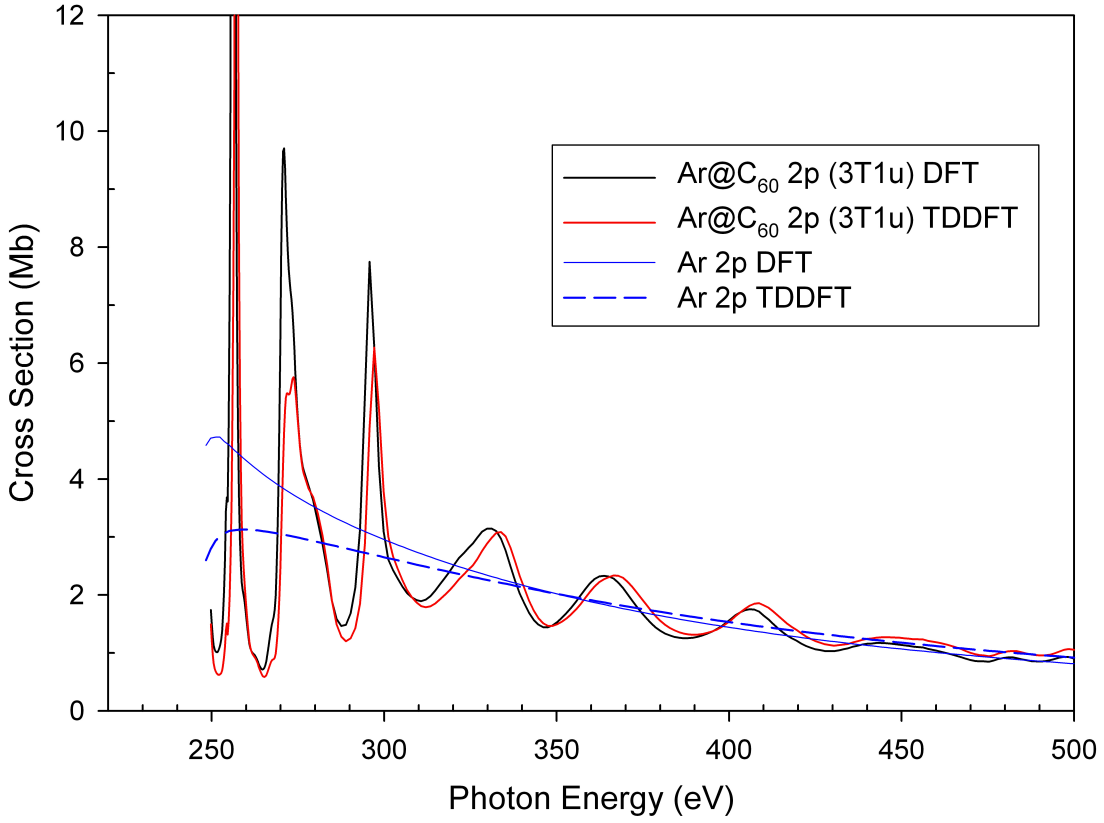

FIGURE 12.1

12.2 Results and discussion

The results of our calculations for the 2p subshell of free Ar and confined Ar@C_{60} are given in Fig. 12.1; in the confined case, in molecular notation, Ar 2p becomes the 3T1u state of the combined Ar@C_{60} system. Let us start to examine first the free case. For this case, the DFT cross section exhibits a small rise from threshold resulting from the shape resonance in the d-wave continuum of the 2p$\rightarrow \epsilon$d transition. Including correlation with the TDDFT result, the shape resonance is still there, although somewhat altered in shape from DFT, and a significant difference in magnitude is seen at threshold, a difference which decreases with increasing energy, eventually disappearing completely. This difference arises from both initial state correlation (configuration interaction with double excitations), and final state correlation (in the form of interchannel coupling among photoionization channels). It is of importance to point out that the present TDDFT results are in excellent agreement with experiment and previous sophisticated calculations [196]. This agreement is of importance because it shows that the present TDDFT calculation

includes all the important atomic effects for this particular case. It is also to be noted that the cross sections, except for the near-threshold shape resonance, are quite smooth as a function of energy.

Examining now the confined case, a rather different picture emerges. The atomic cross section is very substantially modulated; these confinement resonances have been seen experimentally for the case of $4d$ photoionization in the Xe@C_{60} endohedral fullerene [185]. Basically these are caused by interference between the photoelectron wave emerging directly with waves that are scattered from the inner and outer walls of the confining C_{60} shell. It is important to note that these confinement resonances are almost exactly the same in DFT and TDDFT calculations, thereby confirming that confinement geometry is the dominant determinant of this phenomenon; correlation, although it is seen to have some effect, does not play a large role in their behaviour.

Note also that the three lowest resonances closest to threshold are quite sharp, but the higher energy resonances are much smoother. The sharpness of the resonances near threshold is evidently due to the more granular nature of the confinement potential when the molecular structure is considered; the slower photoelectrons have more time to "experience" the different confinement potential. This is rather different than the predictions of a spherical jellium model of the confining potential which predicts all confinement resonances to be rather smooth [197]. However, it does agree with a previous study at the Hartree-Fock level which als predicted sharp near-threshold confinement resonances [192]. The confinement resonances are also stronger than those predicted by a spherical jellium model of the confining potential; even 150 eV above threshold, the amplitude is about 10 % of the cross section. The amplitude of the confinement resonances diminish much more rapidlyn with energy in a jellium model. This difference too is evidently the effect of using the full molecular, as opposed to jellium, confining potential in the calculations.

The sharpness of the lower-energy confinement resonances would probably not be seen in a room temperature experiment owing to the vibrations which would move some of the confined atoms off-center, thereby smearing out the confinement resonances. Such a mechanism was suggested earlier as an explanation as to why confinement resonances had not been seen; they have since been observed [185]. This suggests that, to compare with experiment, a broadening factor would have to be applied to account for this vibrational excitation. This also suggests that experiment work on cold target systems would change the observed shape of the

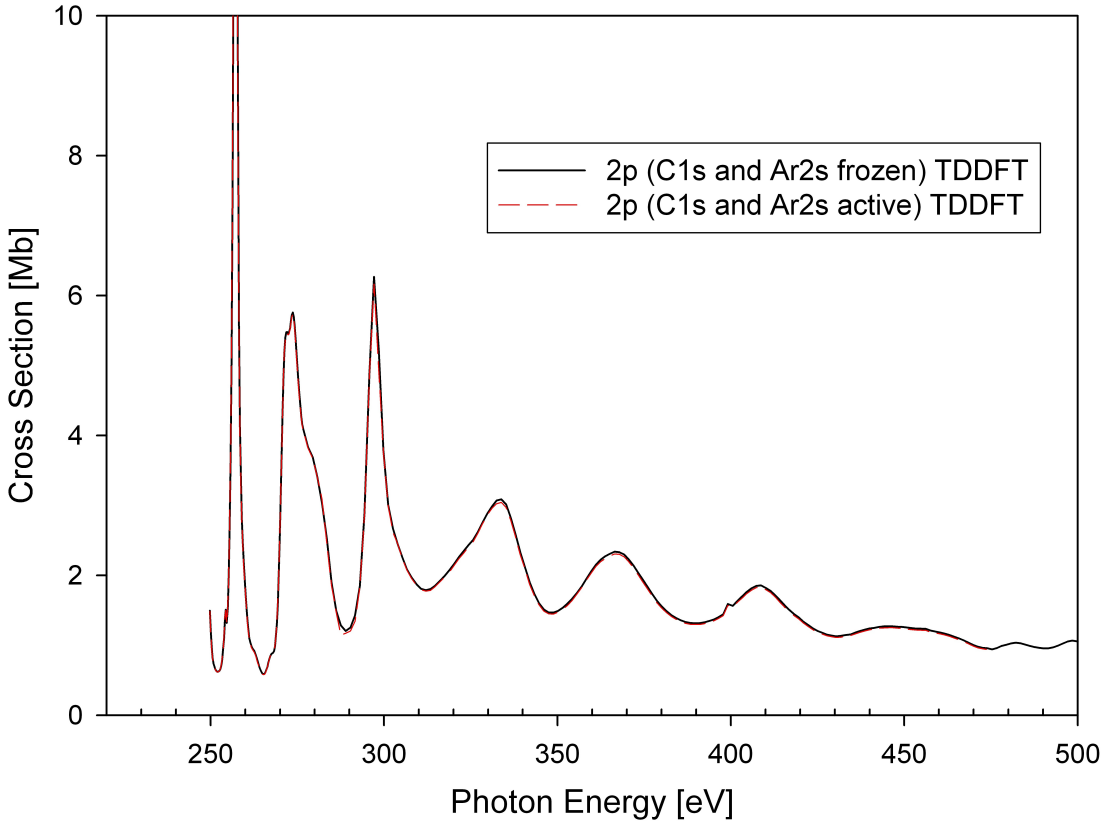

FIGURE 12.2

low-energy near-threshold confinement resonances.

Now, in the results presented in Fig. 12.1, the Ar 2p photoionization channels for the confined system were not coupled the C 1s photoionization channels arising for the C_{60} cage. This could be of some importance since the C 1s threshold is at about 300 eV, so that above 300 eV the Ar 2p and C 1s photoionization channels are both open; furthermore, the threshold C_{60} 1s photoionization cross section is about 60 Mb, which is estimated as 60 times the threshold cross section of the free carbon atom, ant this is an order of magnitude larger than the Ar 2p cross section at that energy, as seen in Fig. 12.1. Thus, with a small mixing of the C_{60} 1s cross section, the Ar 2p cross section could be considerably altered. To explore this possibility, the calculation for the confined system has been redone at the TDDFT to include interchannel coupling with C 1s; the Ar 2p photoionization cross sections are shown in Fig. 12.2, with and without interchannel coupling between Ar 2p and C 1s. The outstanding feature of this comparison is that the curves are almost exactly the same; thus, despite the C 1s cross section being about a factor of ten larger than the Ar 2p cross section around 300 eV, the interchannel coupling is negligible.

To understand this result, it is important to note that two conditions must be fulfilled for interchannel coupling to alter a cross section of a particular photoionization channel. First, the cross section for that channel must be degenerate with a channel with a significantly larger cross section. And second, there must be a non-negligible interchannel coupling matrix element connection the two channels. The first condition is clearly satisfied for Ar 2p with C_{60} 1s, as discussed above. Thus, given the results depicted in Fig. 12.2, it must be the case that the interchannel coupling matrix elements are extremely small. The direct part of the matrix element for this case, the Coulomb interaction between the $2p^5\varepsilon l 1s^{60}$ final state and the $2p^6 1s^{59}\varepsilon' l'$ final state (2p is Ar 2p and 1s is C_{60} 1s), can be written as $\langle 2p\varepsilon l|\frac{1}{r_{12}}|1s\varepsilon' l'\rangle$, and is included in the calculation. This coupling matrix element is, however, negligible because the overlap of the discrete Ar 2p and C 1s wave functions is extremely small because these two wave functions are quite compact ($\sim$0.2 atomic units in radius) and centered about 6 a.u. apart. The exchange part of the interchannel coupling matrix element, $\langle 2p\varepsilon l|\frac{1}{r_{12}}|\varepsilon' l' 1s\rangle$, is treated only approximately in LDA using a local-V_{XC} approximation. This matrix element too is quite small in the present case. Each of the bound orbitals in the exchange matrix element overlaps with the continuum orbital of the other channel. Even at the C 1s threshold, where the exchange matrix element should maximize, while the $\varepsilon' l'$ continuum orbital (arising from C 1s ionization) is slowly varying, the εl orbital, arising from Ar 2p ionization moderately energetic and oscillates rather rapidly. Thus, while the 2p overlaps somewhat with the threshold $\varepsilon' l'$ function, the overlap of the 1s with the εl orbital is negligible, owing to the oscillation in the latter. And this matrix element clearly decreases rapidly with increasing energy a because the continuum wave functions oscillate more rapidly in space as the energy increases so that the overlap with the bound wave function decreases.

This suggests that it might be possible for interchannel coupling to be important if the confined atom or molecule has an inner subshell whose ionization energy was very close to the C 1s ionization energy, in which case, interchannel coupling in the threshold region could be significant, owing to the exchange part of the interchannel coupling matrix element. A molecule containing a carbon atom is a good candidate for this since the 1s electrons of the carbon in the confined molecule will have a threshold energy very close to the 1s carbon atoms of the C_{60} shell.

12.3 Conclusions

The first calculation of the photoionization of an atom confined in a fullerene cage taking into account both correlation and molecular structure has been performed. The Ar@C_{60} system was investigated and the near-threshold confinement resonances were found to be quite sharp, unlike the findings of calculation using spherical jellium models of the confining potential. In addition, as a result of the inclusion of molecular structure, the confinement resonances were found to extend to much higher energy as compared to jellium calculation. It was also seen that interchannel coupling of the small Ar 2p photoionozation cross section with the (degenerate) much more intense C_{60} 1s channels was not found, and the finding explained. As a result of the understanding of why interchannel coupling was negligible in this case, it was also suggested under what conditions interchannel coupling between the C_{60} 1s and the photoionization channels of a confined atom or molecule might be found.

As mentioned in the introduction, this work is the first step of a larger project. We will next look at the photoionization of all of the subshells of the encapsulated Ar atom with an eye to understanding where the simpler jellium results are correct and where they need correction. Based upon that investigation, other systems will be scrutinized.

Finally, by producing cross section of significant accuracy, it is our hope that these and future results will stimulate laboratory investigation of the photoionization of endohedral fullerenes. And with the increasing capabilities of fabricating significant quantities of samples, we urge that photoelectrons spectroscopic studies be performed to separate the cross section by subshell and test theory stringently.

Chapter 13

Dynamical photoionization observables of the CS molecule

A second line of research during my PhD has followed the correlated description of photoionization observables through a new method based on *ab initio* close coupling formalism, as explained in detail in Chapter 5. As first application of this method, we have performed highly correlated calculations on the primary ionic states and the prominent satellite present in the outer valence photoelectron spectrum of CS. Dyson orbitals are coupled to accurate one-particle continuum orbitals to provide a correlated description of energy-dependent cross sections, asymmetry parameters, branching ratios and Molecular Frame Photoelectron Angular Distributions.

13.1 Introduction

The presence of additional bands, satellite or non-KT bands, has attracted great interest, both experimentally and theoretically, since the early years of photoelectron spectroscopy, as they provide a most clear manifestation of electron correlation, being associated with multielectron excitations, forbidden in a one electron picture [198–200]. Very recently, satellite states have been considered also in double core hole states [201, 202]. A major source of satellite lines in the valence shell is constituted by strong correlation between primary (1h) and (2h-1p) configurations in the final ionic states. This effect becomes often very strong in the inner valence shell, so that a single main ionization is no more clearly discernible, as the

intensity is distributed among a multitude of closely spaced lines, a phenomenon appropriately termed breakdown of the one particle picture [5]. On the contrary, both experiments and accurate calculations of dynamical parameters, such as cross sections and angular distributions of satellite lines, for molecules are rather scarce, as they are quite demanding. From the theoretical side, both a sophisticated treatments of correlation effects and accurate continuum calculations have to be linked in a full calculation [203, 204]. From the experimental side, one major problem is a clear identification of a simple satellite line, describing an individual electronic final state [160]. In fact, satellite lines tend to be quite weak, often crammed together, and vibrationally very broad, because of the generally repulsive nature of the associated potential energy surface. A number of recent investigations is reported in Refs. [205, 206], where the interpretation of the mechanism leading to some satellites is still uncertain.

A rather exceptional situation is met in the CS molecule, where an isolated satellite, with a fully developed vibrational structure, is already present in the valence shell, as the third ionic state. This is due to the strong FISCI correlation, illustrated in Chapter 2, which manifests also in the so called breakdown of KT (inversion of the KT ordering of ionic states) which is present in CS. The satellite correlates with the much studied C ionic state in CO and N_2, which is however much weaker, and lying at higher energy. The satellite was observed in the early times of photoelectron spectroscopy [199, 200], and it has been studied and well understood at the bound state level [207, 208]. A recent calculation has offered an accurate characterization of its spectroscopic parameters, in good agreement with experimental values. On the experimental side, the difficulty lies in the production of the unstable CS molecule, and in the separation of the overlapping spectrum due to the accompanying CS_2 species, which have been however successfully overcome [199, 209]. No information is available on the other hand on the dynamical behaviour of the satellite or even of the primary ionic states, and on the influence of the strong correlation effects on the latter. A hint of such effects is however the anomalous intensity of the satellite in the low energy PES spectrum (21.22 eV). In fact, at a first approximation, intensity ratios between a satellite and the primary peak from which it borrows intensity via configuration mixing is given by the ratio of the corresponding spectral strengths (or pole strengths) R_{Ik} [5, 160], which will be examined in more detail below, but which suggest a satellite/primary 6σ ratio around 0.3-0.5, while judging from the spectrum in Ref. [199] it appears larger than 1, even taking into account the diminishing transmission of the analyzer.

With the procedure illustrated in Chapter 5, we have evaluated absolute cross sections, branching ratios, asymmetry parameters, and a set of molecular frame photoelectron angular distributions (MFPADs) over an extended energy range, for both the primary and satellite final states. It has to be noted, though, that IC effects, neglected in the present study, have been found important in the inner valence shell of C_2H_2 and CO close to threshold [203, 204] and could be of relevance for CS as well. At this level of theory, all correlation effects present in the bound states (ISCI and FISCI) are completely described by the single Dyson orbital, which is used in the present implementation for the calculation of correlated dipole matrix elements. Spectral strengths $R_{Ik} = |\chi_{Ik}|^2$ are often employed to estimate the intensity ratio $I_J/I_K = R_{Jk}/R_{Kk}$ between a satellite and the corresponding primary state, in the so called sudden limit, neglecting dynamical effects. Correlated calculations for the initial and final bound states are computed at the CASSCF level, which is also employed for the calculation of the relative Dyson orbitals. Ionization energies have been further corrected for the residual dynamical correlation contribution by employing the NEVPT2 multireference perturbation theory [80, 81], at the Partially contracted (PC(2)) level. Finally all photoionization parameters are computed in terms of dipole matrix elements and K-matrix by well known expressions [66, 210].

13.2 Computational details

Calculations on CS have been performed at the equilibrium geometry, $r_{\rm eq} = 1.545$ Å. Hartree-Fock, CASSCF and NEVPT2 results have been obtained with MOLPRO [130], and special modules developed in collaboration with the theoretical group of Ferrara University. The calculation of the Dyson orbital has been performed with a code set up in our laboratories, carrying out the direct evaluation of the overlap between the CASSCF wavefunctions separately optimized for the ion and for the neutral molecule. The basis set employed is aug-cc-pVTZ. Two CASSCF calculations have been performed, to check convergence level, correlating the 10 valence electrons: 5-7 σ, 1π, and including either (2σ,1π) or (3σ,2π) virtual orbitals, CAS-10/9 and CAS-10/12 calculations, i.e. 5 occupied orbitals, 4 virtual orbitals and 5 occupied orbitals and 7 virtual orbitals respectively. Ground state DFT calculations have been performed with the ADF code [166], employing the DZP STO basis in the ADF database. With this density both occupied

and continuum orbitals are calculated in a basis of products of radial B-splines times spherical harmonics, $B_i(r)Y_{lm}(\theta,\varphi)$. A large one center basis, with maximal expansion up to $L_{max} = 30$, with a range $R_{max} = 25$ a.u., and stepsize h = 0.2 is supplemented by expansions around the C and S atom, with $L_{max} = 2$, $R_{max} = 0.6$ (C) and $R_{max} = 0.3$ (S) . This basis affords a very accurate solution of both the discrete and continuum DFT orbitals. Actually, for ease of evaluating one particle dipole matrix elements, bound state orbitals obtained from ab-initio calculations have been expanded in the B-spline basis by projection, giving a very accurate representation. All DFT calculations have employed the LB94 exchange-correlation potential [165], which has proven to be well suited for the calculation of photoionization observables [211].

13.3 Results and discussion

We shall first discuss the bound state results, i.e. IP's and R_{Ik}'s, which are reported in Tab. 13.1.

	EXP[a]	**KT**	**CASSCF**		**PC(2)**	**ADC(3)**[b]	
ion state	IP	IP	IP	R	IP	IP	R
7 σ	11.33	12.83	10.21	0.85	11.05	11.51	0.85
2 π	12.79	12.55	12.18	0.82	12.72	12.74	0.90
satellite σ	16.05	-	15.13	0.26	15.80	15.54	0.18
6 σ	18.00	18.87	17.43	0.53	17.83	18.02	0.69

TABLE 13.1: CS. IP's values [eV], R is the pole strength; *a*: Ref.[199]; *b*: Ref.[71]

As it can be seen, at the KT level the lowest IP is calculated to be the 2π one, while in the experiment it is more bound than the HOMO 7σ by about 1.5 eV, a rather large error. The correct sequence is recovered at the CASSCF level, although now the IP's are computed too low by about 1 eV, because of the GS dynamical correlation lost upon ionization, which is only partly described by CASSCF. NEVPT2 results, on the other hand, are vastly improved, showing excellent energy separations among the different states, while the absolute values are slightly too low, by about 0.2 eV. Results of comparable quality were obtained by the highly correlated

ADC(3) approach [71]. It is hardly sensible to compare with vertical experimental IP's with accuracy of better than 0.1 eV, however, because vibrational broadening is generally much larger than that. More accurate comparison requires taking into account also vibrational levels. This has been considered in Ref.[212], employing CASSCF + MRCI, with excellent agreement of electronic and vibrational energies with experimental data.

The second interesting comparison concerns spectral strengths R_{Ik}. Here a rather large disagreement may be observed between CASSCF and ADC(3) results for the values relative to the satellite and the inner valence 6σ ionization. This is particularly evident in their ratio, $\frac{R_{sat}}{R_{6\sigma}}$, which is computed to be 0.49 and 0.26 at CASSCF and ADC(3) level, respectively, while a value of 0.52 is obtained from the MRCI of Ref.[212]. This underlines the difficulty of obtaining accurate values of the spectral strengths, despite intensive theoretical work. Unfortunately, these are not easily accessible experimentally, although they can be obtained by very careful high energy electron momentum spectroscopy [73, 213]. Also recent work on branching ratios in photoelectron spectra, coupled to accurate single particle continuum calculations, has shown the possibility to obtain reliable values for such quantities [146].

Let us discuss now cross sections and angular distributions for all states considered. Results for the theoretical cross sections relative to the four ionic states considered are reported in Fig. 13.1.

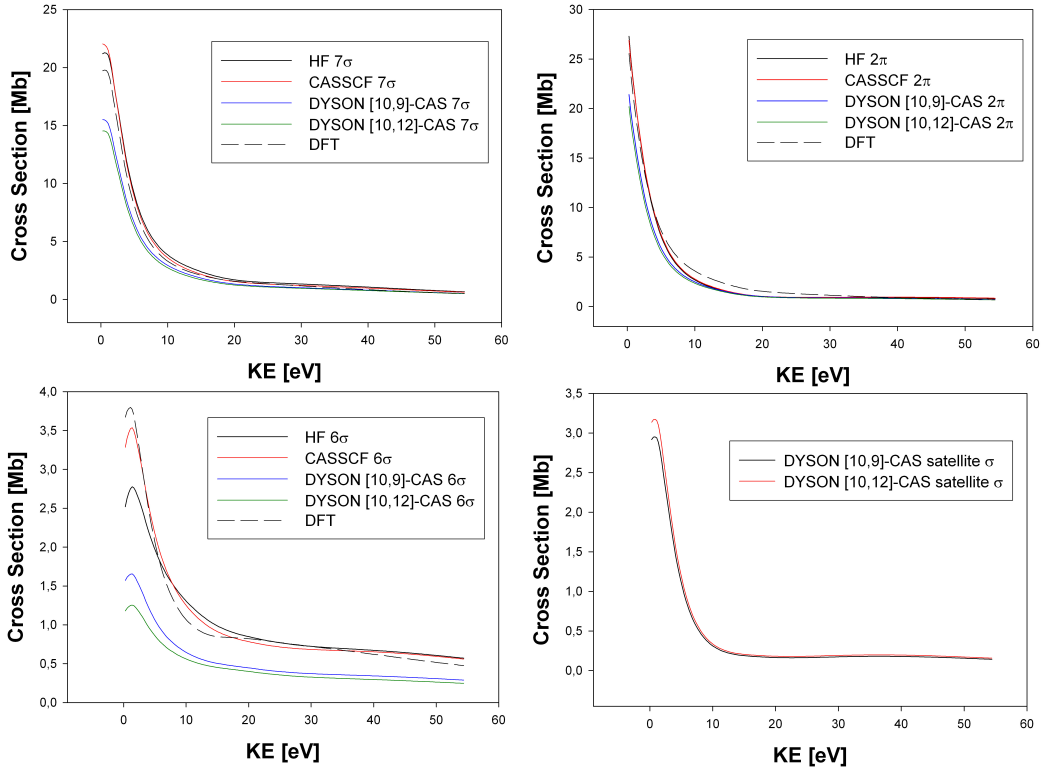

FIGURE 13.1: CS. Theoretical cross sections relative to the four ionic states considered

Five results are reported: HF, CASSCF, DFT, DYSON from CAS 10/9 and from CAS 10/12. Actually, preliminary investigations showed the importance of employing a large basis set, and in particular of augmented diffuse functions, to reach convergence even at the HF level. This is basically due to the fact that basis sets are generally optimized with respect to total energy, which heavily weighs the short range region, where potential is largest. On the contrary, in the length gauge employed in the present work, dipole matrix elements, and therefore photoionization observables, are more sensitive to the long range tails of the molecular orbitals. For the outer ionizations 7σ and 2π, all results are quite similar, although Dyson results are significantly lower, basically because of the reduced spectral strength. The results are more different for the inner ionization 6σ, where correlation effects are larger. Here the Dyson orbital results are much lower, again due to spectral strength reduction, and also the difference between CAS 10/9 and CAS 10/12 results is significant, indicating that full convergence may have not been obtained. There is also a large difference between HF and CASSCF results close to threshold, with the DFT one closer to CASSCF, although it gives a small modulation at intermediate energies, absent in the ab-initio results. Only Dyson results are obviously available for the satellite, and somewhat unexpectedly excellent agreement

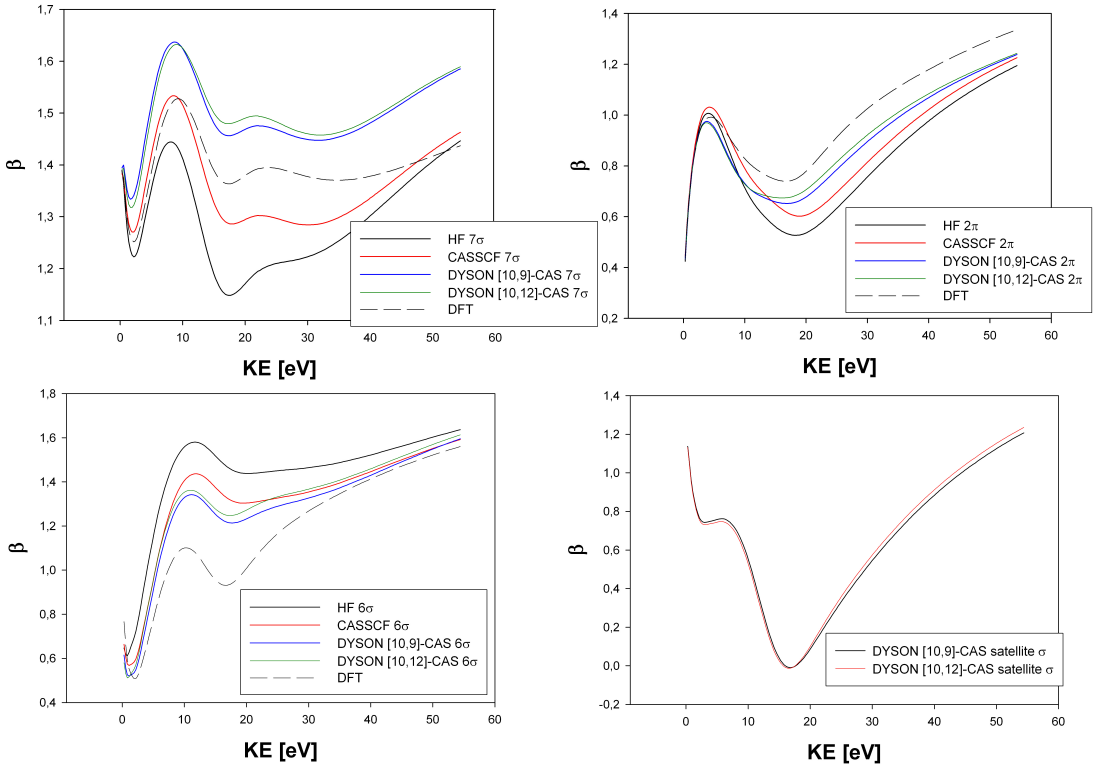

FIGURE 13.2: CS. Theoretical asymmetry parameters relative to the four ionic states considered

between CAS-10/9 and CAS-10/12 results is obtained, so that it appears easier to converge the satellite wavefunction than the one relative to the primary hole. The asymmetry parameters β are reported in Fig. 13.2. They appear much more sensitive to the different approximations, showing much larger variations in all primary ionizations, especially in the intermediate valence region. For instance, at around 20 eV electron kinetic energy (KE), the excursion is about 0.3 β units for 7σ, 0.2 for 2π, over 0.5 for 6σ. In the case of the HOMO ionization 7σ, HF results show the maximum deviation from Dyson ones, while DFT is closest to the latter up to about 40 eV electron KE, while it shows a different and flatter behaviour beyond that. In 2π and 6σ ionizations, DFT results are instead on the opposite side than HF with respect to Dyson, and the deviation is largest for 6σ. In general, the two Dyson results are quite close to each other for all states considered and in particular, again, for the satellite. Noteworthy is the rather different pattern of the β profiles for all ionizations, which appears quite informative for discrimination, and in particular the one associated with the satellite, with a large dip at around 15 eV KE, which does not resemble either that of 7σ or 6σ, showing that

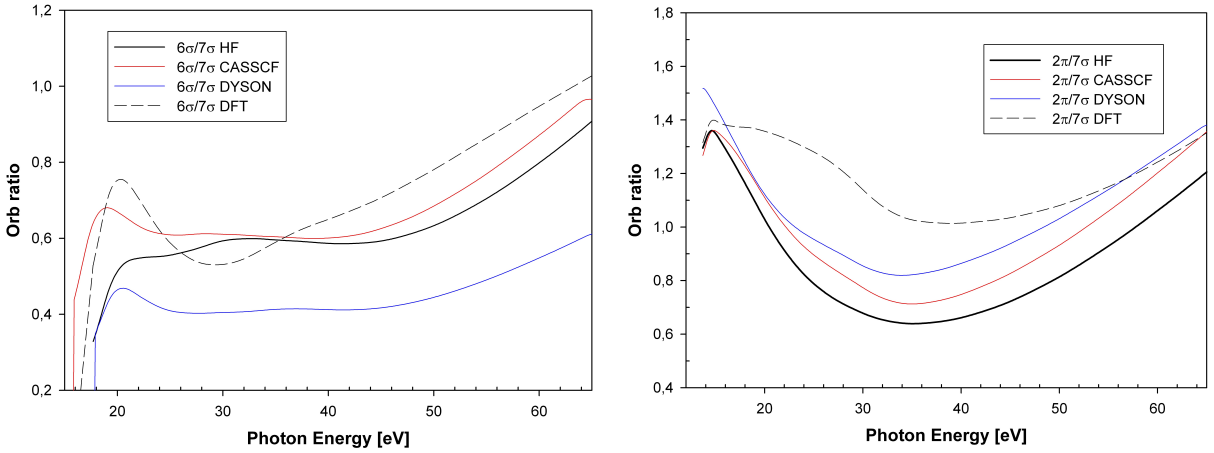

(a) $6\sigma/7\sigma$ ratio (b) $2\pi/7\sigma$ ratio

FIGURE 13.3: CS. Cross section ratios

the assumption of satellite states simply borrowing intensity from a corresponding primary peak is untenable in this case, as will be further illustrated in the following. Also the entity of the β variations between the different approaches is such that careful experimental measurement should be able to easily discriminate among them [214].

While the cross section profiles appear relatively smooth, there are rather large variations among them that can be magnified by taking individual cross section ratios. This is also an observable much more easily accessible experimentally, since accurate absolute cross sections are notoriously difficult to measure. The cross section ratios taken with respect to HOMO 7σ are reported in Fig. 13.3. One can see much larger differences between the various treatment than is apparent in Fig. 13.1, even for the $\frac{2\pi}{7\sigma}$ ratio, where the deviation of the DFT results from the ab-initio ones appears quite large in the intermediate energy range, between 20 and 50 eV photon energy.

The ratio of the satellite to both 7σ and 6σ cross sections is also reported in Fig. 13.4, both in a low energy range and to higher energy, and compared with the $\frac{6\sigma}{7\sigma}$ ratio, at the CAS-10/12 Dyson orbital level. At low energy it is seen that neither ratio approaches a constant, showing again the inadequacy of the simple borrowing mechanism, although a flatter behaviour in the satellite/6σ ratio appears at the highest energy considered, around 60 eV photon energy. Notably, the ratio is maximal close to threshold with respect to both primary ionizations, and declines fast afterwards, reaching a minimum around 28 eV photon energy, and a slow increase afterwards, a rather distinct signature. This cross section effect

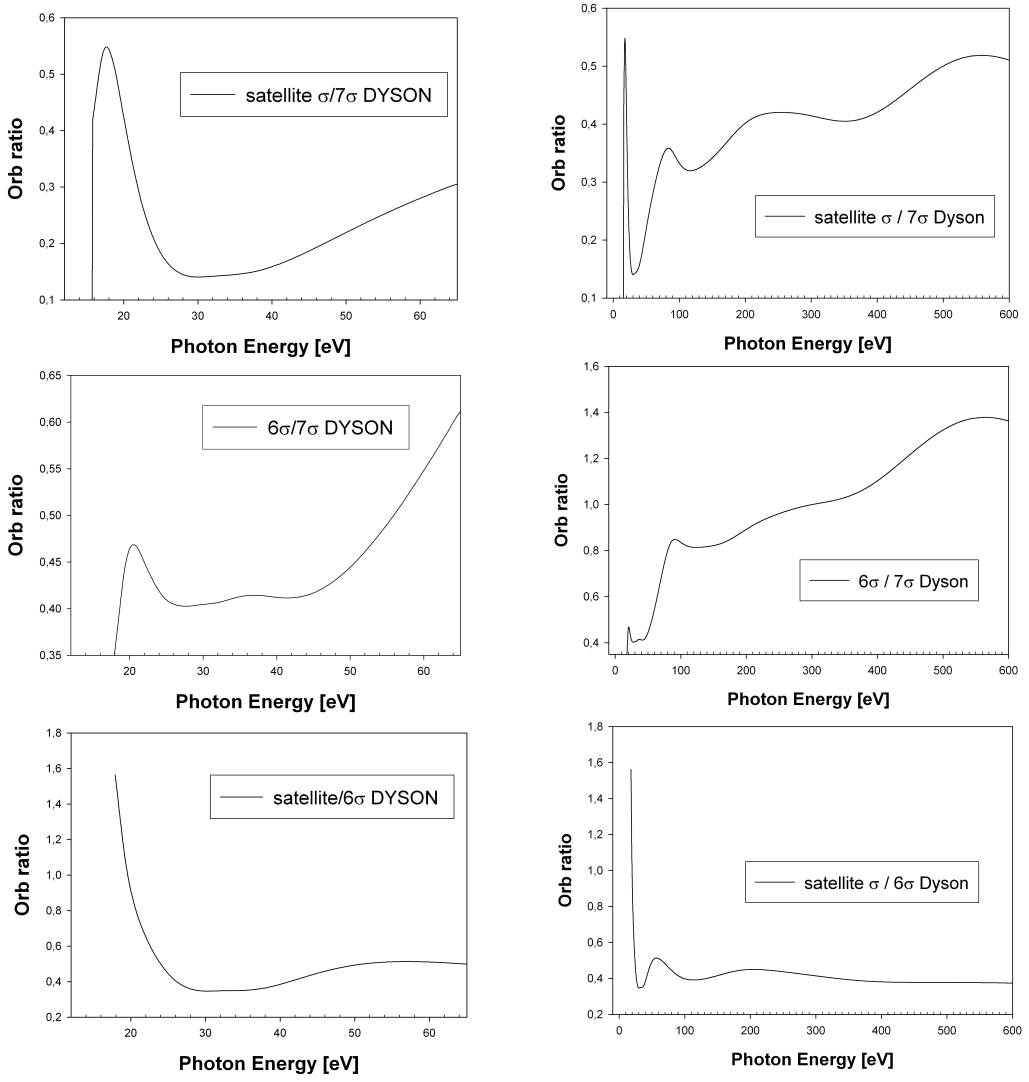

(a) (b)

FIGURE 13.4: CS. Cross section ratios (Dyson orbitals): in the a) panel, the cross-section ratios in a low energy range; in the b) panel, the same cross-section ratios in an energy range up to 600 eV

reproduces quite accurately the anomalous high intensity observed in the 21.22 eV original spectrum, where the intensity is much higher than expected on the basis of its spectral strenght, and seems to support also the higher spectral strenght obtained in the CASSCF (or MRCI [212]) approach. Note, however, that different intensity ratios may be appreciated in the spectrum reported in Ref.[209]. The high energy behaviour of the ratios shows the satellite/6σ ratio slowly approaching a constant limit, around 0.4, which is close to the ratio of the spectral strengths which is 0.39 ($R_{sat,6\sigma} = 0.207$, $R_{6\sigma,6\sigma} = 0.529$), illustrating the limit of validity of the sudden approximation. The limit is reached at rather high energy, around

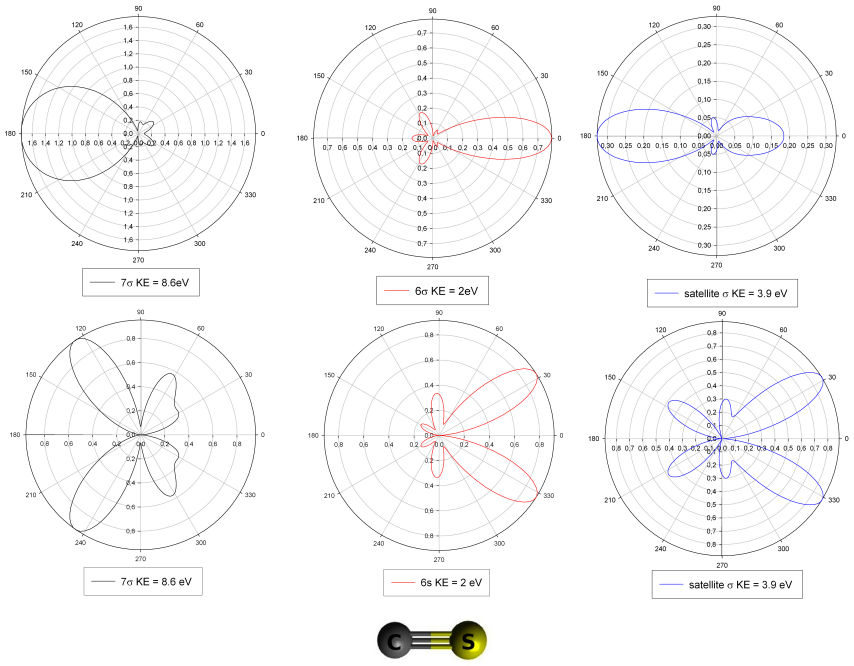

FIGURE 13.5: CS. MFPADs calculated from the Dyson orbitals at photon energy $\omega = 20$ eV. The molecular orientation is shown. The polarization vector is parallel to the molecular axis in the upper panel and is perpendicular to the molecular axis in the lower panel

400 eV photon energy, after a couple of oscillations, which might induce a false expectation if not followed through, like the apparently flat behaviour shown by the same ratio in the left panel around 60 eV. The behaviour of the satellite/7σ ratio is even more structured with the several wide range oscillations on a steadily increasing ratio. The latter is a reflection of the increasing $6\sigma/7\sigma$ ratio, which derives by the larger s AO content of the 6σ state, whose atomic cross section decrease is slower than that of the corresponding p AO orbitals.

Finally, as a signature of the final states, we have also considered the angular distribution of photoelectron in the molecular frame, MFPADs. These can be measured in favourable circumstances from coincidence detection of photoelectron and ionic fragments obtained from fast dissociation [215], or alternatively from molecules aligned in strong laser fields [216]. MFPADs calculated from the relevant Dyson orbitals at 20 and 30 eV photon energies for the three σ final ionic states are reported in Figures 13.5 and 13.6 for either parallel or perpendicular orientation of the linear polarization vector with respect to the molecular axis. MFPADs are very sensitive to the nature of the final state, embodied in the corresponding Dyson orbital. Inspection of Fig. 13.5 shows the completely opposite

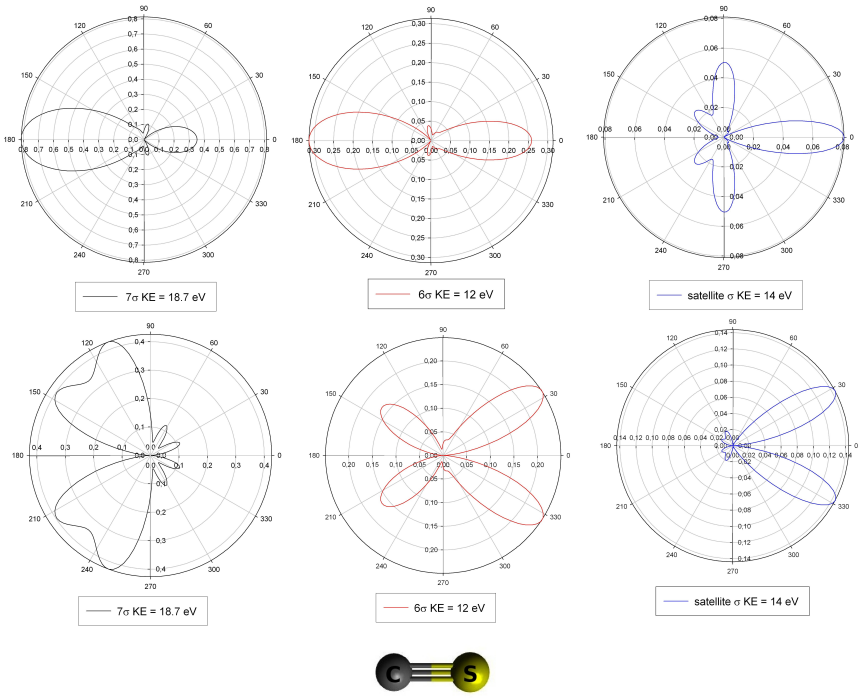

FIGURE 13.6: CS. MFPADs calculated from the Dyson orbitals at photon energy $\omega = 30$ eV. The molecular orientation is shown. The polarization vector is parallel to the molecular axis in the upper panel and is perpendicular to the molecular axis in the lower panel

pattern of the 7σ and 6σ orbitals, reflecting the different localization, 7σ mainly composed of 40.7% $2p_z$ C, 36.2% 2s C, 18.9% $3p_z$ S and 6σ of 35.8% $3p_z$ S, 32.8% 2s C, 31% 3s S. The satellite behaviour is still different, somehow in between, although more similar to the 6σ in the perpendicular orientation. A large change, especially in the parallel orientation, is shown by all three final states at 30 eV. While 6σ shows now similar forward and backward emission, the satellite shows emission concentrated at 0°, but with major lobes perpendicular to the molecular axis. Although less dramatic, large changes in shapes are apparent also for the perpendicular orientation. The 7σ emission becomes completely concentrated in two large butterfly-like lobes, and the satellite into two narrow lobes in the opposite direction, while 6σ develops important secondary lobes, giving an asymmetric four-lobe pattern. Both orbital and energy dependence, known in MFPADs studies, show up promimently also in this case. They provide a very strong signature of the final ionic state, confirming once more that satellites, even if mainly borrowing from a single primary ionization, have a specific individuality, that is best probed by their dynamical photoionization observables, and afford a stringent test of the

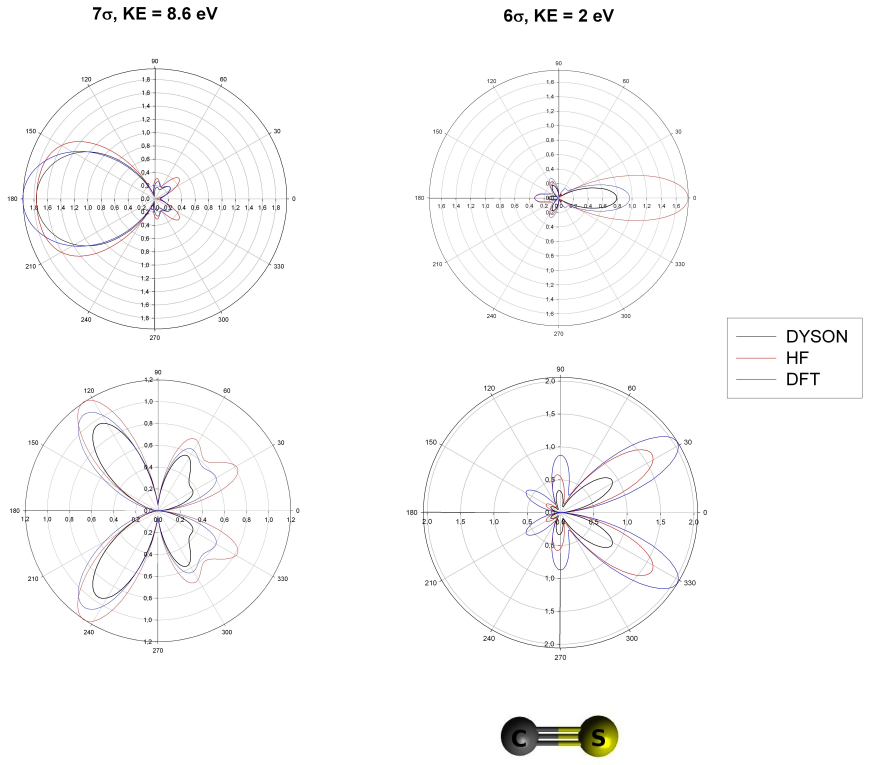

FIGURE 13.7: CS. MFPADs for the different approximations at photon energy ω = 20 eV. The molecular orientation is shown. The polarization vector is parallel to the molecular axis in the upper panel and is perpendicular to the molecular axis in the lower panel

quality of the initial and final wavefunctions. The comparison between MFPADs for 7σ and 6σ states calculated from the Dyson orbitals and those calculated for the other approximations is also reported in the Fig. 13.7. In this case the general shape appears quite similar in all cases, although the DFT results are a bit closer to the Dyson ones than are the HF results. It is interesting the behaviour of the 6σ ionization, where the cross section of the Dyson orbital is expected to be much lower than that of HF or DFT orbitals, because of the much reduced norm. Actually, in the parallel orientation the DFT results are quite close to the Dyson ones, despite the HF been much larger. The behaviour is however opposite for the perpendicular orientation, where both HF and DFT are much larger, as expected, but with the DFT the largest. This reflects tiny differences in orbital composition which are magnified by specific electric field orientation.

13.4 Conclusions

Strong correlation effects are present in the photoionization of the CS molecule, as indicated by the breakdown of the KT already for the two outermost ionizations, and the appearance of a conspicuous satellite in the outer valence region, a rather unique feature. NEVPT2 calculations of ionization energies are in excellent agreement with the experimental results, and compare well with previous accurate theoretical values. Dyson orbitals coupled to accurate continuum orbitals obtained at the DFT level are employed to compute dynamical photoionization observables, cross sections, asymmetry parameters and MFPADs, which are compared with results obtained at the HF, CASSCF and DFT level. Strong sensitivity to the nature of the bound state wavefunctions is shown in all results, and provide a stringent test on the quality of the wavefunction employed. HF and DFT results also show a large difference between each other, and often bracket the correlated result. Distinct features are obtained for the satellite, different from those of both 7σ and 6σ states of the same symmetry, indicating the limitations of the simple intensity borrowing picture, according to which the same cross section is expected for a satellite and the primary peak from which it steals intensity. Notably intensity ratios of the satellite to both 7σ and 6σ states show strong variations with photon energy, and explain the unusual high intensity observed for the satellite at HeI, 21.22 eV photon energy. The present approach takes accurately into account bound state correlations in the initial and final states, and illustrates the power of dynamical photoionization observables as a test of a quality of such wavefunctions. It can be readily applied to larger and more complex systems, given the availability of accurate Dyson orbital calculations. Experimental measurements of matching accuracy are now well within the capabilities of Syncrotron radiation laboratories [214], and reveal a richness of detail which includes further couplings neglected at the present level, and challenge corresponding theoretical advances.

Chapter 14

Conclusions

In this work, we presented a theoretical study of photoionization processes, paying particular attention to the high photon energy region. Indeed, it has recently confirmed that, also above a 100 eV threshold, there are structures in cross section profiles, due to diffraction and interference effects. The extension of the accessible energetic range in photoelectron spectroscopy has been made possible from the availability by latest-generation synchrotron light sources. We have studied the diffraction and interference effects in the photoionization profiles for several systems in the core shell, in the inner valence shell and in the outer valence shell as well. This has been done by means of an approach based on the DFT method combined with the use of a B-spline basis.

The first analysis of photoelectron interference due to the coherent emission from equivalent centers was done by Cohen and Fano in the 1960s. It has only been possible recently to observe these effects in the core photoionization of N_2. Our study has highlighted that the interference effect is more easily visible in the outer-valence region and inner-valence of small polyatomic molecules. The same type of phenomenon has been, surprisingly, observed also in the outer-valence photoionization of C_{60}. The oscillations of the cross section profiles can be amplified by taking into account the ratio of the cross sections relative to the orbitals HOMO and HOMO-1. These oscillations are due to the interference of waves emitted by equivalent centers and they represent further evidence of the interference effects predicted and observed in diatomic molecules. Oscillations similar to those of C_{60} have been also observed for the case of magnesocene. This inspired us to study the photoionization observables of two bis-decamethyl-cyclopentadienyl compounds of Mg and Be: $MgCp_2^*$ and $BeCp_2^*$. We examined the cross section ratios relative to

the outer-valence ionizations of these molecules and we observed that these ratios are very sensitive to the molecular geometry, in particular to the value of the metal-ring distance, as well as to the electronic structure. The substantial difference in the intensity and in the frequency of the oscillations observed confirms that the diffraction patterns, in general, permit one to obtain information both on the geometrical structure and on the electronic structure of the target molecules. The energy-dependent modulations of cross sections, above the threshold, are observed not only for ionizations from the outer-valence shell (as for C_{60} and cyclopentadienyl compounds above mentioned) but also for the ionization from inner-valence shell. This is the case of 2-butyne, for which the intensity ratio C2,3/C1,2 has been analysed. For the two triply bonded carbon atoms in 2-butyne, C2 and C3, there are two core orbitals separated by approximately 100 meV resulting from the bonding and antibonding combinations of the two atomic 1s orbitals. In this case the g-u splitting of the two couples of C2,3 and C1,2 are to close to be resolved, and only the cross section ratio between them can be measured. The C 1s photoelectron spectrum of this molecule has been measured over a range of photon energies from the threshold to 150 eV above threshold. The study of this molecule was inspired by previous theoretical predictions on the effects which were in the C 1s photoionization spectra for several compounds and which were experimentally observed in the case of chlorinated ethanes. Different from that case, 2-butyne there is no atom which can constitute a high-Z scattering center. For this reason, the oscillations observed were unexpected. These energy-dependent oscillations are due to the scattering of photoelectrons from the carbon atoms, in particular to those adjacent to the ionized carbon atom. The scattering effect is greater for the central atoms than the terminal carbon atoms.

If the g/u splitting between 1s orbitals is too small to be observed, it is possible to examine the ionization from the inner-shell orbitals which stem from 2s AOs of the first period atoms. They have a much larger g/u splitting and so they can be experimentally resolved. This allows a direct study of interference patterns for a much larger number of molecular systems. On the basis of this consideration, a further object of research has been the study of interference effects in the photoionization spectra of simple polyatomic molecules (propane, butane, isobutane and cis/trans-2-butene), This was done in order to verify the existence of oscillations in the cross sections profiles and their dependence on internuclear distance. The experimental data, which was compared to the theoretical predictions, was collected at the Soleil synchrotron in Paris. The theoretical and experimental study

of the photoelectron spectra of hydrocarbon molecules was over on an photon energy range between 70 and 700 eV. We observed a strong dependence of the shape and period of oscillations on the C-C distance which is different for the different hydrocarbon molecules considered. In particular, we have highlighted the great potential for the technique in the accurate determination of molecular conformers. The differences between the interference patterns associated with different isomers constitutes an unambiguous signature of the different conformers. This makes it possible to do, at least in the simple cases, a conformational analysis of more than two conformers with the relative populations by an accurate comparison of the experimental and theoretical interference patterns.

A further study on the photoionization dynamical observables was done by considering the endohedral compounds, where the metal is embedded in a cage represented by a fullerene molecule. The interest on the photoionization of these compounds, as well as on that of C_{60}, is related to the fact that cross sections and photoelectron angular distributions allows for a deep study of their electronic structure. The calculations on these compounds show the presence of sharp resonances on the total cross section which are defined as a confinement resonances. We then focused on the photoionization of $Ar@C_{60}$ in the core region relative to Ar 2p ionization. In contrast with spherical models previously used, our treatment accurately describes the molecular effects. For our analysis, we have considered both the DFT approach and the TDDFT approach for the ionization from the core shell of $Ar@C_{60}$, compared with the case of isolated C_{60} molecule, to examine both the influence of an accurate molecular treatment of the cage, and the effect of the possible coupling with the neighbouring C 1s ionizations.

A second line of research was the correlated description of photoionization observables. We worked on a new method based on *ab initio* close-coupling formalism. Although the DFT approach, used for the calculations just illustrated, is very efficient, it can not describe further features in the spectra due to electron correlation. Since the progress of new light-sources and multichannel detectors has opened the possibility of an experimental study much more detailed on small molecules, our aim is extending the methodology of DFT which is already available in the field of *ab initio* Hamiltonians. The theoretical ingredients for the calculation of photoionization observables are the transition dipole moments between initial bound state and continuum wavefunction. The final goal is the implementation of a close-coupling formalism where the final continuum wavefunction is expressed in analogous way to that of CI for bound states. The first level of this

ab initio implementation only takes correlation fully into account for the bound states. In particular, we have implemented subroutines in Fortran to project Gaussian orbitals onto the B-splines basis and an interface to use Dyson orbitals on a Gaussian basis. The Dyson orbitals represent the superposition between the initial N-particle wavefunction and the final N-1 particle wavefunction. This permit one to describe situations where strong correlation effects in the ionic states modify the nature of the initial orbital.
The employment of Dyson orbitals has been applied to the description of photoionization observables for the CS molecule. A strong satellite band is present in the photoelectron spectrum of this molecule. Since it is entirely due to effects of the electron correlation, it can not be described at the DFT level. The results obtained with Dyson orbitals are compared to those from HF and DFT methods. The different features of the cross sections and asymmetry parameters related to the satellites and primary ionic states of the same symmetry indicate that these states can be distinguishable through the study of photoionization observables.

The calculation of photoionization observables through Dyson orbitals can be combined with a semiclassical non-adiabatic dynamics calculation. This combination represents a possible and interesting development of our work. The first steps in this direction have been carried out during the last few months of my PhD, in collaboration with the theoretical chemistry group of the Ruđer Bošković Institute in Zagreb. This project aims to a high-level theoretical description of Time-Resolved Photoelectron Spectroscopy (TRPES) observables obtained from pump-probe experiments.

Publications

Related publications:

1. T. X. Carroll, M. G. Zahl, K. J. Børve, L. J. Sæthre, P. Decleva, A. Ponzi, J. J. Kas, F. D. Vila, J. J. Rehr, T. Darrah Thomas, *Intensity oscillations in the carbon 1s ionization cross sections of 2-butyne*, J. Chem. Phys. 138 (2013) 234310

2. P. Decleva, A. Ponzi and I. Santizo, *Interference Effects in the Valence Shell ionization of Simple Hydrocarbons*, J. Phy. Conf. Ser. 488 (2014) 012016

3. A. Ponzi, C. Angeli, R. Cimiraglia, S. Coriani and P. Decleva, *Dynamical photoionization observables of the CS molecule: the role of electron correlation*, J. Chem Phys. 140 (2014) 204304

4. A. Ponzi and P. Decleva, *Photoelectron interference in metallocenes: a probe of geometrical and electronic structure*, J. Phys. Chem. A 118 (2014) 6692

5. P. Decleva, A. Ponzi and I. Santizo, *Interference and Diffraction in Photoelectron Spectra*, J. Electron Spectrosc. Related Phenom. 195 (2014) 307

Bibliography

[1] J. W. Rabalais. *Principles of Ultraviolet Photoelectron Spectroscopy*. John Wiley and Sons, 1977.

[2] J. H. D. Eland. *Photoelectron Spectroscopy*. Butterworths, 1984.

[3] D. W. Turner, C. Baker, A. D. Baker, and C. R. Brundle. *Molecular Photoelectron Spectroscopy*. Wiley, London, 1970.

[4] U. Hollenstein, R. Seiler, A. Osterwalder, M. Sommavilla, A. Wüest, P. Rupper, S. Willitsch, G. M. Greetham, B. Brupbacher-Gatehouse, and F. Merkt. *Chimia*, 55:759, 2001. URL http://www.ingentaconnect.com/content/scs/chimia/2001/00000055/00000010/art00003?crawler=true.

[5] L. S. Cederbaum, W. Domcke, J. Schirmer, and W. von Niessen. *Adv. Chem. Phys.*, 65:115, 1986. URL http://dx.doi.org/10.1002/9780470142899.ch3.

[6] *Encyclopedia of Physics, Corpuscles and Radiation in Matter I, vol. XXXI*. Springer-Verlag, 1982.

[7] A. F. Starace. The calculation of photoionization cross sections, published in proceedings of the atomic data workshop held at st. catherine's college oxford, edited by w. eissner and a . e . kingston (the queen's university of belfast, 1988). 1988. URL http://digitalcommons.unl.edu/physicsstarace/129/.

[8] H. Hertz. *Ann. Phys.*, 267:983, 1887. URL http://dx.doi.org/10.1002/andp.18872670827.

[9] W. Hallwachs. *Ann. Phys.*, 328:459, 1907. URL http://dx.doi.org/10.1002/andp.19073280807.

[10] J. Elster and H. Geitel. *Annal. of Phys. Chem.*, 302:735, 1898.

[11] P. Lenard. *Ann. Phys.*, 313:149, 1902. URL http://dx.doi.org/10.1002/andp.19023130510.

[12] A. Einstein. *Ann. Phys.*, 322:132, 1905. URL http://dx.doi.org/10.1002/andp.19053220607.

[13] M. Planck. *Ann. Phys.*, 309:553, 1901. URL http://dx.doi.org/10.1002/andp.19013090310.

[14] K. Siegbahn. *Alpha, Beta and Gamma-Ray Spectroscopy*. Amsterdam, North Holland, 1965.

[15] K. Siegbahn, C. Nordling, A. Fahlman, R. Nordberg, K. Hamrin, J. Hedman, J. Johansson, T. Bergmark, S. E. Karlsson, I. Lindgren, and B. Lindgren. *ESCA, Atomic, Molecular and Solid State Structure by means of Electron Spectroscopy*. Almqvist and Wiksell, Uppsala, 1967.

[16] K. Siegbahn, C. Nordling, J. Johansson, J. Hedman, P. E. Heden, K. Hamrin, U. Gelius, T. Bergmark, L. O. Werme, R. Manne, and Y. Baer. *ESCA Applied to Free Molecules*. Amsterdam, North Holland, 1969.

[17] D. W. Turner and M. I. A. Jobory. *J. Chem. Phys.*, 37:3007, 1962. URL http://scitation.aip.org/content/aip/journal/jcp/37/12/10.1063/1.1733134.

[18] D. W. Turner and M. I. Al-Jobory. *J. Chem. Phys.*, 37:3007, 1962. URL http://scitation.aip.org/content/aip/journal/jcp/37/12/10.1063/1.1733134.

[19] M. O. Krause. *Phys. Rev.*, 140:A1845, 1965. URL http://link.aps.org/doi/10.1103/PhysRev.140.A1845.

[20] B. L. Kurbatov and F. I. Viselov. *Sov. Phys. Dokl.*, 6:1091, 1962.

[21] F. R. Elder, A. M. Gurewitsch, R. V. Langmuir, and H. C. Pollock. *Phys. Rev.*, 71:829, 1947. URL http://link.aps.org/doi/10.1103/PhysRev.71.829.5.

[22] P. D. Innes. *P. Roy. Soc. Lond. A Mat.*, 79:442, 1907. doi: 10.1098/rspa.1907.0056.

[23] H. Robinson. *P. Roy. Soc. Lond. A Mat.*, 104:455, 1923. doi: 10.1098/rspa.1923.0121.

[24] R. Steinhardt and E. Serfass. *Anal. Chem.*, 23:1585, 1951. URL http://dx.doi.org/10.1021/ac60059a019.

[25] H. A. Bethe and E. E. Salpeter. *Quantum Mechanics of One- and Two-electron Atoms*. Springer- Verlag, 1957.

[26] T. Young. *Philos. Trans.*, 92:12, 1802. URL http://rstl.royalsocietypublishing.org/content/92/12.full.pdf+html.

[27] H. D. Cohen and U. Fano. *Phys. Rev.*, 150:30, 1966. URL http://link.aps.org/doi/10.1103/PhysRev.150.30.

[28] J. L. Dehmer and D. Dill. *Phys. Rev. Lett.*, 35:213, 1975. URL http://link.aps.org/doi/10.1103/PhysRevLett.35.213.

[29] S. E. Canton, E. Plésiat, J. D. Bozek, B. S. Rude, P. Decleva, and F. Martín. *PNAS*, 108:7302, 2011. URL http://www.pnas.org/content/108/18/7302.abstract.

[30] P. J. Benning, D. M. Poirier, N. Troullier, J. L. Martins, J. H. Weaver, R. E. Haufler, L. P. F. Chibante, and R. E. Smalley. *Phys. Rev. B*, 44:1962, 1991. URL http://link.aps.org/doi/10.1103/PhysRevB.44.1962.

[31] T. Liebsch, O. Plotzke, F. Heiser, U. Hergenhan, O. Hemmers, R. Wehlitz, J. Viefhaus, B. Langer, S. B. Whitfield, and U. Becker. *Phys. Rev. A*, 52:457, 1995. URL http://link.aps.org/doi/10.1103/PhysRevA.52.457.

[32] S. Hasegawa, T. Miyamae, K. Yakushi, H. Inokuchi, K. Seki, and N. Ueno. *Phys. Rev. B*, 58:4927, 1998. URL http://link.aps.org/doi/10.1103/PhysRevB.58.4927.

[33] Y. B. Xu, M. Q. Tan, and U. Becker. *Phys. Rev. Lett.*, 76:3538, 1996. URL http://link.aps.org/doi/10.1103/PhysRevLett.76.3538.

[34] O. Frank and J. M. Rost. *Chem. Phys. Lett.*, 271:367, 1997. URL http://www.sciencedirect.com/science/article/pii/S0009261497004715.

[35] A. Rüdel, R. Hentges, U. Becker, H. S. Chakraborty, M. E. Madjet, and J. M. Rost. *Phys. Rev. Lett.*, 89:125503, 2002. URL http://link.aps.org/doi/10.1103/PhysRevLett.89.125503.

[36] P. Colavita, G. De Alti, G. Fronzoni, M. Stener, and P. Decleva. *Phys. Chem. Chem. Phys.*, 3:4481, 2001. URL http://dx.doi.org/10.1039/B104761M.

[37] P. Decleva, S. Furlan, G. Fronzoni, and M. Stener. *Chem. Phys. Lett.*, 348: 363, 2001. URL http://www.sciencedirect.com/science/article/pii/S0009261401011666.

[38] X.-X. Wang, Y.-B. Xu, H.-N. Li, W.-H. Zhang, and F.-Q. Xu. *J. Electron Spectrosc. Relat. Phenom.*, 165:20, 2008. URL http://www.sciencedirect.com/science/article/pii/S0368204808000777.

[39] D. Toffoli, M. Stener, G. Fronzoni, and P. Decleva. *Chem. Phys. Lett.*, 516: 154, 2011. URL http://www.sciencedirect.com/science/article/pii/S0009261411012589.

[40] D. Toffoli and P. Decleva. *Phys. Rev. A*, 81:061201, 2010. URL http://link.aps.org/doi/10.1103/PhysRevA.81.061201.

[41] U. Becker, O. Gessner, and A. Rüdel. *J. Electron. Spectrosc. Relat. Phenom.*, 108:189, 2000. URL http://www.sciencedirect.com/science/article/pii/S0368204800001286.

[42] S. Korica, D. Rolles, A. Reinköster, B. Langer, J. Viefhaus, Cvejanović, and U. Becker. *Phys. Rev. A*, 71:013203, 2005. URL http://link.aps.org/doi/10.1103/PhysRevA.71.013203.

[43] E. I. Solomon, L. Basumallick, P. C., and P. Kennepohl. *Coordin. Chem. Rev.*, 249:229, 2005. URL http://www.sciencedirect.com/science/article/pii/S0010854504000426.

[44] A. W. Potts, H. J. Lempka, D. G. Streets, and W. C. Price. *Phil. Trans. R. Soc. Lond.*, 268:59, 1970.

[45] H. Winick and S. Doniach. *Synchrotron Radiation Research*. Plenum Press, New York, 1980.

[46] H. Saisho and Y. Gohshi. *Applications of Synchrotron Radiation to Materials Analysis, vol.7*. Elsevier Science, Amsterdam, 1996.

[47] *Handbook on Synchrotron Radiation, vol.2*. Ed. by G. V. Marr, 1987.

[48] T. Koopmans. *Physica*, 1:104, 1934. URL http://www.sciencedirect.com/science/article/pii/S0031891434900112.

[49] D. R. Hartree. *Proc. Cambridge Phil. Soc.*, 24:89, 1927.

[50] V. Fock. *Z. Physik*, 61:126, 1930. URL http://dx.doi.org/10.1007/BF01340294.

[51] J. C. Slater. *Phys. Rev.*, 35:210, 1930. URL http://link.aps.org/doi/10.1103/PhysRev.35.210.2.

[52] C. D. Sherrill and H. F. Schaefer. volume 34, page 143. 1999. URL http://www.sciencedirect.com/science/article/pii/S0065327608605328.

[53] J. C. Green and P. Decleva. *Coord. Chem. Rev.*, 249:209, 2005. URL http://www.sciencedirect.com/science/article/pii/S0010854504000396.

[54] U. Fano and J. W. Cooper. *Rev. Mod. Phys.*, 40:441, 1968. URL http://link.aps.org/doi/10.1103/RevModPhys.40.441.

[55] Ed. by U. Becker and D. A. Shirley. *VUV and Soft X-Ray Photoionization*. Plenum Press, 1996.

[56] B. H. Bransden and C. J. Joachain. *Physics of Atoms and Molecules*. Prentice Hall, 2003.

[57] A. F. Starace. *Theory of atomic photoionization, in Handbuch der Physik*. Flugges ed., Vol. 31 (Springer-Verlag, Berlin), 1982.

[58] R. R. Lucchese and A. Stolow. *J. Phys. B: At. Mol. Opt. Phys.*, 45:190201, 2012. URL http://stacks.iop.org/0953-4075/45/i=19/a=190201.

[59] H. Fukuzawa, X.-J. Liu, T. Teranishi, K. Sakai, G. Prümper, K. Ueda, Y. Morishita, N. Saito, M. Stener, and P. Decleva. *Chem. Phys. Lett.*, 451:182, 2008. URL http://www.sciencedirect.com/science/article/pii/S0009261407016260.

[60] D. Dill. *A Primer on Photoelectron Angular Distributions*, volume 18. 1976. URL http://dx.doi.org/10.1007/978-1-4684-2799-8_22.

[61] F. Heiser, O. Geßner, J. Viefhaus, K. Wieliczek, R. Hentges, and U. Becker. *Phys. Rev. Lett.*, 79:2435, 1997. URL http://link.aps.org/doi/10.1103/PhysRevLett.79.2435.

[62] A. Lafosse, M. Lebech, J. C. Brenot, P. M. Guyon, O. Jagutzki, L. Spielberger, M. Vervloet, J. C. Houver, and D. Dowek. *Phys. Rev. Lett.*, 84:5987, 2000. URL http://link.aps.org/doi/10.1103/PhysRevLett.84.5987.

[63] A. Landers, T. Weber, I. Ali, A. Cassimi, M. Hattass, O. Jagutzki, A. Nauert, T. Osipov, A. Staudte, M. H. Prior, H. Schmidt-Böcking, C. L. Cocke, and R. Dörner. *Phys. Rev. Lett.*, 87:013002, 2001. URL http://link.aps.org/doi/10.1103/PhysRevLett.87.013002.

[64] N. Saito, A. De Fanis, K. Kubozuka, M. Machida, M. Takahashi, H. Yoshida, I. H. Suzuki, A. Cassimi, A. Czasch, L. Schmidt, R. Dörner, K. Wang, B. Zimmermann, V. McKoy, I. Koyano, and K. Ueda. *J. Phys. B: At. Mol. Opt. Phys.*, 36:L25, 2003. URL http://stacks.iop.org/0953-4075/36/i=1/a=104.

[65] J. R. Taylor. *Scattering Theory*. Dover Publications, 1983.

[66] N. Chandra. *J. Phys. B: At. Mol. Phys.*, 20:3405, 1987. URL http://iopscience.iop.org/0022-3700/20/14/013/pdf/0022-3700_20_14_013.pdf.

[67] A. Messiah. *Quantum Mechanics*. North Holland Publishing Company, 1967.

[68] N. Chandra. *J. Phys. B: At. Mol. Phys.*, 20:3417, 1987. URL http://iopscience.iop.org/0022-3700/20/14/014.

[69] M. Martins, K. Godehusen, T. Richter, P. Wernet, and P. Zimmermann. *J. Phys. B: At. Mol. Opt. Phys.*, 39:R79, 2006. URL http://stacks.iop.org/0953-4075/39/i=5/a=R01.

[70] R. L. Martin and D. A. Shirley. *Phys. Rev. A*, 13:1475, 1976. URL http://link.aps.org/doi/10.1103/PhysRevA.13.1475.

[71] A. B. Trofimov and J. Schirmer. *J. Chem. Phys.*, 123:144115, 2005. URL http://scitation.aip.org/content/aip/journal/jcp/123/14/10.1063/1.2047550.

[72] M. Ehara, K. Kuramoto, H. Nakatsuji, M. Hoshino, T. Tanaka, M. Kitajima, H. Tanaka, A. De Fanis, Y. Tamenori, and K. Ueda. *J. Chem. Phys.*, 125:114304, 2006. URL http://scitation.aip.org/content/aip/journal/jcp/125/11/10.1063/1.2346683.

[73] Q. Tian, J. Yang, Y. Shi, X. Shan, and X. Chen. *J. Chem. Phys.*, 136: 094306, 2012. URL http://scitation.aip.org/content/aip/journal/jcp/136/9/10.1063/1.3691103.

[74] L. C. Davis and L. A. Feldkamp. *Phys. Rev. B*, 23:6239, 1981. URL http://link.aps.org/doi/10.1103/PhysRevB.23.6239.

[75] F. Jensen. *Introduction to Computational Chemistry*. John Wiley and Sons, 2007.

[76] A. Szabo and N. S. Ostlund. *Modern Quantum Chemistry*. McGraw-Hill, 1982.

[77] R. McWeeney. *Methods of Molecular Quantum Mechanics*. Academic Press, 1992.

[78] M. W. Schmidt and M. S. Gordon. *Ann. Rev. Phys. Chem.*, 49:233, 1998. URL http://dx.doi.org/10.1146/annurev.physchem.49.1.233.

[79] B. O. Roos, P. R. Taylor, and P. E. M. Siegbahn. *Chem. Phys.*, 48: 157, 1980. URL http://www.sciencedirect.com/science/article/pii/0301010480800450.

[80] C. Angeli, R. Cimiraglia, S. Evangelisti, T. Leininger, and J.-P. Malrieu. *J. Chem. Phys.*, 114:10252, 2001. URL http://scitation.aip.org/content/aip/journal/jcp/114/23/10.1063/1.1361246.

[81] C. Angeli, R. Cimiraglia, and J. P. Malrieu. *J. Chem. Phys.*, 117:9138, 2002. URL http://scitation.aip.org/content/aip/journal/jcp/117/20/10.1063/1.1515317.

[82] C. Angeli, R. Cimiraglia, and J-P. Malrieu. *Chem. Phys. Lett.*, 350: 297, 2001. URL http://www.sciencedirect.com/science/article/pii/S0009261401013033.

[83] P. Hohenberg and W. Kohn. *Phys. Rev.*, 136:B864, 1964. URL http://link.aps.org/doi/10.1103/PhysRev.136.B864.

[84] W. Kohn and L. J. Sham. *Phys. Rev.*, 140:A1133, 1965. URL http://link.aps.org/doi/10.1103/PhysRev.140.A1133.

[85] L. H. Thomas. *Proc. Camb. Phil. Soc.*, 23:542, 1927. URL http://journals.cambridge.org/article_S0305004100011683.

[86] L. H. Thomas. *J. Chem. Phys.*, 22:1758, 1954. URL http://scitation.aip.org/content/aip/journal/jcp/22/10/10.1063/1.1739890.

[87] E. Fermi. *Z. Physik*, 48:73, 1928. URL http://dx.doi.org/10.1007/BF01351576.

[88] E. Fermi. *Z. Physik*, 49:550, 1928. URL http://dx.doi.org/10.1007/BF01333639.

[89] E. Fermi. *Z. Physik*, 36:902, 1926. URL http://dx.doi.org/10.1007/BF01400221.

[90] P. A. M. Dirac. *Proc. Roy. Soc. (London)*, A112:661, 1926.

[91] M. Born and J. R. Oppenheimer. *Ann. Physik*, 389:457, 1927. URL http://dx.doi.org/10.1002/andp.19273892002.

[92] E. Schrödinger. *Ann. Physik*, 81:109, 1926. URL http://dx.doi.org/10.1002/andp.19263840404.

[93] W. Heisenberg. *Z. Physik*, 38:411, 1928. URL http://dx.doi.org/10.1007/BF01397160.

[94] W. Heisenberg. *Z. Physik*, 39:499, 1926. URL http://dx.doi.org/10.1007/BF01322090.

[95] W. Heisenberg. *Z. Physik*, 41:239, 1927. URL http://dx.doi.org/10.1007/BF01391241.

[96] W. Kohn and L. J. Sham. *Phys. Rev.*, 140:A1133, 1965. URL http://dx.doi.org/10.1007/BF01322090.

[97] J. P. Perdew and A. Zunger. *Phys. Rev. B*, 23:5048, 1981. URL http://link.aps.org/doi/10.1103/PhysRevB.23.5048.

[98] S. H. Vosko, L. Wilk, and M. Nusair. *Can. J. Phys.*, 58:1200, 1980. URL http://dx.doi.org/10.1139/p80-159.

[99] J. P. Perdew and Y. Wang. *Phys. Rev. B*, 45:13244, 1992. URL http://link.aps.org/doi/10.1103/PhysRevB.45.13244.

[100] D. M. Ceperley and B. J. Alder. *Phys. Rev. Lett.*, 45:566, 1980. URL http://link.aps.org/doi/10.1103/PhysRevLett.45.566.

[101] C. A. Ulrich and Z. Yang. *Braz. J. Phys.*, 44:154, 2014. URL http://dx.doi.org/10.1007/s13538-013-0141-2.

[102] J. P. Perdew and K. Burke. *Int. J. Quantum Chem.*, 57:309, 1996. URL http://dx.doi.org/10.1002/(SICI)1097-461X(1996)57:3<309::AID-QUA4>3.0.CO;2-1.

[103] A. D. Becke. *Phys. Rev. A*, 38:3098, 1988. URL http://link.aps.org/doi/10.1103/PhysRevA.38.3098.

[104] C. Lee, W. Yang, and R. G. Parr. *Phys. Rev. B*, 37:785, 1988. URL http://link.aps.org/doi/10.1103/PhysRevB.37.785.

[105] J. P. Perdew, K. Burke, and M. Ernzerhof. *Phys. Rev. Lett.*, 77:3865, 1996. URL http://link.aps.org/doi/10.1103/PhysRevLett.77.3865.

[106] A. D. Becke. *J. Chem. Phys.*, 98:5648, 1993. URL http://scitation.aip.org/content/aip/journal/jcp/98/7/10.1063/1.464913.

[107] M. A. L. Marques and E. K. U. Gross. *Annu. Rev. Phys. Chem.*, 55:427, 2004. URL http://dx.doi.org/10.1146/annurev.physchem.55.091602.094449.

[108] K. Burke, J. Werschnik, and E. K. U. Gross. *J. Chem. Phys.*, 123:062206, 2005. URL http://scitation.aip.org/content/aip/journal/jcp/123/6/10.1063/1.1904586.

[109] M. Petersilka, U. J. Gossmann, and E. K. U. Gross. *Phys. Rev. Lett.*, 76:1212, 1996. URL http://link.aps.org/doi/10.1103/PhysRevLett.76.1212.

[110] M. E. Casida. *Recent Developments and Applications in Density Functional Theory*. ed. by J. M. Seminario (Elsevier, Amsterdam), 1996.

[111] E. Runge and E. K. U. Gross. *Phys. Rev. Lett.*, 52:997, 1984. URL http://link.aps.org/doi/10.1103/PhysRevLett.52.997.

[112] P. van der Straten, R. Morgenstern, and A. Niehaus. *Z. Phys. D*, 8:35, 1988. URL http://dx.doi.org/10.1007/BF01384521.

[113] I. J. Schoenberg. *Quart. Appl. Math.*, 4:45, 1946.

[114] I. J. Schoenberg. *Inequalities*. ed. O. Shisha (NewYork:Academic) p.255, 1967.

[115] H. Bachau, E. Cormier, P. Decleva, J. E. Hansen, and F. Martín. *Rep. Prog. Phys.*, 64:1815, 2001. URL http://iopscience.iop.org/0034-4885/64/12/205.

[116] C. de Boor. *A Practical Guide to Splines*. Springer, New York, 1978.

[117] D. Toffoli, M. Stener, G. Fronzoni, and P. Decleva. *Chem. Phys.*, 276: 25, 2002. URL http://www.sciencedirect.com/science/article/pii/S0301010401005493.

[118] G. te Velde, F. M. Bickelhaupt, E. J. Baerends, C. Fonseca Guerra, S. J. A. van Gisbergen, J. G. Snijders, and T. Ziegler. *J. Comput. Chem.*, 22:931, 2001. URL http://dx.doi.org/10.1002/jcc.1056.

[119] P. G. Burke, N. Chandra, and F. A. Gianturco. *J. Phys. B: At. Mol. Phys.*, 5:2212, 1972. URL http://iopscience.iop.org/0022-3700/5/12/015/.

[120] T. Kato. *Comm. Pure Appl. Math.*, 10:151, 1957. URL http://dx.doi.org/10.1002/cpa.3160100201.

[121] M. Stener, A. Lisini, and P. Decleva. *Int. J. Quantum Chem.*, 53:229, 1995. URL http://dx.doi.org/10.1002/qua.560530208.

[122] M. Brosolo, P. Decleva, and A. Lisini. *Chem. Phys.*, 181:85, 1994. URL http://www.sciencedirect.com/science/article/pii/0301010494850178.

[123] C. F. Fischer and M. Idrees. *J. Phys. B: At. Mol. Opt. Phys.*, 23:679, 1990. URL http://iopscience.iop.org/0953-4075/23/4/002.

[124] G. H. Golub and C. F. van Loan. *Matrix computations*. The Johns Hopkins University Press, third edition, p.374, 1996.

[125] A. Zangwill and P. Soven. *Phys. Rev. A*, 21:1561, 1980. URL http://link.aps.org/doi/10.1103/PhysRevA.21.1561.

[126] Z. H. Levine and P. Soven. *Phys. Rev. A*, 29:625, 1984. URL http://link.aps.org/doi/10.1103/PhysRevA.29.625.

[127] G. D. Mahan. *Phys. Rev. A*, 22:1780, 1980. URL http://link.aps.org/doi/10.1103/PhysRevA.22.1780.

[128] G. D. Mahan and K. R. Subbaswamy. *Local Density Theory of Polarizability*. Plenum, New York, 1990.

[129] M. Stener, G. Fronzoni, and P. Decleva. *J. Chem. Phys.*, 122:234301, 2005. URL http://scitation.aip.org/content/aip/journal/jcp/122/23/10.1063/1.1937367.

[130] H.-J. Werner, P. J. Knowles, G. Knizia, F. R. Manby, M. Schütz, P. Celani, T. Korona, R. Lindh, A. Mitrushenkov, G. Rauhut, K. R. Shamasundar, T. B. Adler, R. D. Amos, A. Bernhardsson, A. Berning, D. L. Cooper, M. J. O. Deegan, A. J. Dobbyn, F. Eckert, E. Goll, C. Hampel, A. Hesselmann, G. Hetzer, T. Hrenar, G. Jansen, C. Köppl, Y. Liu, A. W. Lloyd, R. A. Mata, A. J. May, S. J. McNicholas, W. Meyer, M. E. Mura, A. Nicklass, D. P. O'Neill, P. Palmieri, D. Peng, K. Pflüger, R. Pitzer, M. Reiher, T. Shiozaki, H. Stoll, A. J. Stone, R. Tarroni, T. Thorsteinsson, and M. Wang. Molpro, version 2012.1, a package of ab initio programs, 2012. URL http://www.molpro.net.

[131] Reidar Arneberg, Jiri Müller, and Rolf Manne. *Chemical Phys.*, 64: 249, 1982. URL http://www.sciencedirect.com/science/article/pii/0301010482870912.

[132] R. de L. Kronig. *Z. Physik*, 75:468, 1932. URL http://dx.doi.org/10.1007/BF01342238.

[133] P. A. Lee, P. H. Citrin, P. Eisenberger, and B. M. Kincaid. *Rev. Mod. Phys.*, 53:769, 1981. URL http://link.aps.org/doi/10.1103/RevModPhys.53.769.

[134] S. K. Semenov, N. A. Cherepkov, M. Matsumoto, T. Hatamoto, X-J. Liu, G. Prümper, T. Tanaka, M. Hoashino, H. Tanaka, F. Gel'mukhanov, and K. Ueda. *J. Phys. B: At. Mol. Opt. Phys.*, 39:L261, 2006. URL http://iopscience.iop.org/0953-4075/39/12/L02/.

[135] X-J. Liu, N. A. Cherepkov, S. K. Semenov, V. Kimberg, F. Gel'mukhanov, G. Prümper, T. Lischke, T. Tanaka, M. Hoashino, H. Tanaka, and K. Ueda. *J. Phys. B: At. Mol. Opt. Phys.*, 39:4801, 2006. URL http://stacks.iop.org/0953-4075/39/i=23/a=001.

[136] B. Zimmermann, D. Rolles, B. Langer, R. Hentges, M. Braune, S. Cvejanovic, O. Geßner, F. Heiser, S. Korica, T. Lischke, A. Reinköster, J. Viefhaus, R. Dörner, V. McKoy, and U. Becker. *Nature Phys.*, 4:649,

2008. URL http://www.nature.com/nphys/journal/v4/n8/suppinfo/nphys993_S1.html.

[137] M. Hoshino, K. Nakagawa, C. Makochekanwa, T. Tanaka, N. Kuze, M. Matsumoto, K. Fujiwara, A. De Fanis, Y. Tamenori, M. Kitajima, H. Tanaka, and K. Ueda. *Chem. Phys. Lett.*, 421:256, 2006. URL http://www.sciencedirect.com/science/article/pii/S0009261406000868.

[138] L. Argenti, T. D. Thomas, E. Plésiat, X-J. Liu, C. Miron, T. Lischke, G. Prümper, K. Sakai, T. Ouchi, R. Püttner, V. Sekushin, T. Tanaka, M. Hoshino, H. Tanaka, P. Decleva, K. Ueda, and F. Martìn. *New J. Phys.*, 14:033012, 2012. URL http://iopscience.iop.org/1367-2630/14/3/033012/metrics.

[139] N. Stolterfoht, B. Sulik, V. Hoffmann, B. Skogvall, J. Y. Chesnel, J. Rangama, F. Frémont, D. Hennecart, A. Cassimi, X. Husson, A. L. Landers, J. A. Tanis, M. E. Galassi, and R. D. Rivarola. *Phys. Rev. Lett.*, 87:023201, 2001. URL http://link.aps.org/doi/10.1103/PhysRevA.69.012701.

[140] D. S. Milne-Brownlie, M. Foster, J. Gao, B. Lohmann, and D. H. Madison. *Phys. Rev. Lett.*, 96:233201, 2006. URL http://link.aps.org/doi/10.1103/PhysRevLett.96.233201.

[141] O. A. Fojón, J. Fernández, A. Palacios, R. D. Rivarola, and F. Martìn. *J. Phys. B: At. Mol. Opt. Phys.*, 37:3035, 2004. URL http://iopscience.iop.org/0953-4075/37/15/003.

[142] M. Patanen, O. Travnikova, M. G. Zahl, J. Söderström, P. Decleva, T. D. Thomas, S. Svensson, N. Mårtensson, K. J. Børve, L. J. Sæthre, and C. Miron. *Phys. Rev. A*, 87:063420, 2013. URL http://link.aps.org/doi/10.1103/PhysRevA.87.063420.

[143] M. Ilchen, L. Glaser, F. Scholz, P. Walter, S. Deinert, A. Rothkirch, J. Seltmann, J. Viefhaus, P. Decleva, B. Langer, A. Knie, A. Ehresmann, O. M. Al-Dossary, M. Braune, G. Hartmann, A. Meissner, L. C. Tribedi, M. AlKhaldi, and U. Becker. *Phys. Rev. Lett.*, 112:023001, 2014. URL http://link.aps.org/doi/10.1103/PhysRevLett.112.023001.

[144] E. Plésiat, L. Argenti, C. Miron, E. Kukk, K. Ueda, P. Decleva, and F. Martìn. *Phys. Rev. A*, 85:023409, 2012. URL http://link.aps.org/doi/10.1103/PhysRevA.85.023409.

[145] K. Ueda, C. Miron, E. Plésiat, L. Argenti, M. Patanen, K. Kooser, D. Ayuso, S. Mondal, M. Kimura, K. Sakai, O. Travnikova, A. Palacios, P. Decleva, E. Kukk, and F. Martín. *J. Chem. Phys.*, 139:124306, 2013. URL http://scitation.aip.org/content/aip/journal/jcp/139/12/10.1063/1.4820814.

[146] R. K. Kushawaha, M. Patanen, R. Guillemin, L. Journel, C. Miron, M. Simon, M. N. Piancastelli, and P. Decleva. *PNAS*, 110:15201, 2013. URL http://www.pnas.org/content/110/38/15201.abstract.

[147] P. Decleva, G. Fronzoni, M. Stener, M. de Simone, M. Coreno, J. C. Green, N. Hazari, and O. Plekan. *Phys. Rev. Lett.*, 95:263401, 2005. URL http://link.aps.org/doi/10.1103/PhysRevLett.95.263401.

[148] P. Decleva, A. Ponzi, and I. Santizo. *J. Electron. Spectrosc. Relat. Phenom.*, 195:307, 2014. URL http://www.sciencedirect.com/science/article/pii/S0368204813002430.

[149] P. Decleva, A. Ponzi, and I. Santizo. *J. Phys. Conf. Ser.*, 488:012016, 2014. URL http://iopscience.iop.org/1742-6596/488/1/012016.

[150] J. Söderström, N. Mårtensson, O. Travnikova, M. Patanen, C. Miron, L. J. Sæthre, K. J. Børve, J. J. Rehr, J. J. Kas, F. D. Vila, T. D. Thomas, and S. Svensson. *Phys. Rev. Lett.*, 108:193005, 2012. URL http://link.aps.org/doi/10.1103/PhysRevLett.108.193005.

[151] T. X. Carroll, M. G. Zahl, K. J. Børve, L. J. Sæthre, P. Decleva, A. Ponzi, J. J. Kas, F. D. Vila, J. J. Rehr, and T. D. Thomas. *J. Chem. Phys.*, 138:234310, 2013. URL http://scitation.aip.org/content/aip/journal/jcp/138/23/10.1063/1.4810870.

[152] D. Di Tommaso and P. Decleva. *J. Chem. Phys.*, 123:064311, 2005. URL http://scitation.aip.org/content/aip/journal/jcp/123/6/10.1063/1.1994852.

[153] J. J. Rehr and R. C. Albers. *Rev. Mod. Phys.*, 72:621, 2000. URL http://link.aps.org/doi/10.1103/RevModPhys.72.621.

[154] J. J. Rehr, J. J. Kas, M. P. Prange, A. P. Sorini, Y. Takimoto, and F. Vila. *C. R. Phys.*, 10:548, 2009. URL http://www.sciencedirect.com/science/article/pii/S1631070508001084.

[155] M. Bässler, J.-O. Forsell, O. Björneholm, R. Feifel, M. Jurvansuu, and S. Aksela. *J. Electron. Spectrosc. Relat. Phenom.*, 101:953, 1999. URL http://www.sciencedirect.com/science/article/pii/S036820489800379X.

[156] T. D. Thomas, N. Berrah, J. Bozek, T. X. Carroll, J. Hahne, T. Karlsen, E. Kukk, and L. J. Sæthre. *Phys. Rev. Lett.*, 82:1120, 1999. URL http://link.aps.org/doi/10.1103/PhysRevLett.82.1120.

[157] J. J. Pireaux, S. Svensson, E. Basilier, P-ÅMalmqvist, U. Gelius, R. Caudano, and K. Siegbahn. *Phys. Rev. A*, 14:2133, 1976. URL http://link.aps.org/doi/10.1103/PhysRevA.14.2133.

[158] J. F. Ying, H. Zhu, C. P. Mathers, B. N. Gover, M. P. Banjavčić, Y. Zheng, C. E. Brion, and K. T. Leung. *J. Chem. Phys.*, 98:4512, 1993. URL http://scitation.aip.org/content/aip/journal/jcp/98/6/10.1063/1.465010.

[159] E. Plésiat, P. Decleva, and F. Martìn. *Phys. Chem. Chem. Phys.*, 14:10853, 2012. URL http://dx.doi.org/10.1039/C2CP40693D.

[160] A. D. O. Bagawan and E. R. Davidson. *Adv. Chem. Phys.*, 110:215, 1999.

[161] D. C. Calabro, J. L. Hubbard, C. H. Blevins, A. C. Campbell, and D. L. Liechtenberger. *J. Am. Chem. Soc.*, 103:6839, 1981. URL http://dx.doi.org/10.1021/ja00413a010.

[162] P. Jutzi and N. Burford. *Chem. Rev.*, 99:969, 1999. URL http://pubs.acs.org/doi/abs/10.1021/cr941099t?journalCode=chreay&quickLinkVolume=99&quickLinkPage=969&selectedTab=citation&volume=99.

[163] C. Cauletti, J. C. Green, and M. R. Kelly. *J. Electron. Spectrosc. Relat. Phenom.*, 19:327, 1980. URL http://www.sciencedirect.com/science/article/pii/0368204880800582.

[164] R. Fernández and E. Carmona. *Eur. J. Inorg. Chem.*, 16:3197, 2005. URL http://dx.doi.org/10.1002/ejic.200500329.

[165] R. Van Leeuwen and J. Baerends. *Phys. Rev. A*, 49:2421, 1994. URL http://link.aps.org/doi/10.1103/PhysRevA.49.2421.

[166] C. Fonseca Guerra, J. G. Snijders, G. te Velde, and E. J. Baerends. *Theor. Chem. Acc.*, 99:391, 1998. URL http://link.springer.com/article/10.1007/s002140050353.

[167] I. Bytheway, P. L. A. Popelier, and R. J. Gillespie. *Can. J. Chem.*, 74: 1059–1071, 1996. URL http://dx.doi.org/10.1139/v96-119.

[168] R. A. Andersen, R. Blom, J. M. Boncella, C. J. Burns, and H. V. Volden. *Acta Chem. Scand.*, A41:24, 1987.

[169] M. del Mar Conejo, R. Fernández, D. del Río, E. Carmona, A. Monge, C. Ruiz, A. M. Márquez, and J. Fernández Sanz. *Chem. Eur. J.*, 9:4452, 2003. URL http://dx.doi.org/10.1002/chem.200304876.

[170] J. Vollet, E. Baum, and H. Schnöckel. *Organometallics*, 22:2525, 2003. URL http://dx.doi.org/10.1021/om0301031.

[171] H. W. Kroto, J. R. Heath, S. C. O Brien, R. F. Curl, and R. E. Smalley. *Nature*, 318:162, 1985. URL http://www.nature.com/nature/journal/v318/n6042/abs/318162a0.html.

[172] W. Krätschmer, L. D. Lamb, K. Fostiropoulos, and D. R. Huffman. *Nature*, 347:354, 1990. URL http://www.nature.com/nature/journal/v347/n6291/abs/347354a0.html.

[173] J. P. K. Doye and D. J. Wales. *J. Phys. B: At. Mol. Opt. Phys.*, 29:4859, 1996. URL http://iopscience.iop.org/0953-4075/29/21/002.

[174] J. R. Heath, S. C. O' Brien, Q. Zhang, Y. Liu, R. F. Curl, H. W. Kroto, F. K. Tittel, and R. E. Smalley. *J. Am. Chem. Soc.*, 107:7779, 1985. URL http://dx.doi.org/10.1021/ja00311a102.

[175] W. Harneit, C. Boehme, S. Schaefer, K. Huebener, K. Fostiropoulos, and K. Lips. *Phys. Rev. Lett.*, 98:216601, 2007. URL http://link.aps.org/doi/10.1103/PhysRevLett.98.216601.

[176] J. B. Melanko, M. E. Pearce, and A. K. Salem. *Nanotechnology in Drug Delivery*. edited by M. M. de Villiers, P. Aramwit and G. S. Kwon (Springer, New York), p.105, 2009.

[177] R. B. Ross, C. M. Cardona, D. M. Guldi, S. G. Sankaranarayanan, M. O. Reese, N. Kopidakis, J. Peet, B. Walker, G. C. Bazan, E. V. Keuren, B. C. Holloway, and M. Drees. *Nat. Mater.*, 8:208, 2009. URL http://www.nature.com/nmat/journal/v8/n3/suppinfo/nmat2379_S1.html.

[178] Y. Zhao, Y.-H. Kim, A. C. Dillon, M. J. Heben, and S. B. Zhang. *Phys. Rev. Lett.*, 94:155504, 2005. URL http://link.aps.org/doi/10.1103/PhysRevLett.94.155504.

[179] F. D. Weiss, J. L. Elkind, S. C. O' Brien, R. F. Curl, and R. E Smalley. *J. Am. Chem. Soc.*, 110:4464, 1988. URL http://dx.doi.org/10.1021/ja00221a085.

[180] R. Tellgmann, N. Krawez, S. H. Lin, I. V. Hertel, and E. E. B. Campbell. *Nature*, 382:407, 1996. URL http://www.nature.com/nature/journal/v382/n6590/abs/382407a0.html.

[181] L. S. Wang, J. M. Alford, Y. Chai, M. Diener, J. Zhang, S. M. McClure, T. Guo, G. E. Scuseria, and R. E. Smalley. *Chem. Phys. Lett.*, 207:354, 1993. URL http://www.sciencedirect.com/science/article/pii/0009261493890138.

[182] M. Saunders, H. A. Jimenéz-Vásquez, R. J. Cross, S. Mroczkowski, M. L. Gross, D. E. Giblin, and R. J. Poreda. *J. Am. Chem. Soc.*, 116:2193, 1994. URL http://dx.doi.org/10.1021/ja00084a089.

[183] B. Pietzak, M. Waiblinger, T. Almeida Murphy, A. Weidinger, M. Höhne, E. Dietel, and H. Hirsch. *Chem. Phys. Lett.*, 279:259, 1997. URL http://www.sciencedirect.com/science/article/pii/S0009261497011007.

[184] A. Weidinger, M. Waiblinger, B. Pietzak, and T. Almeida Murphy. *Appl. Phys. A*, 66:287, 1998. URL http://dx.doi.org/10.1007/s003390050668.

[185] A. L. D. Kilcoyne, A. Aguilar, A. Müller, S. Schippers, C. Cisneros, G. Alna'Washi, N. B. Aryal, K. K. Baral, D. A. Esteves, C. M. Thomas, and R. A. Phaneuf. *Phys. Rev. Lett.*, 105:213001, 2010. URL http://link.aps.org/doi/10.1103/PhysRevLett.105.213001.

[186] G. Wendin and B. Wästberg. *Phys. Rev. B*, 48:14764, 1993. URL http://link.aps.org/doi/10.1103/PhysRevB.48.14764.

[187] V. K. Dolmatov. *Advances in Quantum Chemistry: Theory of Confined Quantum Systems, vol.58*. edited by J. R. Sabin and E. Brandas (New York: Academic), 2009.

[188] M. Ya Amusia and A. S. Baltenkov. *Phys. Lett. A*, 360:294, 2006. URL http://www.sciencedirect.com/science/article/pii/S037596010601293X.

[189] J. George, H. R. Varma, P. C. Deshmukh, and S. T. Manson. *J. Phys. B: At. Mol. Opt. Phys.*, 45:185001, 2012. URL http://iopscience.iop.org/0953-4075/45/18/185001/article.

[190] M. Venuti, M. Stener, G. De Alti, and P. Decleva. *J. Chem. Phys.*, 111:4589, 1999. URL http://scitation.aip.org/content/aip/journal/jcp/111/10/10.1063/1.479220.

[191] M. Stener, G. Fronzoni, D. Toffoli, P. Colavita, S. Furlan, and P. Decleva. *J. Phys. B: At. Mol. Opt. Phys.*, 35:1421, 2002. URL http://iopscience.iop.org/0953-4075/35/6/302.

[192] J. Jose and R. Lucchese. *J. Phys. B: At. Mol. Opt. Phys.*, 46:215103, 2013. URL http://iopscience.iop.org/0953-4075/46/21/215103/article.

[193] M. E. Madjet, H. S. Chakraborty, and S. T. Manson. *Phys. Rev. Lett.*, 99:243003, 2007. URL http://link.aps.org/doi/10.1103/PhysRevLett.99.243003.

[194] T. W. Gorczyca, , M. F. Hasoglu, and S. T. Manson. *Phys. Rev. A*, 86:033204, 2012. URL http://link.aps.org/doi/10.1103/PhysRevA.86.033204.

[195] H. S. Chakraborty, M. E. Madjet, J. M Rost, and S. T. Manson. *Phys. Rev. A*, 78:013201, 2008. URL http://link.aps.org/doi/10.1103/PhysRevA.78.013201.

[196] M Stener, P. Decleva, and A. Lisini. *J. Phys. B: At. Mol. Opt. Phys.*, 28:4973, 1995. URL http://iopscience.iop.org/0953-4075/28/23/009.

[197] A. S. Baltenkov, V. K. Dolmatov, and S. T. Manson. *Phys. Rev. A*, 66:023201, 2002. URL http://link.aps.org/doi/10.1103/PhysRevA.66.023201.

[198] T. A. Carlson, M. O. Krause, and W. E. Moddeman. *Journal de Physique*, 32:C4–76, 1971. URL http://dx.doi.org/10.1051/jphyscol:1971425.

[199] N. Jonathan, A. Morris, M. Okuda, K. J. Ross, and D. J. Smith. *Faraday Discussion*, 54:48, 1972. URL http://dx.doi.org/10.1039/DC9725400048.

[200] M. Okuda and N. Jonathan. *Electron Spectrosc.*, 3:19, 1974.

[201] M. Tashiro, K. Ueda, and M. Ehara. *Chem. Phys. Lett.*, 521: 45, 2012. URL http://www.sciencedirect.com/science/article/pii/S0009261411014576.

[202] M. Nakano, P. Selles, P. Lablanquie, Y. Hikosaka, F. Penent, E. Shigemasaand, K. Ito, and S. Carniato. *Phys. Rev. Lett.*, 111:123001, 2013. URL http://link.aps.org/doi/10.1103/PhysRevLett.111.123001.

[203] M. Wells and R. R. Lucchese. *J. Chem. Phys.*, 110:6365, 1999. URL http://scitation.aip.org/content/aip/journal/jcp/110/13/10.1063/1.478540.

[204] M. Lebech, J. C. Houver, G. Raseev, A. S. dos Santos, D. Dowek, and R. Lucchese. *J. Chem. Phys.*, 136:094303, 2012. URL http://scitation.aip.org/content/aip/journal/jcp/136/9/10.1063/1.3681920.

[205] X. J. Liu, H. Fukuzawa, T. Teranishi, A. De Fanis, M. Takahashi, H. Yoshida, A. Cassimi, A. Czasch, L. Schmidt, R. Doerner, I. Koyano, N. Saito, and K. Ueda. *Phys. Rev. Lett.*, 101:023001, 2008. URL http://link.aps.org/doi/10.1103/PhysRevLett.101.023001.

[206] T. Jahnke, J. Titze, L. Foucar, R. Wallauer, T. Osipov, E. P. Benis, O. Jagutzki, W. Arnold, A. Czasch, A. Staudte, M. Schöffler, A. Alnaser, T. Weber, M. H. Prior, H. Schmidt-Böcking, and R. Dörner. *J. Electron. Spectrosc. Relat. Phenom.*, 183:48, 2011. URL http://www.sciencedirect.com/science/article/pii/S0368204810000885.

[207] W. Domcke, L. S. Cederbaum, W. Von Niessen, and W. P. Kraemer. *Chem. Phys. Lett.*, 43:258, 1976. URL http://www.sciencedirect.com/science/article/pii/0009261476852980.

[208] Schirmer, W. Domcke, L. S. Cederbaum, and W. von Niessen. *J. Phys. B: At. Mol. Phys.*, 11:1901, 1978. URL http://iopscience.iop.org/0022-3700/11/11/007.

[209] J. M. Dyke, S. D. Gamblin, D. Haggerston, A. Morris, S. Stranges, J. B. West, T. G. Wright, and A. E. Wright. *J. Chem. Phys.*, 108:6258, 1998. URL http://scitation.aip.org/content/aip/journal/jcp/108/15/10.1063/1.476032.

[210] M. Stener, P. Decleva, T. Mizuno, H. Yoshida, and A. Yagishita. *J. Chem. Phys.*, 140:044305, 2014. URL http://scitation.aip.org/content/aip/journal/jcp/140/4/10.1063/1.4862267.

[211] M. Stener, S. Furlan, and P. Decleva. *J. Phys. B: At. Mol. Opt. Phys.*, 33: 1081, 2000. URL http://iopscience.iop.org/0953-4075/33/5/321.

[212] N. Honjou. *Chem. Phys.*, 324:413, 2006. URL http://www.sciencedirect.com/science/article/pii/S0301010405005707.

[213] Y. R. Miao, C. G. Ning, and J. K. Deng. *Phys. Rev. A*, 83:062706, 2011. URL http://link.aps.org/doi/10.1103/PhysRevA.83.062706.

[214] M. Ilchen, S. Deinert, L. Glaser, F. Scholz, J. Seltmann, P. Walter, and J. Viefhaus. *J. Phys. B: At. Mol. Opt. Phys.*, 45:225102, 2012. URL http://iopscience.iop.org/0953-4075/45/22/225102/article.

[215] E. Shigemasa, J. Adachi, M. Oura, and A. Yagishita. *Phys. Rev. Lett.*, 74:359, 1995. URL http://link.aps.org/doi/10.1103/PhysRevLett.74.359.

[216] F. Kelkensberg, A. Rouzee, W. Siu, G. Gademann, P. Johnsson, M. Lucchini, R. R. Lucchese, and M. J. J. Vrakking. *Phys. Rev. A*, 84:051404, 2011. URL http://link.aps.org/doi/10.1103/PhysRevA.84.051404.

Ringraziamenti

Un breve, possibile elenco di motivi per cui ringraziare il Prof. Piero Decleva dovrebbe certamente contenere la sua generosità, la sua costante presenza, il suo rigore e il suo essere insieme guida e compagno di viaggio. Eppure, ce ne sarebbero tanti altri da non poter essere scritti sulla pagina di una tesi. In una riga posso dirle: grazie, caro Piero, per avermi insegnato, per aver ascoltato e condiviso, per le discussioni letterarie e politiche, per i libri scambiati e grazie per essere riuscito a farmi sentire sempre a casa, anche con il vento a 180 km/h (sì, alla fine di questi anni le credo, era davvero un evento eccezionale...).
Grazie Prof.ssa Giovanna Fronzoni e Prof. Mauro Stener per l'accoglienza e l'aiuto che mi avete offerto fin dal primo giorno. Grazie alla Prof.ssa Sonia Coriani, per l'amicizia e le ore passate febbrilmente di fronte al PC. Che poi, cara Sonia, alla fine, rispetto ad Alan Turing, un sospiro di sollievo lo abbiamo tirato! Grazie, Prof. Nađa Došlić, Zagabria è stata un regalo inaspettato e te ne sono grata. A presto.
Grazie dottor Bodo, per aver sempre tenuto salda la presa del filo Trieste-Roma. Grazie al Prof. Stefano Stranges che, per una catena di casualità, mi ha portato fin quassù. Grazie alla Prof.ssa Maria Novella Piancastelli, per il supporto e la sua affettuosa accoglienza a Parigi. Grazie al Prof. Renzo Cimiraglia per avermi introdotto nei segreti di Molpro e per i giorni belli e intensi passati a Ferrara a lavorare insieme. Grazie al Prof. Celestino Angeli, al tempo dedicatomi per far tornare i conti, alle cene e passeggiate ferraresi e grazie al sorriso e al buonumore di tutta la tribù degli Angeli: Lorenzo, Andrea e Marco.

Trieste, sono stata ingiusta con te, ma qualche rimprovero te lo sei meritato. Nonostante i nostri inizi burrascosi, ho ricevuto così tanto da te che non posso che dirti grazie. Grazie a San Giacomo, al porto, alle meduse, al mutare improvviso del cielo, perfino al vento e poi grazie a *lassù San Giusto che ci protegge tutti.*
Thanks Cathal, my special and patient proofreader, for the time dedicated to my

thesis, for that spent together and because although there was a rare wild boar... Thanks Elie, for making me gaze at the fascinating mid-eastern world, for the Benningan's dishes and because *come si dice?* Grazie Elena, per la tua premura materna, per quel nostro primo anno, per le grigliate, gli spritz non consumati e per tutte le volte che mi hai preparato pranzi e cene quando avevo la febbre. Grazie al gruppo-pranzo-C11, insostituibili amici. Grazie Michele, Mimmo, la Ale, ingegnerissima Anna, Nicola, Elenutti, Rudy, Nicole, foto-bomber Cavigli e Glemo. Grazie Guercina e Valeria perché *figo xe altro* ma a noi non ci importa niente. Grazie Nicola, caro zero, per le tue affettuose caramelle alla menta e le risate sul gruppo_del_thè, rigorosamente con underscore. Grazie Erica e Corrado, etruschi di adozione, per la vostra vicinanza e quella premurosa cena di agosto. Grazie Ann, triestina inaspettata.

Grazie Ale, dottoressa Ciavardini, passano gli anni ma il *Consiglio all'attrice C. N.* del povero Bertolt Brecht rimane sempre quello e nessuno lo sa meglio di te. Grazie Michelangelo, perché *in a minute there is a time/for decisions and revisions which a minute will reverse...* Grazie Roz, per le nostre ore al telefono rigorosamente dopo mezzanotte, per saper condividere sempre tutto e per essere così pazzo da viaggiare leggero fino all'altra parte del mondo. Grazie Chiara, per pronunciare quel sì ad ogni domanda, per l'amicizia intatta, perché prima o poi all'Oktoberfest ci andiamo insieme e perché marcobella. Grazie mio hermano Federico, per esserci sempre.
Grazie a tutti i pezzi di cuore che ho lasciato a Roma (soprattutto a quelli che hanno fatto sosta a Trieste) e grazie mamma Roma.
Grazie Eva, quel quaderno lo riempiremo prima e poi e allora sai le risate che ci faremo. Grazie per riuscire ogni volta a cucinare per dieci persone in un pentolino da due, per farmi sentire le mie valigie più leggere e per ricordarmi sempre, come io faccio con te, che la *vita è un walser*. Grazie mamma e papà, siamo arrivati alla terza e ve la dedico con tutto il cuore, questa è per voi.

Trieste e una donna. E allora Letizia, grazie. Conosci uno per uno tutti i motivi per cui ti sono grata. Non mi costringerai mica a ringraziare pubblicamente Duino per averci fatto incontrare?
Ed eccole qui, infine, Oscar e Renato, le mie due colonne. A questo punto vorrei sciogliermi in una incontrollabile risata, come quando quel tale tentò di aprire a testate una porta a vetri. E invece, ora, crepo di malinconia al pensiero di separarmi da voi, nonostante poi lo so che, prima o dopo, ci si rivede al Puzlaiz.